MAGNETIC STUDIES OF COBALT BASED GRANULAR THIN FILMS

Colin John Oates

A Thesis Submitted for the Degree of PhD
at the
University of St Andrews

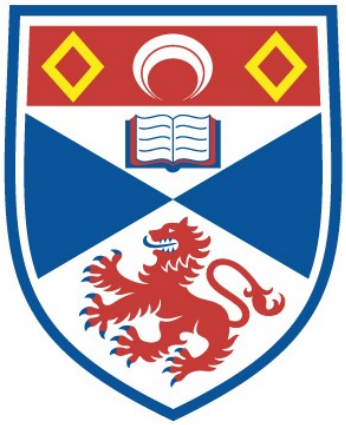

2002

MAGNETIC STUDIES OF COBALT BASED GRANULAR THIN FILMS

Colin John Oates
University of St. Andrews

Thesis submitted for the degree of Doctor of Philosophy,
August 2002

Abstract

The magnetic recording media used for hard disks in laptops and PC's is constantly being improved, leading to rapid increases in data rate and storage density. However, by the year 2010, it is predicted that the superparamagnetic limit will be reached, which is potentially insufficient for data storage. At the beginning of this century, CoCr – based alloys are used in longitudinal media since cobalt has a high magnetocrystalline anisotropy.

In this thesis, the static and dynamic properties of longitudinal recording thin films were investigated in order to explain and correlate their magnetic characteristics to their recording properties. The samples in question were test samples and some were in commercial use. Magnetic techniques such as high field ferromagnetic resonance and torque magnetometry were used to determine accurately the crystalline anisotropy field. High field ferromagnetic resonance is an ideal tool to determine the crystalline anisotropy, magnetisation, Lande g-factor and the gyromagnetic damping factor. In contrast to previous work, there are no FMR simulations and so all the relevant parameters were determined directly from measurement. Ideally, there should be no exchange interactions between the neighbouring cobalt grains; however, interactions between the grains within the CoCr-alloy recording layer exist. Previous work on the measurements of interactions in recording media involves measuring the sample's magnetisation. In this thesis, an alternative novel method involves torque magnetometry.

Another technique that was used in this thesis is small angle neutron scattering, which aims to determine the size of the magnetic grains and compare that with the physical size determined from TEM, by Seagate.

There is an extended section on Co_xAg_{1-x} granular thin films, which involves determining the sample's g-factor, effective anisotropy, grain size, exchange constant and comparing the FMR lineshapes at 9.5 and 92GHz.

Declarations

I, Colin John Oates, hereby certify that this thesis, which is approximately 30000 words in length, has been written by me, that it is the record of work carried out by me and that it has not been submitted in any previous application for a higher degree.

Colin John Oates
August 2002

I was admitted as a research student in October 1998 and as a candidate for the degree of Doctor of Philosophy in October 1999; the higher study for which this is a record was carried out in the University of St. Andrews between 1998 and 2002.

Colin John Oates
August 2002

I hereby certify that the candidate has fulfilled the conditions of the Resolution and Regulations appropriate for the degree of Doctor of Philosophy in the University of St. Andrews and that the candidate is qualified to submit this thesis in application for that degree.

P.C.Riedi
August 2002

In submitting this thesis to the University of St. Andrews I understand that I am giving permission for it to be made available for use in accordance with the regulations of the University Library for the time being in force, subject to any copyright vested in the work not being affected thereby. I also understand that the title and abstract will be published, and that a copy of the work may be made and supplied to any *bona fide* library or research worker.

Colin John Oates
August 2002

Acknowledgements

I would like to thank both Prof. Peter Riedi and Dr. Graham Smith for their support and unlimited patience throughout my PhD. Both Peter and Graham have provided sound advice on problems arisen throughout the four years of my PhD.

I am also grateful to Dr. Feodor Ogrin, now in Exeter University. Feodor was very helpful and his discussions and guidance on FMR and torque magnetometry were invaluable.

I would also like to thank Prof. Steve Lee for allowing me to take part in the SANS experiment as well as participating in the 'torque team', which I feel I have benefited.

Dr. Tom Thomson, who is now working for IBM has been a great help throughout my Ph.D. His providence of recording thin films and background discussions on the materials were of course invaluable and Tom also played an important part in allowing some of my work in this thesis to be published with Seagate's permission.

Dr. Nigel Poolton, who is now working in Daresbury, was a very helpful postdoc who had a lot of patience in explaining how the spectrometer worked as well as the software designs. Dr. Adroja (now in Rutherford Appleton Laboratory in Didcot) has shown how to run the NMR spectrometer and explain other parts of magnetism that I did not fully understand.

Thanks to Prof. John Walton for allowing me to carry out FMR work on the Bruker; Dr. Natalia Lesnik for providing nanocluster samples as well as discussions based on FMR and Prof Bob Cywinski for his discussions on neutron diffraction and fine particle magnetism.

Thanks also to Shannon Brown (soon to be Dr. S.G.Brown), Paul Cruickshank, Prof. Czeslaw Kapusta and Dr. Charles Dewhurst from the ILL.

There are members of the workshop who have worked hard in constructing a 90GHz in-plane sample rotator and prepared samples for FMR measurements, as discussed in chapter four. Thanks to George

Radley, Paul 'neebor' Aitken, Steven Balfour, Andy Barman, Bob Mitchell, Reg Gavine and Fritz Akerboom.

Finally, there are two more people to whom I am in debt to for their unlimited moral support during my undergraduate and postgraduate studies: John and Sheila Oates. This thesis is dedicated to these two special people.

Contents

Chapter 1

Basic Theory: Ferromagnetism and Recording Thin Film Media

This thesis presents methods of determining the magnetic properties of ferromagnetic granular thin films. Examples of films studied are those of the CoCr alloy recording media, which were either test samples or in commercial use.

To start off, it is necessary to cover in this chapter the fundamentals and features of ferromagnetism and recording media.

1.1 Fundamentals

1.1.1 Internal field

The fundamental equation for the magnetic induction $\vec{B}$ inside a magnetic material is given by:

$$\vec{B} = \mu_0\left(\vec{H} + \vec{M}\right) \qquad \text{in SI units} \qquad (1.1)$$

or $$\vec{B} = \vec{H} + 4\pi\vec{M} \qquad \text{in c.g.s. units} \qquad (1.2)$$

From the SI units version, the term μ_0 is the permeability of free space (4π x $10^{-7}Hm^{-1}$), $\vec{H}$ is the magnetic field intensity and $\vec{M}$ is the magnetisation, generally defined as the total magnetic moment per unit volume. (In this thesis, all measurements are in cgs units).

If a magnetic body of finite size is magnetised, free poles are induced on both ends as shown in figure 1.1.

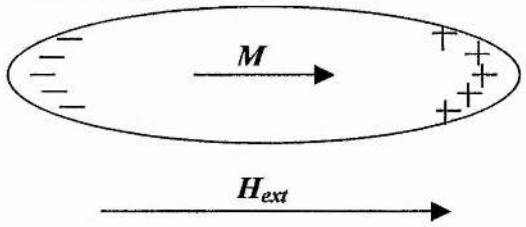

Figure 1.1. Free poles on magnetic materials

These in turn, give rise to a magnetic field in a direction opposite to that of the magnetisation. This field is known as the demagnetising field, $\vec{H}_D$, and is proportional to the intensity of magnetisation, $\vec{M}$.

The intensity of the internal field (which is directed along an axis of symmetry) in the material is therefore $\vec{H}_{int} = \vec{H} - N_D\vec{M}$. The demagnetising factor N_D is only well defined for an ellipse and on the angle between the field $\vec{H}$ and its axis of symmetry: it varies between 0 and 1 in SI units and between 0 and 4π in cgs units. The demagnetising factor for an infinitely narrow cylinder is zero, under the action of a field $\vec{H}$ parallel to its axis, and is equal to $4\pi/3$ for a sphere. Section 2.1.5 in chapter two describes more on demagnetising factors and presents a table of demagnetising terms for ellipsoids.

1.1.2 Magnetic moments

The magnetic moment of a free atom has three principal sources: the spin with which electrons are endowed; their orbital angular momentum about the nucleus; and the change in the orbital moment induced by an applied magnetic field.

The first two effects give rise to paramagnetic contributions to the magnetisation and the third gives a diamagnetic contribution. Contributions to paramagnetism appear only from the partially filled 3d (iron group), 4d (palladium group), 5d (platinum group) or 4f shells (rare earth group) and also outer s electrons.

The magnetic susceptibility (defined as the ratio of the magnetisation $\vec{M}$ and the magnetic field intensity, $\vec{H}$) for a diamagnet and paramagnet is negative and positive, respectively, as shown in figure 1.2.

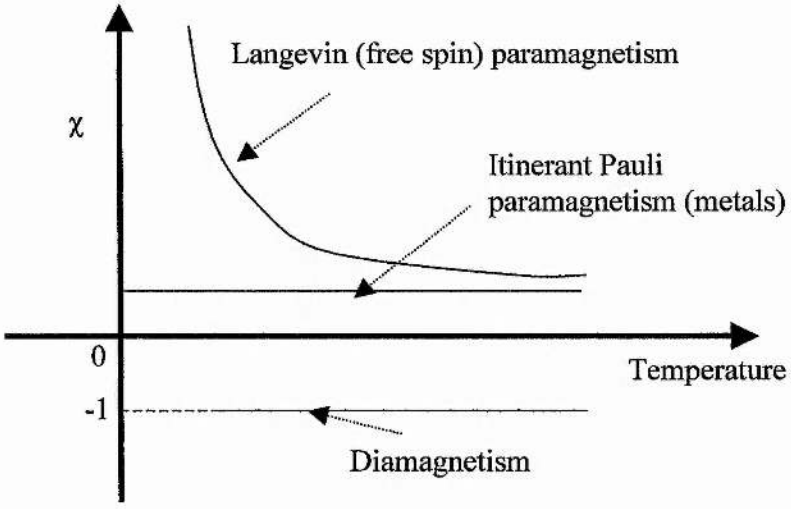

Figure 1.2: Characteristic magnetic susceptibility of diamagnetic and paramagnetic substances [1]

Ordered arrays of magnetic moments may be ferromagnetic, ferrimagnetic, antiferromagnetic or may be more complex in form, as shown in figure 1.3.

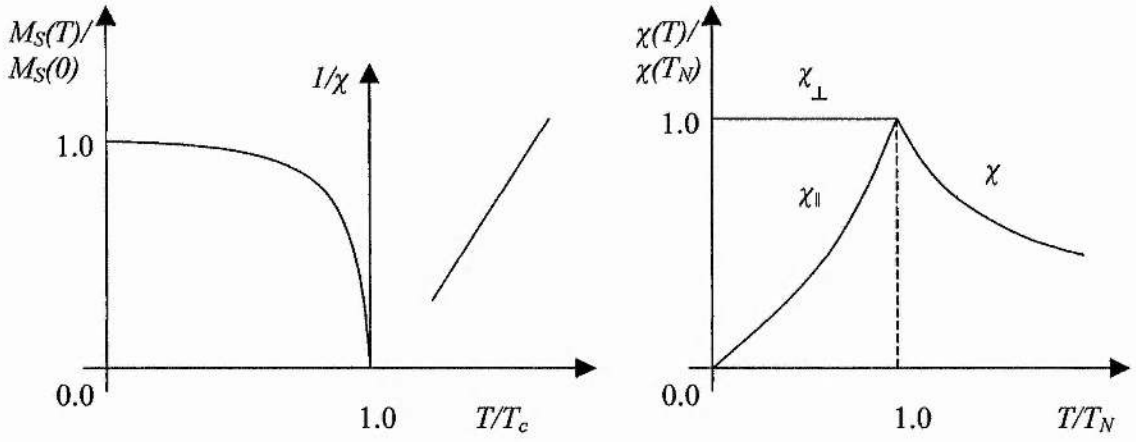

Figure 1.3. Graphs of the temperature dependence of (a) the magnetisation, M, of a ferromagnetic material and the dependence of the inverse susceptibility and (b) of the susceptibility of an antiferromagnetic material. [2]

Nuclear magnetic moments gives rise to nuclear paramagnetism. Magnetic moments of nuclei are of the order of 10^{-3} times smaller than the magnetic moment of electrons, since nuclear mass is 1836 times larger than electron mass.

1.1.3 Basic quantum mechanics of magnetism

Before proceeding with the definition of cooperative phenomena, such as ferromagnetism and paramagnetism, it is necessary to go over the concepts of elementary magnetic moments.

As mentioned previously, the magnetic moments are spin and orbital magnetic moments of electrons. The net moments of all inner (filled) electron shells of atoms are equal to zero. In ionic crystals, the total spin plus orbital magnetic moments of ions can be regarded as elementary magnetic moments.

In quantum mechanics, the state of the electron is characterised by four quantum numbers.

1. Principal quantum number n, which determines the energy of the shell or orbit;
2. Orbital quantum number (integer) l, which determines the orbital angular momentum of the electron, whose magnitude is given by $\sqrt{l(l+1)}\hbar$. The value of l starts from $0, 1, 2, \ldots n-1$;
3. The magnetic quantum number m_l, which gives the component of the orbital momentum along a given direction and may be equal to $l, l-1, l-2, \ldots 0 \ldots -(l-1), -l$; that is, it takes $2l+1$ values. In the spatial representation of the atomic quantities the orbital momentum can only point along certain directions and its projections are given by m_l, as illustrated in figure 1.4 for a 3d electron.

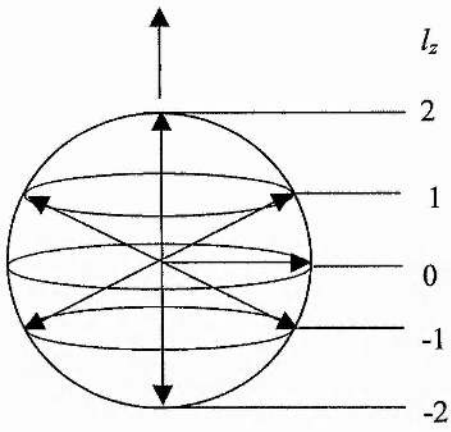

Figure 1.4. Orbital angular momentum of a 3d electron (l=2), and its value along a direction z, showing space quantization [2]

4. Finally, the spin quantum number m_s and for the case of the electrons takes values *1/2* and *–1/2*.

The magnitude of the magnetic moment corresponding to the orbital angular momentum is

$$|\mu_l| = \frac{e\hbar}{2m}\sqrt{l(l+1)} \qquad (1.3)$$

and the component of the magnetic orbital moment μ_l in a direction defined by an applied magnetic field is

$$|\mu_l^z| = \frac{e}{2m} m_l \hbar \qquad (1.4)$$

The magnitude of the magnetic moment corresponding to the spin angular momentum is

$$|\mu_s^z| = \frac{e}{m} m_s \hbar \qquad (1.5)$$

which differs from the orbital magnetic moment only by a factor of 2. The orbital and spin momenta of an electron interact with each other, as well as with the momenta of different electrons of the same atom. This leads to the coupling of spins and orbital momenta of different

electrons, forming the total spin angular momentum S and orbital momentum L. This is called the Russell-Saunders coupling:

$$\begin{aligned} s_i &\rightarrow S \\ l_i &\rightarrow L \end{aligned} \qquad (1.6)$$

In heavy atoms, there is a strong coupling between l_i and s_i of each electron, which leads to the total angular momenta per electron j_i. This is called jj coupling.

Since the total spin and orbital momenta interact through the atomic spin-orbit interaction L and S combine to form the total angular momentum J. The corresponding quantum number J may take values

$$J = L + S,\ L + S - 1,\ \ldots .\ |L - S| \qquad (1.7)$$

and the levels defined by these values of J are called multiplets and the projection of J along an arbitrary direction is quantised with the corresponding quantum number M_J, which take values

$$M_J = J,\ J - 1,\ \ldots .,\ -J. \qquad (1.8)$$

As a result of $\vec{\mu}_L = \mu_B \vec{L}$ and $\vec{\mu}_S = 2\mu_B \vec{S}$, the vector addition of the orbital and spin components to the magnetic moment gives a value $\vec{\mu}_J = g_J \mu_B \vec{J}$ for the overall magnetic moment, where the Lande g-factor has the form

$$g_J = 1 + \frac{S(S+1) + J(J+1) - L(L+1)}{2J(J+1)} \qquad (1.9)$$

which is usually derived in texts on modern physics [2-4]. Typical values of the spectroscopic splitting factor of cobalt, iron and nickel are 2.20, 2.09 and 2.23 [5], respectively. Of course for pure spin or orbital motion these expressions reduce to $\vec{\mu}_L = \mu_B \vec{L}$ and $\vec{\mu}_S = 2\mu_B \vec{S}$, respectively.

The next two sections will now look at the theory of paramagnetism and ferromagnetism.

1.1.4. Paramagnetism

The states with different μ^z values are degenerate in the absence of an external magnetic field. When the magnetic field H is applied, there appears the potential energy of a magnetic moment in this field (the Zeeman energy)

$$E_J^Z = -\mu_J^Z H = -g\mu_B JH \tag{1.10}$$

and the degeneracy is removed. There are $(2J+1)$ equidistant energy levels separated by intervals

$$\Delta E = \gamma\hbar H \tag{1.11}$$

Transitions between these levels, with the absorption of a electromagnetic energy quanta $\hbar\omega$, are called electron paramagnetic resonance, or electron spin resonance. Only transitions between the neighbouring levels are allowed by the selection rules, $\Delta m_J = \pm 1$ and the resonance condition is given as

$$\omega = \gamma H = \frac{g\mu_B}{\hbar} H \tag{1.12}$$

The difference in populations of the levels with different μ^z results in the appearance of the net moment in the direction of the field H. The calculation, with the use of the general formulae of quantum statistics leads to the expression for the magnetisation

$$M = M_0 B_J\left(\frac{M_0 H}{kT}\right) \tag{1.13}$$

where $B_J(x)$ is the Brillouin function [4-6] defined as

$$B_J(x) = \left(1+\frac{1}{2J}\right)\coth\left(\left(1+\frac{1}{2J}\right)x\right) - \frac{1}{2J}\coth\left(\frac{x}{2J}\right) \tag{1.14}$$

where $M_o = \gamma\hbar NJ$ is the saturation magnetisation, N is the number of magnetic moments in a unit volume, and k is the Boltzmann constant.

From the Brillouin function, as x approaches infinity; that is, in the very high magnetic field and/or low temperature limit, $B_J(x)$ tends towards unity, and all the magnetic moments are oriented in the direction of the field. For small x, expanding $B_J(x)$ as a power series, one would obtain from (1.13) the relation $M = \chi_P H$. The paramagnetic

susceptibility χ_P, which does not depend on H in this limiting case, can be written as

$$\chi_P = \frac{C}{T} \tag{1.15}$$

where

$$C = \frac{J(J+1)Ng^2\mu_B^2}{3k} \tag{1.16}$$

is the Curie constant and (1.15) is the Curie law. The constant C contains $g^2J(J+1)$, which is the square of the effective paramagnetic moment:

$$P_{eff}=g(J(J+1))^{1/2} \tag{1.17}$$

The values of the moments P_{eff} of the rare earths (set of elements of atomic number between 57 (La) and 71 (Lu) plus elements Sc and Y [2]) determined experimentally are in good agreement with the P_{eff} computed with the above expression.

If we compare the effective paramagnetic moments of the transition salts of the d series one finds a large disagreement between the computed effective moments P_{eff} and the measured moments [1]. With g equal to 2, agreement is recovered if we write S rather than J in the expression of P_{eff}. This is evidence for the importance of the interaction of these ions with the electrostatic crystalline field. This interaction is larger than the spin-orbit interaction.

The difference in behaviour of the rare earth and the iron group is that the 4f shell responsible for paramagnetism in rare earth ions lies deep inside the ions, within the 5s and 5p shells, whereas in the iron group ions the 3d shell responsible for the magnetism is the outermost shell. The 3d shell experiences the intense inhomogeneous electric field produced by neighbouring ions. This inhomogeneous electric field is called the **crystal field**. The interaction of the 3d paramagnetic ions with the crystal field has two major effects: L-S coupling is largely broken up, so that the states are no longer specified by their J values and the $2L+1$ states for a given value of L may now be split by the crystal field. This splitting diminishes the contribution of the orbital motion to the magnetic moment.

Langevin paramagnetism

In the derivation of the expression of the magnetic moment of an assembly of atoms, the quantization of the angular momentum was taken into account. If the angular momentum were not quantized, as in the classical case, any value of μ^z would be allowed, and the magnetic moments could point along any direction in relation to the direction of the external field, $\bar{B}$.

The magnetic moment's z projection is defined as

$$\langle \mu^z \rangle = g\mu_B NJL(x) \qquad (1.18)$$

where $L(x)$ is the Langevin function. This function describes well the magnetisation of small particles formed of large clusters of atoms, in systems known as superparamagnetic. The effective moments in these systems are very large; for example, 10^5 Bohr magnetons.

1.1.5. Ferromagnetism

In ferromagnetic materials there is a non-zero magnetic moment (inside a domain), even in the absence of an external field. This order disappears above a certain temperature called the Curie temperature, T_C. The formal explanation of this fact was presented by Weiss in 1907 [7]. He postulated that an individual atomic moment is oriented under the influence of other magnetic moments, which act through an effective magnetic field, known as the molecular field

$$H_m = \Delta M \qquad (1.19)$$

and is proportional to the magnetisation. Here Δ is a large constant, the physical nature of which Weiss was not able to explain.

Substituting $H+H_M$ for H in $M = M_0 B_J\left(\frac{M_0 H}{kT}\right)$, equation (1.13), we obtain

$$M = M_0 B_J\left(\frac{M_0(H+\Delta M)}{NkT}\right) \qquad (1.20)$$

Solving the above equation for M in the most interesting case of $H=0$, we see that there is a non-trivial solution. M is non-zero, if $T<T_c$ where $T_c=\Delta C$ and C is the Curie constant. The temperature T_c is the Curie point, and M is the spontaneous magnetisation of a ferromagnet. Table 1.1 is the magnetic data for 3d ferromagnetic metals below the Curie point.

Material	Magnetisation at 290K (kOe)	Magnetisation at 0K (kOe)
iron	1.707	1.752
nickel	0.485	0.510
cobalt	1.408	1.446

Table 1.1 Magnetisation data for 3d iron-group metals[5]

At $T>T_c$ the spontaneous magnetisation is equal to zero; however, under the influence of an external field, a non-zero magnetisation appears, as in the case of a paramagnet and the Brillouin function becomes small. The susceptibility per unit volume is given as

$$\chi_F = \frac{C}{T-\theta_p} \tag{1.21}$$

and

$$T_C = \frac{g^2\mu_B^2 NJ(J+1)\Delta}{3k} \tag{1.22}$$

This relation is the Curie-Weiss law and θ_p is the paramagnetic Curie temperature.

The results of the experimental investigation of the susceptibility of iron, nickel and cobalt [8] above the ferromagnetic Curie point shows that for temperatures a few degrees above T_c, the inverse of the susceptibility versus temperature curves are linear over a considerable temperature range. In the neighbourhood of the ferromagnetic Curie point, however, all three metals show a curvature, concave upward. The intercept on the linear part of the curve with the temperature axis is just θ_p. Since θ_p does not coincide with T_c, as predicted by the Weiss theory, it is often called the paramagnetic Curie temperature.

1.1.6. Exchange interaction

In ferromagnetic materials the individual atomic dipoles are coupled with each other and form ferromagnetically ordered states. Such a coupling is quantum mechanical and electrostatic in nature and is known as the exchange interaction. The lowest value of energy in a material occurs when the magnetic moment and the magnetic field are aligned. The process of alignment due to their own internal fields (molecular fields) is again called the exchange interaction.

The accepted interpretation of the nature of the molecular field was first presented by Heisenberg. According to his theory, the force which makes the spins line up is an exchange force of quantum mechanical nature. The potential energy between two atoms having spin S_i and S_j is given by

$$H_{ij} = -2J\vec{S}_i \cdot \vec{S}_j \qquad (1.23)$$

where J is the exchange integral and is related to the overlap of the charge distributions of the atoms i and j.

The Pauli principle permits an orbit to be occupied by spin up and spin down electrons, while two electrons with the same kind of spin cannot approach one another closely. Thus the mean distance between two electrons should be different for parallel spins from that for anti-parallel spins, and thus the Coulombic energy (electrostatic) of a system will depend on the relative orientation of the spins: the difference in energy defines the exchange energy. For exchange interactions between nearest neighbours, the exchange integral J is proportional to the molecular field constant, Δ, through the expression [2]

$$J = \frac{g^2 \mu_B^2 N \Delta}{2(g-1)^2 z} \qquad (1.24)$$

where z is the number of nearest neighbours and n is the number of atoms per unit volume. As examples, $J(Fe)$ = 0.015meV and $J(Ni)$ = 0.02 meV [2].

There are two ways of interpreting spin configurations in ferromagnetic materials. One is based on a localised model in which the electrons responsible for ferromagnetism are regarded as localised at their respective atoms. Rare earth metals, such as gadolinium are good examples, because the electron spins responsible for the magnetism of these metals are confined to the deep inner 4f shell of individual atoms and the atomic moments interact with one another by an exchange interaction through conduction electrons is an RKKY (Ruderman-Kittel-Kasuya-Yoshida) interaction.

Secondly, the itinerant model, in which electrons responsible for ferromagnetism are thought of as wandering throughout the crystal lattice. Since the 3d shells of the 3d transition metals such as cobalt, iron and nickel are most exposed except for the conducting 4s electrons, the 3d shells of individual atoms are thought to be nearly touching or overlapping with those of neighbouring atoms (direct exchange). Hence the energy levels of the 3d electrons are perturbed and spread to form a narrow energy band [2].

A simple model for the description of transition metal ferromagnetism is the Stoner model (1938) [9], which treats the electron-electron interactions within the mean field approximation. Similar to the treatment of the magnetism of localised electrons, one can obtain the magnetisation of the itinerant electron (Pauli paramagnetism), as discussed in [2, 3, 5] and add an extra magnetic field, the molecular field, to the external field. The Stoner Criterion at $T=0K$ is given as $[1-UN(E_F)]<0$ where $U(=\mu_B^2\Delta)$ is the electron-electron interactions and $N(E_F)$ is the density of states at the Fermi level. From the condition, ferromagnetism is favoured for strong electron-electron interaction (large U) and high density of electronic states at the Fermi level. Computed values of $[1-UN(E_F)]$ give –0.5 to –0.7 for Fe and –1.1 for Ni [10]. For the $T\neq 0K$ case, the Stoner model has a critical value of the parameter θ', which is the molecular field parameter defined as

$\theta' = \frac{N\mu_B^2\Delta}{k}$. If $\frac{k\theta'}{E_F} < \frac{2}{3}$, then there is no ferromagnetic order [2]. This condition is equivalent to the Stoner Criterion. Further discussion on the band theory of ferromagnetism are found in [2-5, 11].

1.1.7. Magnetic anisotropy

Many magnetic materials show preferential directions for the alignment of magnetisation. These directions are energetically favourable and called "easy axes". The energetically unfavourable directions are known as "hard axes" and are rotated through 90 degrees from the easy axes for a hexagonal close packed lattice. The strength of the anisotropy determines the difficulty in rotating the magnetisation direction from its stable alignment along the preferred axis. The anisotropy energy arises mainly from the interaction of the electronic orbital angular momenta with the crystalline field; that is, with the electric field at the site of the magnetic ions. The exchange energy is isotropic, and therefore, cannot be responsible for this anisotropy; the microscopic origin of the anisotropy lies in the interaction of the atomic orbital moment with charges of the lattice. The spin momentum of the atoms, is involved in this interaction through *L-S* coupling. The energy of the **crystal magnetic anisotropy** E_{anis} can be represented in the form of a power series with respect to the directional cosines of the magnetisation vector relative to the crystal's principal axes. In this case, for crystals with cubic symmetry we have [2, 12]

$$E_{anis} = K_0 + K_1\left(\alpha_1^2\alpha_2^2\alpha_3^2\right) + K_2\left(\alpha_1^2\alpha_2^2 + \alpha_1^2\alpha_3^2 + \alpha_2^2\alpha_3^2\right) \qquad (1.25)$$

where α_1, α_2, α_3 are the directional cosines of M relative to the edges of the cube and K_1 and K_2 are first and second anisotropy constants.

When a material, such as cobalt, has only one easy axis, the material is said to have uniaxial anisotropy which is defined as [2, 4]

$$E_{anis} = K_0 + K_1\sin^2\theta + K_2\sin^4\theta + K_3\sin^6\theta \qquad (1.26)$$

where θ is the angle between M and the crystal's main axis. Examples of anisotropy constants for 3d iron-group metals at room temperature are given in table 1.2.

Metal	K_1 (ergs/cc)	K_2 (ergs/cc)
Fe	4.6×10^5	1.5×10^5
Ni	-5×10^4	-
Co	4.1×10^6	1×10^6

Table 1.2. Representative values of the anisotropy constant for ferromagnetic metals at room temperature [4,5].

Ignoring K_0, and because the anisotropy is uniaxial, that is, E_{anis} does not depend on the angle with the directions of the basal plane, the anisotropy energy is written as [2]

$$E_{anis} = K_1 \sin^2 \theta \qquad (1.27)$$

There are other contributions to the anisotropy, related to the shape of the samples, their state of mechanical stress and so on. These are the extrinsic contributions. Anisotropy can also be induced by applying a strong magnetic field during sample preparation.

In the case of thin films and especially multilayer structures, the so-called interface anisotropy (related to the surface and strain) is also of great influence. The magnetic anisotropy field can be determined by torque magnetometry and ferromagnetic resonance [13].

1.1.8. Superparamagnetic behaviour

Thermal fluctuations agitate the magnetic moment of a nanograin and cause a 'Brownian motion' of the magnetisation. Neel [14] proposed that the magnetisation reversal time τ from one energy minima to another can be estimated by Arrhenius exponent [15]

$$\frac{1}{\tau} = f_0 \exp\left(-\frac{E_b}{kT}\right) = f_0 \exp\left(\frac{-K_{eff}V}{kT}\right) \qquad (1.28)$$

where E_b is the anisotropy energy barrier, T is the temperature and f_o is the attempt frequency. The reduction of the volume, V, of the particle leads to a small anisotropy barrier $E_b = K_{eff}V$, which can be less than the thermal energy. The magnetic moment of the nanoparticle can then

jump over the anisotropy barrier between the different equilibrium positions. This effect called superparamagnetism determines the critical particle size. Below this size, the particle loses its magnetic memory. If we use parameters: $K_{eff} = 10^5\ J/m^3$, $T = 300K$, $\tau_0 = 10^{-8}s$, the relaxation time of $\tau=0.1s$ is determined for a critical diameter of $3.4nm$. If the critical diameter is $4.4nm$, then the reversal time is $10^8 s$ [16]. This example shows a very narrow area in which the particle changes from a stable to an unstable state. If the particle of a certain material becomes smaller then the thermal stability ($K_{eff}V/kT$) becomes smaller. In magnetically hard metals with $K_{eff} = 10^6 J/m^3$, the magnetic lifetimes becomes longer than 10 years for a particle diameter of 1nm [17].

1.1.9. Reversing mechansisms

The reversal of the magnetisation is a basic principle of magnetic recording. Magnetisation in a material can be reversed by applying a field and finally the whole material will be saturated in a direction parallel to the field. The two different states of + and – magnetisation are the basic idea for digital information storage. The mode of magnetisation reversal depends on the material and its size and shape. The two principal methods for reversing the magnetisation are rotation and domain-wall motion. Depending on the crystal size and the chemical homogeneity, the thin film structures can operate as a continuous layer (reverse by domain wall motion) or more like a particulate medium (less exchange between the crystallites), which reverses its magnetisation by one of the rotation mechanisms. From the schematic next page, figure 1.5, in the coherent rotation mode the atomic spins remain parallel during reversal process and this may apply only for small particles. If the particle size increases, incoherent switching mechanisms like curling, buckling and fanning are used [16].

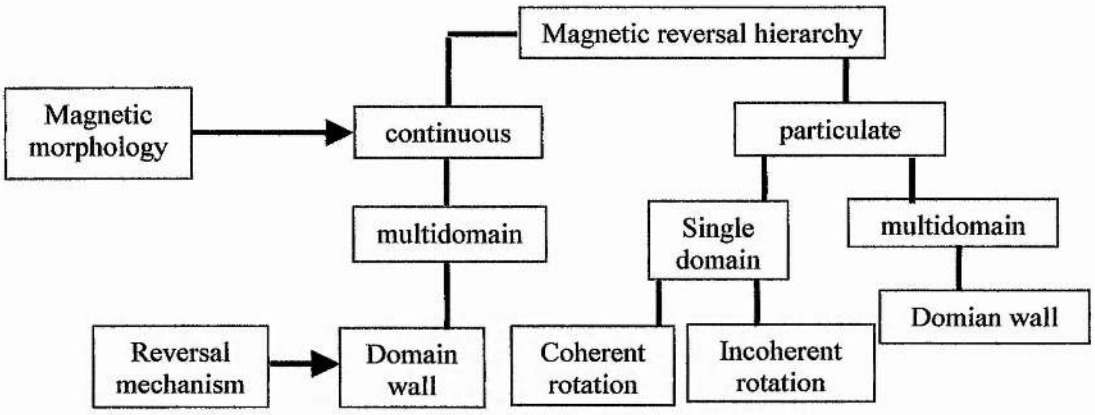

Figure 1.5. Schematic overview of the possible reversal mechanisms depending in the dimensions of the sample [16].

The ideal magnetic structure for a magnetic recording medium consisting of polycrystalline microstructure is a crystallite that reverses its magnetisation by rotation and not by domain-wall motion. In other words, for high density recording the crystallites should act as independent single-domain particles without exchange interaction.

Of course for this type of medium, magnetostatic interaction will play an important role and depends on the type of material and the intercrystalline distances.

In practice, thin films possessed a wide distribution of grain size and not all crystallites are completely separated from each other. This mixture of exchange and magnetostatic coupling will influence the reversal behaviour. Measurements on the interactions in particulate recording media are discussed in chapter three, section 3.3.

Table 1.3 is a list of the critical single domain diameters of spherical particles.

material	D_{crit} (nm)
Cobalt	70
Iron	14
Nickel	55

Table 1.3. Critical diameters of single domain particles for a magnetisation reversal of 10 years at 300K [16].

Advanced magnetic recording systems are designed for extremely high areal densities and data rate. These two aspects require both magnetisation reversal at very short times (<1ns) and long term (5 to 10 years) stability against thermal fluctuations. These are two basic physics problems associated with these requirements. The first is an understanding of the physics of the relaxation mechanisms for magnetisation motions. The second is a characterisation of thermally agitated magnetisation reversal over wide time range. Chapter two, section 2.1.7 explains the magnetisation dynamics with a discussion in the damping mechanisms. The Landau-Liftschitz and Gilbert equation is applicable to coherent rotation.

Further discussions on the thermal fluctuations and on mechanisms associated with small and large magnetisation motions are found in ref [17].

1.2. Magnetic recording media

1.2.1 Compound annual growth rate

Magnetic storage has played a key role in audio, video and computer development since it was first patented in 1898 by the Danish telephone and telegraph engineer, Valdemar Poulsen [16]. IBM built the original hard disk drive, known as RAMAC in 1956. It had an areal density of 2kbits/in^2, a data rate of 70 kbits/s and stored 5Mbytes of information on fifty 24-inch disks. From 1956 to 1991, the areal density has been increasing at an average rate of 23% per year (10 fold in 10 years). The areal density of magnetic recording has accelerated to 100%/year at present, figure 1.6. This rapid increase is made through the introduction of advanced components such as the GMR (giant magnetoresistance) head and fine-grain recording media.

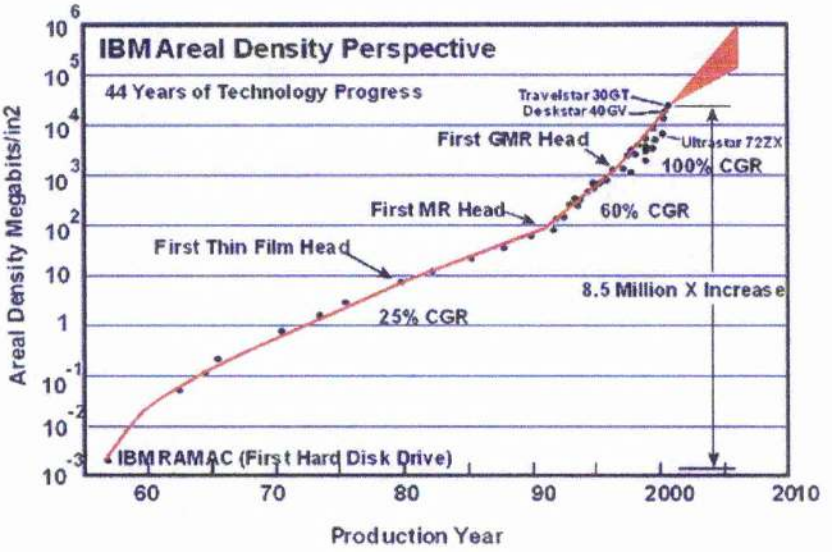

Figure 1.6 The storage density road map [18]

Currently, it takes about 2 years from a laboratory demonstration to market introduction. With the rapid advancement of areal density and data rate in magnetic disk drives, 100Gb/in^2 and 100Mbytes/sec will be reached early in this decade [18]. Current PC's and laptops operate at around 2GHz with data rates around 500 Mbytes/sec [18].

To support high density recording, the magnetic media must be very thin with small grain size and high coercivity (the point on the hysteresis curve where the magnetisation is zero). The coercivity ascertains how easily data can be recorded and erased or changed. On the other hand it also controls the ease with which data can be destroyed, for example, by stray fields. The lower the coercivity, the more sensitive the medium is to all kinds of fields.

The areal density of the recording media in disk drive products is now increasing at a 100% compound annual growth rate, which involves a corresponding small bit cell size. As this areal density increases, the individual storage bit cell size and cell volume decrease correspondingly, and since the signal to noise is proportional to the number of magnetic particles or grains in each bit cell, a smaller grained media is required [18]. However, grains cannot be made arbitrarily small since the magnetic thermal stability is determined by

the grain volume. The thermal energy of a grain can exceed an energy barrier and reverse from one stable direction to another.

One example in overcoming this problem is to introduce hard magnetic materials. Here, continued grain size scaling to diameters considerably below 10-12nm would be possible and allow densities well beyond the current perceived 40 – 100 Gbits/in^2 mark [19]. This prospect has been the main driving force behind industrial and academic research in the area of thin film hard magnetic materials, which promise minimal thermally stable grain sizes down to 2-3nm and a more than tenfold potential density gain [19]. Table 1.4 is a list of alloy systems and their crystalline anisotropy. All these materials are capable of sustaining particle diameters less than 10nm over storage times of 10 years [17, 19].

Alloy system	**Material**	**M_s (emu/cc)**	**H_K (kOe) Crystal anisotropy field**	**Particle diameter (nm)**
Co-alloys	CoCrPtB	320	20	8
	Co	1400	6.4	8.4
	hex Co_3Pt	1100	36	4.8
$L1_0$ Phases	FePd	1100	33	5.0
	FePt	1140	116	2.8 – 3.3
	CoPt	800	123	3.8
	MnAl	560	69	5.1
Rare-earth Transition metals	$Fe_{14}Nd_2B$	1270	73	3.7
	$SmCo_5$	910	240-400	2.8-2.3

Table 1.4. Properties of magnetic materials capable of sustaining grain sizes less than or equal to 10nm over storage times of ten years [17,19].

At the time of writing this thesis, the maximum areal density for research samples has now reached up to 206Gbits/in^2. This has been

achieved by using patterned media, $CoCr_{18}Pt_{12}$ of 60nm islands with a spacing of 100nm [20].

The development of new media alloys which will support high areal densities requires advanced studies in alloy compositions and new sputter deposition equipment, a materials science understanding of the interactions of these alloys, and finally the development of new measurement and testing procedures to identify the microstructure [20].

There are two types of recording media: longitudinal and perpendicular media but only the longitudinal media have been studied for this thesis.

1.2.2. Longitudinal recording media

Today's state-of-the-art longitudinal magnetic recording media are granular, figure 1.7. They are composed of several hundred weakly coupled and randomly oriented ferromagnetic grains per unit cell. These grains may be viewed as small permanent-magnet-particles, supporting two magnetic states along an internal easy axis, which is determined by the magnetocrystalline anisotropy.

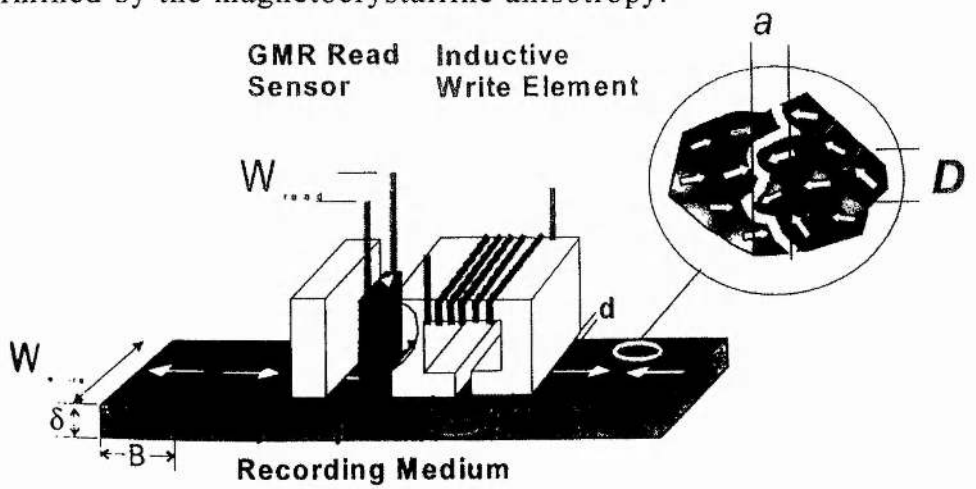

Figure 1.7 Basic recording process and dimensions in longitudinal recording [19]. Fundamentally, a bit of information is stored by applying a pulsed field in a negative direction to a previously saturated material where the saturation field was applied in the opposite direction. In this way, an output signal is produced due to the voltage pulses generated at either end of the bit.

From the above diagram, the inductive write element is used to record horizontally aligned N-S and S-N magnetic transitions (S=South, N=North). The flux emanating from these transitions is detected with a giant magneto-resistive sensor element. The medium is a granular CoCr-based magnetic alloy, composed of 100-500 weakly coupled ferromagnetic grains per bit cell. Typical grain diameters, D, are 10 to 15nm. The achievable areal density is inversely proportional to the product of the transition spacing (bit length), B; the write track width W_{write}; δ: medium thickness in nm and a: transition width parameter in nm. Further discussion on the various requirements and dynamic strategies for extremely high-density magnetic recording media are found in [17-19].

A typical structure of a thin film used for magnetic recording is shown in figure 1.8. The magnetic layer is in contact with an intermediate layer, which in turn is in contact with an underlayer. The seedlayer and the underlayer set up the grain size as well as the crystallographic orientations in the layers. The intermediate layer enhances the epitaxy growth of the magnetic layer. Furthermore, atoms from the intermediate layer may diffuse up the grain boundaries, giving rise to magnetic isolation of the grains within the magnetic layer. All these processes affect the magnetic properties of the film [16, 17].

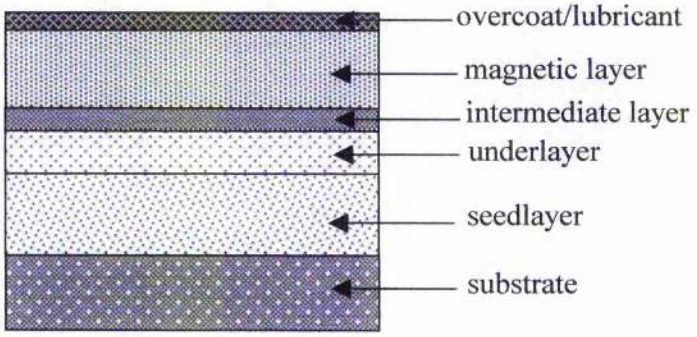

Figure 1.8. Schematic of the layer structure of thin films used for longitudinal magnetic recording [17]

For particulate media, the major source of media noise is the stationary background noise often referred to as dc-erased noise because it is measured in the absence of written transitions [17, 19]. This noise arises from particle size distributions, particle misorientation, particle agglomeration, or from nonmagnetic inclusions such as aluminium oxide particles or coating voids. It has been understood for years that this type of noise decreases as the average particle size is reduced. Chapter three determines the static properties of low and high noise media and correlates differences found in these 3Gbits/in^2 CoCrPtTa samples to differences in their recording performance.

The major technique for the control of noise in thin film media has been the use of compositional segregation. Such materials are generally of the form $Co_{69}Cr_{18}Pt_{10}Ta_3$. High magnetocrystalline anisotropy is generally desired in the Co-alloys to provide high coercivity and thermal stability. In these alloys, it is found that the platinum serves to expand the c-axis of the HCP cobalt lattice giving rise to a high coercivity [19]. The inclusion of tantalum has been long known to produce a low noise medium and recently it was observed that this feature arises not due to the tantalum itself but due to the fact that the presence of tantalum within the cobalt lattice promotes the movement of chromium to the grain boundaries. Chromium has been used extensively due to its limited solubility in cobalt and its tendency to migrate to grain boundaries to decouple the grains in the alloy [19]. Apart from tantalum, boron is also used in production disks. In the CoCrPtB media, the addition of boron has been shown to increase the coercivity and the role of boron in reducing noise is through reduced grain size and grain boundary segregation [19]. Chapter four examines any trends in the static and dynamic properties of the CoCrPtB media with varying platinum and boron content from high field FMR.

Throughout the 1990's, CoCrTa, CoCrPt and CoCrPtTa were the most popular alloys used by the hard disk industry. CoCrTa has very low noise properties, CoCrPt has a high magnetocrystalline anisotropy and coercivity, while CoCrPtTa is a compromise between the former two alloys.

The study of CoCrPtB alloys began in 1991 [19, 21]. The coercivity of the CoCrPtB film was found to be very large and the noise level was low compared to other alloys of the same period of time. Recently, CoCrPtB was also found to have a narrow grain size distribution and better intergranular de-coupling than the CoCrPtTa alloys thin film [19, 22]. Therefore, CoCrPtB is now being widely used at the beginning of the 21st Century.

The saturation magnetisation and coercivity of CoCrPtB thin films with boron additions up to 15%, platinum up to 20% and chromium up to 20% have been studied [19, 23]. The saturation magnetisation decreases linearly with boron additions. A recent study [19, 24] showed that the saturation magnetisation decrease rate caused by adding boron is similar to that caused by adding platinum. It has also been shown that the anisotropy increase rate due to boron addition is similar to that due to platinum addition.

1.3. References

[1] C. Kittel, *Introduction to Solid State Physics* 7th ed., Wiley, New York, 1996

[2] A.P. Guimaraes, *Magnetism and Magnetic Resonance in Solids*, Wiley, New York, 1998

[3] S. Chikazumi, *Physics of Magnetism*, Wiley, New York, 1964

[4] D. Craik, *Magnetism. Principles and Applications*, Wiley, Chichester, 1995

[5] A.H. Morrish, *The Physical Principles of Magnetism*, Wiley, 1964

[6] L. Brilloun, J. Phys. Radium, 8 (1927) 74

[7] P. Weiss, J. Phys., 6 (1907) 667

[8] W. Sucksmith and R. R. Pierce, Proc. Roy. Soc. (London), A-167 (1938) 189

[9] E.C. Stoner, Proc. Roy. Soc. (London) A-165 (1938) 372, Phil. Mag. 25 (1938) 899

[10] E.P. Wohlfarth, in E.P. Wohlfarth, Ed., *Ferromagnetic Materials Vol 1*, North-Holland, Amsterdam, 1980

[11] T. Moriya, *Spin Fluctuations in Itinerant Electron Magnetism*, Springer-Verlag, 1985

[12] S.V. Vonsovskii, Fer*romagnetic Resonance*, Pergamon Press, New York, 1966

[13] J.J.K. Chang, Q. Peng, H.N. Bertram, R. Sinclair, IEEE Trans. Magn. 32 (1996) 4902, U. Netzelmann, J.Appl. Phys., 68 (1990) 1800

[14] L. Neel, Compt. Rend. (Paris), 228 (1949) 604

[15] J.L. Dormann and D. Fiorani, Ed., *Magnetic Properties of Fine Particles*, North-Holland, Amsterdam, 1992

[16] J.C. Lodder 1998, in *Handbook of Magnetic Materials*, ed Buschow K.H.J. (North-Holland), vol 11, ch2

[17] D. Weller and M.F. Doerner, Annu. Rev. Mater. Sci. 30 (2000) 611

[18] www.ibm.com

[19] M.L.Plummer, J.van Ek and D. Weller, *The Physics of Ultra-High Density Magnetic Recording*, Springer-Verlag, New York, 2001

[20]T.Thomson, *private communications*, 2002

[21] N. Tani, T. Takahashi, M. Hashimoto, M. Ishikawa, Y. Ota, K. Nakamura, IEEE Trans. Magn. 27 (1991) 4736

[22] G.R.Jones, K. O'Grady, X. Bian, M. Mirzamaani, M.F. Doerner, #BP06, Intermag 2000

[23] C.R. Paik, I. Suzuki, N. Tani, M. Ishikawa, Y. Ota, K. Nakamura, IEEE Trans. Magn. 28 (1992) 3084

[24] R. Ranjan, H.J. Richter, J. Chen, S.D. Harkness, S.Z. Wu, R. Ristau, Er. Girt, C. Chang, R.M. Brochie, G.C. Rauch, S. Gangopadhyay, K. Subramanian, #HA-01, the 8th Joint MMM-Intermag Conference, 2001

Chapter 2

Ferromagnetic resonance

This chapter explains the main principles of ferromagnetic resonance.

2.1 Theory of FMR

2.1.1. Introduction

V.K.Arkad'yev (1912)[1] discovered the selective absorption of cm radio waves in iron and nickel wires and the change in magnetisation accompanying it. He also explained the appearance of absorption bands in the magnetic spectrum by the resonance response of elementary carriers of a magnetic moment in the ferromagnet to the applied rf field. The first quantum theory explanation of this phenomenon was given by Ya.G.Dorfman (1923) [2] and N.S.Akulov (1926) [3] was the first to pose the question of the effect of parallel and perpendicular magnetising fields on the magnetic spectra of ferromagnetism.

In 1944, E.K.Zavoiskii [4] discovered experimentally the phenomenon of EPR absorption. He and Griffiths [5] (working independently) in 1946, discovered FMR absorption in metals in their purest form. The Landau-Lifschitz theory (1935) [6] as applied to the new experimental facts was developed by Kittel (1947[7], 1948 [8]) and Polder (1949) [9].

This subchapter looks at the basic theory of ferromagnetic resonance using a semi-classical approach. Magnetism books [10-13] adopt this method in explaining the theory of this technique. The theoretical basis for this is that the quantum numbers of the corresponding energy levels are of the order of 10^{22} and above [14]. On the basis of the correspondence principle, one expects the results of the classical and the quantum mechanical treatment of the problem to be identical [10].

The electron may be considered as a spinning mass, which is charged electrically and is similar in many respects to the classical mechanical gyroscope. The dc magnetic forces acting on the magnetic dipole are analogous to the gravitational force acting on a spinning mechanical top. When the high frequency (hf) magnetic field is applied perpendicular to the dc field it will exert a periodic sidewise thrust or torque.
Figure 2.1 illustrates the precessional motion of a magnetic moment in a field H with torque vectors.

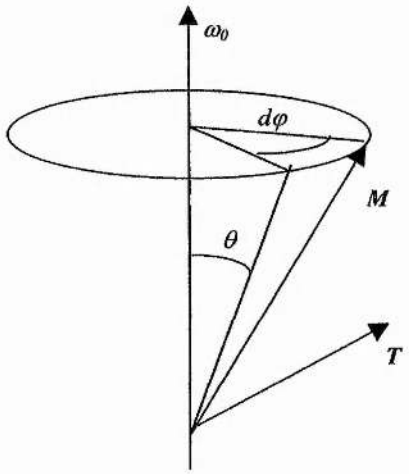

Figure 2.1: The precessional motion of a magnetic moment with angular momentum and torque vectors.

The rate of change of angular momentum, $\vec{p}$, defines the torque $\vec{T}$. In the time interval dt, the change in angular momentum is Tdt and the change in φ is $d\varphi$. The angle $d\varphi$ is equal to the arc Tdt divided by the radius of the precession circle $p\sin\theta$, thus

$$\frac{d\theta}{dt} = \omega_0 = \frac{T}{p\sin\theta} \qquad (2.1)$$

From (2.1), we obtain $\frac{dp}{dt} = \omega_0 p\sin\theta$ and thus in vector notation:

$$\frac{d\vec{p}}{dt} = \vec{\omega}_0 \times \vec{p} \qquad (2.2)$$

which is the equation of motion of the angular momentum vector.

The angular momentum and magnetic moment are aligned vectors with a constant value of p and μ_e: for the electron, they are oppositely directed.

The gyromagnetic ratio is defined as $\gamma = -\frac{\mu_e}{p}$ and the equation of motion is $\frac{dp}{dt} = T$. It is convenient to evaluate the torque from the potential energy U of a magnetic dipole in a constant field H.

Since $$U = \mu_e H\cos\theta \qquad T = -\frac{dU}{d\theta} = \mu_e H\sin\theta \tag{2.3}$$

then $$\frac{d\vec{p}}{dt} = \vec{\mu}_e \times \vec{H} = -\gamma\left(\vec{p}\times\vec{H}\right) = \gamma\left(\vec{H}\times\vec{p}\right) = \vec{\omega}_0 \times \vec{p} \tag{2.4}$$

From equations (2.2) and (2.4), a relation $\omega_0 = \gamma H$ is established, which is the natural precession frequency of a magnetic dipole in a constant field. Equation (2.4) is therefore refined in terms of the magnetisation of a system of magnetically aligned spins. The macroscopic equation of the magnetisation vector form is

$$\frac{d\vec{M}}{dt} = -\gamma\left(\vec{M}\times\vec{H}\right) \tag{2.5}$$

The minus sign in this equation is due to the negative charge of the electron. In practice [13], the absolute value of the electronic charge is used and the macroscopic equation of motion is stated as

$$\frac{d\vec{M}}{dt} = |-\gamma|\left(\vec{M}\times\vec{H}\right) \tag{2.6}$$

where $\gamma = \frac{ge}{2mc} \equiv \frac{g\mu_B}{\hbar}$ ($2.8 MHzOe^{-1}$, for $g=2$), e is the absolute value of the electronic charge, m is the rest mass of the electron, c is the velocity of light, and g is the spectroscopic splitting factor, or the Lande g-factor and is approximately equal to 2 (as discussed in section 1.1.3.).

Throughout the theory, we shall resort to equation (2.5).

Note that this equation does not allow for 'losses'; that is, the dissipation of magnetic energy. Equation (2.5) is valid strictly for uniform magnetisation and approximately as $\vec{M}$ varies sufficiently slowly in space [13].

An important feature of the equation of motion is that it ensures the conservation of the vector $\vec{M}$ length. A dot product on both sides by $\vec{M}$, provides us

$$\frac{d\vec{M}^2}{dt} = 0 \qquad (2.7)$$

If we regard $\vec{M}$ as a vector with one end fastened, the other end, according to equation (2.7), will move on the surface of a sphere. Such movement is called the precession of magnetization [13].

2.1.2. High frequency magnetic susceptibilty

We shall first consider the oscillations of magnetisation in a ferromagnet, under the influence of a given internal ac magnetic field as shown in figure 2.2. Having solved this problem we shall find the high-frequency magnetic susceptibility of a ferromagnet.

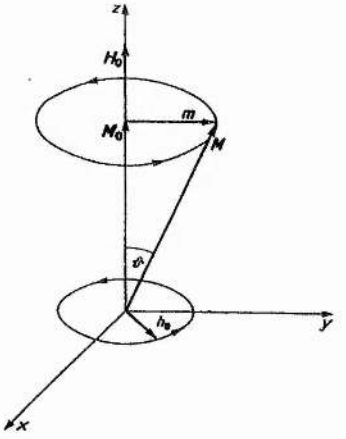

Figure 2.2. Precession of the magnetization vector $\vec{M}$ in a static magnetic field $\vec{H}_0$ and hf magnetic field $\vec{h}$ [10].

We take the magnetic field and magnetisation in equation (2.5) to be the sums of the steady and alternating parts:

$$\vec{H} = \vec{H}_0 + \vec{h}e^{i\omega t} \qquad \vec{M} = \vec{M}_0 + \vec{m}e^{i\omega t} \qquad (2.8)$$

with an added assumption that $h \ll H_0$ and $m \ll M_0$. Here M_0 is the maximum steady dc magnetisation at a given temperature below the Curie temperature and H_0 is the internal field. We are also assuming that there is a harmonic (sinusoidal) time dependence associated with $\vec{h}$ and thus $\vec{m}$. Direct substitution of (2.8) into (2.5) and assuming that $\vec{M}_0 \| \vec{H}_0$, so that $\vec{M}_0 \times \vec{H}_0 = 0$ and neglecting the cross product of ac quantities, $\vec{h}$ and $\vec{m}$, yields the following relation:

$$i\omega\vec{m} + \gamma\vec{m} \times H_0 = -\gamma\vec{M}_0 \times \vec{h} \qquad (2.9)$$

Projecting (2.9) onto the axes of a Cartesian coordinate system with the z-axis coinciding with the direction of $\vec{H}_0$and $\vec{M}_0$, we get

$$\begin{aligned} i\omega m_x + \gamma H_0 m_y &= \gamma M_0 h_y \\ -\gamma m_x H_o + i\omega m_y &= -\gamma M_o h_x \\ i\omega m_z &= 0 \end{aligned} \qquad (2.10)$$

and thus

$$\begin{aligned} m_x &= \chi h_x + i\chi_a h_y \\ m_y &= -i\chi_a h_x + \chi h_y \\ m_z &= 0 \end{aligned} \qquad (2.11)$$

with

$$\chi = \frac{\gamma M_0 \omega_H}{\omega_H^2 - \omega^2} \qquad \text{and} \qquad \chi_a = \frac{\gamma M_0 \omega}{\omega_H^2 - \omega^2} \qquad (2.12)$$

where $\omega_H = \gamma H_0$

They can also be written in tensor form:

$$\vec{m} = \bar{\bar{\chi}}\vec{h} \qquad (2.13)$$

where the high-frequency magnetic susceptibility $\ddot{\chi}$ is a non-symmetric second rank tensor [9].

$$\ddot{\chi} = \begin{vmatrix} \chi & i\chi_a & 0 \\ -i\chi_a & \chi & 0 \\ 0 & 0 & 0 \end{vmatrix} \tag{2.14}$$

The solution (2.11) can also be written in vector form:

$$\vec{m} = \chi \vec{h}_\perp + i\vec{h}_\perp \times \vec{G}_m \tag{2.15}$$

where $\vec{h}_\perp = h_x\hat{x}_0 + h_y\hat{y}_0 = \vec{h} - h_z\hat{z}_0$ (2.16)

and $\vec{G}_m = \chi_a\hat{z}_0$ is the magnetic gyration vector.

In the considered case of an isotropic and lossless ferromagnet, magnetised to saturation, the longitudinal component of the ac field, h_z, does not produce any ac magnetisation. However, the transverse ac field, $h_\perp$, excites not only the magnetisation component parallel to the field, but also a component perpendicular to it. Such property of a medium, caused by the non-symmetry of the susceptibility tensor, is called **gyrotropy**. It is observed from figure 2.3, that the components grow without limit when ω or H approaches the asymptote $\omega = \omega_0 = \gamma H_0$.

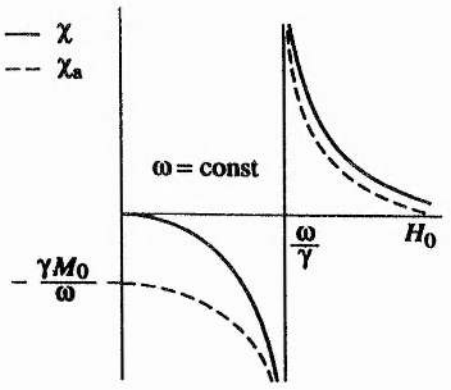

Figure 2.3. Dependence of the susceptibility tensor components on steady magnetic field $\vec{H}_0$ (frequency is kept constant) [13].

This resonant dependence of the tensor results in the phenomenon of **ferromagnetic resonance.**

2.1.3. High frequency susceptibilty with damping

Oscillations of magnetisation are accompanied by dissipation of energy, which is transferred into other kinds of energy, mainly thermal energy. Theoretically, the energy transfer (relaxation) from coherent magnetization rotation to the thermal bath can occur by interactions with itinerant electrons, spin waves (magnons), lattice vibrations (phonons) and crystal imperfections (impurities and defects) [15]. Discussions on the mechanisms of gyromagnetic damping are found in references [13, 15, 16]. The equation of motion of magnetisation (2.5) is modified; such that, an extra term leading to dissipation should be added onto the right hand side of this equation [13].

$$\frac{\partial \vec{M}}{\partial t} = -\gamma \vec{M} \times \vec{H} - \frac{\gamma \lambda}{M^2} \vec{M} \times \left(\vec{M} \times \vec{H} \right) \qquad (2.17)$$

This is the Landau–Lifschitz equation, where λ is the dissipation parameter. This is illustrated in figure 2.4.

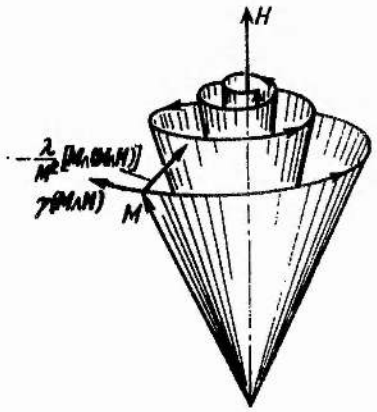

Figure 2.4. Damped precession of magnetization vector when there is no hf field [10].

If the term $\vec{M}\times\vec{H}$ is replaced by $\frac{-1}{\gamma}\frac{\partial\vec{M}}{\partial t}$ (using the equation of motion without dissipation) and we introduce a dimensionless parameter $\alpha=\frac{\lambda}{M}$, then the Gilbert equation is obtained [17,18]:

$$\frac{\partial\vec{M}}{\partial t}=-\gamma\vec{M}\times\vec{H}_{eff}+\frac{\alpha}{M}\left(\vec{M}\times\frac{\partial\vec{M}}{dt}\right) \qquad (2.18)$$

where α is the Gilbert damping factor. The dissipative term in this equation can be written supposing that an effective field of friction, proportional to the rate of change of $\vec{M}$, is acting on $\vec{M}$. If one were to change from (2.17) to (2.18), then one needs to substitute

$$\gamma\rightarrow\frac{\gamma}{1+\alpha^2} \quad \text{and} \quad \lambda\rightarrow\frac{\alpha M}{1+\alpha^2}$$

into (2.17). It is clear that when the damping term is far less than unity, then equations (2.17) and (2.18) are equivalent [13]. One should note that the LLG equation is only rigorously applicable for the case of coherent rotation of a given unit volume [15].

From section 2.1.2, equation (2.9) is the derived linearisation of the equation of motion. If one were to include loss, then (2.9) is modified and yields:

$$i\omega\vec{m}+\gamma m\times H_0+\frac{i\alpha\omega}{M_0}\vec{m}\times\vec{M}_0=-\gamma\vec{M}_0\times\vec{h} \qquad (2.19)$$

We will use this equation, again, in section 2.1.5. in determining the resonant condition.

To find the susceptibility tensor components in the presence of loss it is found that the result is the same as replacing ω_H by $\omega_H+i\alpha\omega$.

From (2.12), we directly substitute the ω_H term. Thus

$$\chi=\chi'-i\chi''=\frac{\gamma M_0(\omega_H+i\alpha\omega)}{(\omega_H+i\alpha\omega)^2-\omega^2} \qquad (2.20)$$

Similarly $\chi_a = \chi_a' - i\chi_a''$

we have
$$\chi_a' = \frac{\gamma M_0 \omega\left(\omega_H^2 - \omega^2\left(1+\alpha^2\right)\right)}{\left[\omega_H^2 - \omega^2\left(1+\alpha^2\right)\right]^2 + 4\alpha^2\omega^2\omega_H^2} \tag{2.21}$$

and

$$\chi_a'' = \frac{2\alpha\omega^2\omega_H M_0\gamma}{\left[\omega_H^2 - \omega^2\left(1+\alpha^2\right)\right]^2 + 4\alpha^2\omega^2\omega_H^2}. \tag{2.22}$$

The dependence of the real and the imaginary parts of the tensor $\ddot{\chi}$ components on $\vec{H}_0$ is shown in figure 2.5. Here, resonance takes place when $\omega = \frac{\omega_H}{\left(1+\alpha^2\right)}$.

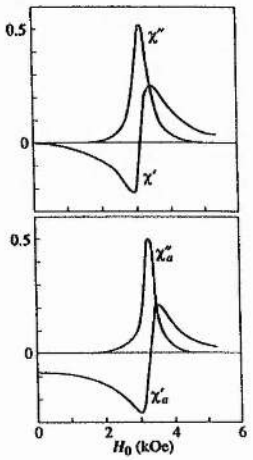

Figure 2.5. Real and imaginary parts of the susceptibility tensor components versus $\vec{H}_0$ [13].

2.1.4. Circular polarisation of h-f radiation

It should also be pointed out that the resonant behavior of the oscillation amplitudes occurs only under the influence of an ac magnetic field circular component with right-hand rotation (relative to the direction of $\vec{M}_0$). The circular components of the susceptibility tensor in the presence of loss are [13]

$$\chi_{\pm} = \chi \pm \chi_a = \frac{\gamma M_0}{\left(\omega_H \mp \omega\right) + i\alpha\omega} \tag{2.23}$$

where χ_+ and χ_- are right and left-hand rotation, respectively. If the field is right hand polarised, then this corresponds to the circular polarised wave that rotates in the same sense as the precessional motion [13,19]. Thus, $\chi_+ = \chi + \chi_a$, which can be expanded to $\chi_+ = (\chi' + \chi_a'') - i(\chi'' + \chi_a'')$. The dispersion and absorption components are $(\chi' + \chi_a')$ and $(\chi'' + \chi_a'')$, respectively.

Conversely, for left-hand polarisation, which describes the response of the medium to a circularly polarised magnetic field rotating in the opposite sense; then the quantities χ_-' and χ_-'' are close to zero, as shown in figure 2.6. The positive susceptibility has a singularity at $\omega = \omega_0$ whilst χ_- has no singularity.

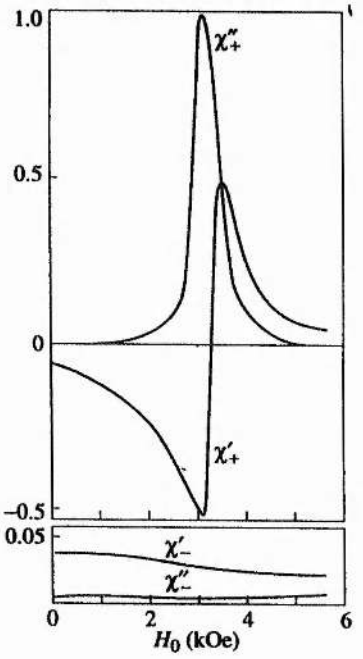

Figure 2.6. Plots of the real and imaginary parts of the susceptibility tensor versus applied field [13].

This shows that for FMR measurements, it is the right hand polarisation that is resonantly absorbed by the medium.

2.1.5. Internal fields in ferromagnetics

So far, there has been no discussion of demagnetising effects, preferred directions of magnetisation and crystalline imperfections. The resonance frequency is influenced by all of these in any real speciman. In practice, we deal with finite samples and in this thesis, the medium is lossy, with its thickness small compared with the hf wavelength. The hf magnetic field inside the sample has uniform intensity, but it is not equal to the field outside the sample because the normal component of the susceptibility is discontinuous at the sample's interface [13]. It is also difficult, or impossible, to solve the electromagnetic problem for an arbitrary sample shape.

If we consider a small ferromagnetic ellipsoidal sample in a uniform magnetic field, the relation between the internal and external magnetic field is given by

$$\vec{H} = \vec{H}_e - \ddot{N}\vec{M} \equiv \vec{H}_e + \vec{H}_{dem} \qquad (2.24)$$

where $\vec{H}_e$ is the external magnetic field, $\vec{H}$ is the internal magnetic field, and $\vec{M}$ is the magnetisation. Both $\vec{H}$ and $\vec{M}$ are uniform if $\vec{H}_e$ is uniform in and near the ellipsoid. $\ddot{N}$ is the demagnetising tensor. The tensor is symmetric and becomes diagonal when the axes coincide with the axes of the ellipsoid. The components of $\ddot{N}$ in these axes, N_x, N_y and N_z are called demagnetising factors and depend only on the shape of the ellipsoid and the sum in cgs units is $N_x + N_y + N_z = 4\pi$ (in SI units the sum of the demagnetizing factors is unity) [20]. The quantity $\vec{H}_{dem} = -\ddot{N}\vec{M}$ is the demagnetising field. If one were to substitute the ac and dc components of $\vec{H}_e$, $\vec{H}$ and $\vec{M}$ into the above equation, then

$$\vec{H}_0 = \vec{H}_{e0} - \ddot{N}\vec{M}_0 \qquad (2.25)$$

$$\vec{h} = \vec{h}_e - \ddot{N}\vec{m}$$

Substitution of equation (2.25) in the linearised equation of motion (2.19), from section 2.1.3, gives the following relation:

$$i\omega\vec{m}+\gamma\vec{m}\left(\vec{H}_{e0}-\ddot{N}\vec{M}_0\right)+\gamma\left(\ddot{N}\vec{m}\right)\times\vec{M}_0-\frac{i\alpha\omega}{M_0}\vec{m}\times\vec{M}_0=-\gamma\vec{M}_0\times\vec{h}_{e0} \qquad (2.26)$$

We set the external hf field, h_e and the damping term, α, to zero. Equation (2.26) is projected onto the axes of a Cartesian coordinate system in which the z-axis coincides with the direction of $\vec{M}_0$. The demagnetisation tensor have, in these axes, the form [13]

$$\ddot{N}=\begin{vmatrix} N_{11} & N_{12} & N_{13} \\ N_{21} & N_{22} & N_{23} \\ N_{31} & N_{32} & N_{33} \end{vmatrix} \qquad (2.27)$$

When substituted into (2.26), the linearized equation is rewritten as

$$\begin{aligned} &\left(i\omega+\gamma N_{12}M_0\right)m_x+\gamma\left(H_{e0z}-N_{33}M_0+N_{22}M_0\right)m_y=0 \qquad (2.28)\\ &-\gamma\left(H_{e0z}-N_{33}M_0+N_{11}M_0\right)m_x+\left(i\omega+\gamma N_{12}M_0\right)m_y=0 \end{aligned}$$

which results in an expression for the eigenfrequency:

$$\omega_0=\left[\left(\gamma\left(H_{e0z}-N_{33}M_0\right)+\gamma N_{11}M_0\right)\left(\gamma\left(H_{e0z}-N_{33}M_0\right)+\gamma N_{22}M_0\right)-\gamma^2N_{12}^2M_0^2\right]^{\frac{1}{2}} \qquad (2.29)$$

The maximum absorption of electromagnetic energy by a small ferromagnetic ellipsoid takes place at a frequency very near to the eigenfrequency. This frequency, which depends on the shape of the sample, is the frequency of ferromagnetic resonance.

If the external field $\vec{H}_{e0}$ is directed along one of the axes of the ellipsoid, then $\vec{M}_0$ and the z-axis are also oriented along this ellipsoidal axis. The tensor $\ddot{N}$ becomes diagonal, and thus in cgs units,

$$\omega_0=\gamma\left\{\left[H_{e0}+\left(N_x-N_z\right)M_0\right]\left[H_{e0}+\left(N_y-N_z\right)M_0\right]\right\}^{\frac{1}{2}} \qquad (2.30)$$

which is Kittel's equation [8].

Examples of the use of equation (2.30) for three types of ellipsoid are tabulated below:

Sample	Magnetisation direction	Demagnetising factor			Eigenfrequency
		N_x	N_y	N_z	
Infinitely thin film	Tangential	0	4π	0	$\left(\frac{\omega_0}{\gamma}\right)^2 = H_{e0}(H_{e0}+4\pi M_0)$
	Normal	0	0	4π	$\left(\frac{\omega_0}{\gamma}\right) = (H_{e0}-4\pi M_0)$
Infinite thin cylinder	Longitudinal	2π	2π	0	$\left(\frac{\omega_0}{\gamma}\right) = (H_{e0}+2\pi M_0)$
	Transverse	2π	0	2π	$\left(\frac{\omega_0}{\gamma}\right)^2 = H_{e0}(H_{e0}-2\pi M_0)$
Sphere		$4\pi/3$	$4\pi/3$	$4\pi/3$	$\left(\frac{\omega_0}{\gamma}\right) = H_{e0}$

Table 2.1. Set of FMR conditions with application of Kittel's equation. The resonant equation and demagnetizing factors are expressed in cgs units.

2.1.6. Methods of analysis of FMR in anisotropic ferromagnets

The equations of motion may be expressed in terms of the total free energy E instead of effective fields. There are several advantages to the energy formulation of the equations of motion: first, they are rather general in form. Second, when the free energy terms are complicated functions of angular coordinates, they can be introduced routinely into the equations. Thirdly, when the easy direction of the various anisotropies have different orientations, the computations are more straightforward with the energy equations. One other method that is used to determine the FMR in anisotropic media is the method of spherical coordinates proposed by Smit and Beljers [21] and Suhl [22]. Suppose the magnetisation M_s of a ferromagnetic speciman has the static equilibrium direction described by the azimuth φ_0 and polar angle θ_0 as shown in figure 2.7:

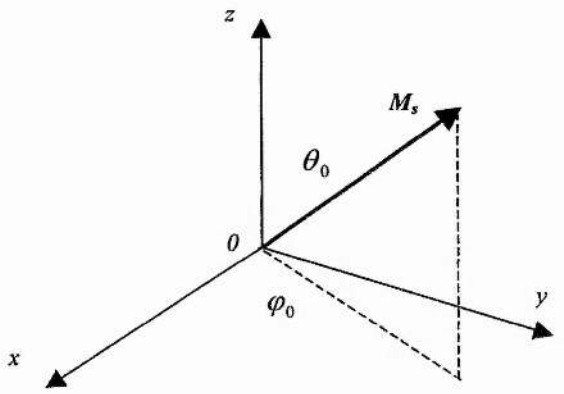

Figure 2.7. Static equilibrium position of magnetisation.

This method is based on the transition from the variables M_x, M_y and M_z to the variable θ, φ and M_s, where θ and φ are the angles of $\vec{M}$ in spherical co-ordinate system, and M_s is the vector $\vec{M}$ length. It is assumed that the magnetization vector has the same length.

From the Landau-Lifschitz and Gilbert relation:

$$\frac{\partial \vec{M}}{\partial t} = -\gamma \vec{M} \times \vec{H}_{eff} + \frac{\alpha}{M}\left(\vec{M} \times \frac{\partial \vec{M}}{dt}\right) \tag{2.31}$$

where H_{eff} is the effective field and is defined as

$$\vec{H}_{eff} = -\frac{\partial U}{\partial \vec{M}} \tag{2.32}$$

and U is the total energy of the system.

Substitution of the x, y and z-components of the H_{eff} term into the LLG will give us

$$\frac{\partial \theta}{\partial t} = -\frac{\gamma}{M_s \sin\theta}\frac{\partial U}{\partial \varphi} - \frac{\alpha\gamma}{M_s}\frac{\partial U}{\partial \theta}$$

$$\frac{\partial \varphi}{\partial t} = \frac{\gamma}{M_s \sin\theta}\frac{\partial U}{\partial \theta} - \frac{\alpha\gamma}{M_s \sin^2\theta}\frac{\partial U}{\partial \varphi} \tag{2.33}$$

For small deviations of M from M_s, the angles θ_0 and φ_0 of M_s can be found from the equilibrium conditions

$$\left(\frac{\partial U}{\partial \theta}\right)_{\theta=\theta_0,\varphi=\varphi_0} = 0 \quad \text{and} \quad \left(\frac{\partial U}{\partial \varphi}\right)_{\theta=\theta_0,\varphi=\varphi_0} = 0. \tag{2.34}$$

One has to make sure that the obtained θ_0 and φ_0 values correspond to an energy minimum. The derivatives $\left(\frac{\partial U}{\partial \theta}\right)$or U_θ and $\left(\frac{\partial U}{\partial \varphi}\right)$or $U_\varphi$can be written as

$$U_\theta = U_{\theta\theta}\delta\theta + U_{\theta\varphi}\delta\varphi \text{ and } U_\varphi = U_{\varphi\varphi}\delta\varphi + U_{\varphi\theta}\delta\theta \tag{2.35}$$

and the deviations from equilibrium are defined as

$$\delta\theta(t) = \theta(t) - \theta_0 = \delta\theta e^{i\omega t} \text{ and } \delta\varphi(t) = \varphi(t) - \varphi_0 = \delta\varphi e^{i\omega t} \tag{2.36}$$

Substituting (2.35, 2.36) into (2.33), we obtain the linear equations

$$\left(i\omega + \frac{\gamma}{M_s \sin\theta_0} U_{\theta\varphi} + \frac{\alpha\gamma}{M_s} U_{\theta\theta}\right)\delta\theta + \left(\frac{\gamma}{M_s \sin\theta_0} U_{\varphi\varphi} + \frac{\alpha\gamma}{M_s} U_{\theta\varphi}\right)\delta\varphi = 0$$

$$\left(i\omega - \frac{\gamma}{M_s \sin\theta_0} U_{\theta\varphi} + \frac{\alpha\gamma}{M_s \sin^2\theta_0} U_{\varphi\varphi}\right)\delta\varphi - \left(\frac{\gamma}{M_s \sin\theta_0} U_{\theta\theta} - \frac{\alpha\gamma}{M_s \sin^2\theta_0} U_{\theta\varphi}\right)\delta\theta = 0 \tag{2.37}$$

where $U_{\theta\theta} = \left(\frac{\partial^2 U}{\partial \theta^2}\right)$, $U_{\varphi\varphi} = \left(\frac{\partial^2 U}{\partial \varphi^2}\right)$ and $U_{\theta\varphi} = \left(\frac{\partial^2 U}{\partial \theta \partial \varphi}\right)$ at equilibrium (where $\theta = \theta_0$ and $\varphi = \varphi_0$).

We can express (2.37) in matrix form, set the determinant of the matrix to zero and finally gather the real and imaginary components separately, so that one can obtain expressions [12, 13, 21]:

$$\left(\frac{\omega}{\gamma}\right) = \frac{\left(1+\alpha^2\right)^{\frac{1}{2}}}{M_s \sin\theta_0}\left(U_{\theta\theta}U_{\varphi\varphi} - U_{\theta\varphi}^2\right)^{\frac{1}{2}} \tag{2.38}$$

and

$$\Delta\omega \equiv \left(\frac{d\omega}{dH}\right)\Delta H = \frac{\alpha\gamma}{M_s}\left(U_{\theta\theta} + \frac{U_{\varphi\varphi}}{\sin^2\theta_0}\right) \qquad (2.39)$$

Equation (2.38) is often called in FMR papers, the Smit-Beljers or Smit-Suhl equation. This is the resonant condition of an anisotropic elliptical medium. The equation is strictly valid only for $\theta_0 \neq 0^\circ$. One has to look at the equilibrium condition and make sure that the applied field is not along the z-axis, otherwise at saturation, the magnetisation will align with the field (assuming that the angle between the magnetization and field is small).

The linewidth of resonance is defined by the full width half maximum, ΔH, on the field scale. If $\alpha << 1$, then there is an insignificant shift in the resonance frequency.

2.1.7. Features of FMR of metals

Previous work on the FMR of linewidth measurements [23, 24, 25] has related the linewidth to the intrinsic mechanism (viscous damping) and the extrinsic mechanism caused by structural imperfections.

There are two main methods which allows one to extract each of the contributions to the entire linewidth. The first approach entails multi-frequency linewidth measurements, in which the damping term is determined from the frequency dependent curve. The frequency independent term is related to the presence of magnetic inhomogeneities.

The second approach [26, 27] deals with the dependence of the field-swept linewidth ΔH (at a constant frequency). The dependence of ΔH on the angle θ between the applied field and film normal may be transformed to the frequency-swept linewidth $\frac{\Delta\omega}{\gamma} = \frac{\alpha\omega}{\gamma}$ (α is the Gilbert damping and γ is the gyromagnetic ratio), which is nearly angle-independent in most perfect films [28]. Any anomalous increase in $\frac{\Delta\omega}{\gamma}$ is due to two-magnon

scattering on defects, which is operative when the magnetisation lies in-plane. The contributions of two-magnon process caused by non-uniform elastic stresses are large in poorly annealed samples [13]. If the magnetisation is however out-of-plane, then this mechanism is inoperative and ΔH ($\theta=0$) should be minimal. A mathematical description of two-magnon contribution in linewidth measurements in ferromagnetic metals is discussed in Cochran [23]. In some studies on the FMR linewidth, in the high frequency limit (assuming that the magnetisation precession is circular rather than elliptical), the linewidth is represented by

$$\Delta H(\omega) = \Delta H(0) + \frac{2\alpha\omega}{\gamma}. \qquad (2.40)$$

For a homogeneous metal, the frequency independent linewidth is expected to be quite small (of the order of a few oersteds), it is a consequence of exchange-conductivity broadening [23, 24]. Two magnon scattering can also be included in the frequency independent term [29]. Chappert's work [30] on polycrystalline ultrathin cobalt films involved determining two sources of the linewidth, which arises from the spatial variation of the c-axis: $\Delta H = \Delta\varphi_H \left(\partial H_{res} / \partial\varphi_H \right)$ ($\Delta\varphi_H$ is the angular spread of the c-axis) and the distribution of internal field: $\Delta H = \Delta H_i \left(\partial H_{res} / \partial H_i \right)$ (ΔH_i is the internal field inhomogeneity).

The resonance lineshape changes if the sample thickness is greater than the skin depth. Estimates of the skin depth for pure metals at 90GHz at room temperature are shown in table 2.2. However, the granular thin films for this study have a skin depth greater than the effective sample thickness [31].

sample	Conductivity at room temperature ($x\ 10^5\ \Omega^{-1}cm^{-1}$)	Skin depth (μm)
Iron	1.03	0.52
Cobalt	1.60	0.42
Nickel	1.46	0.44

Table 2.2: Values of the skin depth at 90GHz for $\mu_r=1$.

It is clear that from many books on the theory of ferromagnetic resonance, the relative permeablilty of the sample is not unity when the sample is at resonance. As a result, from equation (2.41),

$$\delta = \left(\frac{2}{\omega\sigma\mu}\right)^{\frac{1}{2}} \qquad (2.41)$$

the skin depth, which is inversely proportional to the permeability will be close to zero, since at resonance the permeability reaches a significantly high value. The samples of interest in this thesis have thicknesses below the skin depth.

2.1.8. Spin Wave Resonance

Kittel [32] suggested that a uniform microwave field should be able to excite standing spin waves in thin films. In order that microwave energy may be absorbed, the spins must be pinned at least at one boundary of the film. Three cases, figure 2.8, represent (a) complete pinning at both surfaces, (b) complete pinning at one surface but not at the other surface, and (c) no pinning at either surface of the film.

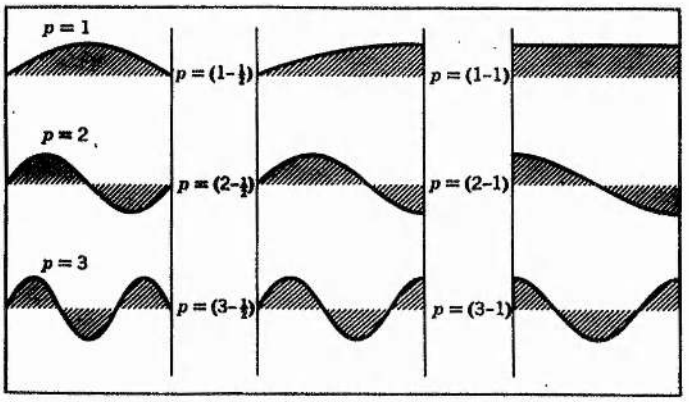

Figure 2.8. Complete pinning at both ends (a), pinning at one end and not at the other (b), and no pinning at either boundary of the thin film (c) [13].

For (a), there will be a net absorption of energy only for modes with an odd number of half-wavelengths, $p=1, 3, 5...$ For (b), all modes will absorb energy and for (c), only the uniform mode ($k=0$) couples with the microwaves [13].

The resonance condition for standing spin waves for the field normal to the film surface is

$$\frac{\omega}{\gamma} = H_{\perp} - 4\pi M + \frac{2Ak^2}{M_s} \qquad (2.42)$$

If the static field is applied parallel to the film surface, then the resonance condition is

$$\left(\frac{\omega}{\gamma}\right)^2 = \left(H_{\parallel} + \frac{2Ak^2}{M_s}\right)\left(H_{\parallel} + 4\pi M + \frac{2Ak^2}{M_s}\right) \qquad (2.43)$$

where A is the exchange constant (ergs/cm) and $k = \frac{p\pi}{L}$ where p is the number of half-wavelengths in the film in the film thickness, L, and $p=n-\delta$, where n is an integer and δ lies between zero and unity, depending on the pinning conditions at the boundaries. Examples of the exchange constant for nickel and cobalt at room temperature are $0.75x10^{-6}$ ergs/cm [33] and $1.30x10^{-6}$ ergs/cm [34], respectively.

An example of SWR at 87GHz is shown in figure 2.9. The sample is 100nm thick iron thin film.

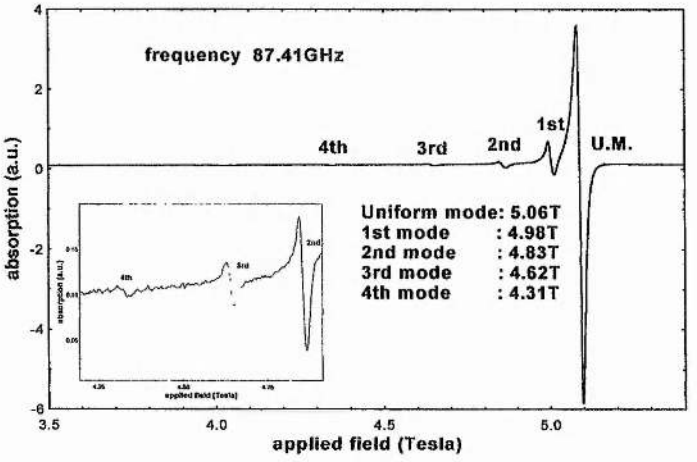

Figure 2.9. SWR of iron thin film at 87GHz with the field, H, applied normal to the film surface.

2.2. FMR spectrometer

2.2.1. 12 Tesla quasi-optical spectrometer

FMR measurements of thin films were measured using an in-house quasi-optical continuous wave high field 90 to 270 GHz spectrometer [35] (Some measurements were also performed on a conventional X band Bruker spectrometer).

The cryostat is a vapour shielded Oxford instruments design, capable of holding 40 litres of liquid helium. It has a 12T superconducting magnet and its magnetic field homogeneity is one part in 10^5 over $1cm^3$. The cryostat is fitted to an ITC4 (Intelligent Temperature Controller), which allows the temperature to be varied from 2.5K to room temperature. The cryostat has inbuilt modulation coils which ensure that problems associated with coil vibrations are minimised.

The spectrometer is controlled and all instruments are interfaced using LABVIEW. Conventionally, an FMR spectrum is obtained by slowly sweeping the dc magnetic field while keeping the mm-wave frequency fixed. The reflected signal is encoded by simultaneously modulating the magnetic field and using a lock-in amplifier after detection. The lock-in amplifier is used to display the spectrum in the derivative mode.

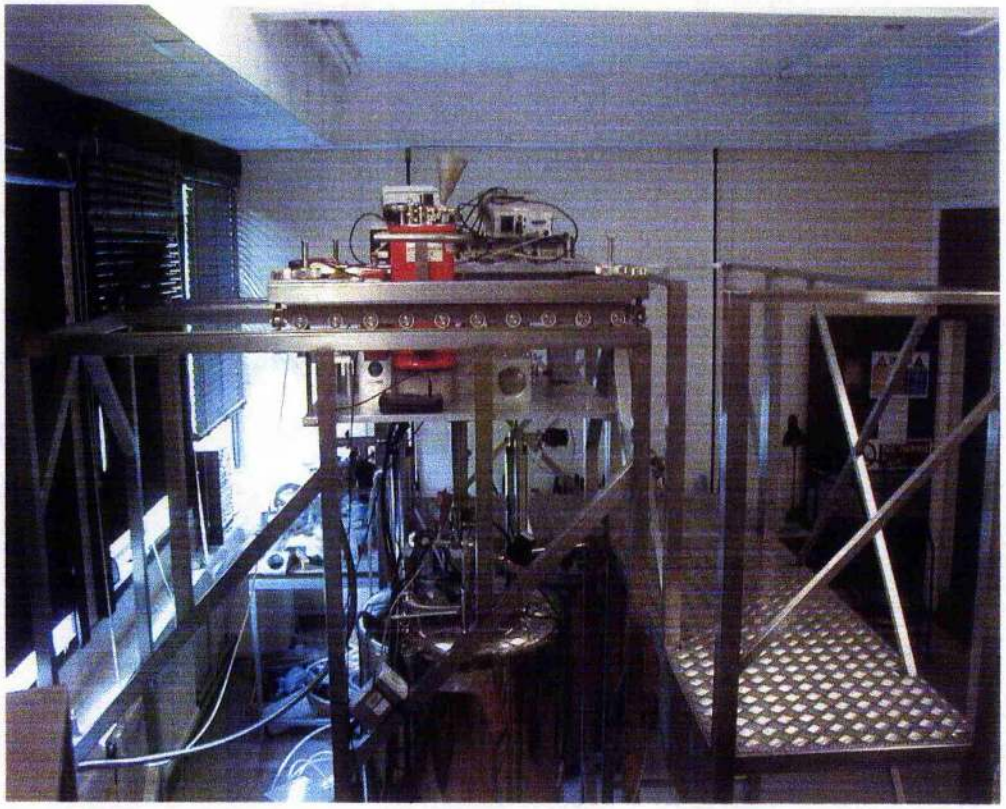

Fig 2.10. Quasi-optical spectrometer

The system is constructed using a reconfigurable "half-cube" system on an optical bread board and sits on top of a large metal frame that allows it to be positioned over the cryostat. The breadboard may be axially tilted by four gimbals to give fine adjustment of the alignment of the bread board over the cryostat.

The sample is inserted into a non-resonant system; that is, there is no cavity as shown in figure 2.11.

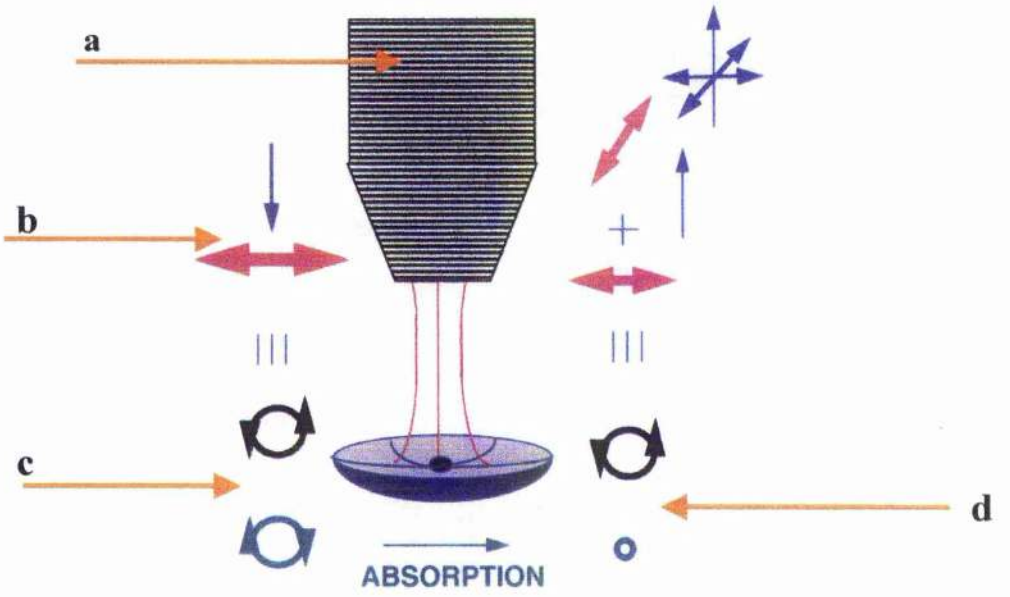

Fig 2.11. A linearly polarised mm-wave beam travels down a HE_{11} corrugated waveguide (a). This linear polarised beam (b), can also be represented as a left and right hand polarized (LHP, RHP) beam (c). On resonance, only one circular polarized beam is absorbed, transferring power in the orthogonal linearly polarized state which is detected in the spectrometer (d) [35].

The W-band Gunn oscillator has a maximum power output of around 20mW at 94 GHz. FMR signals have not been observed after frequency doubling or trebling because of the low power available.

The key advantage of this type of technique is that sample handling is easier at high frequencies than placing the thin film in a cavity, but even

more important, multi-frequency FMR is possible. Multi-frequency high field FMR offers many practical advantages over low frequency measurements. In most cases, the sample will be saturated by the dc field, it is easier to measure extremely broad lines and multi-frequency analysis and orientational studies can help to evaluate the static and dynamic properties of thin films with small ferromagnetic content.

The reason why samples were not placed in a cavity is due to the fact that at 90 GHz, the sample holder which fits into the cavity has an inner bore of 0.6mm. This means that the sample needs to be cut in order to fit into the sample holder, which may give rise to a subtle change to the intrinsic properties of the sample. Also, it would be difficult to determine whether the sample is in parallel or perpendicular configuration. The samples are also lossy (highly absorbing) and so the signal to noise of the FMR spectra would not improve greatly in a resonant system.

2.2.2 In-plane sample holder

FMR on thin films were carried out in perpendicular configuration; however, it is also necessary to measure in-plane to fully characterize the material. There was no available holder to carry out the latter configuration so an in-plane sample holder was therefore designed and constructed in the physics workshop in St. Andrews.

A basic theory of Gaussian Beam Optics [36, 37] was required to determine the relevant parameters, such as the mirror radius, the distance between the reflecting mirror and sample mirror and the focusing lens. Appendix A is a Mathcad sheet which shows the derivation of the relevant parameters as mentioned above.

The holder, shown below, was designed to operate at 94GHz and to fit into a cryostat with a sample bore of 49mm.

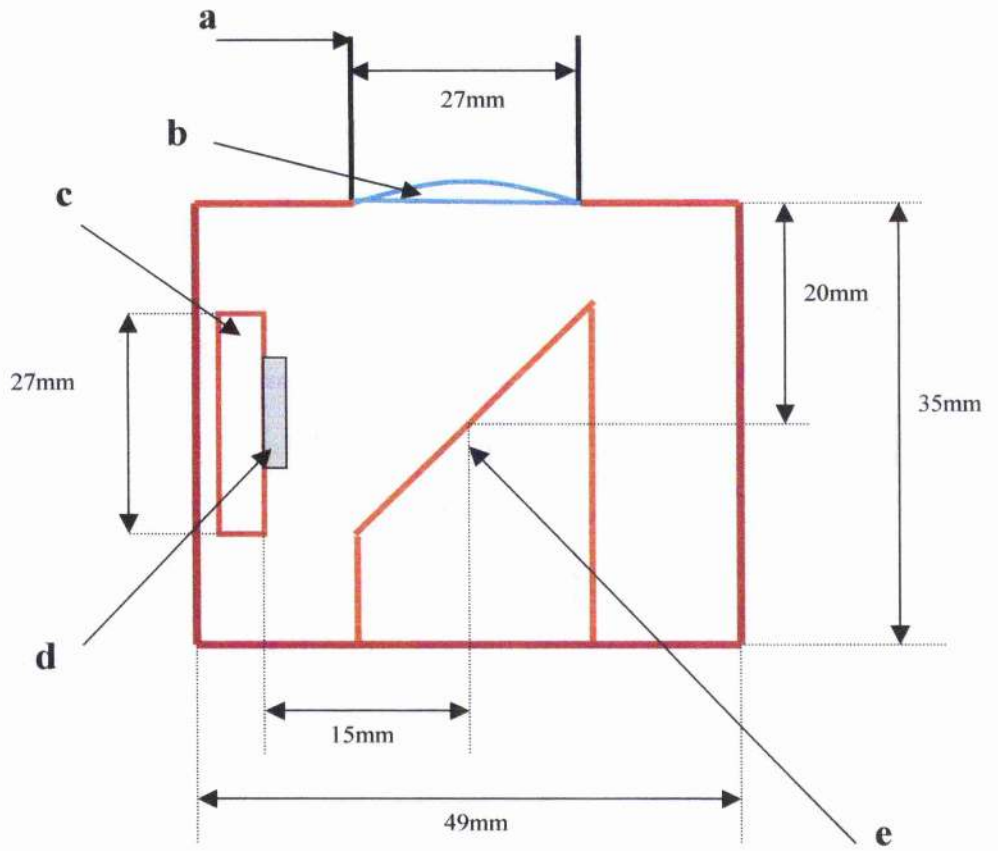

Figure 2.12. A 94GHz sample holder for in-plane FMR. The outercasing is made of tufnol. The HDPE (high density polyethylene) lens (b) sits on top of the tufnol casing, which focuses the Gaussian beam from the waveguide (a) onto the 45 degree mirror (e), which is reflected to the copper sample mirror (c) and FM sample (d). The FM sample is stuck onto the sample holder with vacuum grease.

The sample change over requires lifting the waveguide and the attached sample holder out of the cryostat. The sample mirror, labeled *c* in figure 2.12, can be removed and a thin film sample is inserted into the holder. The sample holder was only ready towards the end of the period when the work was completed. However, a preliminary example of use is shown in the next section on FeTiN samples.

2.2.3. Preliminary experiments

Two examples are given of preliminary multi-frequency (75 to 95GHz) FMR experiments. The results on one sample, a cobalt thin film, are compared to the known properties of cobalt. The FMR of in and out-of-plane configurations has been studied on samples of FeTiN with varying compositions of nitrogen.

2.2.3.1 Cobalt (30nm)

A 30nm cobalt thin film was prepared by MBE at Leeds on a silicon substrate with a gold capping layer. NMR work on this sample shows the presence of strains with an admixture of different cobalt phases: fcc and hcp phases [38, 39]. Figure 2.13 illustrates an NMR spectra of the sample at 4.2K.

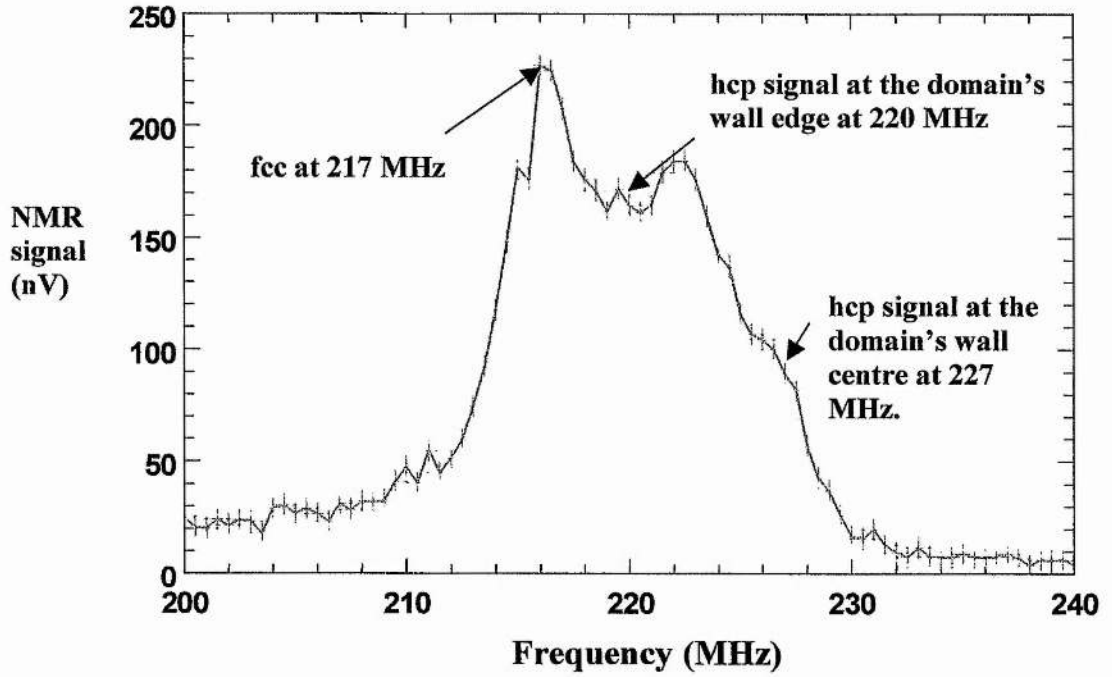

Figure 2.13. Zero field ^{59}Co NMR spectra of the cobalt (30nm) thin film at 4.2K showing the presence of FCC and HCP phases [39].

Multi-frequency FMR on cobalt film at frequencies between 75 to 95 GHz was carried out with the field normal to the film surface. A typical FMR signal of the cobalt sample at 91.25GHz is shown in figure 2.14a and 2.14b.

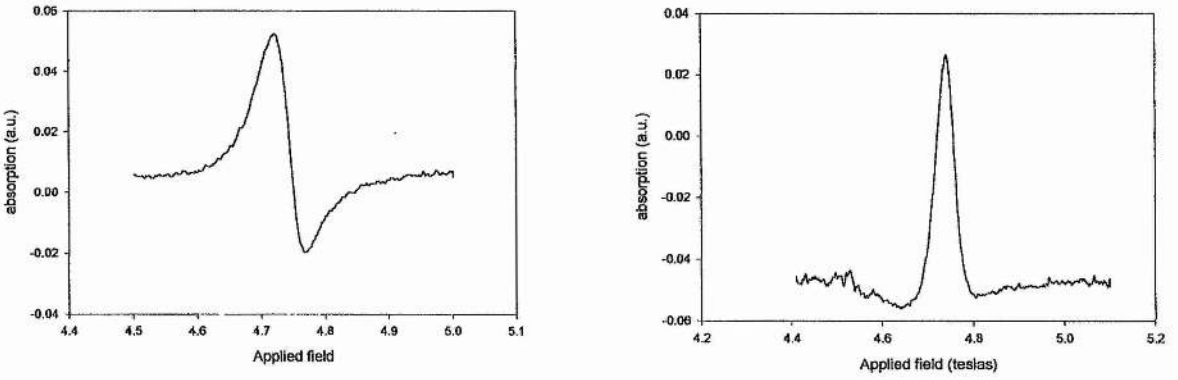

Figure 2.14. First derivative absorption (a) and dispersion (b) lineshapes.

The reader should note that obtaining decent FMR signals from the quasi-optical set-up is time consuming, particularly if one were to carry out multi-frequency FMR on films with small ferromagnetic content.

A fitting to the lineshape is required in order to determine the resonant field and the linewidth because it was not always possible to phase the signal correctly. A fitting package in Easyplot software provides a Levenberg-Marquardt fit to the data. The equation used is an admixture of a Lorentzian absorption and dispersion lineshape [40] of the following form:

$$y(H)=\frac{a\cdot\left(\frac{H_r-H}{\Delta H_{\frac{1}{2}}}\right)+9b-3b\cdot\left(\frac{H_r-H}{\Delta H_{\frac{1}{2}}}\right)^2}{\left[3+\left(\frac{H_r-H}{\Delta H_{\frac{1}{2}}}\right)^2\right]^2}+background \qquad (2.44)$$

where $y(H)$ is the FMR signal, H and H_r are the scanning and resonant fields, respectively. The coefficients a and b are the amplitudes of absorption and dispersion signals, respectively. $\Delta H_{\frac{1}{2}}$ is half the peak to peak linewidth. In order to test the validity of the above equation, figure 2.14a and 2.14b illustrate the derivative of an absorption and dispersion lineshape, respectively. Four repeat measurements on the absorption and dispersion measurements on the cobalt sample were carried out and a fitting to the lineshape using equation (2.44) was used and compared.

	Lineshape A (kOe) absorption	Lineshape B (kOe) dispersion	Difference (Oe)
H_r	47.37	47.35	13.5
$\Delta H_{\frac{1}{2}}$	0.54	0.54	7.8

Table 2.3. Extracted resonant field and linewidth from a fit to the dispersion and absorption lineshape.

The results in table 2.3 shows that the equation used to determine the resonant field and linewidth is valid.

Appendix B shows a Mathcad simulation of an FMR signal with an admixture of absorption and dispersion lineshapes for the field normal to the plane of a thin film.

From the fit to the resonant field, it is possible to determine the spectroscopic splitting factor and the perpendicular anisotropy. Here, the perpendicular anisotropy is attributed to shape and perpendicular uniaxial anisotropy (due to crystalline, stress and interface effects on the thin film) [39, 41]. The resonance condition is given as $\frac{\omega}{\gamma} = H_r - H_{eff}$, where H_{eff} is the sum of the demagnetising and uniaxial perpendicular anisotropy [39]. Applying this analysis to the cobalt film, the g-factor is 2.16 ± 0.01 and the effective anisotropy is 17.15 ± 0.20 kOe. If it is assumed that the saturation magnetisation for this film is the same as for bulk cobalt (17.6kOe [18]), the crystalline anisotropy field extracted in this way is 0.5kOe. Consequently, the magnetocrystalline anisotropy constant K_u is deduced to be $(3.15 \pm 1.45)x10^5$ ergs/cc. This value is much less than that of bulk hcp cobalt, which is typically $(3\text{-}4)x10^6$ ergs/cc at room temperature [12, 39] and most likely, is a result of the mixture in the crystalline phases and the polycrystalline nature of the sample [41]. Previous measurements showed that torque magnetometry of the same cobalt film has a perpendicular anisotropy of 16.20 ± 0.70 kOe which is slightly lower than that determined from FMR [41].

2.2.3.2 FeTiN thin films

FeTiN alloys are promising candidates for next generation inductive read heads due to their high moments and soft magnetic properties ($4\pi M_s \cong 18$ to 21 kOe) [42]. The nitrogen atoms occupy interstitial sites in the iron lattice and the stability of the anisotropy upon transverse field annealing depends on the nitrogen content [43]. Samples with atomic percent nitrogen less than about 6.5% exhibit stable anisotropy, whilst those above it are unstable. All samples except for 10 at.% nitrogen have a film thickness of 75nm with 3at.% titanium and tantalum capping layer. The sample with 10at.% nitrogen has a film thickness of 60nm with

approximately 3 at.% titanium and no capping layer [43]. This section does not concentrate on the physics of these samples, but aims to show that the magnetic properties of these films deduced from measurements in the range 75 to 95 GHz, in perpendicular configuration are consistent with in-plane and out-of-plane measurements at 94 GHz. These experiments were designed to test the new sample holder described in section 2.2.2 and appendix A.

Figure 2.15 is an FMR spectra of FeTiN with 0 at.% nitrogen. It is observed that the spectra have lines below the main resonance due to spin waves. This will be discussed shortly.

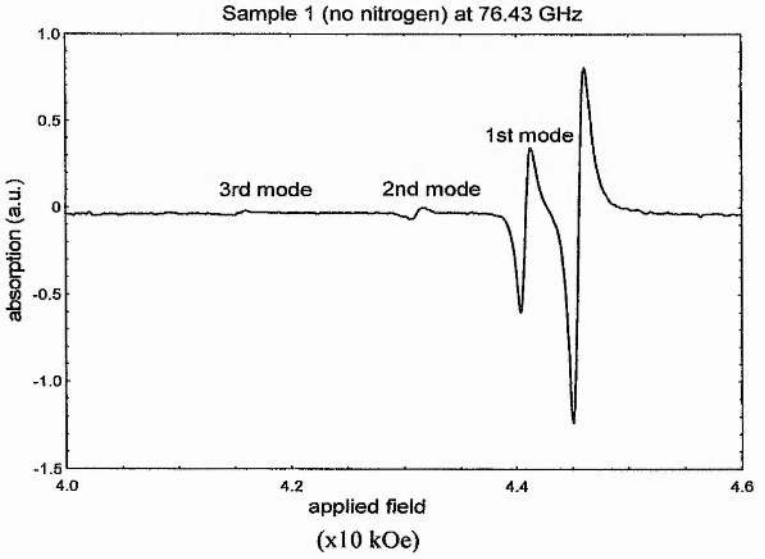

Figure 2.15. SWR of FeTi film at 76GHz.

From table 2.4, the spectroscopic splitting factor from both methods is around that of bulk iron, 2.09 [18]. In addition, the perpendicular anisotropy for both types of measurements almost agree with each other. The FMR equations for in-plane

$$\left(\frac{\omega}{\gamma}\right)^2 = H_{\parallel}\left(H_{\parallel} + H_{eff}\right) \qquad (2.45)$$

and out-of-plane

$$\frac{\omega}{\gamma} = H_{\perp} - H_{eff} \qquad (2.46)$$

were deduced from (2.38). H_{eff} is the perpendicular uniaxial anisotropy, which includes the shape and crystalline anisotropy.

Nitrogen content (%) with sample number in brackets	Lande g-factor from in and out-of-plane at 94 GHz	Lande g-factor from multi-frequency measurements 76 – 97 GHz	Perpendicular anisotropy (kOe) from in and out-of-plane at 94 GHz	Perpendicular anisotropy (kOe) from multi-frequency measurements 76 – 97 GHz
0 (1)	2.08	2.11 ± 0.01	18.41	18.66 ± 0.34
4.35 (2)	2.07	2.08 ± 0.02	17.97	18.17 ± 0.48
5 (3)	2.08	2.12 ± 0.03	17.60	17.52 ± 0.30
6.5 (4)	2.07	2.09 ± 0.03	17.22	17.27 ± 0.37
7.8 (5)	2.07	2.09 ± 0.03	15.66	15.40 ± 0.47
10 (6)	2.08	2.07 ± 0.03	14.51	14.74 ± 0.64

Table 2.4. The g-factor and H_{eff} determined from the two methods discussed above. Determining the error for values in columns two and four was not straight forward, therefore, a comparison of the two parameters from one method to another is required. Note, for the two orientations at 94GHz, values of the perpendicular anisotropy coincide with those determined from multi-frequency measurements.

Samples with 0, 4.35, 5 and 10 at.% nitrogen exhibit spin wave resonance. It was not possible to determine the exchange constant A (in ergs/cm), equation 2.42, as this requires knowledge of the sample's saturation magnetization. However, from another expression,

$$\frac{\omega}{\gamma} = H_r - H_{ef} + \frac{D}{g\mu_B}\left(\frac{n\pi}{L}\right)^2 \qquad (2.47)$$

the spin wave stiffness constant D, is determined [44]. The spin wave stiffness constant D for iron is 4.48×10^{-29} ergs cm^2 [44]. From equation

(2.47) and figure 2.16 (as an example), the stiffness constant D is close to bulk iron for mode numbers $n = 1, 2$ and 3 for samples listed in table 2.5.

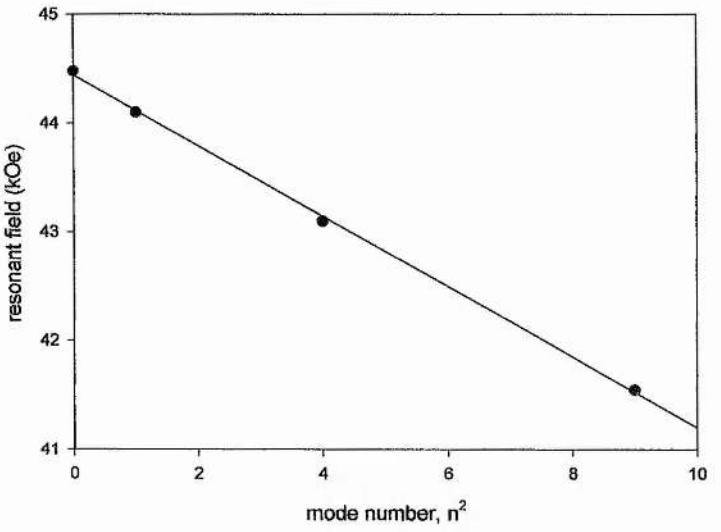

Figure 2.16. Plot of the resonant field (measured from the 0% nitrogen sample) of lines below the main resonance with the square of the mode number, n^2.

Nitrogen content (%)	Spin wave stiffness constant (x 10^{-29} ergs cm^2)
0	3.50
4.35	3.35
5	2.53
10	3.90

Table 2.5. Spin wave stiffness constant, D, determined from FMR.

2.3. References

[1] V.K. Arkad'yev., J.Russ. Phys.-Chem. Soc. Phys. 44 (1912) 165

[2] Ya.G. Dorfman, Zs. f. Phys., 17 (1923) 98

[3] N.S. Akulov, J. Russ. Phys.-Chem. Soc. Phys., 58 (1926) 577

[4] E.K. Zavoiskii, J.Phys. USSR 10 (1944) 197

[5] J.H.E. Griffiths, Nature, 158 (1946) 670

[6] L.D. Landau and E.M.Liftschitz, Phys. Zs. Soviet Union 8 (1935) 153

[7] C. Kittel, Phys. Rev., 71 (1947) 270

[8] C. Kittel, Phys. Rev., 73 (1948) 155

[9] D. Polder, Phil. Mag. 40 (1949) 99

[10] S.V. Vonsovskii, *Ferromagnetic Resonance*, Pergamon, Press, New York, 1966

[11] A.H. Morrish., *The Physical Principles of Magnetism*, Wiley, 1964

[12] D. Craik., *Magnetism. Princples and Applications*, Wiley, Chichester, 1995

[13] A.G. Melkov and G.A. Gurevich, *Magnetisation Oscillations and Waves*, CRC Press, 1996

[14] J.M. Luttinger and C. Kittel., Helv. Phys. Acta., 21 (1948) 480

[15] M.L. Plummer, J.van Ek and D. Weller, *The Physics of Ultra-High Density Magnetic Recording*, Springer-Verlag, New York, 2001

[16] R. Urban, G. Woltersdorf, B.Heinrich, Phys. Rev. Lett., 87 (2001) 217204

[17] T.L. Gilbert, Phys. Rev. 100 (1955) 243

[18] S. Chikazumi, *Physics of Magnetism*, John Wily and Sons, Inc (1964)

[19] B. Lax and K.J. Button, *Microwave Ferrites and Ferrimagnetics*, M^{c}Graw-Hill, New York, 1962, Chap 4.

[20] J.A. Osborn, Phys. Rev., 67 (1945) 351

[21] J. Smit and H.C. Beljers, Philips Res. Rep. 2 (1955) 113

[22] H. Suhl., Phys. Rev. B. 97 (1955) 555

[23] J.F. Cochran, R.W. Qiao and B. Heinrich, Phys. Rev. B. 39 (1989) 4399

[24] B. Heinrich, in *Ultrathin Magnetic Structures II*, edited by Heinrich amd J.A.C.Bland.,Springer, Berlin, 1994, Chap 3.

[25] F. Schreiber, Z.Frait, Solid State Commun., 93 (1995) 965

[26] M. Farle, Rep. Prog. Phys. 61 (1998) 4344

[27] H. Hurdequint, J. Magn. Magn. Mat., 242-245 (2002) 521

[28] R.D. McMichels, M.D. Stilles, P.J. Chen, W.F. Egelhoff, J. Appl. Phys. 83 (1998) 7037

[29] J.F. Cochran, R.W. Qiao, B. Heinrich, Phys. Rev. B., 39 (1989) 4399

[30] C. Chappert, K.Le Dang, P. Beauvillain, H. Hurdequint, D. Renard, Phys. Rev. B., 34 (1986) 3192

[31] P.C.Riedi, *private communications,* 2002

[32] C. Kittel, Phys. Rev., 110 (1958) 1295

[33] S.M. Bhagat and L.L. Hirst and J.R. Anderson, J. Appl. Phys., 37 (1966) 194

[34] P.E. Tannenwald and R. Weber, Phys. Rev. 121 (1961) 715

[35] G.M. Smith, J.C.G.Lesurf, R.H.Mitchell and P.C.Riedi, Rev. Sci. Instrum. 69 (1998) 3924

[36] P.F. Goldsmith, *Quasi-optical Systems: Gaussian Beam Qausioptical Propagation.*, IEEE Press/Chapman and Hall Publishers, 1998

[37] J. Lesurf, *Millimetre-Wave Optics, Devices and Systems*, Adam Hilger, Bristol, 1990

[38] P.C. Riedi, T. Thomson and G.J. Tomka, *NMR of Thin Magnetic Films and Superlattices*, Handbook of Magnetic Materials 12 (1999), edited by K.H.J.Buskow, Elsevier Science, B.V., 1999, Chap 2.

[39] C.J. Oates, F.Y. Ogrin, P.C. Riedi, S.L. Lee, G.M. Smith, T. Thomson, J. Magn. Mag. Matt. 242-245 (2002) 402

[40] C.P. Poole, *Electron Spin Resonance – A Comprehensive Treatise on Experimental Techniques*, Wiley, New York, 1967.

[41] F.Y. Ogrin, S.L. Lee, Y.F. Ogrin, J. Magn. Magn. Mat., 219 (2000) 331

[42] C. Alexander Jr., IEEE Trans. Magn. (2001) In press

[43] C. Alexander Jr., *private communications,*2001

[44] A. Butera, J.N. Zhou, J.A. Barnard, Phys. Rev. B, 60 (1999) 12270

Chapter 3

FMR and torque magnetometry of high and low noise CoCr alloy longitudinal recording media

3.1 Introduction

This chapter, which is in two parts, centres on CoCr alloys longitudinal recording thin films. The first half looks at how it is possible to determine the magnetic characteristics of recording media with high field FMR, without introducing micromagnetic and/or mean field simulations, followed by correlating these characteristics to their recording properties and comparing the anisotropy field derived from torque magnetometry measured in Seagate with that of FMR, in St. Andrews. The second part of this chapter examines low field torque magnetometry as a technique to measure exchange and/or dipole interactions and the anisotropy. Both the technique and simulation of results will be presented.

The samples are of two types: high and low noise media, the difference being attributed to their different grain size and grain size distributions. This is discussed again in section 3.2.2.

3.2 Ferromagnetic resonance

3.2.1 Summary of previous works on the FMR of CoCr-alloy recording media

The first group to measure the in-plane uniaxial anisotropy of planar random polycrystalline grains CoCrPt longitudinal recording media was that of Igarashi et al [1]. The composition of the media concerned was

30nm CoCrPt/10nm CrTiB/10 nm Ta/32nm Zr and was dc magnetron sputtered onto a glass substrate. In their experiment a high-intensity magnetic field was applied normal to the film surface at frequencies 71 and 117 GHz, figure 3.1. As will be seen in figure 3.1, the signal to noise was very poor in this experiment.

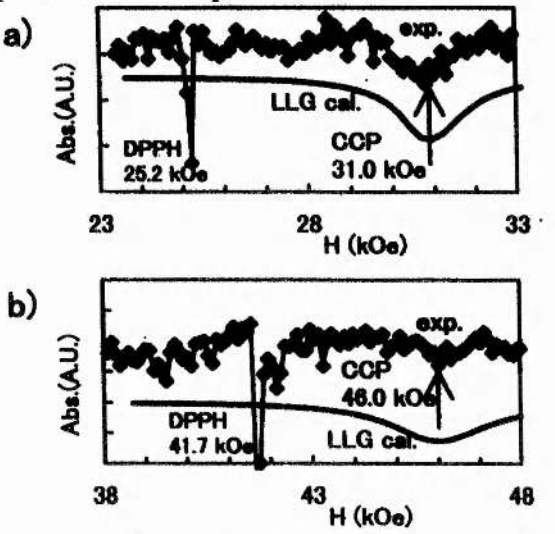

Figure 3.1. FMR absorption spectra of the polycrystalline CoCrPt thin film at 70.51 (a) and 116.8 GHz (b) [1].

The group carried out micromagnetic simulations (based on the Landau-Lifschitz-Gilbert equation) and confirmed that magnetic (exchange and/or magnetostatic) interactions and the uniaxial anisotropic field distributions had very little effect on the resonant field in the configuration used. The important physical parameters that affect the recording performance were estimated using the linewidth of the FMR spectra for different frequencies with the aid of micromagnetic simulations. From the simulation, they deduced the uniaxial anisotropy and its dispersion to be 7.0 ± 0.2kOe and 1.2 ± 0.5kOe, respectively; the Gilbert damping constant α as 0.03 ± 0.01 and the Lande g-value of 2.19 ± 0.02 which is in the region of bulk cobalt, 2.18 to 2.25 [2,3]. The simulation agreed very well with the results obtained from the resonant field measurements. The FMR equation, which they used for obtaining the g-factor and uniaxial anisotropy is used in this chapter and a section on the derivation of the resonant condition is discussed in 3.2.3.

The group also deduced (from their simulations) that the linewidth of the FMR spectra becomes large of the order of exchange interaction, dispersion in the uniaxial anisotropy and the Gilbert damping constant.

Another group, which measured FMR of materials of interest for media thin films was Inaba et al [4]. Here, they looked at the Gilbert damping constants of single crystal CoCrTa and CoCrPt thin films by Q-band FMR with the high field applied within the film surface. The samples were epitaxially grown on MgO (110) substrate with the HCP c-axis in-plane and parallel to MgO [001]. From the FMR measurements, they showed that the damping factor, α, of $Co_{77}Cr_{19}Ta_4$ increased from 0.016 to 0.028 with respect to its film thickness, as illustrated in figure 3.2.

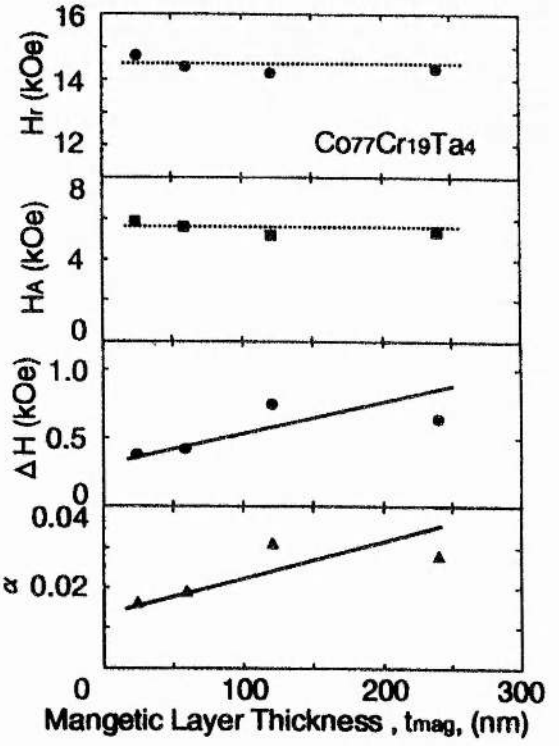

Figure 3.2 Variations of resonance magnetic field, anisotropy field, linewidth and damping constant with magnetic layer thickness ranging from 25 to 240nm [4].

The group believes that an increase in α is likely to be caused by eddy current losses induced in the film when a high frequency magnetic field is applied.

When the Cr concentration in the 60nm thick $Co_{96-x}Cr_xTa_4$ magnetic layer is increased from 8 to 19 at.%, the damping factor increased from 0.009 to 0.019. They also found that the damping factor in 25nm thick $Co_{81}Cr_{15}Pt_4$ film is 2.5 times larger (0.038) than the $Co_{81}Cr_{15}Ta_4$ film (α = 0.014) with the same thickness. The group concluded that the difference in α between the CoCrTa and CoCrPt films may be related to the polarisation of platinum in the CoCrPt layer.

3.2.2 High and low noise recording media

The two samples were dc magnetron sputtered on a super-smooth glass ceramic substrate by Seagate Technologies in California. The magnetic layers of both media were sputtered from the same CoCrPtTa alloy target. The underlayer of the 2D in-plane isotropic media consisted of 50nm thick CrMn for media A and 40nm/10nm thick NiAl/CrMn for media B, as shown in figure 3.3. Both types of media were processed under identical deposition conditions, including substrate heating, sputtering gas pressure and deposition rate. The thickness of the recording thin film for both media is 27.5 ± 0.5 nm. These films had very different recording performance, grain size and grain size distributions, but similar magnetic properties [5,6].

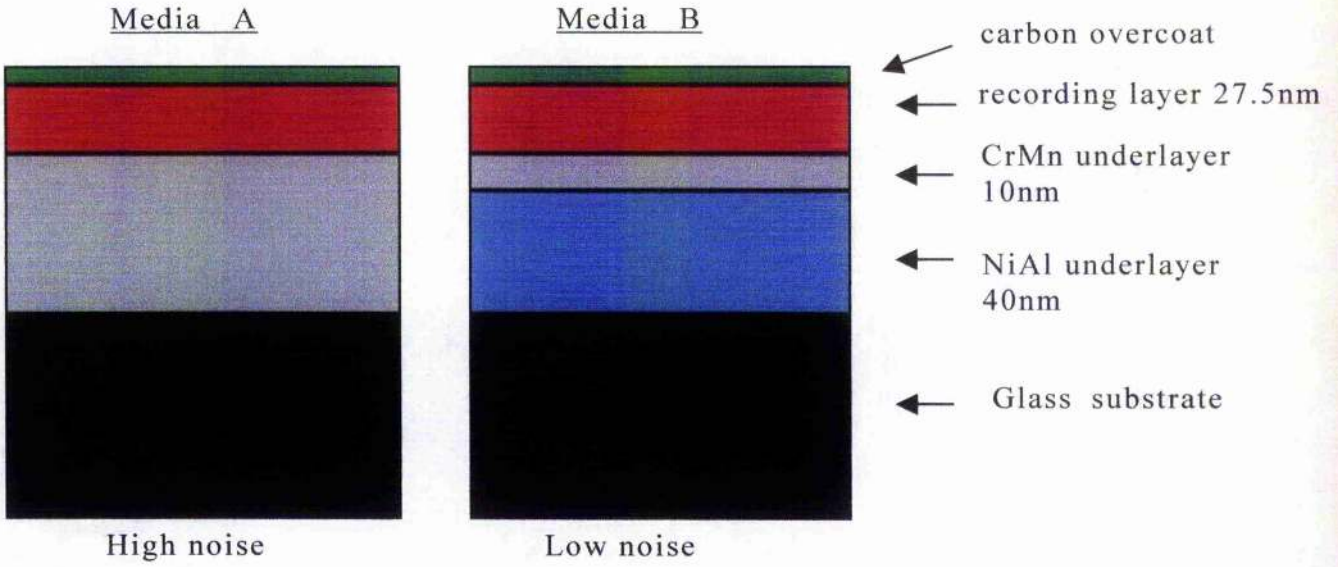

Figure 3.3. Layout of two thin film media.

The mean physical grain size was obtained from TEM by Seagate Technologies as shown in figure 3.4. Media A (sample 15A) has a wide dispersion of grain sizes ranging from 20 to 200nm. The large regions appear to be composed of smaller sub-grains. To a first approximation, the mean size of these regions is of the order of 50nm. Media B (sample 15B) has a grain size of 17 ± 1.5nm [5].

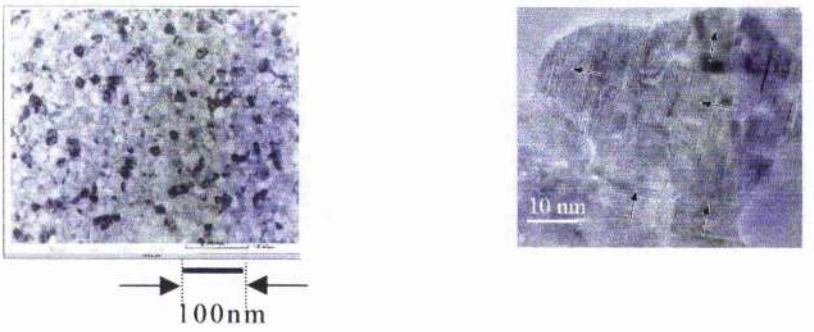

Figure 3.4. TEM image of low (a) and high noise (b)

(courtesy of Yen et al)[5,6].

Yen [5] and Laidler [7] found that the magnetic thin films sputtered onto the glass ceramic substrate when CrMn is used as a single underlayer possessed high medium noise. This is absent from otherwise identically sputtered media with a NiAl/CrMn double underlayer structure.

Magnetisation measurements, figure 3.5, were measured using a non-destructive Seagate rotating disk magnetometer at room temperature. The saturation magnetisation was measured with the field in the plane of the sample. Hysteresis plots of the high and low noise media are shown in figure 3.5. The saturation magnetisation was found to be 4.87 ± 0.10 kOe and 4.47 ± 0.09 kOe for the high and low noise media, respectively [6]. The uncertainty in the saturation magnetisation arises as a combination of errors: the measured total magnetic moment, magnetic layer thickness and sample area; for example, the high noise media has a moment, (209 ± 1) μemu, with a film area of 19.6 ± 0.2 mm^2; similarly for low noise media, the moment size is (192 ± 1) μemu, with the same film area.

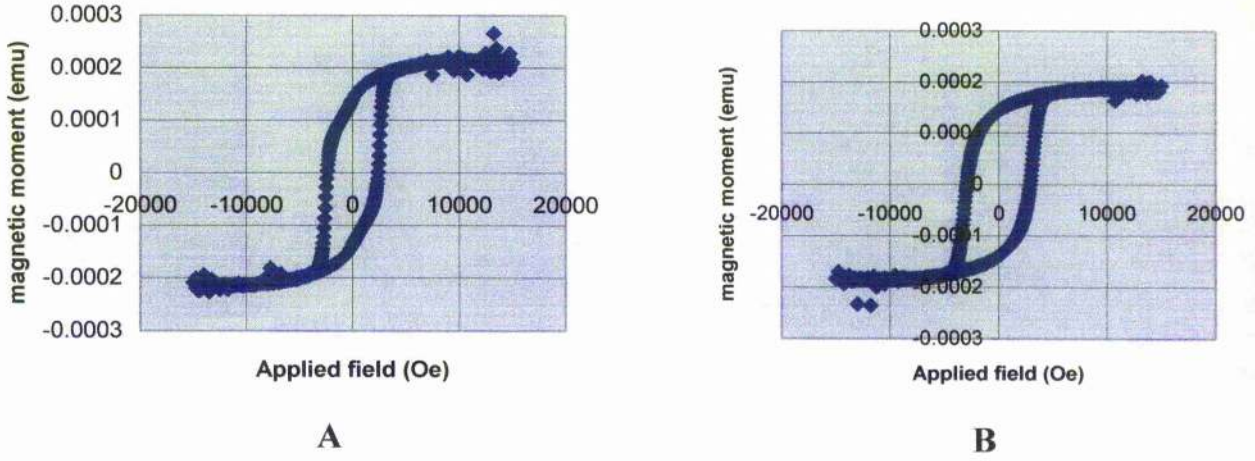

Figure 3.5. Hysteresis of low (A) and high (B) noise media [6].

The anisotropy field of the low and high noise media was measured using a DMS model 800 combined VSM/torque magnetometer at room temperature in Seagate. The angular dependence of the torque was

measured in an applied field of 13 kOe at room temperature and the resulting data fitted to a uniaxial anisotropy model containing a constant term K_0, a term in $K_1 sin^2$ and a term in $K_2 sin^4$. K_2 was found to be negligible allowing the anisotropy to be determined solely from K_1. The anisotropy field was subsequently calculated using $H_K = 2K_1/M_s$. Torque magnetometry measurements of both the high and low noise media gave a value of 9.65 kOe for the magnetocrystalline anisotropy [6,8].

3.2.3 Modelling

The high field FMR data of the recording media is modelled as non-interacting HCP cobalt grains with the c-axis distributed randomly within the film plane. We will look at the general case where the c-axis of the HCP grain is at an angle ρ relative to the x-axis as illustrated in figure 3.6.

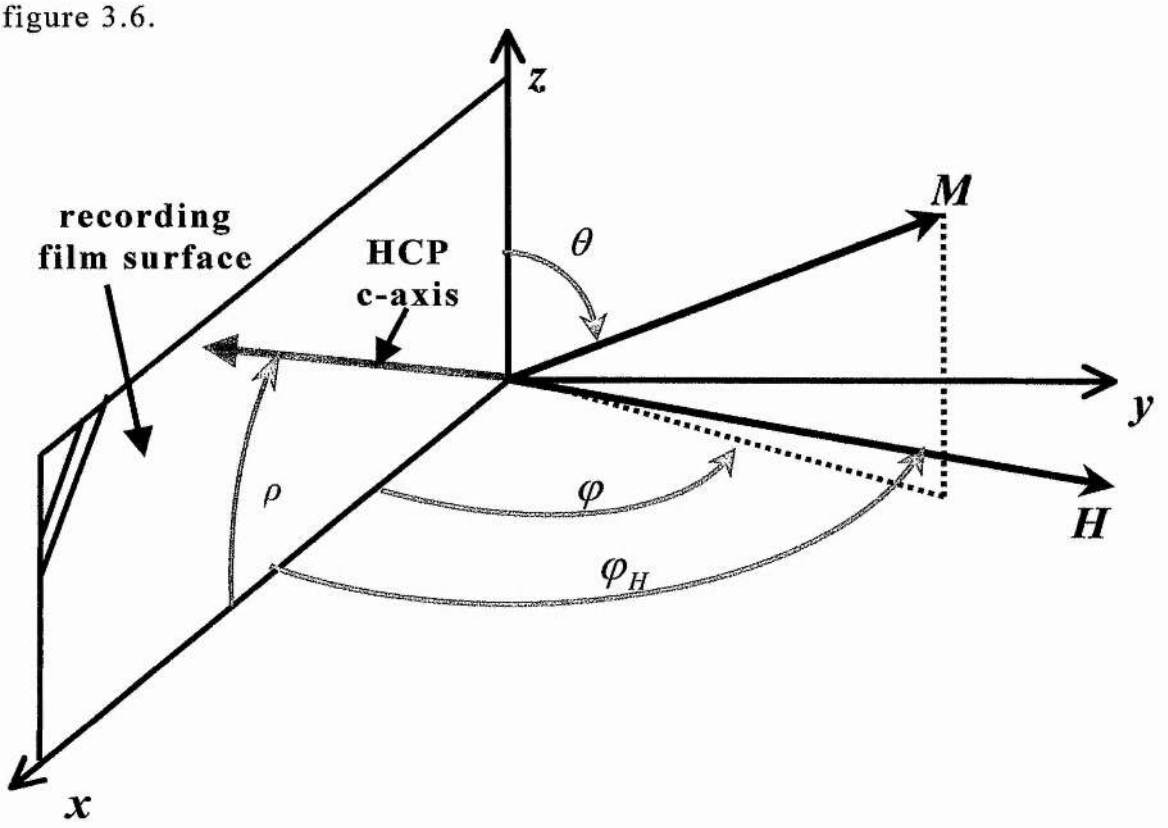

Figure 3.6 Longitudinal recording thin film with the c-axis of one of the HCP grains, which lies within the film surface at an angle ρ relative to the x-axis.

Actually, the derivation of the FMR condition below, which is in spherical polar coordinates, shows that for any value of ρ the resonant frequency is exactly the same. This is true for the case for an applied field, which is directed perpendicular to the film surface.

We consider the total energy of the system; that is, the sum of the Zeeman interactions, magnetocrystalline and shape anisotropy. The exchange energy is not included as it is assumed that for high field FMR (around 40 kOe with the mm-wave frequency set to 90 GHz) the neighbouring grains are decoupled from exchange interactions. The total energy of each grain is:

$$E_{Total} = E_{Zeeman} + E_{anisotropic} + E_{shape} \tag{3.1}$$

with the Zeeman energy given as

$$E_{Zeeman} = -MH(\sin\theta\cos(\varphi_H - \varphi)\sin\theta_H + \cos\theta\cos\theta_H) \tag{3.2}$$

the demagnetising contributions due to dipole-dipole effects is

$$E_{shape} = 2\pi M^2 \sin^2\theta\sin^2\varphi \tag{3.3}$$

and the in-plane uniaxial anisotropy is expressed in the form

$$E_{anisotropy} = K_u \sin^2\alpha \tag{3.4}$$

where α is the angle between the c-axis of the hcp grain and the magnetisation, M. Hence the anisotropy is re-written in terms of the polar and azimuthal angles as

$$E_{anisotopy} = K_u(1-\sin^2\theta\cos^2\varphi\cos^2\rho - \cos^2\theta\sin^2\rho - \frac{1}{2}\sin 2\theta\sin 2\rho\cos\varphi) \tag{3.5}$$

The c-axis was randomly oriented within the film plane and the uniaxial anisotropy of each grain is considered to be magnetocrystalline [6].

Minimizing the energy with respect to the polar and azimuthal angles defines the magnetisation's equilibrium position (provided that the

double derivative of the energy with respect to the polar and azimuthal angles is greater than zero).

$$\frac{\partial E_{Total}}{\partial \theta} = -MH\left(\cos\theta\cos(\varphi_H - \varphi)\sin\theta_H - \sin\theta\cos\theta_H\right) + 2\pi M^2 \sin 2\theta \sin^2\varphi - K_u\left(\sin 2\theta\cos^2\varphi\cos^2\rho - \sin 2\theta\sin^2\rho + \cos 2\theta\cos\varphi\sin 2\rho\right) \tag{3.6}$$

and

$$\frac{\partial E_{Total}}{\partial \varphi} = -MH\left(\sin\theta\sin(\varphi_H - \varphi)\sin\theta_H\right) + 2\pi M^2 \sin^2\theta\sin 2\varphi + K_u\left(\sin^2\theta\sin 2\varphi\cos^2\rho + \frac{1}{2}\sin 2\theta\sin\varphi\sin 2\rho\right) \tag{3.7}$$

and that

$$\left.\frac{\partial^2 E_{Total}}{\partial\theta^2}\right|_{\theta=\theta_0,\varphi=\varphi_0} > 0, \qquad \left.\frac{\partial^2 E_{Total}}{\partial\varphi^2}\right|_{\theta=\theta_0,\varphi=\varphi_0} > 0 \quad \text{and}$$

$$\frac{\partial^2 E_{Total}}{\partial\varphi\partial\theta} < \frac{\partial^2 E_{Total}}{\partial\vartheta^2}\cdot\frac{\partial^2 E_{Total}}{\partial\varphi^2} \tag{3.7a}$$

Since the dc field is applied normal to the film plane, a trivial solution to the static equilibrium position of the magnetisation is given by $\theta_{eq} = \frac{\pi}{2}$ if $\rho = 0$ and thus φ_{eq} is given by

$$\sin\varphi_{eq} = \frac{H}{\left(4\pi M + \frac{2K_u}{M}\right)} \tag{3.8}$$

Otherwise one would employ an iterative procedure such as the Newton Rhapson method in order to determine individual values of θ_{eq} and φ_{eq} for corresponding values of ρ.

Figure 3.7 shows the equilibrium angle φ_{eq} with respect to H, the applied field, for different values of the uniaxial anisotropy field. The saturation magnetisation is fixed to 4.90 kOe and ρ, the angle between the c-axis of the HCP grain and the x-axis, is set to zero.

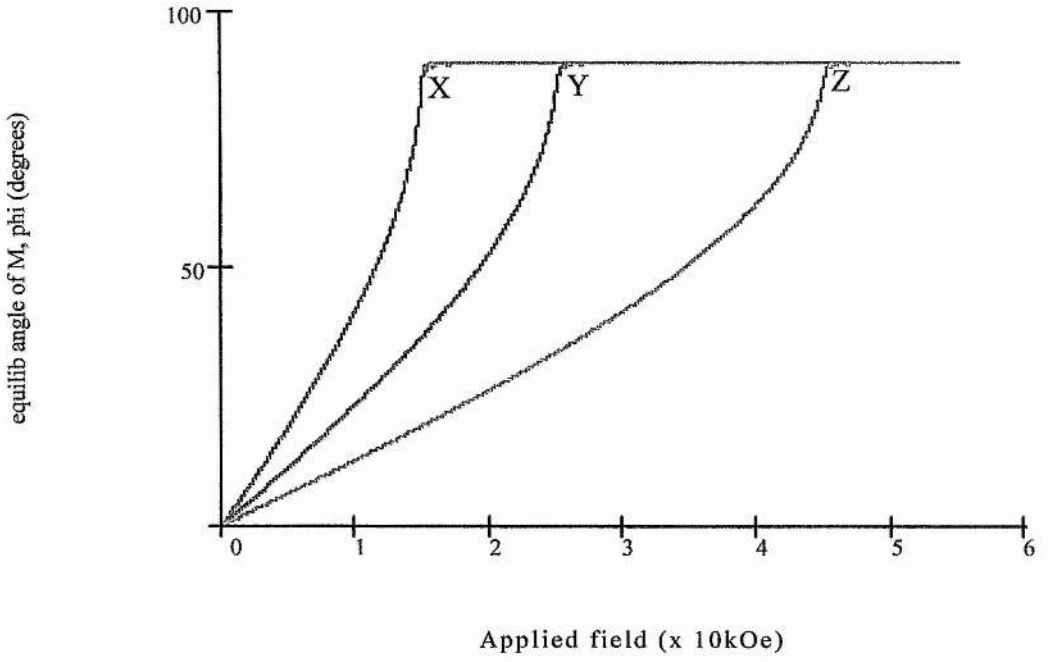

Figure 3.7. A plot of the moment's equilibrium position, φ_{eq} in degrees, for different values of the uniaxial anisotropy.

If the in-plane uniaxial anisotropy is varied from 10.0 kOe (red line) to 20.0 kOe (blue) to 40.0 kOe (magenta) then a much larger field is required to orient the moment from in-plane (easy axes) to out-of-plane (normal to the film plane). The point at which the angle of orientation of the moment is normal to the film surface (labelled X, Y and Z on figure 3.7) occurs when the applied field is equal to the sum of the demagnetising field and the in-plane uniaxial anisotropy field.

It was assumed in this calculation that there are no exchange interactions between the grains, which may not be valid at lower fields. There is an added assumption that the sample is a perfect longitudinal recording media: one with no out-of-plane deviation of the grain's c-axis.

From the Smit-Beljer's equation (2.38) [9]:

$$\left(\frac{\omega}{\gamma}\right)^2 = \frac{\left(1+\alpha^2\right)}{M^2 \sin^2\theta_0}\left(\frac{\partial^2 E}{\partial \vartheta^2}\cdot\frac{\partial^2 E}{\partial \varphi^2} - \left(\frac{\partial^2 E}{\partial \vartheta \partial \varphi}\right)^2\right) \tag{3.9}$$

it is clear that double and partial derivatives are required in order to fully determine the resonant condition. Note that for perpendicular FMR, the sine term in the denominator must be non-zero. We are also assuming that the contribution from the damping factor in the above equation is negligible.

$$\frac{\partial^2 E_{Total}}{\partial \theta^2} = MH\left(\sin\theta\cos\left(\varphi_H-\varphi\right)\sin\theta_H + \cos\theta\cos\theta_H\right) + \tag{3.10}$$
$$4\pi M^2\cos 2\theta\sin^2\varphi - 2K_u\begin{pmatrix}\cos 2\theta\cos^2\varphi\cos^2\rho - \cos 2\theta\sin^2\rho - \\ \sin 2\theta\cos\varphi\sin 2\rho\end{pmatrix}$$

and

$$\frac{\partial^2 E_{Total}}{\partial \varphi^2} = MH\left(\sin\theta\cos\left(\varphi_H-\varphi\right)\sin\theta_H\right) + \tag{3.11}$$
$$4\pi M^2\sin^2\theta\cos 2\varphi + K_u\left(2\sin^2\theta\cos 2\varphi\cos^2\rho + \frac{1}{2}\sin 2\theta\cos\varphi\sin 2\rho\right)$$

and

$$\frac{\partial^2 E_{Total}}{\partial \theta \partial \varphi} = MH\left(\cos\theta\sin\theta_H\sin\left(\varphi-\varphi_H\right)\right) + 2\pi M^2\sin 2\theta\sin 2\varphi + \tag{3.12}$$
$$K\left(\sin 2\theta\sin 2\varphi\cos^2\rho + \cos 2\theta\sin\varphi\sin 2\rho\right)$$

Equations (3.10) to (3.12) are substituted into the Smit-Beljer's equation, which results in the general resonant condition.

$$\left(\frac{\omega}{\gamma}\right)^2 = \frac{1}{M^2\sin^2\theta_0}\left(\begin{pmatrix}\left(\begin{pmatrix}MH\left(\sin\theta_0\cos\left(\varphi_H-\varphi_0\right)\sin\theta_H + \cos\theta_0\cos\theta_H\right) + \\ 4\pi M^2\cos 2\theta_0\sin^2\varphi_0 - 2K_u\begin{pmatrix}\cos 2\theta_0\cos^2\varphi_0\cos^2\rho - \cos 2\theta_0\sin^2\rho - \\ \sin 2\theta_0\cos\varphi_0\sin 2\rho\end{pmatrix}\end{pmatrix}\times \\ \begin{pmatrix}MH\left(\sin\theta_0\cos\left(\varphi_H-\varphi_0\right)\sin\theta_H\right) + \\ 4\pi M^2\sin^2\theta_0\cos 2\varphi_0 + K_1\left(2\sin^2\theta_0\cos 2\varphi_0\cos^2\rho + \frac{1}{2}\sin 2\theta_0\cos\varphi_0\sin 2\rho\right)\end{pmatrix}\end{pmatrix} - \\ \begin{pmatrix}MH\left(\cos\theta_0\sin\theta_H\sin\left(\varphi_0-\varphi_H\right)\right) + 2\pi M^2\sin 2\theta_0\sin 2\varphi_0 + \\ K_u\left(\sin 2\theta_0\sin 2\varphi_0\cos^2\rho + \cos 2\theta_0\sin\varphi_0\sin 2\rho\right)\end{pmatrix}^2\end{pmatrix} \tag{3.13}$$

Thus, for high field FMR and from figures 3.5 and 3.6 where both the equilibrium angles θ_0 and φ_0 is equal to $\frac{\pi}{2}$ (for perpendicular configuration), the resonant condition is given by

$$\left(\frac{\omega}{\gamma}\right)=\sqrt{(H_r-4\pi M)(H_r-4\pi M-H_K)} \qquad (3.14)$$

where H_r is the resonant field. This is the same equation derived by Igarashi and Netzelmann [1,10]. Regardless of what value ρ takes (the angle which the grain's c-axis subtends relative to the x-axis), the resonant condition is still the same, as shown in appendix C. From geometry, this is obvious as the axis of symmetry is normal to the film plane.

3.2.4 Experimental set up and results

The thin film is sandwiched between the waveguide and the sample holder so that the mm-wave is tidily focussed onto the sample without scattering of the mm-wave from the sample edge.

At the time of measurement, the sensitivity of the spectrometer at 180 and 270 GHz was insufficient for FMR; hence, measurements were confined within the 75 to 95 GHz range at room temperature, figure 3.8. Multi-frequency FMR within the range of interest was necessary in order to determine the three intrinsic properties of the recording media. Because we were restricted to a small range of frequencies, it was necessary to carry out multiple measurements at each frequency.

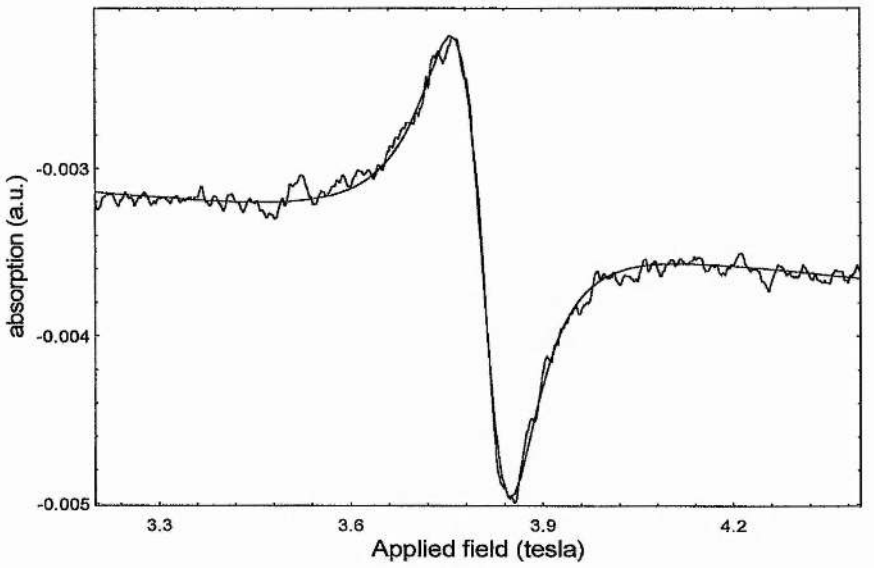

Figure 3.8. Typical FMR spectra with a fitting to the lineshape using equation 2.44 from section 2.2.3.1.

Similarly to the cobalt thin film measurements, there were problems in the phasing of the FMR signal. Again, absorption and dispersion lineshape fitting was included to determine the relevant features of the spectra.

3.2.4.1 Static properties

Since the significant error in our measurements comes from the values of the field for resonance, equation (3.14) is re-written as

$$H_r = 4\pi M_s + \frac{H_K}{2} + \sqrt{\frac{H_K^2}{4} + \frac{\omega^2}{\gamma^2}}. \qquad (3.15)$$

From the resonant condition over the range 75 – 95 GHz, it is not possible to determine the individual values of the Lande g-factor, saturation magnetisation and magnetocrystalline anisotropy uniquely; this is a limitation inherent to high field FMR. The application of non-

linear regression method to equation (3.15) showed that while the sum $4\pi M_s + \frac{H_K}{2}$ for 15A and 15B is 9.75 ± 0.75 kOe, a range of values of $4\pi M_s$ and H_K will lead to an equally good fit to the data. A binomial expansion of equation 3.15 will give a linear and non-linear term. At higher fields, the non-linear term is very small but necessary in order to accurately determine the magnetic parameters.

From (3.15), one obtains

$$H_r = \left(4\pi M_S + \frac{H_K}{2}\right) + \frac{H_K}{2} \cdot \frac{\omega}{\gamma} \sqrt{\frac{\gamma^2}{\omega^2} + \frac{4}{H_K^2}}$$

Since we are dealing with high frequency measurements, the term $\frac{\gamma^2}{\omega^2}$ will tend towards zero, thus the whole expression for the resonant field becomes linear,

$$H_r = 4\pi M_S + \frac{H_K}{2} + \frac{\omega}{\gamma} \qquad (3.16)$$

(Note that in X and Q band FMR the non-linear term becomes important and values of the g-factor, saturation magnetisation and the mean uniaxial anisotropy may be obtained. However, the whole point of our exercise is to work at high field so that the interactions between the grains are decoupled.)

Figure 3.9 shows the V-shaped valley of the possible sets of solutions found by X-Y non-linear regression fits to the data for sample 15A (high noise media), for a given g-value of 2.16. The z-axis is the mean square error of the difference between the calculated and experimental values of the resonant field (for sample 15A), in oersteds. It is clear that the smallest residual is about 40 Oe for a wide range of values of the demagnetising field and the uniaxial anisotropy field separately.

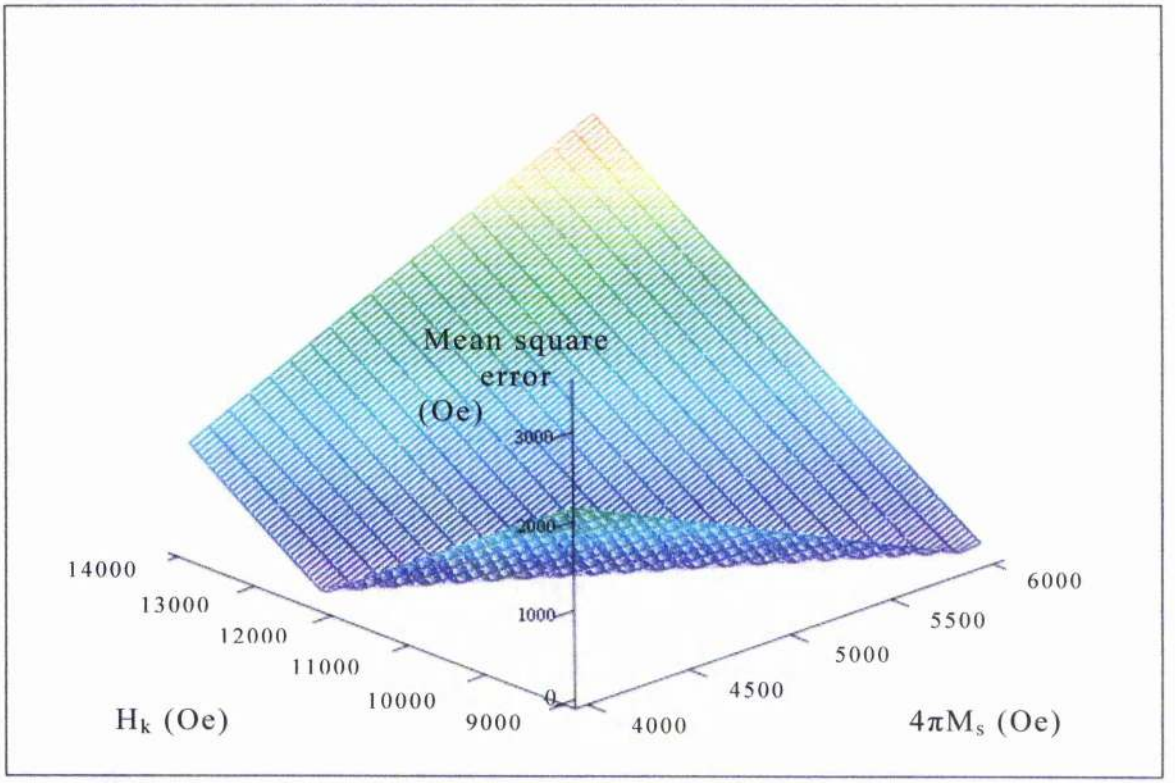

Figure 3.9. V-shaped profile of the possible set of solutions with the g-value set to 2.16. Note the difference does not take into consideration the error of each field point.

To overcome this problem it is clear that another technique is required in order to determine one of the parameters: this is the saturation magnetisation, which is described in section 3.2.2.

Figure 3.10 is a plot of the resonant field to the mm-wave frequency for the high and low noise media, which is fitted to equation 3.15 in order to solve the g-factor and magnetocrystalline anisotropy (for a given value of the sample's saturation magnetisation).

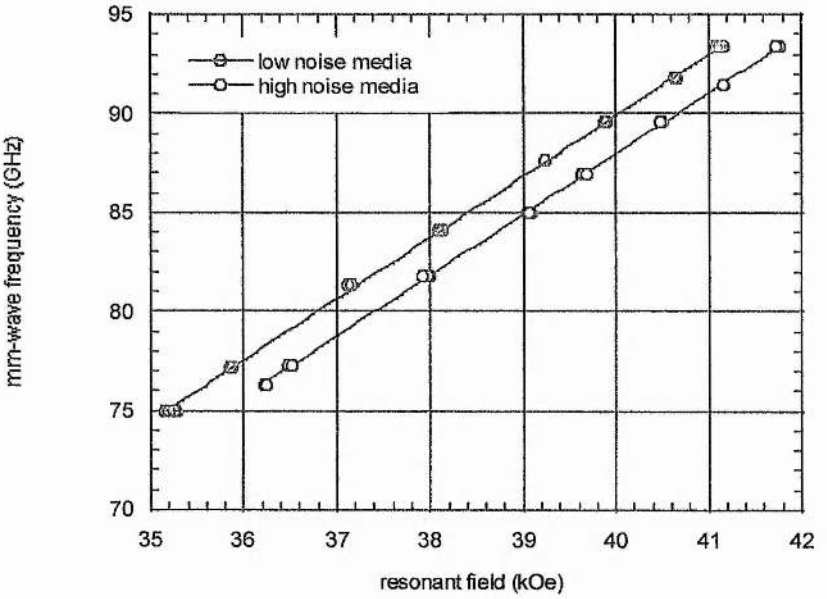

Figure 3.10. Plots of the resonant field, for samples 15A and 15B, against the frequency of the mm-wave.

A summary of the results is shown in table 3.1.

Types of noise media	$4\pi M_S$ (VSM)	Lande g-factor	Mean H_K (kOe)	
			FMR	Torque magnetometry
High noise (15A)	4.86 ± 0.10	2.16 ± 0.01	10.85 ± 0.20	9.65
Low noise (15B)	4.47 ± 0.10	2.17 ± 0.01	10.73 ± 0.20	9.65

Table 3.1 Magnetic properties obtained from TM, VSM and high field FMR.

From the results, there is not much difference in the anisotropy between the two media samples. At lower fields, the exchange interaction can play a significant role in the collective behaviour of the magnetic grains. In the magnetisation or torque measurements this may

be seen as an effect of the reduced anisotropy field as observed in section 3.2.2 [1,7]. At high field, however, the effects of coupling are not significant as the sample is completely saturated and the resonance is only due to the uniform precession. As a result, the high field FMR measurements demonstrate the higher value of H_K. Consequently, the presence of the difference between the anisotropy field values from the two techniques is a good indicator of the presence of exchange coupling.

3.2.4.2 Dynamic properties

The Gilbert damping factor of both media was derived from equation (2.39) [11]. Here, we directly substitute (3.13) into (2.39). The equilibrium angle θ_0 is taken to be $\frac{\pi}{2}$ for magnetic fields above 20kOe and applied normal to the film surface. The precession of magnetisation is assumed to be circular. As a result, the Gilbert damping term is determined from

$$\Delta H(\omega)_{pp} = \frac{2\alpha\omega}{\sqrt{3}\gamma} + \Delta H_{pp}(0) \qquad (3.17)$$

The factor of $\sqrt{3}$ arises due to the fact that the signal is recorded as the first order derivative of the lineshape and the ratio of the Lorentzian linewidth FWHM and derivative peak-peak linewidth is $\sqrt{3}$. From figure 3.11, a fit to the linewidth using 3.17 enables one to determine two features: Gilbert damping factor and the inhomogeneous broadening where the latter is determined from the linewidth intercept, as discussed in section 2.1.7. Table 3.2 presents results for both sample's dynamic properties.

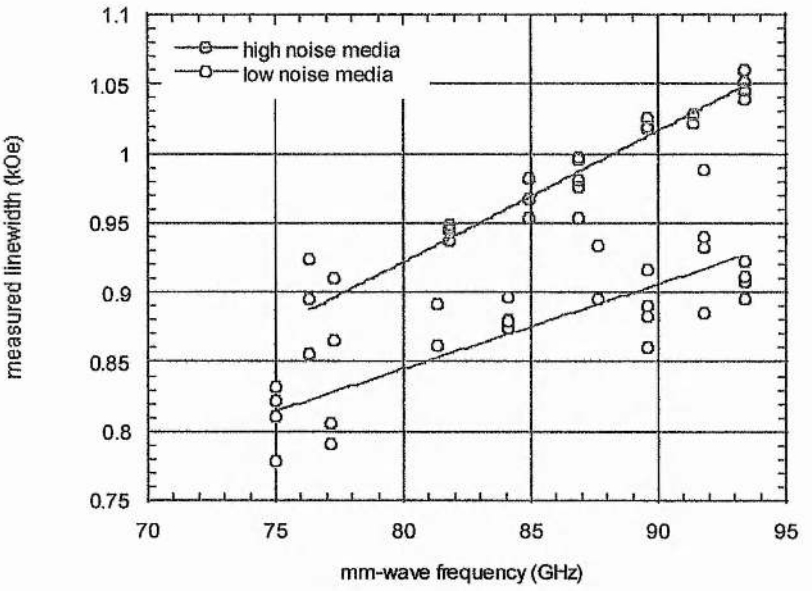

Fig 3.11. A fit to the measured line width for (a) low noise and (b) high media noise.

Types of media	Gilbert damping factor	Inhomogeneous broadening (kOe)
High noise (15A)	0.025 ± 0.003	0.15 ± 0.08
	(0.027 ± 0.003)	(0.13 ± 0.08)
Low noise (15B)	0.016 ± 0.002	0.36 ± 0.07
	(0.017 ± 0.003)	(0.32 ± 0.11)

Table 3.2 Dynamic properties of high and low noise media. The values in brackets were deduced from the average linewidth at each frequency.

It is clear that from table 3.2, the values of the Gilbert damping term, α lie within those quoted from previous work, typically between 0.01 and 0.04 [1,4,12].

3.2.5 Conclusions

From tables 3.1 and 3.2, it appears that there is little difference in the static and magnetic properties of the high and low noise media samples. The crystalline anisotropy of the low and high noise media is 10.73 ± 0.20 and 10.85 ± 0.20 kOe, respectively. However, it is clear that the Gilbert damping and inhomogeneous broadening terms, which characterises the dynamic response are significantly different. The inhomogeneous term for the low noise media (0.36 ± 0.07kOe) is more than twice as much as the high noise media (0.15 ± 0.08kOe). The Gilbert damping term for the high noise media (0.025 ± 0.003) is higher than the low noise media (0.016 ± 0.002).

The low noise media is comprised of smaller grains with better grain segregation than that of the high noise media. This segregation leads to better isolation of the magnetic moments and hence reduces the exchange coupling between the grains. Consequently, the inhomogeneity of the medium is greater as a result of a larger number of spins in different local magnetic environments which is reflected in the value of $\Delta H_{pp}(0)$[6,13]. Lower exchange coupling contributes to reduced noise in the case of the medium with smaller grains [6]. This interpretation is supported by the values of the Gilbert damping factor. For the sample with larger grains (high noise medium) the damping factor is greater. The fastest relaxation time would occur for critical damping where the Gilbert damping factor is unity [3], thus the sample with larger grains has a faster relaxation time. This faster relaxation time may again be as a result of stronger intergrain coupling in the high noise medium. It is clear that more work is required in order to back-up our suggestions.

3.3 Torque magnetometry

3.3.1 Introduction

The torque section is split into two parts: the first part provides a method of determining the uniaxial anisotropy of the high and low noise media. It is based on the closing point measurements, which is a process of relating the completed magnetic moment reversal at a certain field and angle to the magnetic grain's anisotropy and magnetisation.

The final part concerns an alternative, but similar method, to ΔM measurements. Using this technique, the progress of magnetisation reversal is compared for the sample having the magnetisation in the maximum remanent state (magnetised) and in the zero remanent state (demagnetised). Using the fact that for non-interactive media [14], both processes are equivalent, a deviation from zero is then taken as a result of interaction between the moments. This method has been shown to be useful for studying dipole-dipole and exchange interactions in particulate and polycrystalline media. In section 3.3.4, this method is applied to torque magnetometry so that intergranular coupling in longitudinal recording media is measured. Micromagnetic simulations and experimental data carried out on the low noise media will be shown in section 3.3.4.

The author feels that Dr. Feodor Ogrin and Professor Stephen Lee should be acknowledged at the start of this sub-chapter since they developed the theory behind the closing point and ΔT method. Dr. Ogrin also carried out micromagnetic simulations, as discussed in section 3.3.4, and fits to the data. Throughout this chapter, Dr. Ogrin and Prof. Lee are often referenced as [15], as part of private communications. The author's contribution in this project was to carry out the torque measurements for the closing point and ΔT method.

3.3.2. Torque magnetometry

Torque magnetometry is ideal for anisotropy measurements. In ferromagnetic thin films, this anisotropy results from intrinsic (crystalline) and shape anisotropy. The torque magnetometer, in St. Andrews, that was used for recording media measurements is illustrated below.

Figure 3.12. In-house torque magnetometer which has a capacitance detection system.

The ferromagnetic thin film is attached to a cantilever using a mixture of Bostik glue and acetone. The magnetometer has a detection system that is based on cantilever techniques, which is operated in capacitance mode. (Both the capacitance plates and the cantilever were made from phosphor bronze.) The cantilever is caused to deflect through tiny distances in response to the torque exerted on it, which results in a variation in capacitance between the cantilever and the fixed capacitance plates. A typical noise level detected is one microvolt. Prior to torque measurements, the voltage across the capacitance bridge was balanced to zero for zero deflection.

The cantilever is inserted into an orange cryostat, supplied by A.S. Scientific products Ltd, which was mounted on a rotation rig, which allowed the cryostat and therefore the cantilever to be rotated 360 degrees in the horizontal plane relative to a fixed field direction. The field could also be swept through a field range of 9.6 kOe and temperatures as low as 1.4K could be attained.

3.3.3 Closing point measurements

The closing point can be defined as the last point in the magnetisation reversal, as illustrated in figure 3.13. The 'markers' (orange arrows) of the closing point are from the moments whose easy axis is perpendicular to the direction of the applied field [15].

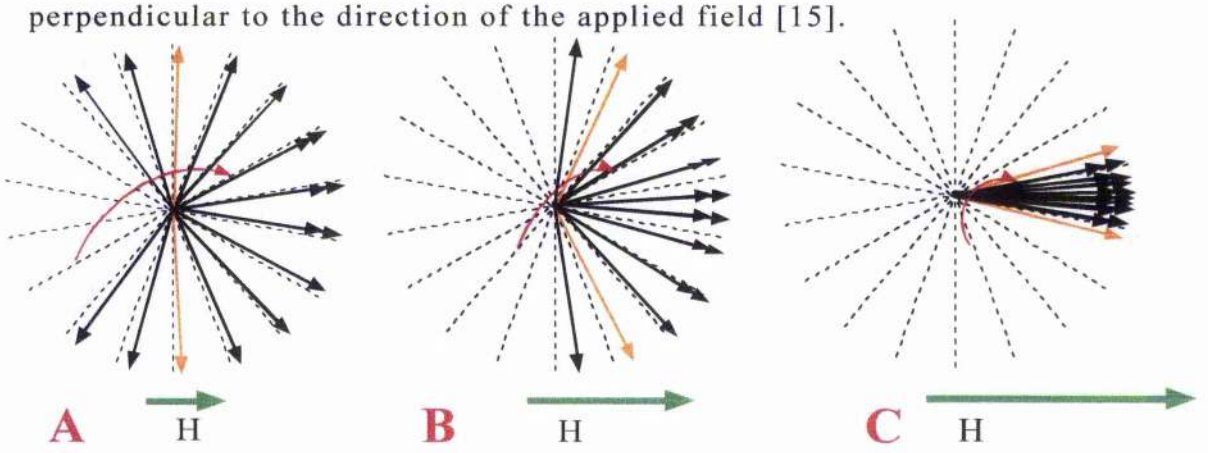

Fig 3.13. Consider a random distribution of moments where each moment has an easy axis. For case (A), a small field is applied and the moments from the grains whose easy axis are either parallel or anti-parallel to the field start to rotate towards that field. The moments whose easy axes were initially anti-parallel (or at an angle greater than ninety degrees) to the field direction then irreversibly flip over their energy barrier, as shown by the red arrow (here there is a flip from the left to the right hand side). In (B), a higher field is applied and other moments follow this irreversible flip (from the left to the right) and in (C), the last moments (orange arrows) to complete the reversal (flip) are from grains whose easy axis is perpendicular to the applied field. Eventually, all the moments will coherently rotate towards that field as field the increases.

3.3.3.1 Mean field model

The thin film is considered to be composed of a large number of crystallites, which are closely packed within the film surface. For simplicity, we look at the single domain model with the c-axis of the HCP grain directed along the y-axis and perpendicular to the field direction, $\vec{H}$, as shown in figure 3.14.

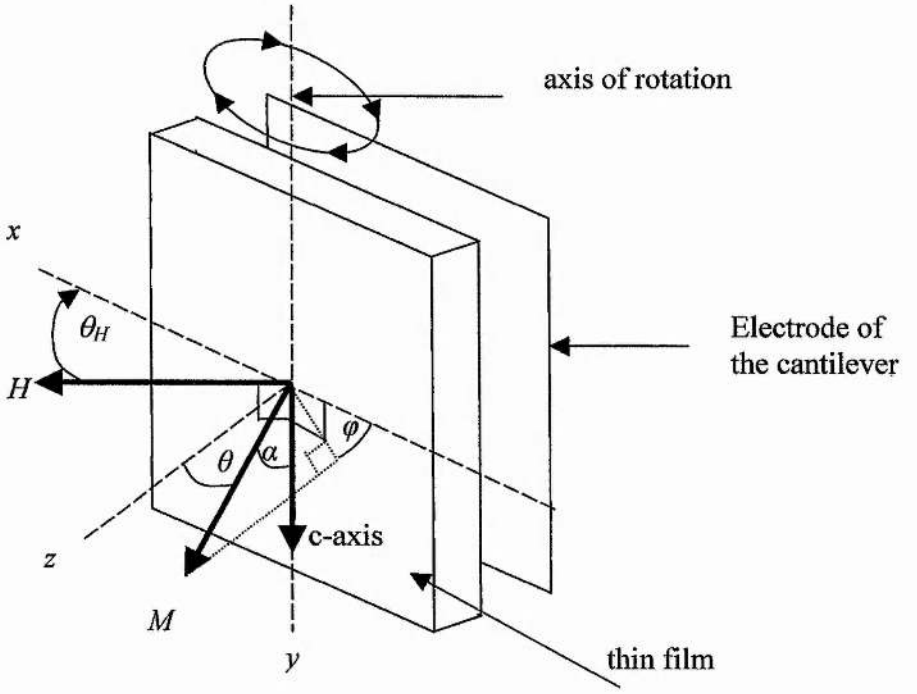

Figure 3.14. Schematic diagram of the thin film that was used to model the closing point method.

The total energy of the system is given as (N.B. units are cgs):

$$E = -\overline{M} \cdot \overline{H} + K \sin^2 \alpha + 2\pi M_s^2 \cos^2 \theta \qquad (3.18)$$

where the uniaxial anisotropy term is expressed as

$$E_K = K - K \sin^2 \theta \sin^2 \varphi \qquad (3.19)$$

The energy density is thus written as

$$E = -M_S H(\sin\theta\cos\varphi\cos\theta_H + \cos\theta\sin\theta_H) + K - K\sin^2\theta\sin^2\varphi + 2\pi M_S{}^2\cos^2\theta \tag{3.20}$$

The derivatives with respect to θ and φ determine their equilibrium positions:

$$\frac{\partial E}{\partial\theta} = -M_S H(\cos\theta\cos\varphi\cos\theta_H - \sin\theta\sin\theta_H) - \sin 2\theta\cdot\left(\frac{H_K}{2}\sin^2\varphi + 2\pi M\right) = 0 \tag{3.21}$$

and

$$\frac{\partial E}{\partial\varphi} = HM_S\sin\theta\cos\theta_H\sin\varphi - \frac{H_K}{2}\cos 2\varphi\sin^2\theta = 0 \tag{3.22}$$

thus

$$\cos\varphi = \frac{H\cos\theta_H}{H_K\sin\theta} \tag{3.23}$$

which can also be re-written as

$$\sin^2\varphi = 1 - \cos^2\varphi = \left(1 - \frac{H\cos\theta_H}{H_K\sin\theta}\right)^2. \tag{3.24}$$

From the equilibrium condition, if $\varphi = 0$, then from (3.23),

$$\sin\theta = \frac{H\cos\theta_H}{H_K} \tag{3.25}$$

From the first equilibrium condition, the $\sin\theta\cos\theta$ term is removed so that one has

$$\frac{\partial E}{\partial\theta} = -H\left(\frac{\cos\theta_H}{\sin\theta} - \frac{\sin\theta_H}{\cos\theta}\right) - 4\pi M_S = 0. \tag{3.26}$$

Equation (3.25) is substituted in (3.26) and the closing point, H_{cp}, is determined from the expression [15]:

$$H_{cp} = \frac{1}{\sqrt{\frac{\sin^2\theta_H}{(4\pi M + H_k)^2} + \frac{\cos^2\theta_H}{H_k^2}}} \tag{3.27}$$

Figure 3.15 illustrates the relation, 3.27, between the closing point and the angle of applied field, θ_H, relative to the film surface. Here, the anisotropy is set to 10kOe and the saturation magnetisation to 4.4kOe (for the low noise media).

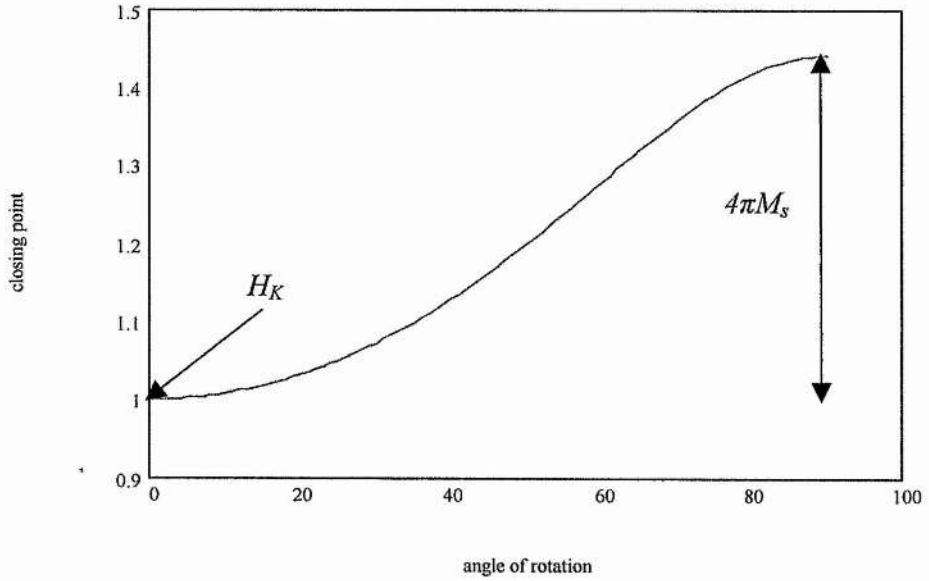

Figure 3.15. Plot of the closing point (x10kOe) with respect to θ_H (degrees) the angle of applied field relative to the film surface. The field, H, is perpendicular to the in-plane c-axis, as shown in figure 3.14.

From equation 3.27, if the field is applied within the film surface, then the closing point provides a measure of the sample's magnetocrystalline anisotropy. If the field is applied normal to the film surface, the closing point is therefore the sum of the crystalline and shape anisotropy.

3.3.3.2 Experiment

In order to carry out closing point measurements, the sample was cooled down to 2K: this allows one to determine the maximum anisotropy in the media. After cooling, the field, $\vec{H}$, initially lies within the film surface, $\theta_H = 0$ degrees. A field sweep from –9.6kOe to

+9.6kOe and back to –9.6kOe produces a torque signal as shown in figure 3.16.

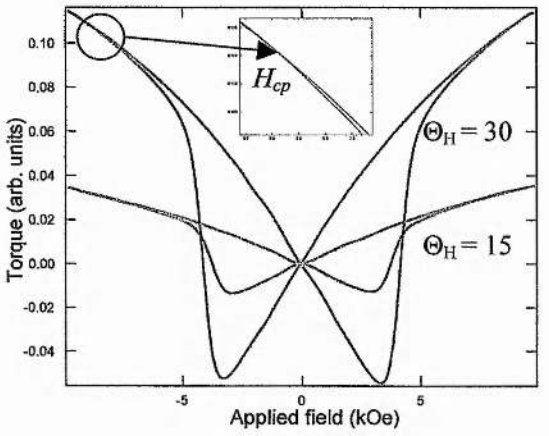

Figure 3.16. Torque signals for the low noise media, as a function of applied field at 15 and 30 degrees to the film plane [15]. The raw data of the two torque curves were not signal averaged and the signal to noise is high even before smoothing the curves (using IGOR) in order to determine the closing point (shown in inset).

The sample is rotated at another angle and again a field sweep is carried out. There is however a limit in the angle to which you can rotate the sample: where the observed closing point exceeds the field limit, which is ±9.6kOe.

Here, the closing point with respect to the angle of film rotation to the field $\vec{H}$ is fitted using equation 3.27, providing values of the low noise medium's anisotropy and saturation magnetisation of 8.4 and 4kOe, respectively.

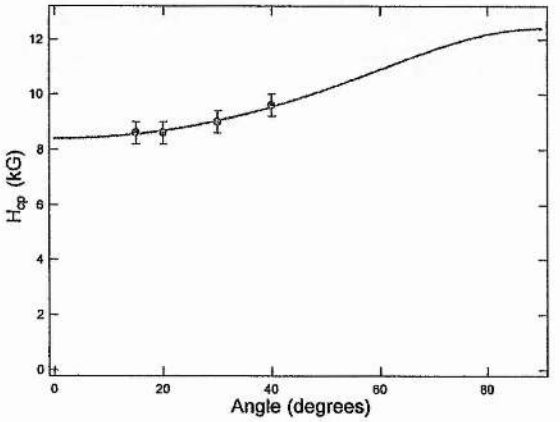

Figure 3.17. Plots of closing point with angle of rotation of field for the low noise media [15].

An alternative method in determining the anisotropy is through simulating the torque signal. A **mean field model** of the torque signal was used; however, the simulation failed to trace the experimental torque curve [15]. Here, a **micromagnetic model** was used with a Gaussian distribution of the anisotropy (with a FWHM of 2kOe) for the low noise media, as shown in figure 3.18.

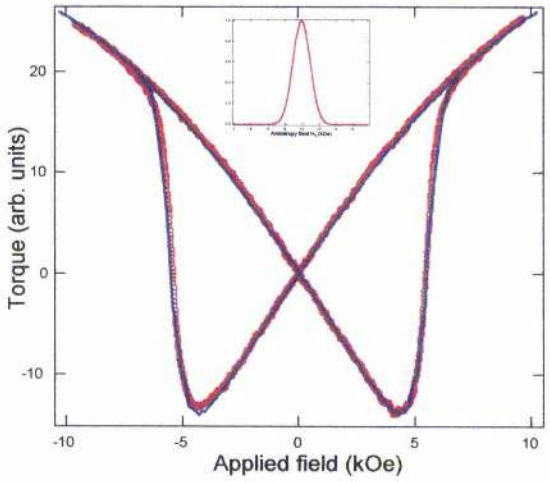

Figure 3.18 Torque as a function of the applied field for low noise media sample with a gaussian distribution of the anisotropy. The red curve is the experimental data and the blue line is a simulation from micromagnetic modelling [15].

From the micromagnetic model, the anisotropy of the low noise media was found to be 10kOe, which is slightly lower than that determined from FMR, 10.8(2)kOe, and the intergranular exchange constant (discussed in section 3.3.2.1), C, was 0.2 [15].

The high noise media has a lognormal distribution of the anisotropy field, as shown in figure 3.19. The anisotropy is 10.6kOe with an intergranular constant of 0.4 [15].

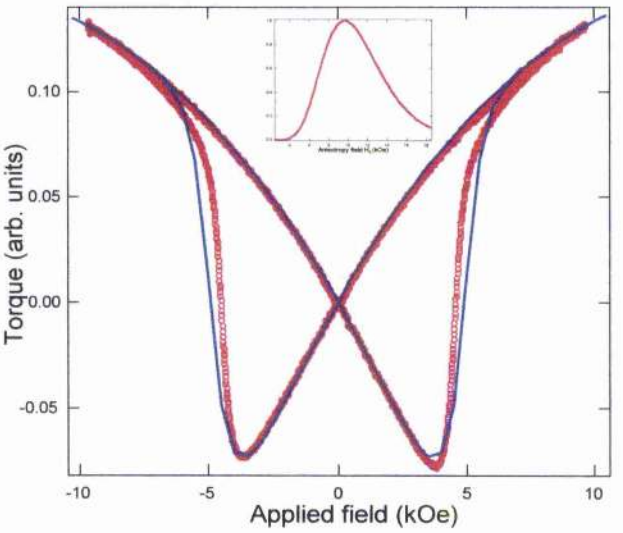

Figure 3.19 Torque as a function of the applied field for high noise sample. The lognormal distribution of H_k with σ=0.3 [15]

3.3.4 Determination of interactions

Realistically there are interactions within the thin film due to exchange or dipole coupling. In order to observe these interactions, the ΔM method is used [16-18].

In this section, another novel technique is introduced which is analogous to the ΔM method. We will look at how accurate this technique is with previous measurements carried out by the magnetic recording group in Seagate.

First we shall look at the definition of the ΔM method. Although there were no magnetometry measurements carried out using this method, a micromagnetic model is used to illustrate the results of this technique.

3.3.4.1 The ΔM and ΔT technique

Theory of the ΔM method

In the ΔM method there are two types of measurements: IRM (isothermal) remanence curve and the DCD (dc-magnetising remanent) curve.

The IRM method starts off with the sample in the demagnetised state. After demagnetising, the field is raised to H_1, as shown in figure 3.20, then set to zero, so that there exists a remanence of M_1. The field is then raised to H_2 and set to zero giving rise to a remanence of M_2 and so on until there is a maximum remanence, termed $M_r(\infty)$. Each of the remanence points M_1, M_2 to M_∞ are represented by $M_r(H)$.

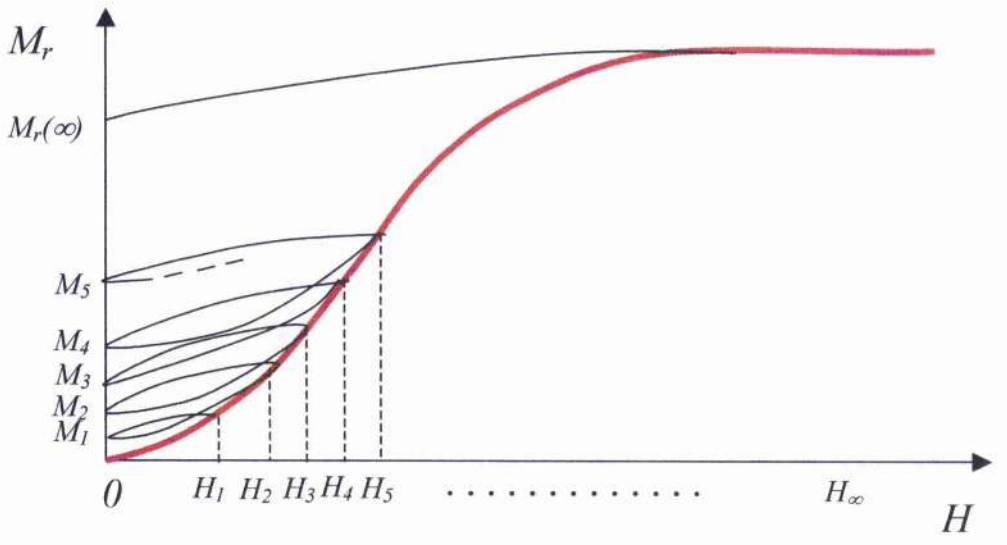

Figure 3.20. Illustration of the IRM curve.

A DCD curve starts off with the sample in the negative remanent state (magnetised state) and a positive field is applied the same way as the IRM curve, as shown in figure 3.21. The value of each successive remenent point is denoted as $M_d(H)$.

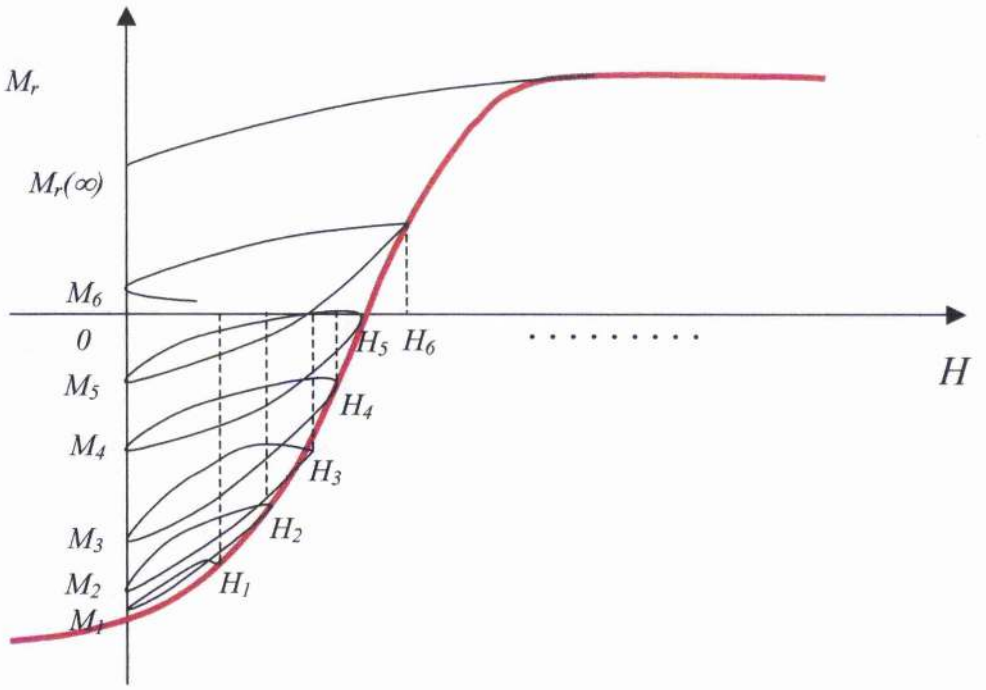

Figure 3.21. Illustration of the DCD curve.

The difference between the IRM and the DCD curve is described by the Wohlfarth relation [14]:

$$M_d(H) = M_r(\infty) - 2M_r(H) \qquad (3.28)$$

This expression is correct if there are no interactions in the thin film. If interactions were present, then the difference between the left and right hand side of the Wohlfarth relation would be non-zero. This difference between the two sides of the equation is denoted as ΔM [14]

$$\Delta M = M_d(H) - M_r(\infty) + 2M_r(H) \qquad (3.29)$$

An example of this ΔM result is shown in figure 3.22. This was simulated using micromagnetic simulations and each moment represents a magnetic grain with its own uniaxial anisotropy. The

model used for this simulation and for other simulations has a distribution of axes in random orientation. The total free energy for each grain is described as [19]:

$$E_i = -\vec{m}_i \cdot \vec{H} + \sum_j \frac{\vec{m}_j \cdot (\vec{m}_j \cdot \vec{n}_j)}{\vec{r}_{ij}} + K \sin^2 \phi + C \sum_{j:r_{ij}<R_{loc}} \vec{m}_i \cdot \vec{m}_j \qquad (3.30)$$

The first term is the Zeeman energy, the second is magnetostatic, the third is the anisotropy and the last term is the exchange energy. The magnetostatic interaction is accounted as a dipole-dipole interaction between the grains in the micromagnetic model. $\vec{m}_i = \frac{M}{M_s}$ is the unit magnetisation vector, $K = \frac{H_K}{2M_s}$ is the magnetocrystalline anisotropy constant, $\vec{n}$ is the unit vector normal to surface, C is the intergranular exchange constant and R_{loc} defines the radius of the exchange interaction.

With reference to figure 3.22, there are two types of simulations: one with only dipolar contributions (blue squares); that is, where C is set to zero and the ΔM curve results in having a negative dip at $H/H_k = 0.4$. The other has exchange and dipolar coupling (red circles); that is, C is set to unity, and the resulting ΔM curve is positive.

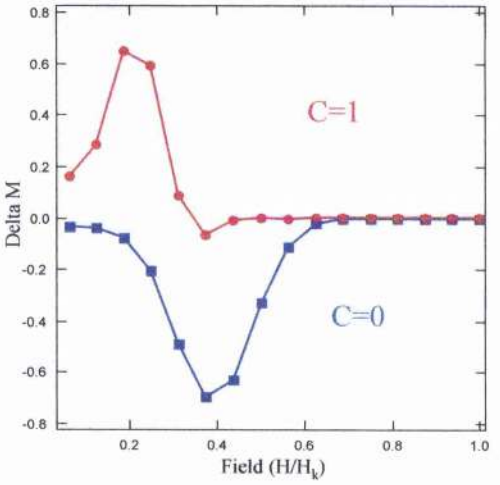

Figure 3.22. Micromagnetic simulation of ΔM curve for dipolar interactions only ($C=0$, marked in blue squares) and exchange and dipolar contributions ($C=1$, marked in red circles) [19].

ΔT method and results

The ΔT method is similar to the ΔM method: it is the torque that is measured instead of the remanent magnetisation. The sample was measured at 2K, the reason for this is to reduce the thermal reversal, $\frac{1}{\tau} = f_0 \exp(-E_K / kT)$ and obtain an accurate value of the anisotropy.

There are three parts of the measurement that is required in order to determine the type of interaction in the thin film. The first is that of the $T_r(H)$ measurement which is similar to the IRM curve. The sample is in a demagnetised state, which was achieved by setting the field to 9.6kOe and cycling the field down to zero in steps of 0.2kOe. After demagnetising, a field of value H_1 is applied within the film surface and the sample is rotated 90 degrees out-of-plane where a torque signal is measured. The maximum torque for a given field H_1 is defined as $T_r(H_1)$. The sample is rotated back to zero degrees and a higher field H_2 is applied. Again, the sample is rotated 90 degrees with a higher torque signal $T_r(H_2)$. This experiment continues until we reach the field limit, which is 9.6kOe.

The second and third part of the measurements is the $T_{r\infty}(H)$ and $T_d(H)$ curve. Here the sample is in the magnetised state whose 'single domain' is at an arbitrary direction within the film plane. The sample is rotated to 90 degrees out-of-plane, where $T_{r\infty}(H_1)$ is measured. The sample is rotated another ninety degrees where the torque is zero; that is, the field is applied in the opposite direction to the moment. The sample is then rotated back to ninety degrees until $T_d(H_1)$ is measured, as shown in figure 3.23 [19].

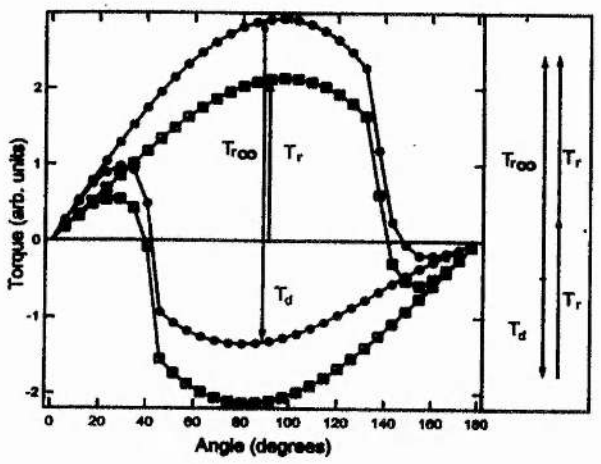

Figure 3.23. Simulation of the angular dependence of torque for initially demagnetised (squares) and magnetised (filled circles) sample. Vectors T_r, $T_{r\infty}$ and T_d are determined by measuring the torque amplitude at 90 degrees. The intergranular coupling (both dipolar and exchange) is not present in this case; the inset demonstrates that the Wohlfarth relation (3.28) is satisfied.

After measuring $T_{r\infty}(H_1)$ and $T_d(H_1)$, the sample is rotated back to zero degrees; that is, the field is finally applied within the film surface. A higher field, H_2, is applied so that $T_{r\infty}(H_2)$ and $T_d(H_2)$ are determined. Again, higher fields are applied until we reach the field maximum. All values of $T_r(H)$, $T_d(H)$ and $T_{r\infty}(H)$ for H ranging from zero to the field maximum are plotted as shown in figure 3.24.

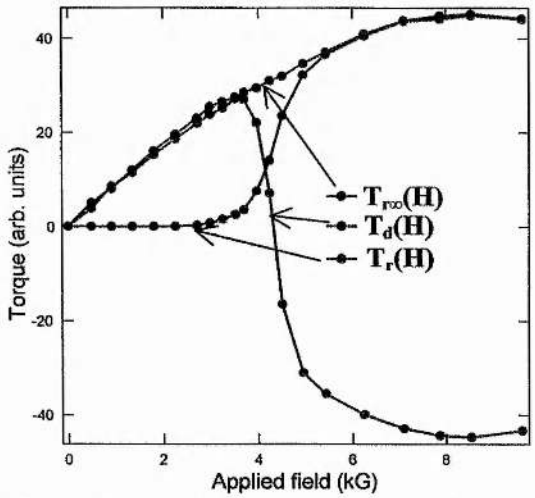

Figure 3.24. $T_r(H)$, $T_d(H)$ and $T_{r\infty}(H)$ curves measured for low noise media, 15B.

With no interaction, the relation is similar to that of Wohlfarth [19]:

$$T_d(H) = T_{r_\infty}(H) - 2T_r(H) \qquad (3.31)$$

Where interactions are present, ΔT is a measure of deviation from the left and right side of the equation. The relation for the case of interactions can be defined in the following way:

$$\Delta T = 2T_r(H) - T_{r_\infty}(H) + T_d(H) \qquad (3.32)$$

A positive value of ΔT is associated with intergranular exchange interaction; a negative value is associated with mostly dipolar coupling. A simulation of ΔT, figure 3.25, using the micromagnetic model (3.30) shows that for no exchange, a negative peak is observed; the sample with strong exchange coupling (C=1), a positive peak occurs.

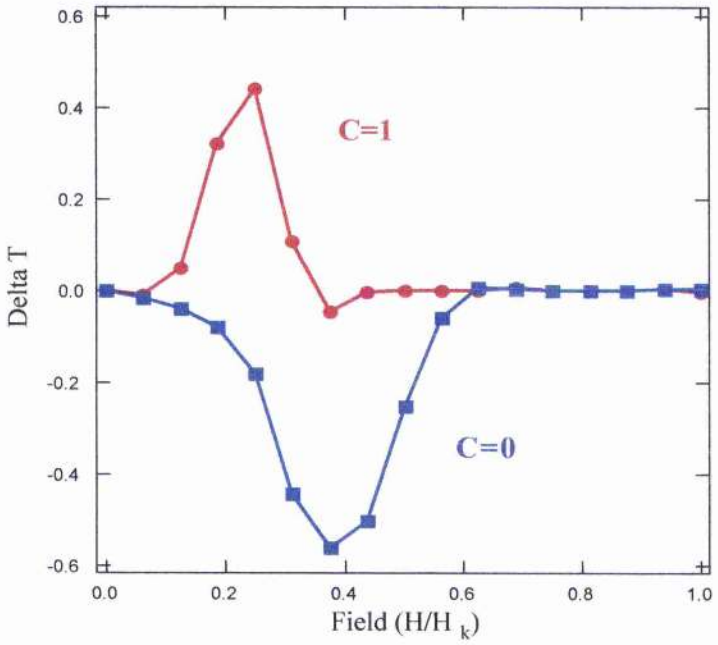

Figure 3.25. Simulation of the ΔT curve [19].

A simulation of the ΔT curve of the low noise media, figure 3.26, required the following parameters of the exchange coupling and the anisotropy field: C=0.5 and H_k = 9.0(4) kOe [19].

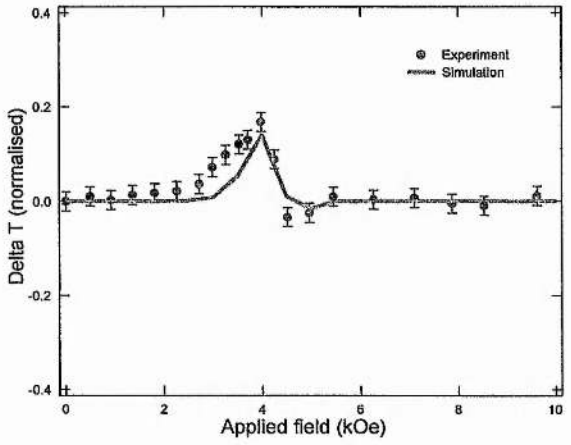

Figure 3.26. ΔT plot of low noise media with simulation and data points.

The uniaxial anisotropy field value is slightly lower than that measured from a vector VSM, which was 9.6 kOe and from FMR it was 10.7(2) kOe. The problem here is that the field is restricted to 9.6 kOe, which is insufficient for completely saturating or demagnetising the sample. The presence of intergranular exchange coupling in the low noise media agrees with the conclusions in the FMR section; that is, the low field measurements exhibit lower values of anisotropy due to the presence of exchange coupling.

Previous ΔM measurements as shown in figure 3.27 [5] shows that the presence of exchange in the low and high noise media is very small for all values of the applied field, which suggests that there are minimal interactions [14,19]. There may be an effect of balance when exchange compensates the dipolar interactions resulting in ΔM curves close to zero [17]. A negative ΔM signal does not necessarily imply no exchange.

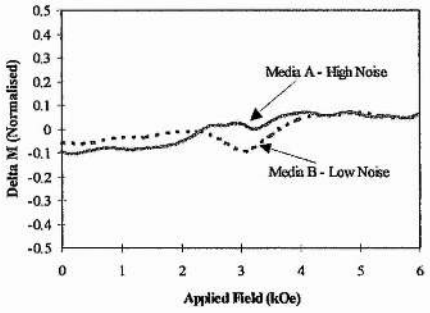

Figure 3.27. ΔM curves of high and low noise media [5]

3.4 Conclusions

The first part of this chapter has shown that high field FMR with greatly improved resolution and signal to noise allows one to determine the static and dynamic properties of the recording media without introducing micromagnetic modelling. Although the FMR condition restricts the user from obtaining the magnetisation and anisotropy uniquely, one can determine from equation 3.15 (using Mathcad) the sum of the two static properties. However, one needs to know the magnetisation in order to solve for the anisotropy.

In section 3.2.4.1, the anisotropy determined from FMR is higher than that obtained from torque magnetometry. In torque magnetometry measurements, the field is below saturation and thus the field is not strong enough to decouple exchange interactions between the grains. Torque magnetometry measured in St. Andrews has shown that if one were to employ the closing point method and apply micromagnetic modelling to simulate the torque signal, then there exists an exchange interaction and the anisotropy agrees with that determined from FMR. Another method, with the aid of torque magnetometry is the ΔT method, which is similar to the conventional technique ΔM for observing interactions in polycrystalline media. For the case of the low

noise media, there exists exchange coupling and the anisotropy however was lower than that determined from the closing point method, FMR and also torque measured in Seagate. The problem with the torque magnetometer in St. Andrews is that the magnetic field is not high enough to saturate the media in order to accurately determine the anisotropy.

A table of the anisotropy values through FMR, torque in Seagate and St. Andrews is shown below.

Sample	FMR	Torque magnetometry		
		Seagate	St.Andrews	
			Closing point	ΔT
High noise media (15A)	10.7(2) kOe	9.6 kOe	10.6 kOe	-
Low noise media (15B)	10.8(2) kOe	9.6 kOe	10.0 kOe	9.6 kOe

3.5 References

[1] M. Igarashi, T. Kambe, K. Yoshida, Y. Hosoe, Y. Sugita, J. Appl. Phys. 85 (1999) 4720

[2] C. Kittel, *Introduction to Solid State Physics* 7ed. John Wiley & Sons, Inc (1996)

[3] S. Chikazumi, *Physics of Magnetism* John Wiley & Sons, Inc (1964)

[4] N. Inabi, Y. Uesaka, A. Nakamura, M. Futomoto, Y. Sugita, IEEE Trans. Magn. 33 (1997) 2989

[5] E.T. Yen, S.Z.Wu, T.Thomson, R.Ristau, R. Ranjan, G.C. Rauch, IEEE Trans. Magn. 35 (1999) 2730

[6] T. Thomson, *private communications* 2001

[7] H. Laidler et al. Submitted to MMM/Intermag 2001

[8] C.J. Oates, F.Y.Ogrin, P.C.Riedi, S.L.Lee, G.M.Smith, T.Thomson, JMMM, 242-245 (2002) 402

[9] J. Smit, H.C. Beljers, Philips Res. Rep. 10 (2) 1955 113

[10] U. Netzelmann, J. Appl. Phys. 68 (1990) 1800

[11] S.V.Vonsovskii, *Ferromagnetic Resonance*, Pergamon, Press, New York, 1966.

[12] M. Futomoto, N. Inaba, A.Nakamura, Y.Honda, Acta Metall. 46 (1998) 3777

[13] C.J.Oates, F.Y. Ogrin, S.L. Lee, P.C. Riedi, G.M. Smith, T. Thomson, J. Appl. Phys, 91 (2002) 1417

[14] E.P.Wohlfarth, J. Appl. Phys. 595 (1958)

[15] F.Y. Ogrin, *private communications*, 2001.

[16] P.E. Kelly, K. O'Grady, P.I. Mayo, R. W. Chantrell, IEEE Trans. Magn. 25 (1989) 3881

[17] C.Dean, R.W.Chantrell, H. Suzuki, N. Kodama, P.R. Bissell, J. Appl. Phys. 79 (1996) 6467

[18] N.S. Walmsley, R.W. Chantrell, J. Appl. Phys. 85 (1999) 6154

[19] F.Y. Ogrin, C.J. Oates, S.L. Lee, J. Magn. Mag. Mat., 242-245 (2002) 321

Chapter 4

High field FMR of CoCrPtB longitudinal media with varying compositions of platinum and boron.

4.1 Introduction

The recording layer of interest in this chapter is different from that discussed in chapter three, as it contains boron instead of tantalum in the CoCrPt layer. The samples studied in this chapter are classed as one with varying platinum and cobalt content, the other with varying boron and cobalt content. These are in fact test samples, unlike the high and low noise media, which were in commercial use.

This chapter is split into two parts. The first part presents a discussion on previous methods used to characterise the platinum and boron series, carried out by Seagate and IBM, and also the sample preparation of the two series for FMR measurements. The next part involves multi-frequency FMR of the two batches and provides explanations extracted from the analysis.

There are two main aims in this chapter: first to compare the average uniaxial anisotropy data measured by FMR with previous measurements carried out by Seagate. Secondly, to examine any trends in the dynamic and static properties of the recording media with respect to changes in the platinum and boron concentration.

4.2. Sample characteristics

The schematic diagram of the recording media, discussed in this chapter, is shown in figure 4.1. The platinum and boron samples were DC sputtered on a NiAl/P substrate, which is a soft ferromagnet with a coercivity of 85 Oe.

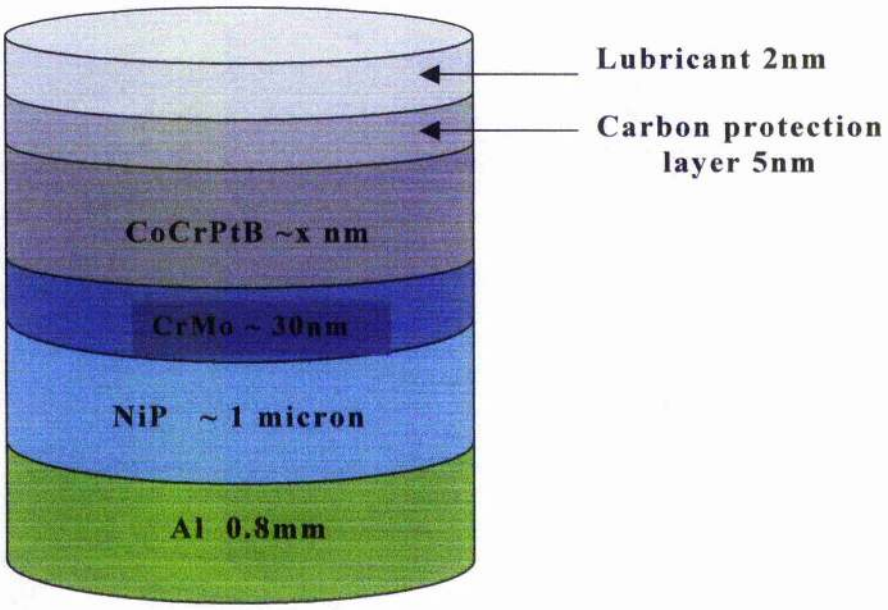

Figure 4.1 Layout of the recording media studied in this chapter [1].

The hard discs have a small variation in magnetisation from inner diameter (12.5mm) to outer diameter (42mm). The samples were prepared by cutting 8mm diameter mini-disks 30 mm from the disc centre as explained in detail in section 4.3. Any region of the disc that lies between 20 to 38mm (which is the flat, middle section of the disk) from the disc centre has a fairly uniform magnetisation and remanence [1].

The magnetic properties of both sides of the disk are not the same. Each side of the disk was sputtered from a different physical target, so that both sides of the disk were fabricated simultaneously. Because these disks are test samples, it was not the chief goal of the process engineer, in Seagate, to match the properties of both sides.

Independent magnetisation and anisotropy measurements on the 2-D isotropic in-plane media were carried out on a vector VSM by IBM [1] and Seagate [2]. Table 4.1 presents the following magnetisation and uniaxial anisotropy values for both the platinum and boron series. The thickness of the magnetic layer was determined from TEM by Seagate [2].

Serial number	Composition of Cr-Pt-B (X-Y-Z in at.%)	Thickness (nm)	Saturation magnetisation (kOe)			Uniaxial anisotropy from vector VSM measurements (kOe)		$4\pi M_s + H_k/2$ (kOe) deduced from $4\pi M_s$ and H_k measured from	
			Seagate (vector VSM)	St. Andrews (SQUID)	IBM (vector VSM)	Seagate	IBM	Seagate	IBM
F4059C-7A	15-12-12 (P)	19.8	3.57	4.42 ± 0.14	3.81	23.5	14.86	15.32	11.24
F4059C-14A	15-14-12 (P)	25.0	3.34	3.83 ± 0.19	3.71	18.7	23.06	12.69	15.24
F4059C-21A	15-16-12 (P)	28.0	3.27	3.86 ± 0.16	3.42	23.8	23.15	15.17	15.00
X2624C-7B	14-8-4 (B)	13.5	5.72	-	5.06	8.5	7.34	9.97	9.39
X2624C-14A	14-8-8 (B)	17.0	5.37	-	4.21	11.1	9.46	10.92	8.91
X2624C-21A	14-8-12 (B)	22.1	3.96	-	3.62	17.9	11.71	12.91	13.48
X2624C-7A	14-8-16 (B)	30.4	3.47	-	2.66	14.9	15.29	10.92	10.31

Table 4.1. Data of the platinum and boron series measured by Seagate and IBM with given values of their saturation magnetisation and uniaxial anisotropy. (P) and (B) denotes the platinum and boron series, respectively. The SQUID loops (which was carried out in St. Andrews) of the 3 samples in the platinum series are in appendix D. The final column will be compared with that deduced from FMR.

Each sample has its own product code where F4059C and X2624C are the platinum and boron varying media, respectively. It is clear that from the boron series, in table 4.1, there is a maximum in the uniaxial anisotropy at 12 at.% boron measured by Seagate; however, measurements carried out by IBM show that the anisotropy increases with boron content. Another independent measurement, again carried out by Seagate was based on the dynamic coercivity, figure 4.2. From the plot, the anisotropy is much smaller than that from the vector VSM, although there is a maximum in H_k, again, at 12 at.% boron.

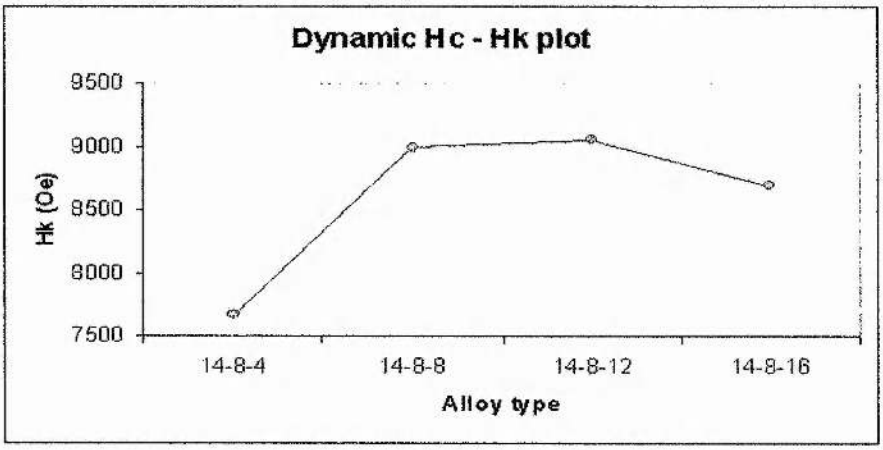

Figure 4.2. Dynamic coercivity measurements of the boron series with a maximum in anisotropy at 12 at.% boron [2].

From table 4.1, in the platinum series, the magnetisation measured from SQUID in St. Andrews (as shown in appendix D) differs from that in Seagate and IBM. Because of this, one has to question how accurate or reliable is the magnetisation and therefore the uniaxial anisotropy measurement for each sample? The reader should note that it was not possible to obtain hysteresis plots from IBM and Seagate in order to verify their values to the sample's saturation magnetisation and anisotropy field. Instead the sample parameters, as shown in table 4.1, were given.

The final column in table 4.1 is the sum of the saturation magnetisation, $4\pi M_s$ (measured from IBM and Seagate, as tabulated in

the forth column) and half the anisotropy field, $H_k/2$ (again measured from IBM and Seagate, as tabulated in the fifth column). This term is compared with the high field FMR result, as shown in table 4.2 (for the platinum series) and table 4.5 (for the boron series).

4.3. Sample preparation

The samples were prepared by Seagate and were presented as a series of hard disks. Figure 4.3 illustrates a hard disk in which four samples were cut out for FMR measurements.

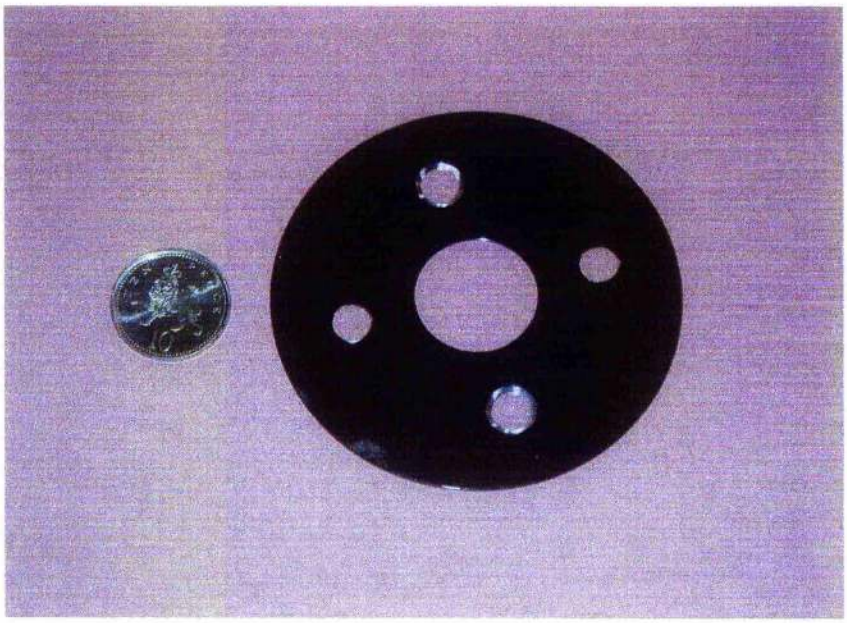

Figure 4.3. CoCrPtB hard disk with inner and outer radius of 12.5mm and 42mm, respectively.

The workshop in the School of Physics in St. Andrews constructed a two-flute mill which is made of high speed steel, and attached it to a Bridgeport milling machine, figure 4.4. With reference to figure 4.4, a mandrel (labelled B on the figure) was constructed for positioning and clamping the disks (labelled D), which was then centred on the cutter

at a radius 30mm from the centre of the hard disc. The mandrel was made from aluminium with a brass retaining ring (C). A paper shim was used on both sides of the sample to prevent contact to the aluminium mandrel: the sample would have been contaminated, otherwise.

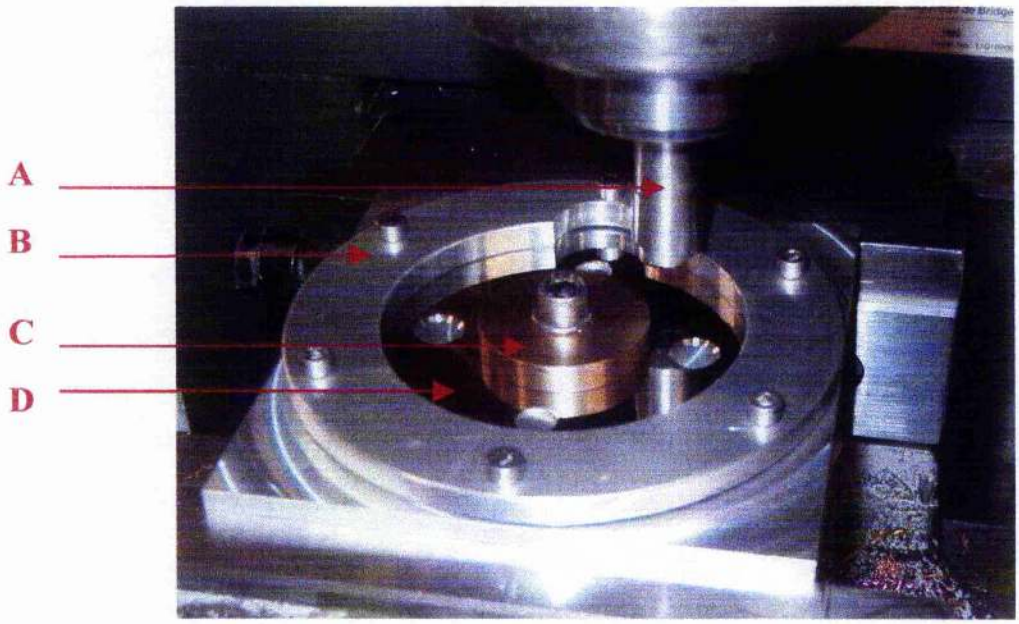

Figure 4.4. A bridgemill set up with the two flute mill. Labels A: two-flute mill with inner and outer bore of 8mm and 12mm, respectively; B, aluminium mandrel; C, brass retaining ring and D, hard disk. Note, the paper shim was not included this is purely for illustration.

A jig, figure 4.5, was also constructed so that one side of the sample, which was not used for FMR, was cleaved off with the use of emery paper. It has an inner bore of 8mm with a depth less than the disc thickness. For each sample, a new piece of emery paper and paper shim was used to prevent any cross contamination from previous samples. After removing the unused layer, the jig was cleaned with acetone to remove any residual pieces.

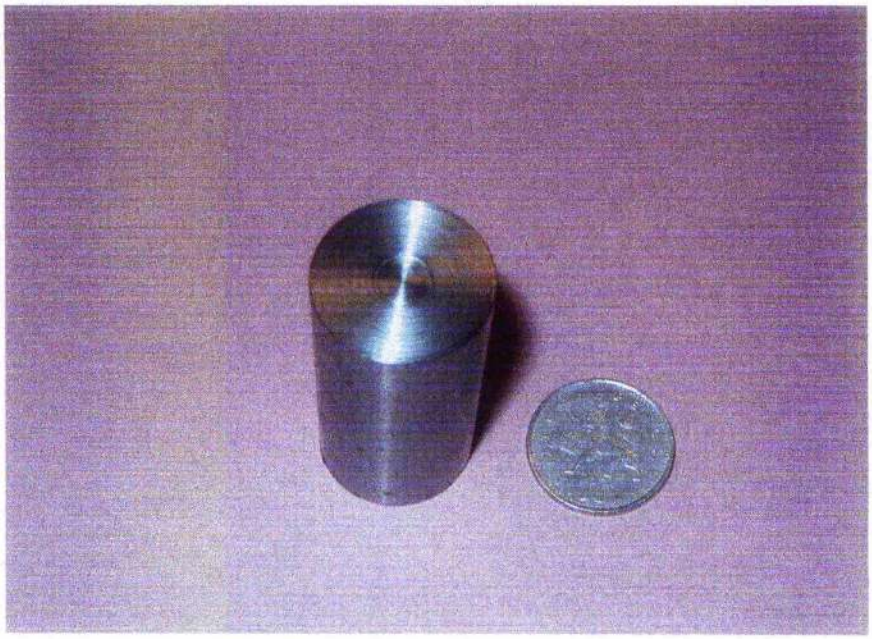

Figure 4.5. The jig, which was used for cleaving one side of the layer to form a substrate.

4.4.1 FMR:

Platinum series

4.4.1.1 Static properties

High frequency FMR on the recording media was measured in the range 77 to 95 GHz. Typical lineshapes of the three samples at 94 GHz are shown in figure 4.6.

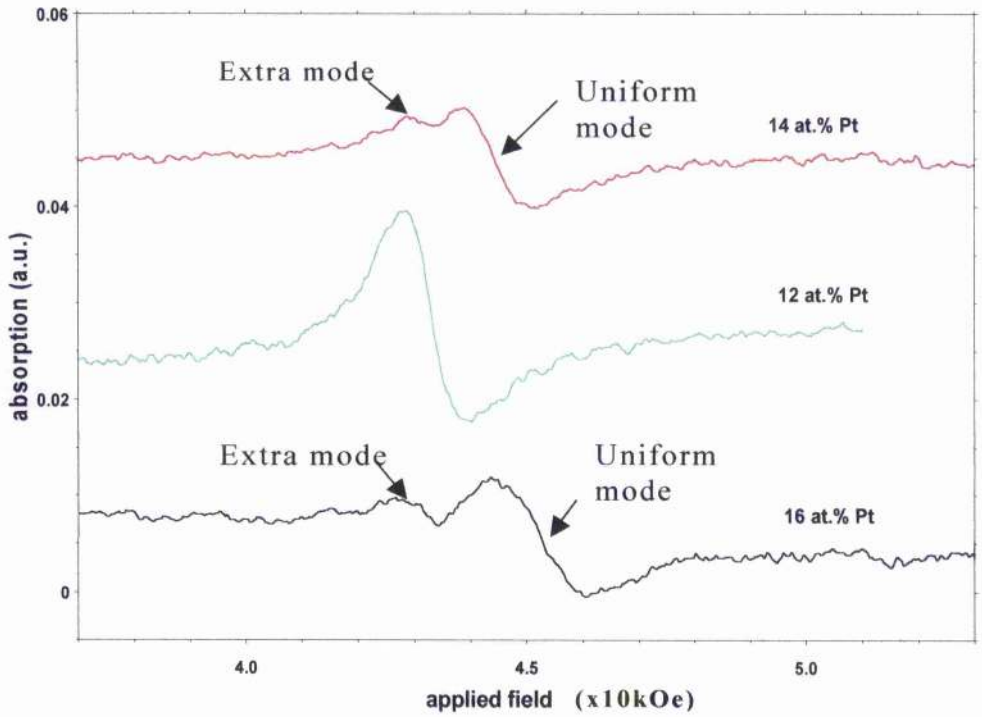

Figure 4.6. FMR signals of the platinum series at 94 GHz.

The method of determining the static and dynamic properties of the recording media was the same way as in chapter three. A fit to the resonant field at different frequencies is shown in figure 4.7. The results presented in table 4.2 are based on the saturation magnetisation provided by Seagate, IBM and from the SQUID in St. Andrews.

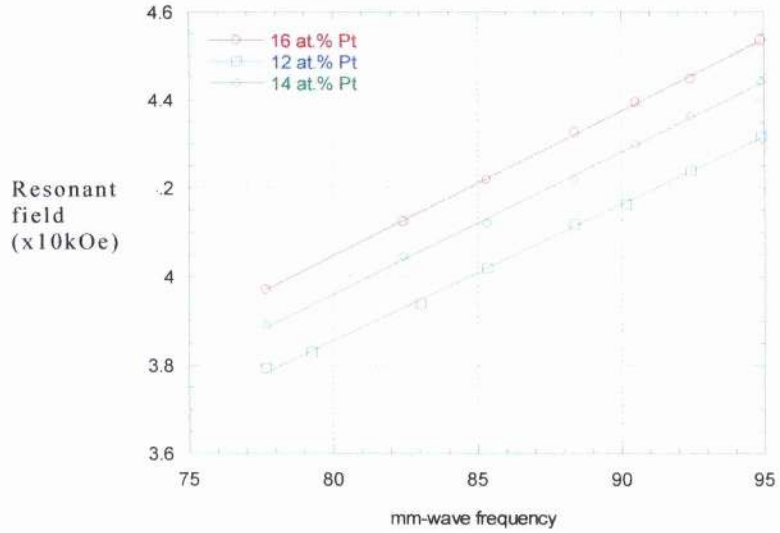

Figure 4.7. Main line resonant field as a function of frequency for samples with different platinum content.

From tables 4.1 and 4.2, it is observed that the higher the platinum content, the smaller the saturation magnetisation, this may be due to the reduction of cobalt in the magnetic layer. Although the measured saturation magnetisation of the three samples differ from laboratory to laboratory, from FMR analysis, the mean uniaxial anisotropy increases and the Lande g-factor decreases **slightly** as the concentration of platinum increases. The g-factor of each sample is the same, regardless of what value the magnetisation takes. However, the derived mean uniaxial anisotropy coincides within error. The uniaxial anisotropy, in table 4.1, measured in Seagate differs significantly with that from FMR, in table 4.2. Independent measurements from IBM have also deduced the anisotropy of 14 and 16 at.% Pt to be 23kOe, which is 6 to 7kOe higher than that determined from FMR. From the results, one can only state that FMR provides reasonable values for the anisotropy as well as the Lande g-factor for each sample, even though their largest difference in the saturation magnetisation is around 21%.

Sample	Saturation magnetisation (emu/cc)			Lande g-factor using $4\pi M_s$ measured from		
(at.% Pt)	Seagate	St. Andrews	IBM	Seagate	St. Andrews	IBM
12	284	352 ± 11	303	2.23 ± 0.02	2.24 ± 0.02	2.23 ± 0.02
14	270	305 ± 15	295	2.14 ± 0.03	2.14 ± 0.03	2.14 ± 0.03
16	260	307 ± 13	272	2.10 ± 0.02	2.10 ± 0.02	2.10 ± 0.02

Sample	$4\pi M_s+H_k/2$ deduced from	$4\pi M_s+H_k/2$ *(kOe)* deduced from $4\pi M_s$		Mean uniaxial anisotropy (kOe) deduced		
(at.%	non-linear regression	and H_k measured from		from FMR using $4\pi M_s$ measured from		
Pt)	(kOe)	Seagate	IBM	Seagate	St. Andrews	IBM
12	12.00 ± 0.50	15.32	11.24	16.14 ± 0.43	15.05 ± 0.58	15.83 ± 0.43
14	11.75 ± 0.75	12.69	15.24	16.48 ± 0.56	15.85 ± 0.79	16.06 ± 0.57
16	11.75 ± 0.25	15.17	15.00	17.14 ± 0.35	16.35 ± 0.58	16.94 ± 0.35

Table 4.2: Static properties of the platinum series from FMR analysis. The Lande g-factor, the values of $4\pi M_s+H_K/2$ and the mean uniaxial anisotropy were derived from FMR using magnetisation values from Seagate, St. Andrews and IBM. The relevance of the $4\pi M_s+H_k/2$ column is to show that the sum, $4\pi M_s+H_k/2$, deduced from non-linear regression (equation 3.15) for each sample does not agree with that measured in IBM and Seagate.

From figure 4.6, the sample with 12 at.% platinum shows only the uniform FMR mode. However, as the composition of platinum increases there exists a lower field mode as well as the usual Kittel mode. This feature is also observed on another part of the disk, 27mm from the disk centre. At all measureable frequencies in the range 75 to 95 GHz, the lower field line is more obvious from samples with 16 at.% than 14 at.% platinum. This lower field signal may be attributed to the existence of an additional layer, called the transition layer. This result is similar to that of Artman [3,4] on the Q-band FMR of CoCr perpendicular recording media. From his measurements, he found that there were two signals present and suggested that one signal is due to the bulk magnetic layer and the other signal from a transition layer. This transition layer is situated between the substrate and the bulk layer and it is a highly disordered, small grained region. In his FMR analysis, he assumed that the magnetisation of the layers was the same and determined the fractional thickness of the transition and bulk layer. He also deduced the total effective anisotropy (taken to be the sum of the intrinsic and shape anisotropy) of the recording media, which agreed with his previous torque magnetometry measurements.

If we follow the same method, then a fit to the lower signal's resonant field at different frequencies, figure 4.8, will provide values of the mean uniaxial anisotropy and g-factor, table 4.3. Similar to Artman's work, the saturation magnetisation of the two layers were assumed to be the same and there is an assumption that there is no exchange coupling between the two magnetic layers.

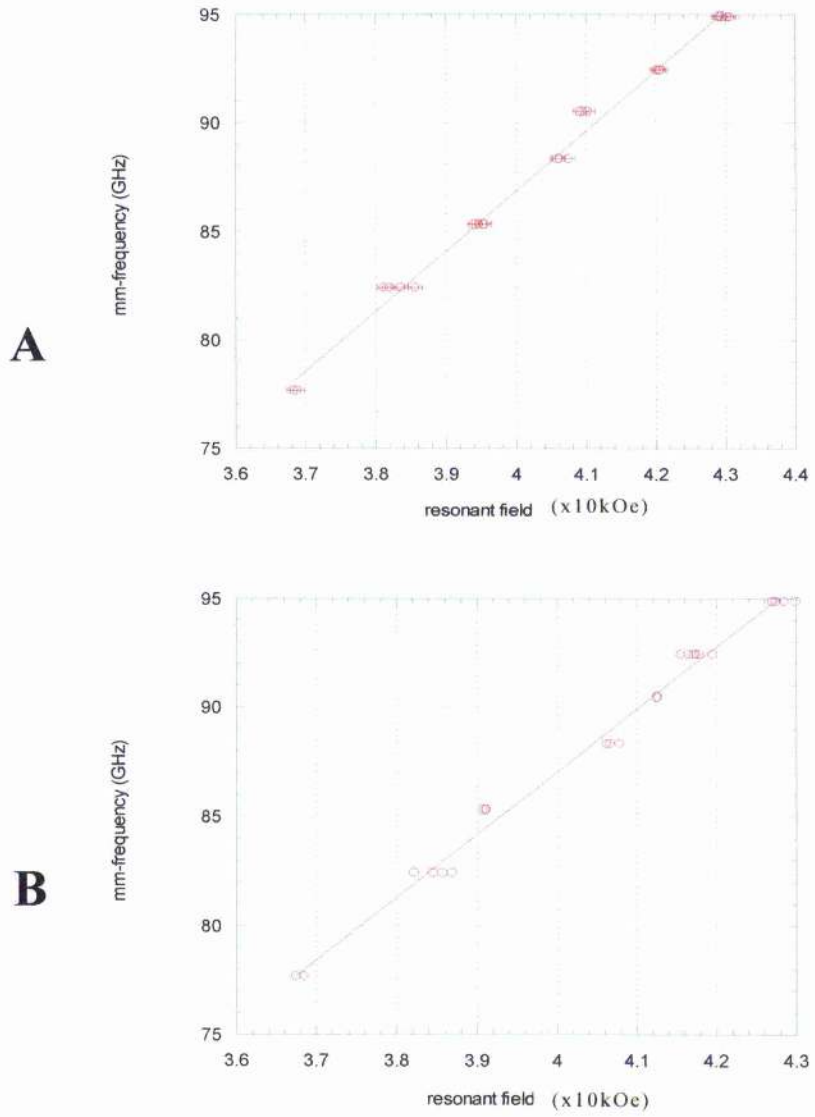

Figure 4.8. Resonant frequency versus field plots of the lower field mode shown in figure 4.6. Plots A and B represent the lower field mode of 14 and 16 at.% Pt, respectively. The fit to the data in this figure required magnetisation values from Seagate.

Sample (at% Pt)	Lande g-factor		Average uniaxial anisotropy (kOe)	
	Seagate	St. Andrews	Seagate	St. Andrews
14	1.95 ± 0.03	1.85 ± 0.01	9.09 ± 0.09	5.23 ± 0.32
14	2*	2*	10.27 ± 0.06	9.63 ± 0.32
16	2.02 ± 0.03	2.02 ± 0.01	10.90 ± 0.08	9.85 ± 0.25
16	2*	2*	10.35 ± 0.06	9.33 ± 0.30

Table 4.3. The g-factor and the average uniaxial anisotropy of the low field mode derived from FMR is based on magnetisation measurements carried out in Seagate and St. Andrews. The star (*) beside the two in the g-factor column is a set value. It is assumed that the saturation magnetisation in the transition layer is the same as the bulk layer.

In table 4.1, the highest measured magnetisation was in St. Andrews and the lowest by Seagate. The static properties of the lower field signal in 14 and 16 at.% Pt were determined from FMR, using two extreme values of their magnetisation as tabulated in table 4.3. Here, the calculated g-value of the 14 at.% Pt sample is less than two: for cobalt, the g-factor is expected to be slightly higher than two. If one were to set the g-value to two, then the anisotropy of 14 and 16 at.% coincide within error.

It was suggested [1] that the transition layer is sandwiched between the bulk magnetic layer and the underlayer; that is, it is the region where the magnetic layer of interest was first deposited. There may be a mixed region from the underlayers and so the first few monolayers of the deposited film has not formed a full anisotropy.

4.4.1.2 Dynamic properties

Linewidth analysis on the platinum series is not straight forward. If one used the equation

$$\Delta H_{pp}(\omega) = \frac{2\alpha\omega}{\sqrt{3}\gamma} + \Delta H_{pp}(0) \qquad (4.1)$$

and fitted it to the data points as shown in figure 4.9, then one would obtain the Gilbert damping term and the inhomogeneous broadening.

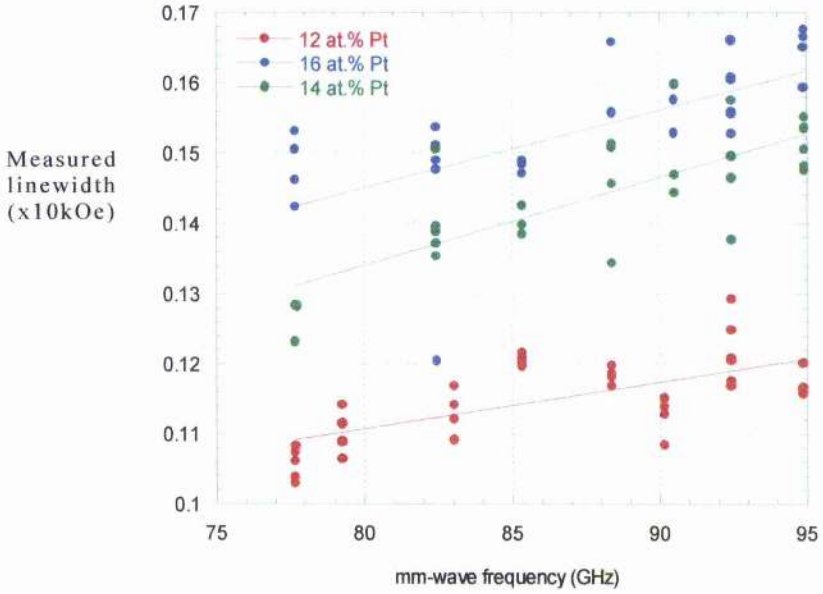

Figure 4.9. Plot of the measured linewidth with frequency. Note that the plot shows all the linewidth points at each frequency and were fitted to equation 4.1.

Because the signal to noise on the lower field signal is poor, it is difficult to determine its linewidth. Table 4.4 provides values to the damping factor and inhomogeneous broadening from linewidth measurements to the uniform mode.

Samples (at.% Pt)	Gilbert damping factor	Inhomogenous broadening (kOe)
12	0.017 ± 0.003	0.592 ± 0.104
	(0.017 ± 0.006)	(0.605 ± 0.222)
14	0.035 ± 0.005	0.275 ± 0.170
	(0.030 ± 0.014)	(0.367 ± 0.090)
16	0.025 ± 0.004	0.696 ± 0.142
	(0.027 ± 0.007)	(0.605 ± 0.239)

Table 4.4 Values of the Gilbert damping term and inhomogenous broadening. The values in brackets were derived from the fit to the average linewidth at each frequency.

From figure 4.9, it is clear that as the cobalt and platinum content decrease and increase, respectively, the measured linewidth also increases. Inaba's [5] work on the damping term, as discussed in chapter three, states that the large increase in the Gilbert damping term in the CoCrPt series compared to CoCrTa is due to the polarisation of platinum in the magnetic layer. The polarisation of platinum means a spin and/or orbital polarisation of platinum electrons (mainly 5s and 6sp) induced by magnetic neighbours [6]. This feature may account for the rise in linewidth as there is more platinum in the layer of interest.
Table 4.4 shows that there is no obvious trend between the Gilbert damping factor and the platinum concentration. The main problem in applying equation 4.1 to the linewidth measurements is that of the limited range of frequencies; in addition, the measured value of the linewidth, at a fixed frequency, for one signal shows a large spread from run to run. The inhomogeneous terms are between 0.2 to 0.7kOe, which is in the same region as the high and low noise media in chapter three. At this stage, it is difficult to correlate both terms to the sample's recording properties.

4.4.2 Boron series

4.4.2.1 Static properties

Multi-frequency work on the boron series shows that there is only a single resonance peak, as shown in figure 4.10 and 4.11.

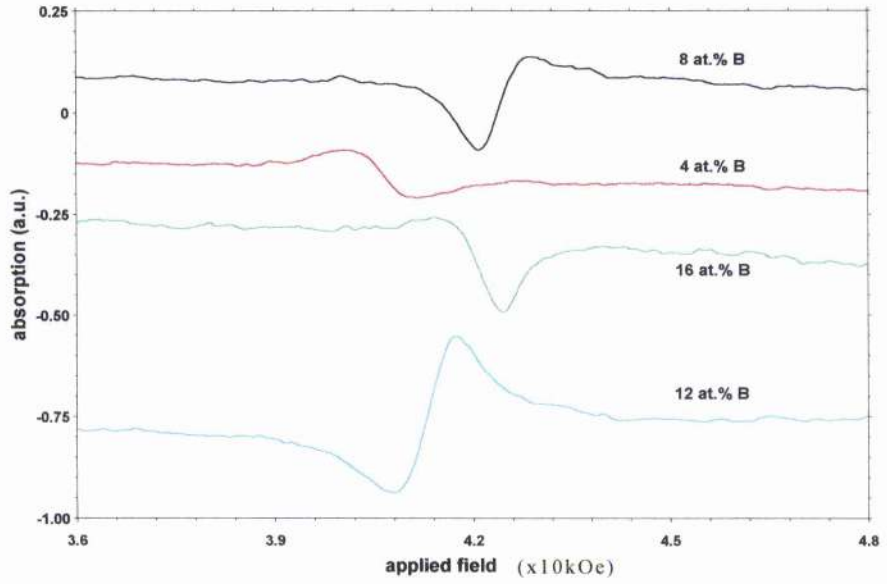

Figure 4.10. The FMR spectra as a function of field of the boron series at 94.63 GHz. It is clear that there is only the uniform mode of precession with no other lower or higher field signal.

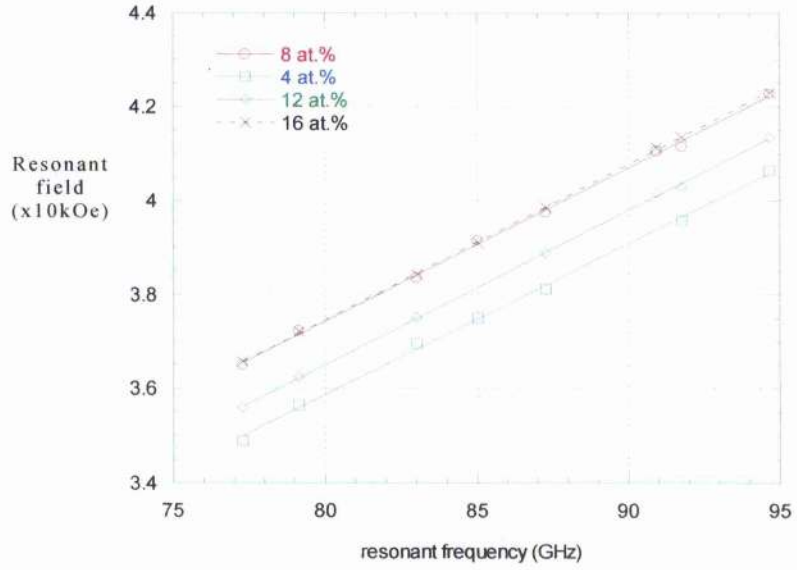

Figure 4.11. Plots of the resonant field with respect to the frequency of the mm-wave at different concentrations of boron.

The analysis of the fit is tabulated below, table 4.5, with the use of magnetisation values measured in IBM and Seagate. Due to limited time, it was not possible to carry out SQUID measurements on the boron series.

Sample (at.% B)	Saturation magnetisation (emu/cc)		Lande g-factor using $4\pi M_s$ measured from		Mean uniaxial anisotropy (kOe) deduced from FMR using $4\pi M_s$ measured from		$4\pi M_s+H_K/2$ (kOe) deduced from non-linear regression.	$4\pi M_s+H_k/2$ (kOe) deduced from $4\pi M_s$ and H_k measured from	
	Seagate	IBM	Seagate	IBM	Seagate	IBM		Seagate	IBM
4	455	403	2.20 ± 0.04	2.19 ± 0.04	7.68 ± 0.80	8.69 ± 0.78	9.05 ± 0.55	9.97	9.39
8	427	335	2.15 ± 0.03	2.14 ± 0.03	10.02 ± 0.68	11.72 ± 0.65	10.25 ± 0.25	10.92	8.91
12	315	288	2.14 ± 0.02	2.13 ± 0.02	10.51 ± 0.39	11.01 ± 0.39	8.75 ± 0.75	12.91	13.48
16	276	212	2.11 ± 0.01	2.11 ± 0.01	12.45 ± 0.25	13.58 ± 0.26	9.15 ± 0.35	10.92	10.31

Table 4.5: Static properties of the boron series from FMR analysis. The Lande g-factor and the mean uniaxial anisotropy were derived from FMR using magnetisation values from Seagate and IBM. From non-linear methods to equation (3.15) the sum, $4\pi M_s+H_K/2$, agrees with that for 4 at.% boron (IBM column).

Again, we have a slight change in the g-factor with respect to the concentration of boron in the media layer; in addition, the average derived FMR uniaxial anisotropy surprisingly increases. Unlike previous measurements carried out by Seagate (Dr. J-P. Chen and Dr. Thomson), there is no turning point in the uniaxial anisotropy term. However, another set of measurements carried out by Dr. Thomson (now at IBM) has shown that the magnetocrystalline anisotropy, table 4.5, increases with respect to boron content which agrees with the FMR measurements.

4.4.2.2 Dynamic measurements

Multi-frequency linewidth measurements on the boron series, figure 4.12 were fitted to equation 4.1. Table 4.6 shows the derived values of the Gilbert factor and inhomogenous term for linewidths at each frequency and the averaged linewidth at each frequency, respectively.

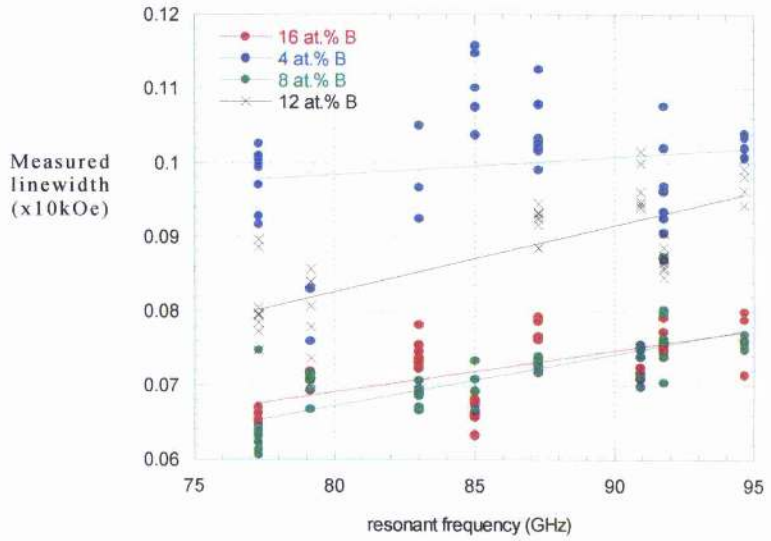

Figure 4.12. Plot of the measured linewidth with frequency. The lines through the data points are straight line fits to equation 4.1.

Sample (at.% B)	Gilbert damping factor	Inhomogeneous term (kOe)
4	0.007 ± 0.005	0.82 ± 0.21
	(0.017 ± 0.015)	(0.45 ± 0.53)
8	0.018 ± 0.002	0.19 ± 0.08
	(0.017 ± 0.004)	(0.14 ± 0.14)
12	0.023 ± 0.021	0.11 ± 0.10
	(0.021 ± 0.017)	(0.10 ± 0.58)
16	0.022 ± 0.002	0.24 ± 0.08
	(0.013 ± 0.008)	(0.29 ± 0.19)

Table 4.6. Damping and inhomogenous terms deduced from all the linewidth data points at each frequency. The values in brackets were derived from the fit to the average linewidth at each frequency.

Unlike the platinum series, there is no trend to the change in linewidth with boron composition. However, the damping factor varies between 0.01 and 0.04, just like the platinum series in section 4.4.1.2. It is very difficult to explain why the inhomogeneous term deduced from the average linewidth at each frequency for 4, 8 and 12 at.% boron has an associated error that is comparable or larger than its estimated value. This was not observed for the platinum series or the high and low noise media.

4.5 Summary

Previous measurements on the uniaxial anisotropy field for both types of recording media (platinum and boron series) do not seem to agree very well with that of FMR. Initial measurements by Seagate showed that the anisotropy in the boron series has a turning point at 12 at.% boron but from FMR, the anisotropy still increases with boron content. From table 4.5, if one were to apply values of the sample's saturation magnetisation (measured in Seagate and IBM) to the resonant

condition, equation (3.14), then the g-value for each sample in the boron series coincides within error. The same applies to the anisotropy for samples 4 and 12 at.% boron. It is encouraging to learn that another independent measurement by Dr. Thomson in IBM, using the VSM, follows this trend on the increase of the average uniaxial magnetocrystalline anisotropy with boron content. However, it is uncertain, as to why measurements in Seagate have a peak value in the anisotropy.

SQUID measurements, in St. Andrews, on the platinum series shows that the coercivity is around 3.5kOe and that the product of the remanence and film thickness, $M_r t$ agrees very well with that deduced from the vector VSM in Seagate [1]. Although the saturation magnetisation of each sample from the SQUID measurements is **not** significantly different from that measured in Seagate, this parameter is required for FMR analysis and so a slight change in one parameter will create a shift to the sample's g-factor and anisotropy. As mentioned earlier, in the platinum series section, the g-value has not changed although the largest difference in the anisotropy is approximately 2kOe for each sample. The smaller peak in the 14 and 16 at.% Pt series may be attributed to the deposited layer which has not reached its full anisotropy. It is clear that more platinum samples with different compositions are required to enhance our understanding of the lower field signal and to ascertain if there is a genuine trend of the sample's g-factor and uniaxial anisotropy with platinum content.

Since the magnetocrystalline anisotropy and the g-factor of a transition element is attributed to spin-orbit coupling, one assumes that if the anisotropy increases then the g-factor will also increase. Yet it is the reverse for both the platinum and boron series.

Non-linear regression (NLR) to equation (3.15) shows that in table 4.2 (the platinum series), the sum $4\pi M_s + H_K/2$ for each sample varies between 11.0 to 12.5 kOe. However, only sample 7A (12 at.% Pt, measured in IBM) in table 4.1, has the sum lying within that range. For the boron series and with reference to table 4.1, the sum for sample 7B (4 at.% boron) measured in IBM also lies within the range determined

from NLR. If one were to add $4\pi M_s$ (measured from IBM, Seagate and St. Andrews) to $H_K/2$ (deduced from FMR), then for each sample in both series, the sum deduced from experiment lies in the same region generated from NLR. This suggests that high field FMR is a reliable method for finding $4\pi M_s+H_K/2$.

For both the platinum and boron series, the damping factor agrees with previous damping values [5,7]. Although a wider frequency range is required for accurate values of the damping and inhomogeneous term.

4.6 References:

[1] T. Thomson, private communications 2002

[2] S.D. Harkness and J-P. Chen, private communications 2002

[3] J.O. Artman, J. Appl. Phys. 61 (1987) 3137

[4] P.V. Mitchell, A. Layadi, N.S. VanderVen, and J.O. Artman, J. Appl. Phys. 57 (1985) 3976

[5] N. Inaba, Y. Uesaka, A. Nakamura, M. Futamoto, and Y. Sugita, IEEE Trans. Mag. 33 (1997) 2989

[6] Cz. Kapusta, private communications 2002

[7] M.L.Plummer, J.van Ek and D.Weller, *The Physics of Ultra-High Density Magnetic Recording*, Springer-Verlag, New York 2001

Chapter 5

Small Angle Neutron Studies (SANS) of Longitudinal Recording Media.

5.1 Introduction

This chapter examines neutron diffraction of longitudinal recording media measured at different fields. Three types of samples were examined in this chapter: 2D-isotropic, 2D-anisotropic media (the moments are preferentially aligned along the disk radius) and a NiAlP substrate. The author's contribution was to carry out SANS measurements and assemble the data, which was then analysed by Prof. Stephen Lee. (Participants in the group include Dr. Feodor Ogrin and Dr. Tom Thomson.) The analysis on the recording media was not straight forward and there are discussions on methods that were used to analyse the spectra. The main feature, here, is to compare the physical mean grain size, determined from TEM to the magnetic grain size, deduced from SANS. Before describing the results, a background introduction to neutron diffraction and SANS is required.

5.2 Basic theory of neutron diffraction

5.2.1. Why neutron diffraction?

The basic properties of the neutron are tabulated below:

basic properties of the neutron	
mass m	1.675×10^{-27} kg
charge e	0
Spin	½
magnetic dipole moment	$\mu_n = -1.913\mu_N$ *

* μ_N is the nucleon magneton, which is equal to 5.051×10^{-27} JT^{-1}

Table 5.1. Basic properties of the neutron [1]

The kinetic energy of a neutron is related to its wavevector $\bar{k}$ by the equation,

$$E_K = \frac{\hbar^2 k^2}{2m_N} = \frac{1}{2} m\bar{v}^2 = \frac{81.81}{\lambda^2} \qquad (5.1)$$

In these equations, λ is in $\mathring{A}$, k is in 10^{10}m^{-1}, $\bar{v}$ in kms^{-1}, E in meV, and T in Kelvin.

With reference to equation 5.1, a neutron at 293K has an average wavelength of $1.8\,\mathring{A}$, its energy is 25.3meV and it travels at a speed of 2.20 kms^{-1}. For example, if we diffract neutrons from the planes of metallic iron at room temperature (having the atomic spacing, $2.88\,\mathring{A}$), then planes (111) and (200) have very different scattering angles and are therefore easily resolved.

Other advantages of neutron scattering are as follows:

(a) neutrons have energies comparable to thermal energies of the sample;

(b) neutrons are deeply penetrating;

(c) neutrons are scattered with a strength that varies randomly from element to element;

(d) neutrons have a magnetic moment;

(e) the time a neutron passes an atom is of the order of 10^{-13} s, which is comparable to the relaxation times of the sample and

(f) neutrons interact with nuclei at a range between 10^{-14}m and 10^{-15}m, which is smaller than the thermal neutron wavelength, implying that the neutron is scattered isotropically by a nucleus (S-wave scattering) and is therefore an ideal probe of the solid state.

5.2.2. Nuclear diffraction

Figure 5.1 shows a typical scattering system in which neutrons of wavevector k and energy E are scattered by a target sample. If a neutron counter was used to measure the number of neutrons scattered in a given direction as a function of their energy E', and the distance of the counter from the target is assumed to be large compared to the dimensions of the counter and the target, then the small angle $d\Omega$ subtended by the counter at the target is well defined. Let the direction of the scattered neutrons be θ,ϕ. k_i and k_f is the neutron's incident and scattered wavevector, respectively.

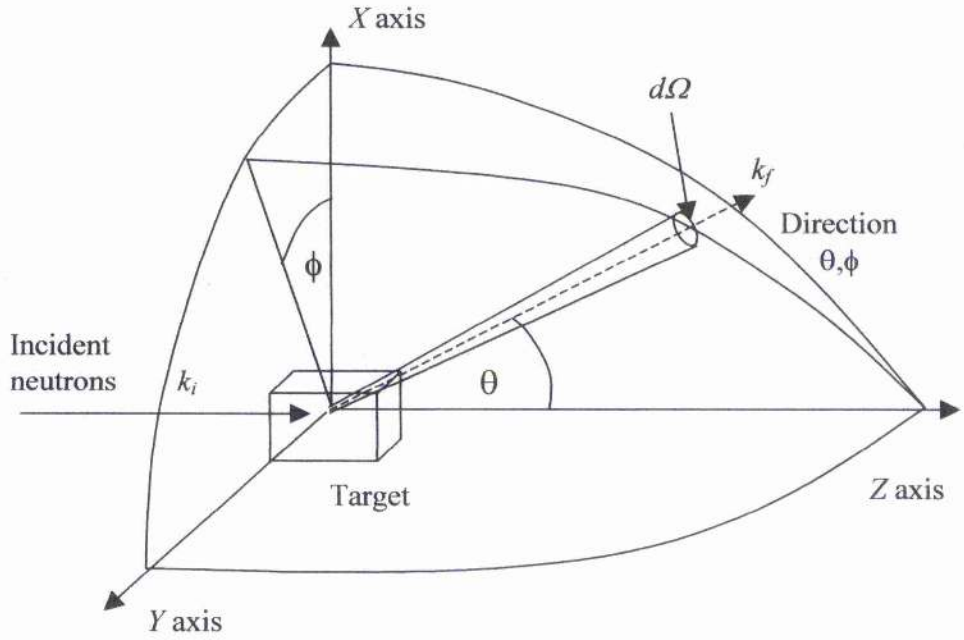

Figure 5.1. Geometry for scattering experiment [1]

The **partial differential cross-section** is defined by the equation [1]

$$\frac{d^2\sigma}{d\Omega dE} = \begin{array}{l}\text{(number of neutrons scattered per second into a small angle}\\ \text{solid angle } d\Omega \text{ in the direction } \theta,\phi \text{ with final energy}\\ \text{between } E' \text{ and } E'+dE') \,/\, \Phi d\Omega dE'\end{array} \qquad (5.2)$$

where Φ is the incident neutron flux; that is, the number of neutrons through unit area per second, the area being perpendicular to the direction of the neutron beam.

If we do not analyse the energy of the scattered neutrons, but count all the neutrons scattered into the solid angle $d\Omega$ in the direction θ,ϕ, then the cross-section corresponding to these measurements is known as the **differential cross-section**, which is defined by [1]

$$\frac{d\sigma}{d\Omega} = \frac{\text{(number of neutrons scattered per second into } d\Omega \text{ in the direction } \theta,\phi)}{\Phi d\Omega} \qquad (5.3)$$

The **total scattering cross-section** is defined by the equation [1]

$$\sigma_{total} = \text{(total number of neutrons scattered per second)}/\ \Phi \qquad (5.4)$$

The total number means the number of neutrons scattered in all directions.

With reference to figure 5.1, the intensity of the scattered neutrons is measured as a function of momentum transfer:

$$\hbar\overline{Q} = \hbar\left(\overline{k}_i - \overline{k}_f\right) \qquad (5.5)$$

where $\overline{Q}$ is the scattering vector. The corresponding energy transfer is given by

$$\hbar\omega = \frac{\hbar^2}{2m}\left(k_i^2 - k_f^2\right) \qquad (5.6)$$

There are two types of scattering: elastic and inelastic. Figure 5.2 is an illustration of scattering triangles for the types of scattering.

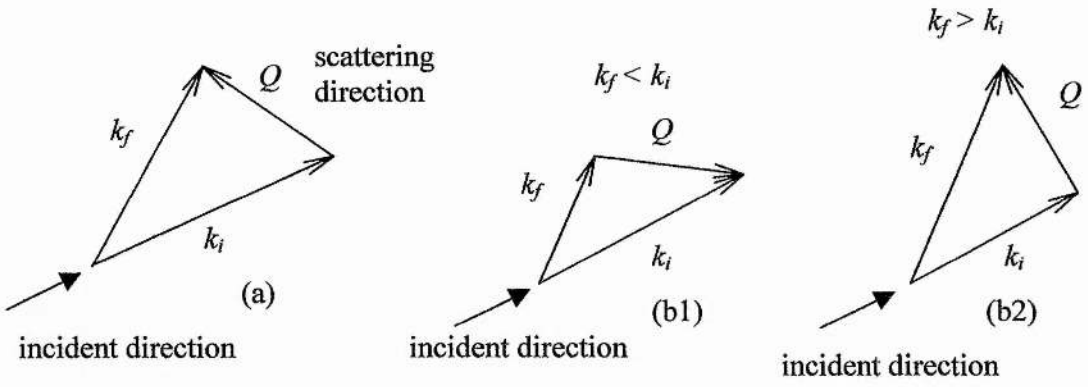

Figure 5.2 (a) Elastic scattering where $k_i = k_f$ and (b) $k_i \neq k_f$ for inelastic scattering. (b1) is where the neutron losses energy and (b2) is the neutron absorbing energy.

The interaction of a neutron with a nucleus can be thought of as a neutron in the presence of a potential well, with a potential of V_0. The neutron can be considered as a plane wave, $e^{i\bar{k}\cdot\bar{r}}$. Outside the well, the neutron's wavevector is $k=\sqrt{\frac{2mE}{\hbar^2}}$ and inside the well, the wavevector becomes $q=\sqrt{\frac{2m(E+V_0)}{\hbar^2}}$. The total wave function outside the well is $\varphi(\bar{r})=e^{i\bar{k}\cdot\bar{r}}+\frac{f}{r}e^{i\bar{k}\cdot\bar{r}}$, where f is the scattering amplitude. In the limit of $k\to 0$ (low energy scattering), $b=-\lim_{k\to 0} f$ is defined, where b is the neutron scattering length. This scattering length is dependent on the type of nucleus scattering the neutron. The physical interpretation of a negative f value is that the scattered wave in the $k\to 0$ limit is shifted by 180 degrees in phase with respect to the incoming wave. Scattering of neutrons from fixed nuclei is well approximated by the Fourier transform of the interaction potential, which is given by the Fermi pseudo-potential [2,3]: $V(\bar{r})=\frac{2\pi\hbar^2}{m}\sum_i b_i\delta(\bar{r}-\bar{R}_i)$ (5.7).

References [1,4] cover a mathematical background on the partial differential cross-sections resulting from the Fermi pseudo-potential.

5.2.3. Elastic Magnetic scattering

The neutron has a magnetic moment, which interacts with the atomic moments on the atoms. The interaction is actually $-\overline{\mu}\cdot\overline{B}$, the neutron moment interacts with the flux density associated with the unpaired electrons in the sample. An appropriate scale for the interaction is the Bohr radius [2,3]:

$$r_0 = \left(\frac{e^2\gamma}{2mc^2}\right) \tag{5.8}$$

where r_0 is the Bohr radius, $0.54\text{x}10^{-12}$ m and γ is the gyromagnetic ratio of the neutron. An effective magnetic scattering length is given by $P = \frac{e^2\gamma}{2mc^2} gJf(Q)$, where g is the Lande g-factor of the ion, J is the total angular momentum and $f(Q)$ is the magnetic form factor, $f(Q) \propto \int \rho_m e^{i\overline{Q}\cdot\overline{r}} d^3r$. This form factor is the Fourier transform of the magnetic density of the magnetic ion. Because the magnetic scattering process involves an interaction with electrons over long distances comparable to neutron wavelengths, the magnetic scattering intensity is reduced as Q increases. The form factor represents the non-isotropic scattering from magnetic ions caused by the spatial extent of the electron distribution [1].

If we assume that the neutrons are unpolarised and that we are dealing with elastic scattering, then the elastic cross-section is defined for a Bravais lattice with localised electrons [1,2]:

$$\left.\frac{d\sigma}{d\Omega}\right|_{magnetic} = (\gamma r_0)^2 N \left|\frac{1}{2} gf(Q)\right|^2 \exp(-2W) \sum_{\alpha,\beta} \left(\delta_{\alpha\beta} - \hat{Q}_\alpha \hat{Q}_\beta\right) \sum_{i,j} \exp\left(i\overline{Q}\cdot\left(\overline{R}_i - \overline{R}_j\right)\right) \left\langle S_i^\alpha \right\rangle \left\langle S_j^\beta \right\rangle$$

Equation (5.9), above, involves the sum over all lattice sites i and j and over all Cartesian directions, $\alpha,\beta = x, y, z$. The exp(-2W) term is the Debye-Waller factor as discussed in [1].

$\langle S_i^\alpha \rangle$ and $\langle S_j^\beta \rangle$ are the time averaged spin components on sites *i* and *j*.

For a ferromagnet, the cross-section for a sample with many domains is [1]

$$\left.\frac{d\sigma}{d\Omega}\right|_{magnetic} = (\gamma r_0)^2 N \frac{(2\pi)^3}{V_0} \langle S^\eta \rangle^2 \sum \left\{ \frac{1}{2} g f(Q) \right\}^2 \exp(-2W) \left\{ 1 - (\hat{\tau} \cdot \hat{\eta})_{av}^2 \right\} \delta(\overline{Q} - \overline{\tau}) \quad (5.10)$$

where $\langle S^\eta \rangle$ is the mean value of the component of the spin in the direction of $\hat{\eta}$ for each domain, V_0 is the volume of the reciprocal lattice, $\hat{\eta}$ is a unit vector in the mean direction of the spins, $\hat{\tau}$ is a unit vector in the direction of $\overline{\tau}$ (in the reciprocal lattice), $\overline{\tau}$ is an arbitrary direction in k-space and we take the scattering vector $\overline{Q} = \overline{k}_f - \overline{k}_i = \overline{\tau}$. The average $(\hat{\tau} \cdot \hat{\eta})_{av}$, is taken over all the domains, and so equals to *2/3* if all directions in space are equal.

If an external magnetic field is applied in the direction of τ, then the spin directions of all the domains will tend to align so that $\hat{\eta}$ is along -τ [1]. Therefore $\hat{\tau} \cdot \hat{\eta} = -1$ and the magnetic scattering vanishes. The difference in the cross-section with and without a high external field gives the magnetic scattering alone [1].

5.2.4. Small angle neutron scattering

Small angle neutron scattering provides structural information on a scale ranging from a few angstroms up to regions with dimensions of the order of 5000 angstroms in bulk specimens [4].

In an ideal SANS experiment, figure 5.3, the momentum of the incident and scattered neutrons must be defined in order to investigate the properties of the sample. In the SANS experiments, no energy discrimination is carried out on the scattered beam and thus the

inelastic contribution is measured along with the elastic scattering to give the total scattering. For elastic scattering, the magnitude of the scattering vector [4,5,6], $|\overline{Q}|$, is $\frac{4\pi}{\lambda}\sin\theta$. The term small angle neutron scattering is used in materials science to cover the Q range $0 \leq Q \leq \frac{\pi}{d}$ where d is the interatomic distance in the material under investigation.

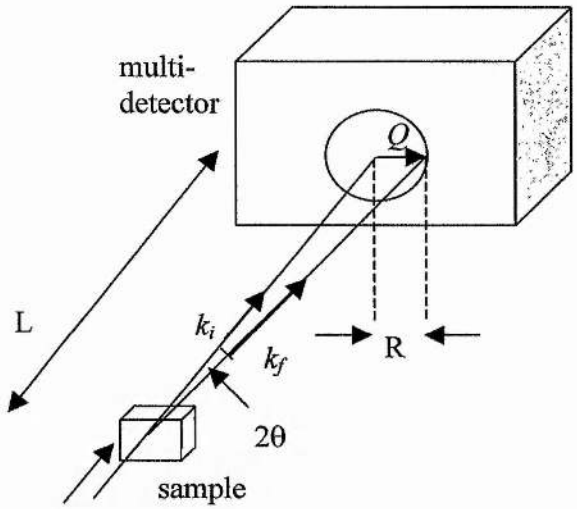

Figure 5.3. Schematic representation of a SANS experiment [7].

If one were to investigate magnetic samples, then there exists two contributions to the scattering: nuclear and magnetic scattering.
Considering nuclear scattering first, the coherent scattering cross-section (arising due to interference effects between the scattered neutrons from each nucleus) per atom is [6]

$$\frac{d\sigma}{d\Omega} = \frac{1}{N}\left|\sum_R b_R e^{(i\overline{Q}\cdot\overline{R})}\right|^2 \qquad (5.11)$$

where N is the number of scattering nuclei exposed in the beam, b_R is the coherent scattering length of the elements occupying the site with the position vector $\overline{R}$. $\overline{Q}$ is defined as the scattering vector, which is the difference between the incident and scattered wavevector.
The scattering cross section for the whole sample is

$$\frac{d\sigma}{d\Omega} = \frac{1}{N}\left|\int_V \{\rho_b(\bar{r}) - \bar{\rho}_b\} e^{(i\bar{Q}\cdot\bar{r})} d^3\bar{r}\right|^2 \qquad (5.12)$$

where b_R is replaced by $\rho_b(\bar{r})$, which is the locally averaged scattering length density and $\bar{\rho}_b$ is averaged over all volumes and the integral is over a sample volume, V.

If one were to consider a binary system; that is a sample that contains N_p particles with a homogenous scattering length density $\rho_{bp} = \frac{b_p}{V_{ap}}$ (where b_p is the scattering length, which is averaged over the particle volume, and V_{ap} is the atomic volume in the particle), which is embedded in a matrix of homogeneous scattering length density $\rho_{bm} = \frac{b_m}{V_{am}}$, then one obtains the expression [6]

$$\frac{d\sigma}{d\Omega} = \frac{1}{N}\left(\rho_{bp} - \rho_{bm}\right)^2 \left|\int_V e^{(i\bar{Q}\cdot\bar{r})} d^3\bar{r}\right|^2 \qquad (5.13)$$

where the integral extends over the volume V occupied by all particles. This can be re-written as

$$\frac{d\sigma}{d\Omega} = \frac{V_P^2 N_P}{N}\left(\rho_{bp} - \rho_{bm}\right)^2 \left|F(\bar{Q})\right|^2 \qquad (5.14)$$

where $F(\bar{Q}) = \frac{1}{V_P}\int_V e^{(i\bar{Q}\cdot\bar{r})} d^3\bar{r}$ is the single particle form factor [6].

The form factor above is used for different particle shapes; for example, for a sphere [6]

$$F(Q) = 3\frac{(\sin(Qr) - Qr\cos(Qr))}{(Qr)^3}. \qquad (5.15)$$

Other form factors for cylinders and ellipses can be found in Kostorz [6].

For a concentrated system of interacting spheres, the interference between these particles become important and so the scattering cross-section becomes [6]:

$$\frac{d\sigma}{d\Omega} \propto (\rho_{bm} - \rho_{bp})^2 (F(\overline{Q}))^2 S(\overline{Q}) \qquad (5.16)$$

where $S(\overline{Q})$ is the structure factor.

Another example of the structure factor is that for hard spheres, where the volumetric packing fraction is between 30 to 50%. Therefore, one employs the Perkus-Yevik model [8,9]

The definition of the structure factor is that it provides the intereference effects from a collection of different grains; the form factor is the Fourier transform of the shape and size of the grains.

Examples of the structure factor and form factor are shown in figure 5.4.

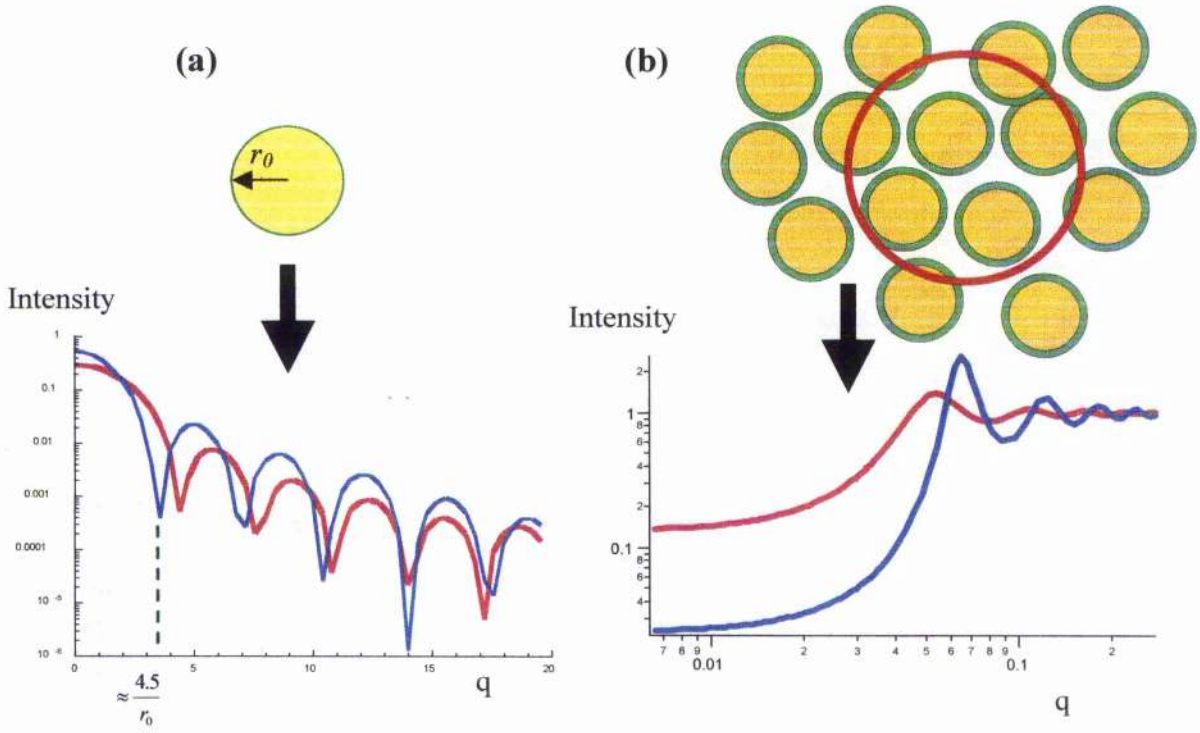

Figure 5.4. Form factor (a) of a sphere, the red and blue line represents a sphere with different radii, which is the first minima of the I vs q curve; (b) is the structure factor where the red and blue lines represent a group of spheres with different packing densities. These are simulations provided by Prof. S.L.Lee [10].

For magnetic scattering, if $M(\bar{r})$ is the local magnetisation at position $\bar{r}$, then $M(\overline{Q})$ is its Fourier transform [6]:

$$M(\overline{Q}) = \int M(\bar{r}) e^{(i\overline{Q}\cdot\bar{r})} d^3\bar{r} \qquad (5.17)$$

and the magnetic contribution to the scattering cross-section is [4]

$$\frac{d\sigma}{d\Omega} = \frac{\gamma^2 e^2}{h^2 c^2} \left| M^{+}(\overline{Q}) \right| \qquad (5.18)$$

where $M^{+}(\overline{Q})$ is the component of $M(\overline{Q})$ perpendicular to the scattering vector $\overline{Q}$ and γ is the neutron magnetic moment in nuclear magnetons.

For a system composed of different magnetic states [4]

$$\frac{d\sigma}{d\Omega} = \left| \langle \overline{M}_i \rangle - \langle \overline{M}_m \rangle \right|^2 \left[1 - \left(\hat{Q} \cdot \hat{M} \right)^2 \right] \left[F(\overline{Q}) \right]^2 \qquad (5.19)$$

where $\hat{Q}$ is a unit vector in the direction of $\overline{Q}$, M_i is the moment of the impurity, M_m is the moment of the matrix and $\hat{M}$ is a unit vector parallel to the direction defined by the vector $\langle \overline{M}_i \rangle - \langle \overline{M}_m \rangle$.

As previously mentioned, a system composed of random magnetisation vectors, in the absence of a magnetic field, the term $1 - \left(\hat{M} \cdot \hat{Q} \right)^2$ is equal to *2/3*, thus isotropic scattering is observed. If the field is above the saturating field, then the magnetic contribution to the scattering is zero (as $\hat{M} \parallel \hat{Q}$) in the field direction and maximum perpendicular to it. Nuclear scattering is unaffected and remains isotropic [4,6].

5.3. SANS experiment

All neutron measurements were carried out at the I.L.L (Institut-Laue-Langevin) on instruments D11 and D22. The ILL is the world's most powerful reactor source, with a peak flux of 57MW, producing neutrons for a wide range of instruments. Figure 5.5 shows a schematic representation of the experimental arrangement for a SANS experiment.

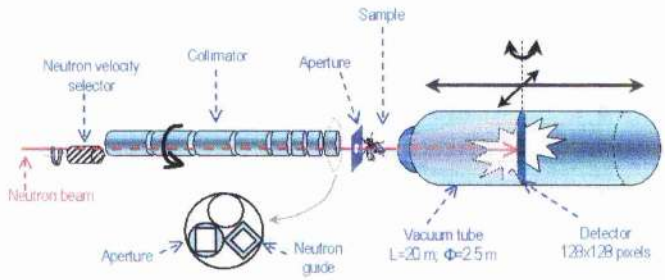

Figure 5.5. Schematic representation of the SANS experiment in D22, in the I.L.L. [7]

The specifications of both D11 and D22 are tabulated below.

Diffractometer specifications					
Instrument in ILL	Sample detector distance (m)	Collimation distance (m)	Wavelength (angstroms)	Detector array	Pixel size (mm^2)
D11	2.5 – 41	2.5 – 41	4.5 – 40	128 x 128	10 x 10
D22	1.4 – 18	1.4 - 18	4.5 - 40	64 x 64	7.5 x 7.5

Table 5.2. Specifications of D11 and D22 [7], which were used during investigations carried out in this chapter.

The neutron beam passes through a velocity/wavelength selector for the incoming neutrons. It then passes through a monitor, which records the number of neutrons incident on the sample. After passing through a source slit, the beam travels along an evacuated tube and is incident on the sample. The collimation length is variable to allow the optimum trade-off between resolution and intensity to be obtained.

The detector can be moved back and forth relative to the sample so that one can obtain a full q-range of the neutron scattering intensity.

The software, called GRASP, designed by Dr. Charles Dewhurst from the ILL is a user friendly package that is used for graphical inspection, analysis and reduction of multi-detector data produced by D11 and D22. The software has the added advantage of quickly processing and

extracting information, as a function of position of the multi-detector or as a function of temperature.

5.4. Recording media samples

The media was dc magnetron sputtered onto an aluminium substrate. The samples of interest have a 20nm CoCr magnetic layer, as shown below.

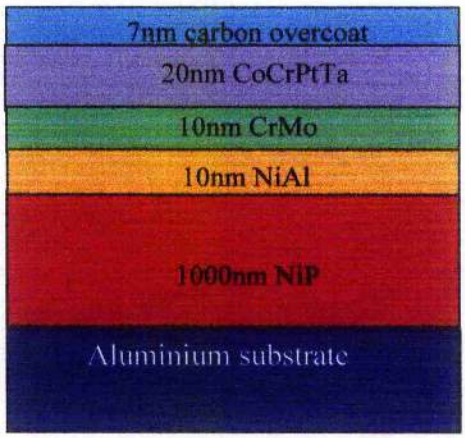

Figure 5.6. A schematic representation of magnetic recording media that was used for SANS measurements [11].

The carbon overcoat prevents oxidation to the CoCrPtTa layer and the CrMo is a seed layer, which determines the grain size.

The three samples concerned are that of isotropic media, x1646; anisotropic media (the moments are preferentially aligned along the disc radius) [11], x341, and the background sample, x1821. The background sample has the same layers and layer thickness as the other two samples, except there is no CoCr layer.

The saturation magnetisation, coercivity and uniaxial anisotropy measured from VSM at room temperature and the mean physical grain size diameter (measured from TEM) in samples x1646 and x341 are provided in table 5.3. (The uniaxial anisotropy was determined by carrying out VSM measurements with the field normal to the film surface.) These measurements were carried out by Seagate.

samples	$4\pi M_s$ (kOe)	Coercivity (kOe)	Uniaxial anisotropy (kOe)	Mean grain size diameter, d (nm)	*Size dist.* $\Delta d/d$
X1646	5.73	2.87	10.11	10	0.2
X341	8.50	2.31	5.98	30	0.4

Figure 5.3. Magnetic properties of the isotropic and anisotropic media.

Hysteresis loops of both types of media were carried out by Seagate [11], as shown below, figure 5.7.

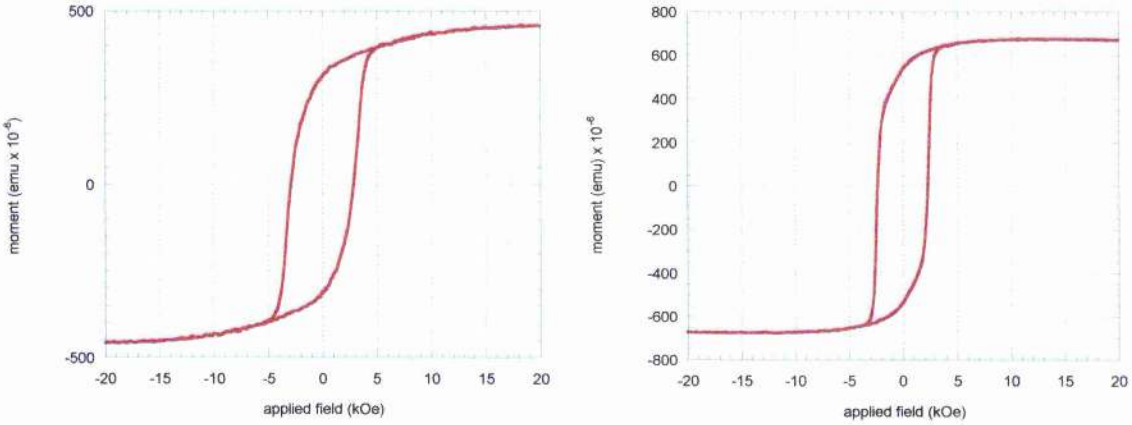

Figure 5.7. In-plane magnetisation loops of the isotropic, x1646, (A) and anisotropic, x341, (B) media.

5.5. SANS measurements

5.5.1. Sample preparation for measurements

Since there is a very small amount of active layer for SANS measurements, it is necessary to use a composite system of some thirty disks. Background scattering from the aluminium substrate on which the magnetic layers were grown must be reduced without damaging the active layer. However, this still leaves the substrate of the order of one hundred microns thick, which gives rise to a large background signal.

The disks were wrapped in an aluminium foil and placed into a sample holder, as shown below, which had a cadmium cover around the edge of the holder [10].

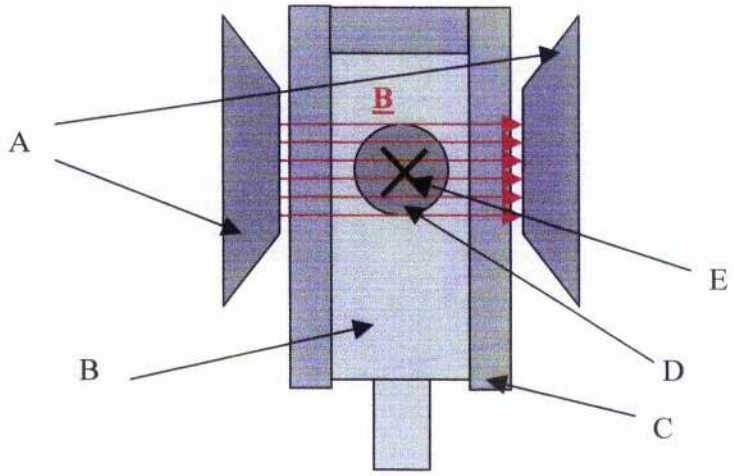

Figure 5.8. Aluminium holder with sample for neutron measurements. The labels, (A) represents the pole pieces of the electromagnet; (B), the aluminium sample holder; (C), cadmium cover, which was used to sandwhich the samples between the aluminium plates; (D), the thin film samples and (E) represents the neutron flux into paper [10].

As mentioned previously, the detector can be moved back and forth relative to the sample so that one can obtain a full q-range of the scattering intensity. However, there was a higher incident neutron flux at higher q (where the sample detector distance is as small as 1 to 2m), than that at lower q (sample detector distance is of the order of 18m for D11 and D22). In order to obtain a good signal to noise ratio, there must be more statistics; that is, longer runs at lower q than at higher q.

An example of this is shown later in figure 5.12, for the in-plane isotropic media, where the error bars are bigger at lower q.

5.5.2. SANS of 2D - isotropic longitudinal recording media

The fields of interest in this section are 14.5 and 4.5kOe. This is because these were the two fields in which we obtained a full q-range (which was available at the time of measurement). The 2D multi-detector plot of scattering at 14.5kOe is shown.

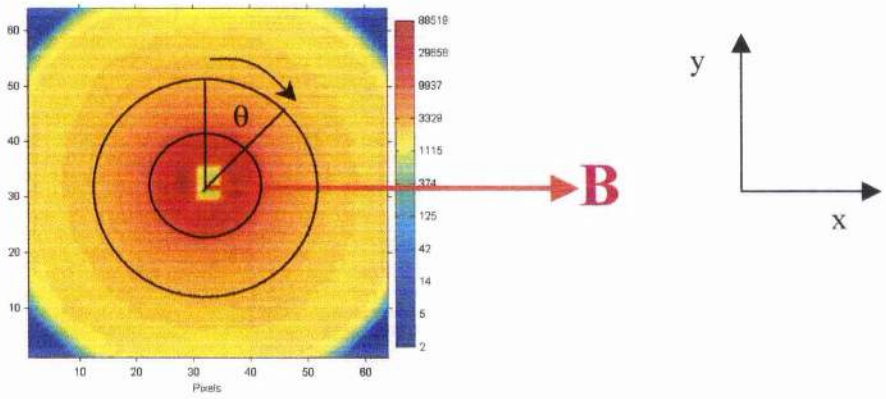

Figure 5.9. Apparent isotropic scattering detected at 14.5kOe. The field line represents the direction of the applied field, B, and the yellow square in the middle of the detector is a beam stopper, which prevents the detector from saturating. The two black circles represent an annulus, which was used in GRASP for observing magnetic scattering; that is, we were looking for a $\left(1-\left(\hat{M}\cdot\hat{Q}\right)^2\right)\equiv\left(1-\cos^2\theta\right)$ *curve as shown in equation (5.19).*

With reference to figure 5.9, the magnetic field was applied horizontally. From theory, there should be no magnetic scattering along the field direction if the sample is magnetically saturated, but there should be magnetic scattering along the y-direction; therefore, if the electromagnet were strong, then one would expect from equation (5.19), to observe a figure eight-like distribution of the magnetic scattering [10]. However, as shown in figure 5.9, there was no obvious

figure eight-like distribution of the magnetic scattering. In fact, the 2D detector plot for 14.5kOe looks very similar to zero field measurement (where the sample is in a randomised isotropic state). If we used GRASP to take an annulus of the 2D detector for 14.5kOe, then there is no clear sine square dependence, figure 5.10. This is because there is more nuclear scattering (isotropic) than magnetic scattering, plus a random fluctuation in the background arising from the stack of substrates. Therefore, in order to observe magnetic scattering, the moments in the recording media must be magnetically saturated and there should be no nuclear scattering present [10].

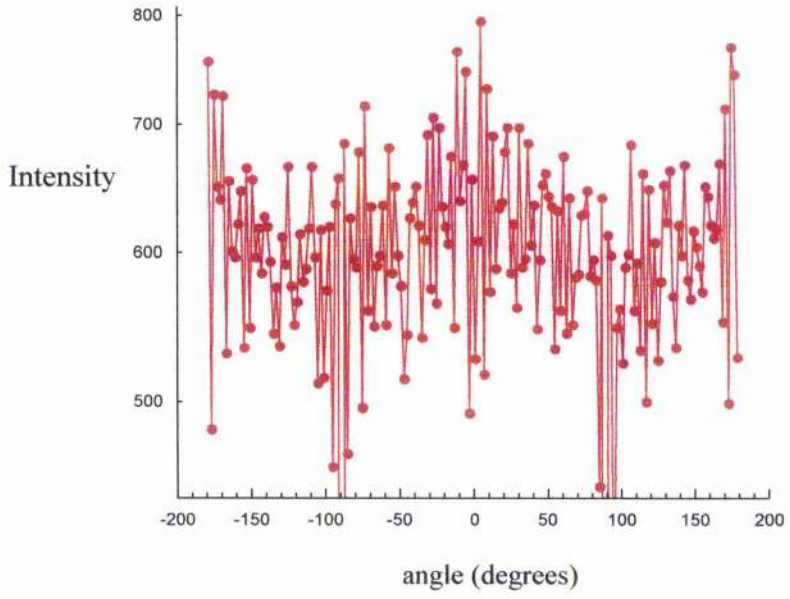

Figure 5.10. The scattering intensity versus the angle of sweep around the detector, where zero degrees is represented by a black straight line as shown in figure 5.9.

The highest field available was 14.5 kOe, which was around the sample's saturation field (see figure 5.7a). Magnetic scattering can then be observed by **subtracting** the randomised (isotropic) state from the magnetised state at B=14.5kOe. (Ideally, the demagnetised state should be subtracted from the magnetic state, but it was not possible to demagnetise each disk. Instead the disks were re-shuffled and stacked together to produce a randomised isotropic state.) Figure 5.11a, is a 2D

multi-detector plot of anisotropic magnetic scattering with a figure eight-like distribution at 14.5kOe in D11. Another example of magnetic scattering in the isotropic media was measured at D22 with the field set to 11.8kOe.

If we plot the scattering intensity against the angle of sweep around the detector, then a $\sin^2\theta$ trace (which is based on $1-\left(\hat{M}\cdot\hat{Q}\right)^2$, from equation 5.19) shows that there is magnetic scattering present, as illustrated underneath the 2D detector plots in figure 5.11.

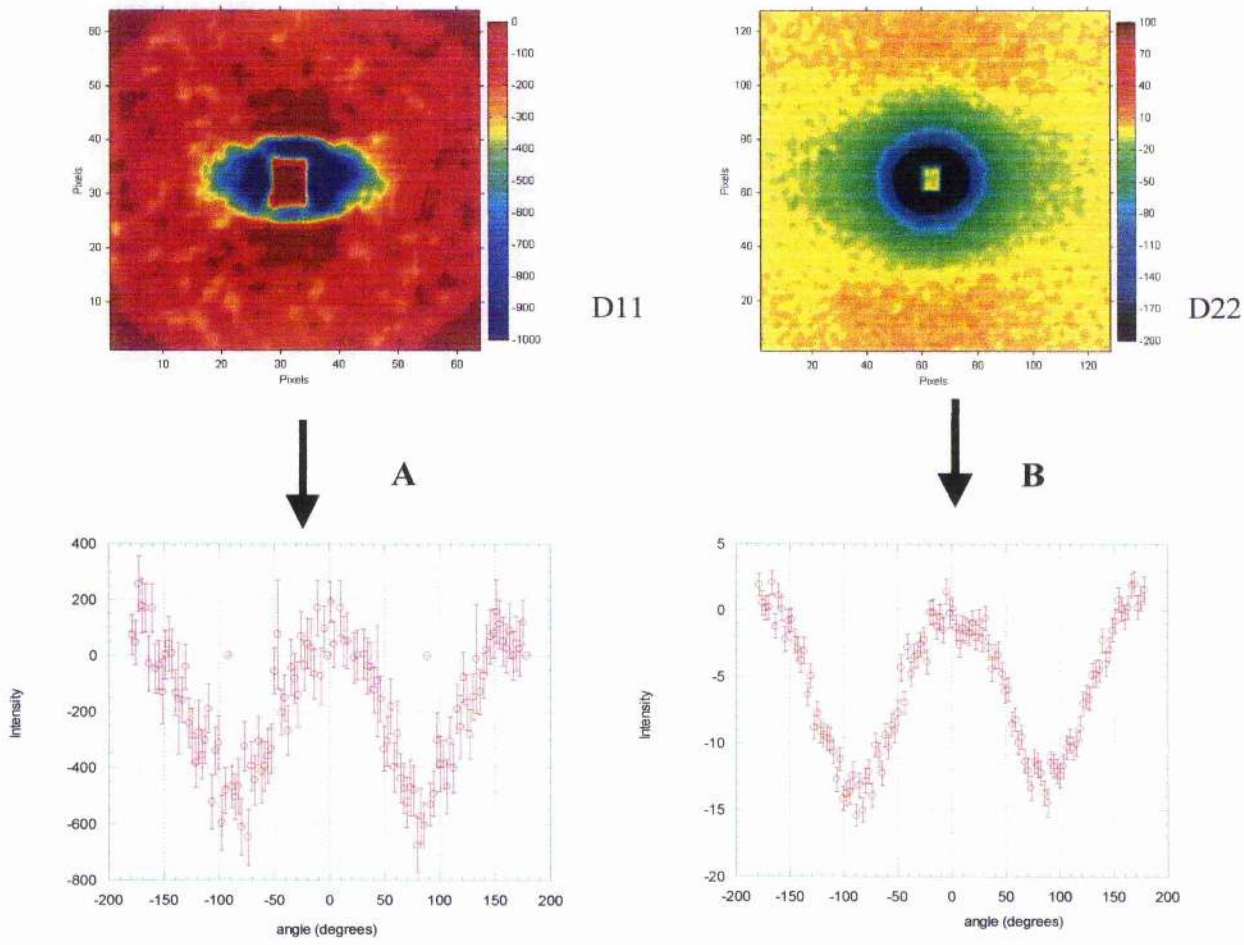

Figure 5.11. 2D detector plots of the isotropic media. D11 plot at high Q (at 14.5kOe) with evidence of magnetic scattering, underneath. D22 plot at middle Q (at 11.8kOe) with a $\sin^2\theta$ trace, underneath.

The total nuclear scattering for all q-ranges at 14.5 kOe is shown in figure 5.12. The magnetic signal is a level of 0.1% to 1% of the total scattering.

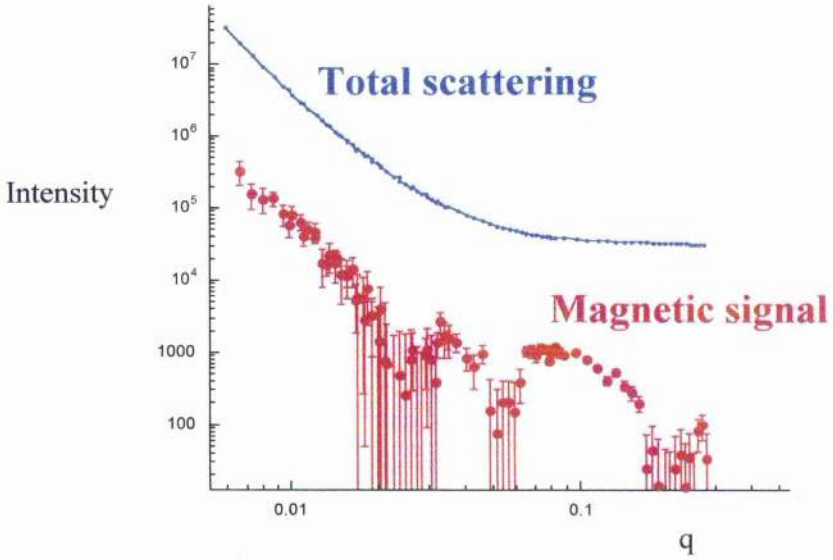

Figure 5.12. A comparison of the magnetic and total scattering at 14.5kOe.

A note to the reader. In the GRASP package [7], there are options in which you can present and/or analyse the data:

1. The **sine-squared amplitude**. This measures the difference in Q scattering parallel and perpendicular to the field direction. This is defined as $FT\{x, m_y(x)\}$-$FT\{y, m_x(y)\}$, which is the difference between the Fourier transform (FT) of the moment's x-component, $m_y(x)$ and the moment's y-component, $m_x(y)$ [10]. The expression $FT\{x, m_y(x)\}$-$FT\{y, m_x(y)\}$ is derived from equation (5.10) where $m_x(y)=m\cos\theta$, $m_y(x)=m\sin\theta$ and θ is the orientation of the magnetisation relative to the x-direction. The sine-squared amplitude plot will have the same angular dependence as the magnetic scattering cross-section; however, to extract the absolute cross-section, one needs to introduce factors such as the sample transmission, detector efficiency, the neutron's wavelength and the incident neutron flux.

2. The **scattering intensity with respect to the angle around the detector** (I vs θ). This is based on $1-\left(\hat{M}\cdot\hat{Q}\right)^2$, which shows that there is magnetic scattering taking place in the experiment.
3. The **phase of the sine-squared relative to the x-direction**. The phase of the scattering depends on the sign of $FT\{x,m_y(x)\}$-$FT\{y,m_x(y)\}$ [10]. If the value $FT\{x,m_y(x)\}$ is greater than $FT\{y,m_x(y)\}$ in one q-range, and vice versa in another q-range, then the phase of the scattering is changed by ninety degrees. An example of this is shown in figure 5.13, one with the phase taken into consideration; the other without. Here, we have to accept that the difference in Q scattering, $FT\{x,my(x)\}$-$FT\{y,mx(y)\}$, can change sign [10].

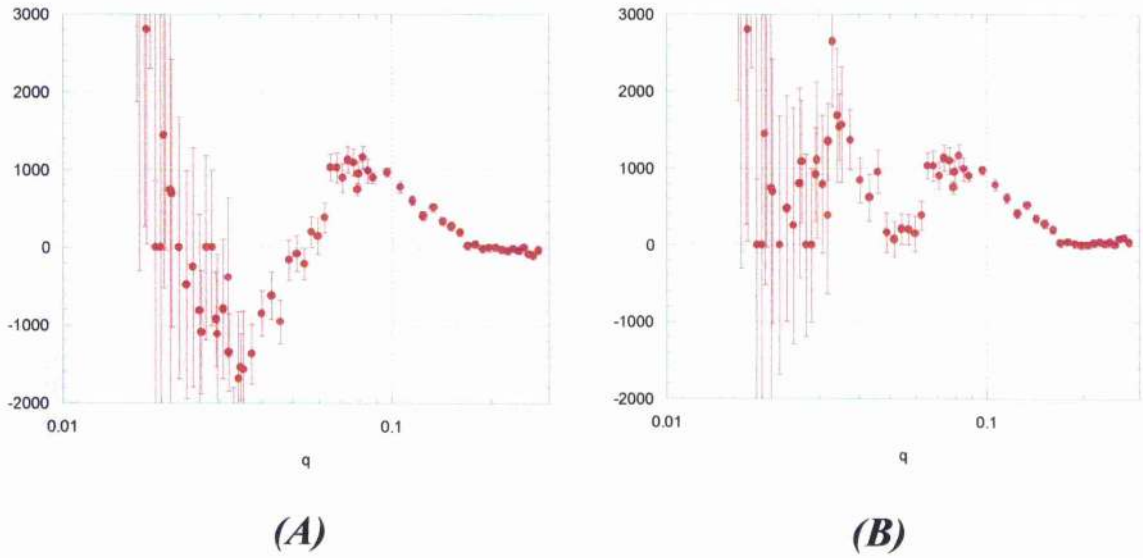

Figure 5.13. Plots of the sine-squared amplitude where (A) the phase is considered and (B) where the phase is ignored. In order to obtain reasonable signal to noise, it is necessary to carry out longer runs at lower q than higher q.

Figure 5.14 illustrates 2D-detector plots at 14.5kOe and 4.5kOe, each at a different q-range. A $\sin^2\theta$ dependence shows that there is a ninety degree phase shift between the two. This may suggest that the moments

at 4.5 kOe are not saturated and so transverse components (moments whose component are along the field direction) exist [10].

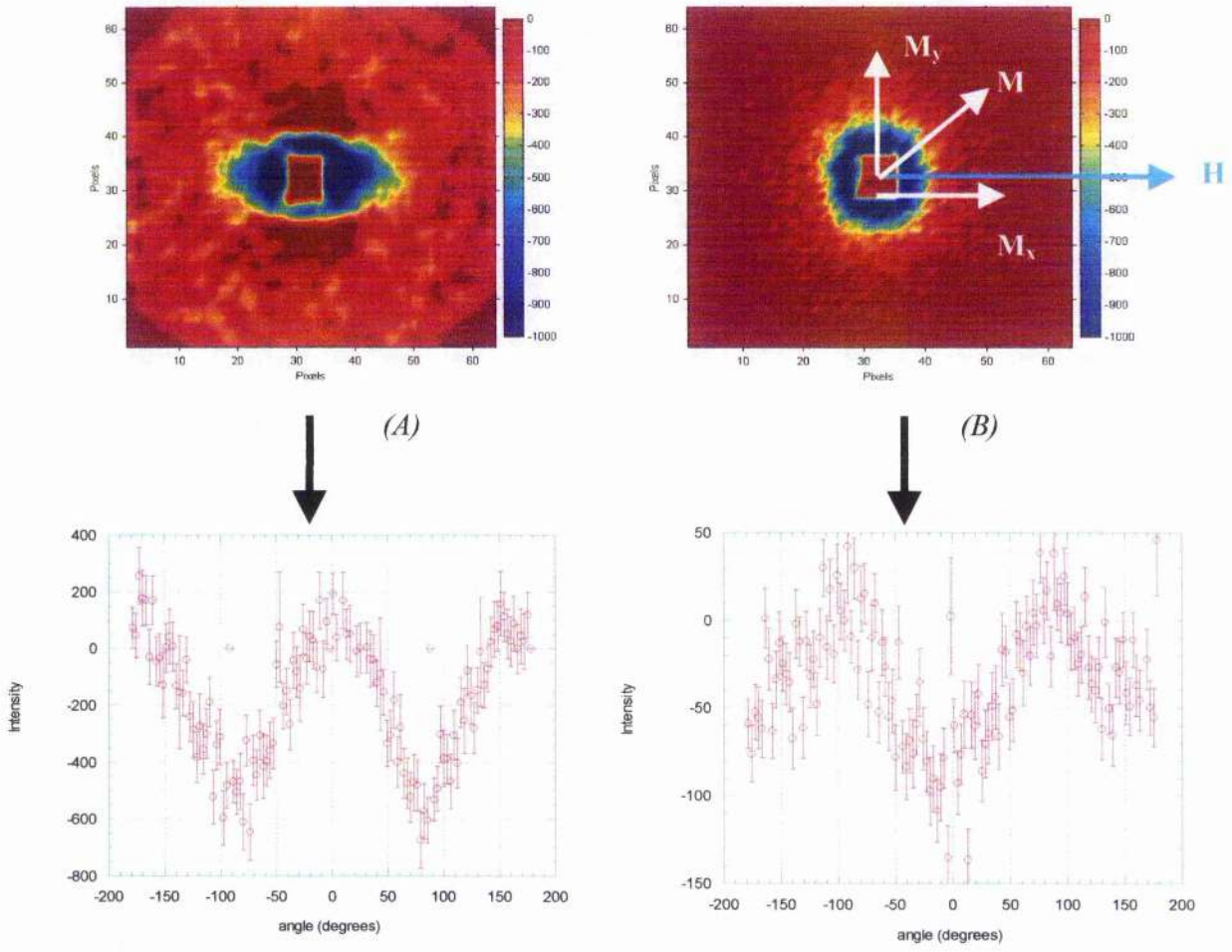

Figure 5.14. 2D detector plot and sine squared dependence on the magnetic scattering at (A) 14.5kOe and (B) 4.5kOe.

5.5.2.1. SANS model and results for the isotropic media

The reader should note that the author's contribution to this project involved measuring the SANS data and assembling it in a meaningful form so that Professor Stephen Lee could analyse it. Throughout this section, Professor Lee is often referenced as [10], which means that Prof. Lee provided the modelling, the physics and the fit to the data.

Since the cobalt grain structure is approximately close packed (locally, but with no long range order) it was not possible to fit the

Fourier transform of such structure to the sine-squared amplitude spectra as it involves complex Monte-Carlo calculations [10]. Instead, the model was based on a single elliptical grain composed of a hard core and a soft shell [10]. A Perkus-Yevik model [8], as discussed briefly in 5.2.4, was used to model the interference between the ellipsoidal grains; that is, the positional relationship between the neighbouring grains. Figure 5.15 illustrates features that were used to determine the grain size of the recording media at different fields.

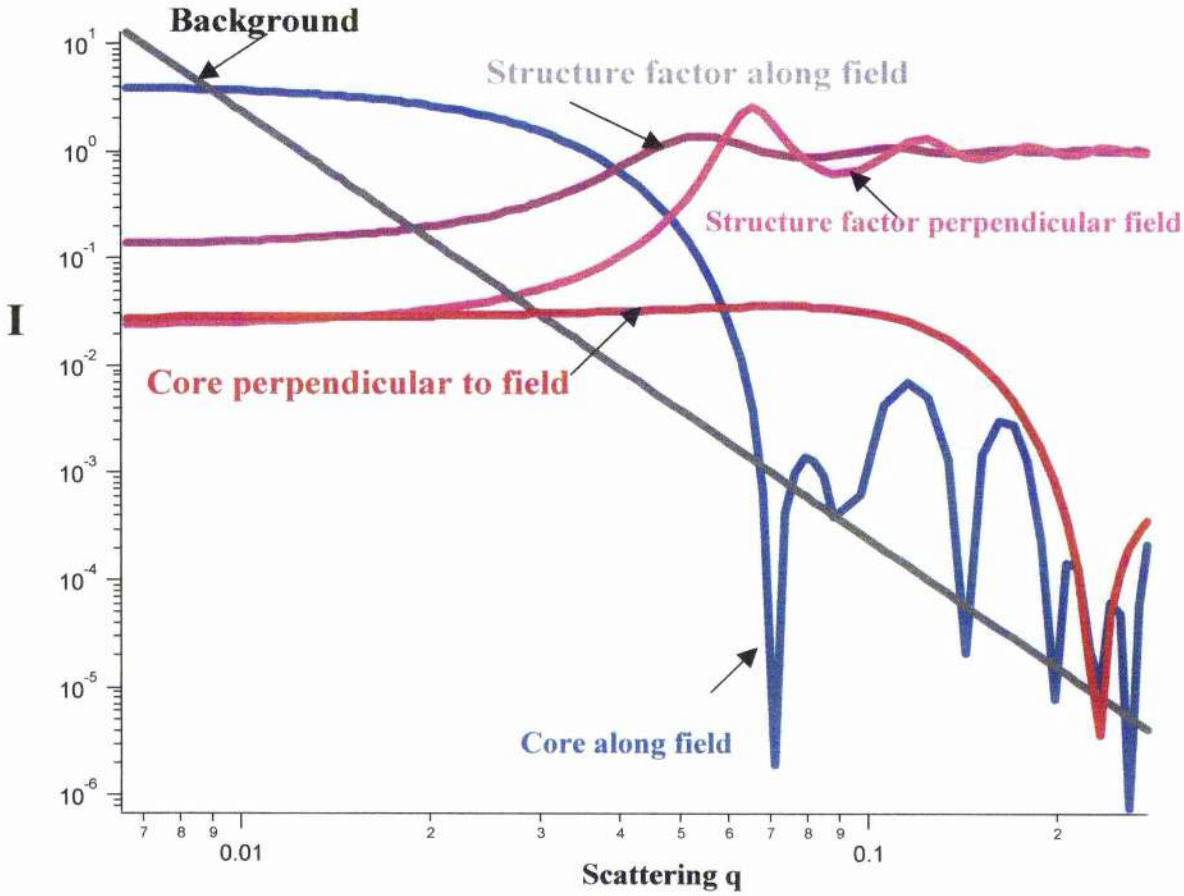

Figure 5.15. Models that were used on the isotropic media [10].

The model is composed of a background of the form, $\frac{A}{q^n}$, which was attributed to the NiP layer in the background sample, as shown in figure 5.16.

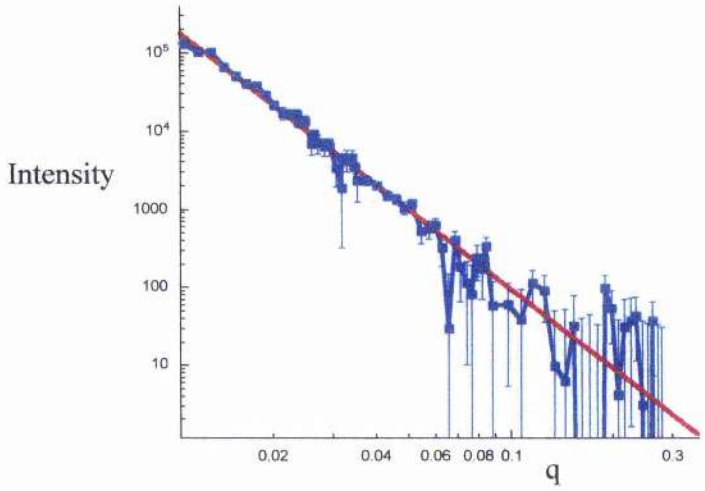

Figure 5.16. A fit to the scattering intensity data on the NiP substrate. This arises from a large scale disorder of soft ferromagnetism in zero field [10].

The power law exponent n represents the spatial symmetry of the microstructure in a sample: $n = 3$ for the case of particles which have a rod like shape elongated in one direction and $n = 4$ for spherical particles [12]. For the background sample, $n = 4$ [10]. With reference to figure 5.15, the structure factor $S(Q)$ is included along and perpendicular to the field direction and the form factor $F(Q)$, again along and normal to the field direction [10].

As a result, the sine squared amplitude is proportional to $F^2(Q,\Delta\rho_1,\Delta\rho_2)S(Q)+\frac{A}{q^n}$, where $\Delta\rho_1=\rho_1-\rho_3$, $\Delta\rho_2=\rho_2-\rho_3$ and ρ_1, ρ_2, ρ_3 is the scattering density (which is equivalent to $\frac{\sum n_i b_i}{V}$ with n the number of atoms, b is the scattering length and V is the volume) [10].

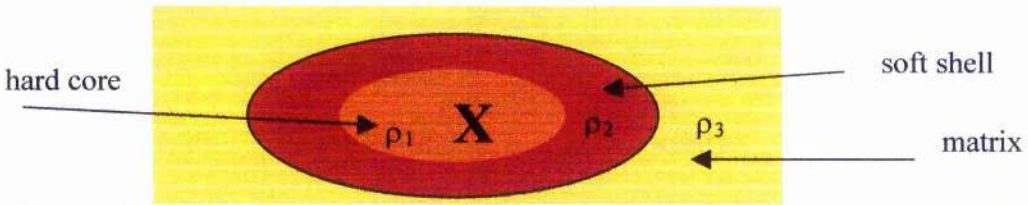

Figure 5.17. The layout of an elliptical granule with varying scattering densities.

The ellipsoidal grain lies within the film surface and it is assumed that the field is applied along the grain's major axis. The incident neutron beam, labelled X in figure 5.17, is applied normal to the surface of the film. The plots below are those of a fit to the magnetic scattering of the isotropic media at 14.5kOe.

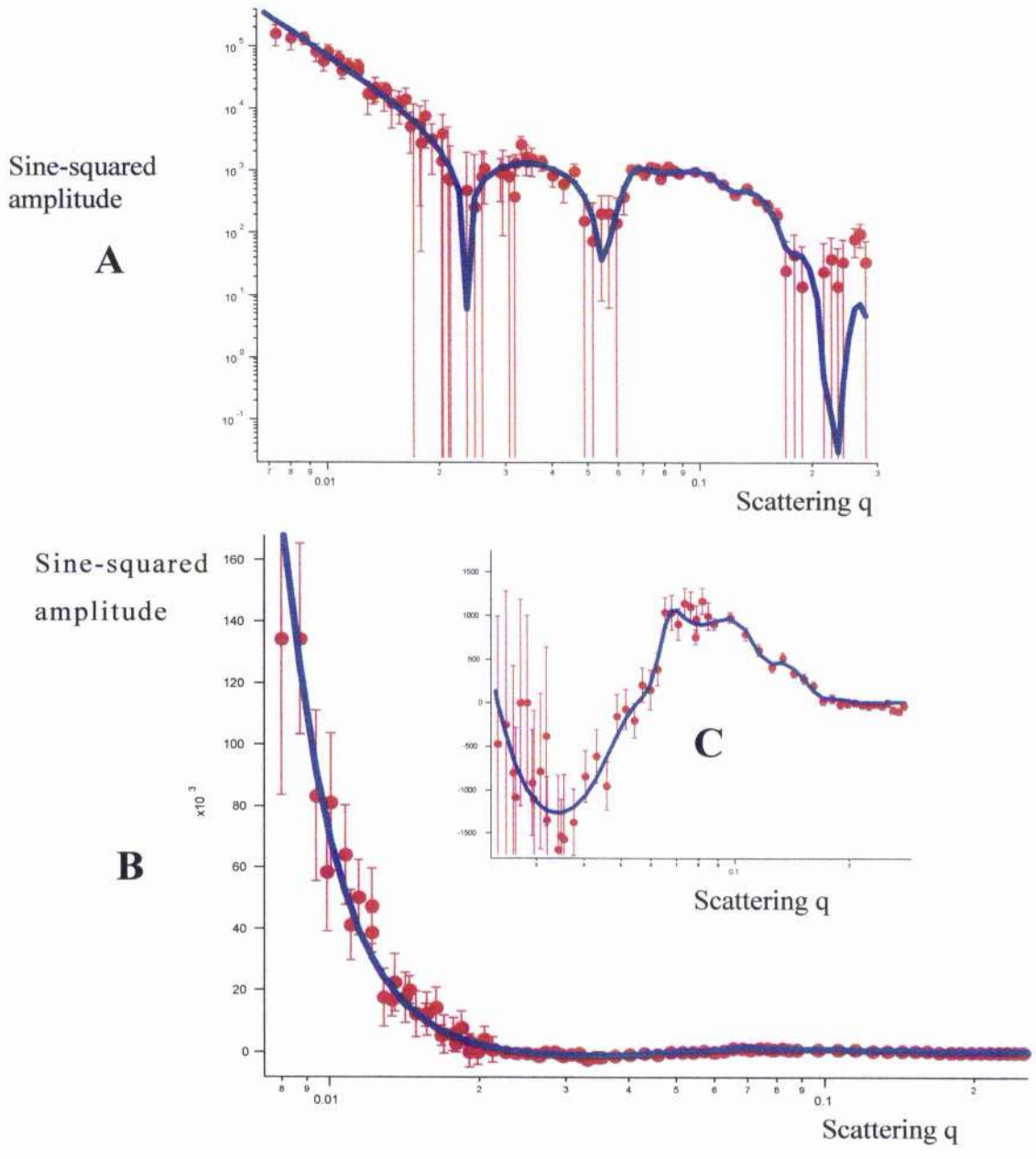

Figure 5.18. (A) is a log-log plot of the sine-squared amplitude, (B) is log-linear and the inset (C) is linear-linear plot with fits to the data [10].

The sine-squared amplitude of the isotropic media, at 4.5kOe is slightly different from the 14.5kOe spectra, as shown in figure 5.19. The blue line is a fit to the data using the same model for the 14.5kOe spectra.

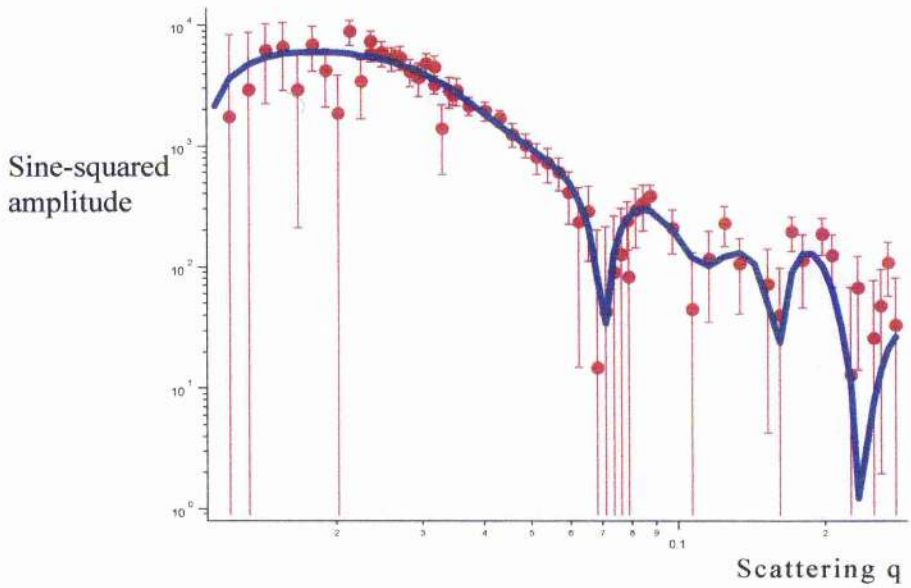

Figure 5.19. Log-log plot of the sine-squared amplitude at different q ranges for B=4.5kOe [10].

Table 5.4 presents results of the fit to the data for 14.5kOe and 4.5kOe. The terms $2r_y^{in}$ and $2r_x^{in}$ in the ellipsoidal parameters column represent the cobalt core's dimensions. The $2r_y^{out}$ and $2r_x^{out}$ terms represent the dimensions of the shell, as shown in figure 5.20. d_x and d_y represent the distance between the centres of the cores along the x and y-direction, respectively.

Although the single grain model was used in the fit to the sine-squared amplitude at 4.5kOe and 14.5 kOe, the angles of the chromium and cobalt moment relative to the field direction, as shown in table 5.4, is assumed to be the same for each grain in the recording media sample. Thus, these angles are averages for an ensemble of grains. The single domain model is reasonable at fields close to saturation.

Ellipsiod's parameters	14.5 kOe	4.5 kOe
$2r_y^{in}$	38 Å	42 Å
$2r_x^{in}$	68 Å	64 Å
$2r_y^{out}$	88 Å	86 Å
$2r_x^{out}$	150 Å	128 Å
d_y	104 Å	105 Å
d_x	115 Å	119 Å
The angle between the cobalt moment and the field, *H* (degrees)	52	69
The angle between the moment in the chromium shell and the field (degrees)	93	27

Table 5.4. Parameters determined from the fit to the sine-squared amplitude [10].

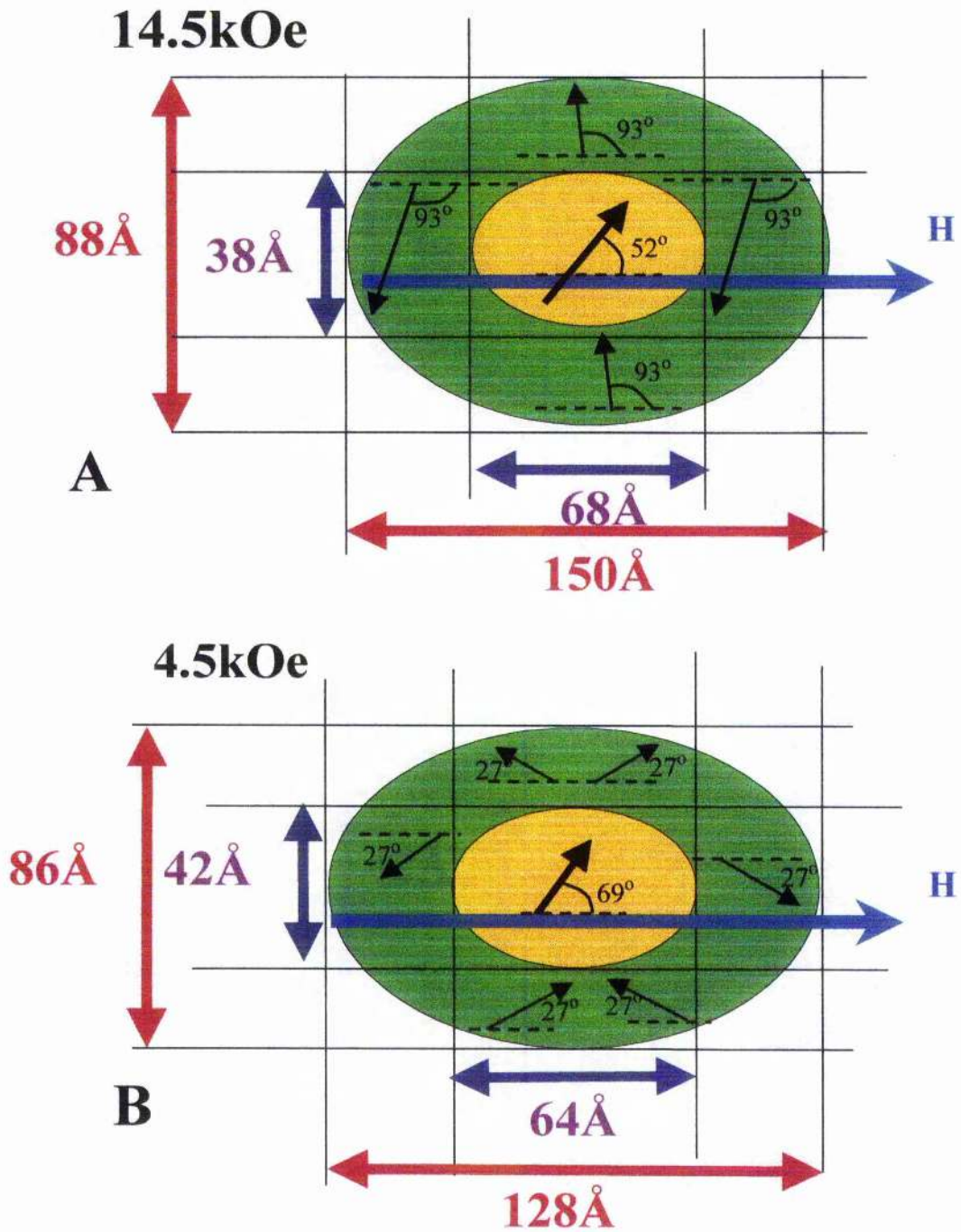

Figure 5.20. A schematic representation of an ellipsoidal grain at 14.5kOe and 4.5kOe,with dimensions of the core and shell. The directions of the magnetic moment in the cobalt core (yellow) and the weakly magnetic shell (green) are also shown. The blue arrow represents the direction of the applied field.

The size of the core and chromium shell does not seem to change much from 4.5 kOe to 14.5kOe; similarly, the distance between the centres of the neighbouring grains are almost the same at both fields.

With reference to figure 5.20a, the direction of the moment in the chromium shell and the cobalt core is 93 degrees and 52 degrees to the field direction, respectively. From the 4.5kOe analysis, the direction of the moment in the chromium shell and cobalt core is 27 and 69 degrees to the field direction, respectively. From micromagnetic simulations [10], even at 14.5kOe the directions of the moments in the cobalt cores are not aligned along the field. In fact, they are less than 45 degrees to the field direction, as shown in figure 5.21. From the SANS analysis, the chromium moments are not aligned along the field. The reason for this may be due to the core moments being responsible for the orientation of the moments in the chromium shell. As the field is increased from 4.5kOe to 14.5kOe, there is a large influence from the cobalt core on the chromium moments, therefore the moments follow the field line generated by the core and are surprisingly normal to the direction of the applied field rather than along it [10].

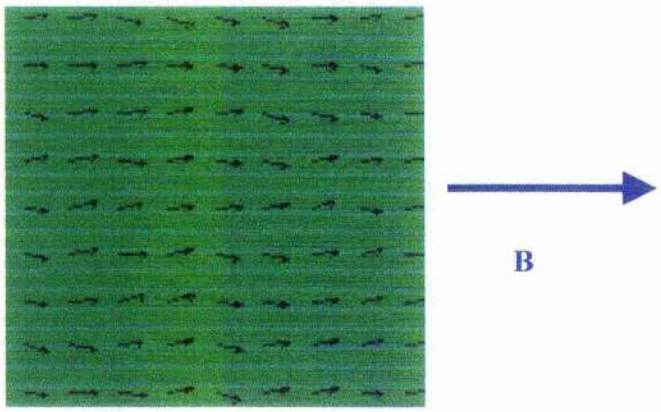

Figure 5.21. Micromagnetic simulation of core moments (represented by arrows) at a field of 14.5kOe [10].

5.5.3. SANS of anisotropic media

Figure 5.22 illustrates magnetic scattering on D11 (at 10.8 kOe) and D22 (11.8 kOe). With reference to figure 5.7b, both fields were above

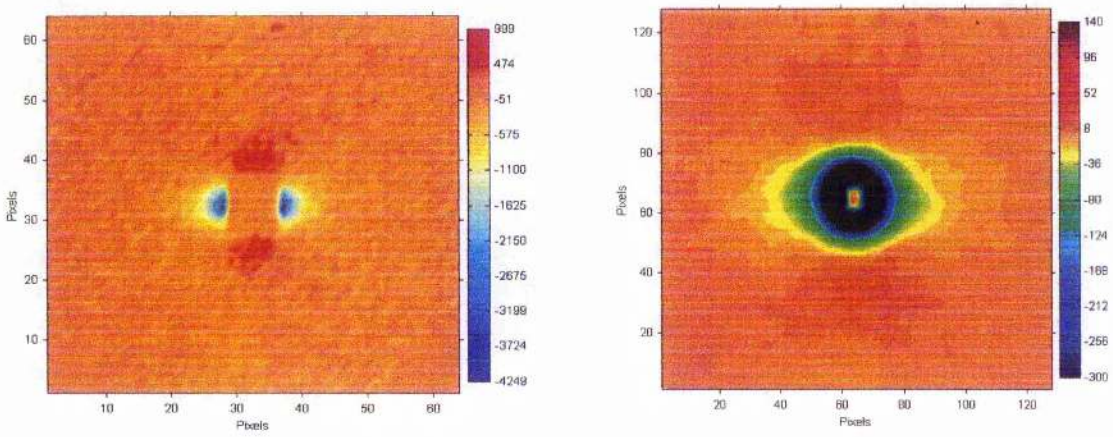

Figure 5.22. High Q magnetic scattering at 10.8kOe (A) and middle Q at 11.8 kOe (B).

the saturation field, which is approximately 9kOe.

The magnetic scattering is around 2.5 to 15% of the total scattering, as shown in figure 5.23.

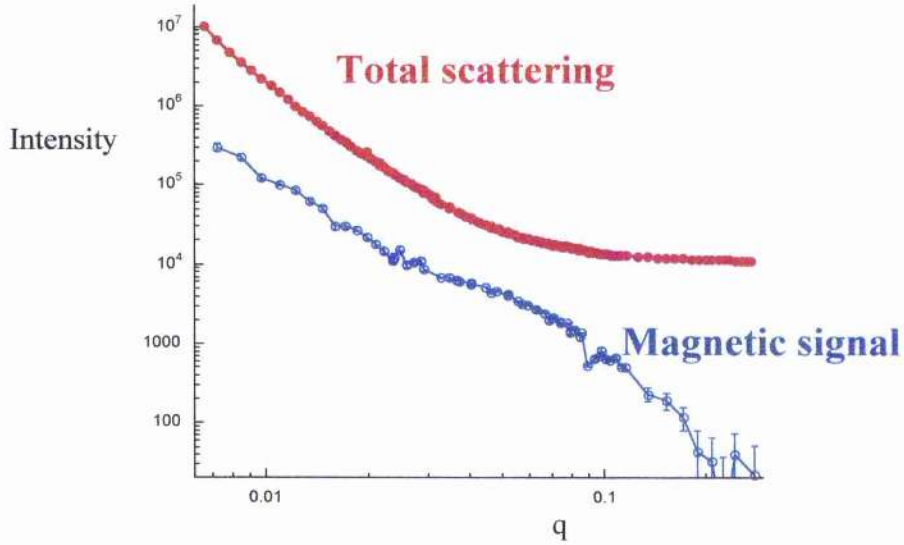

Figure 5.23. Total and magnetic scattering of x341.

Work is still being carried out on the anisotropic media. Since the grain size of this type of media is larger than that of x1646 (isotropic media), then it is necessary to push measurements to a q-range lower than that already measured. There is an indication of a very short length scale, which is most likely to be due to the non-magnetic shell in the saturated state, as shown in figure 5.24 [10].

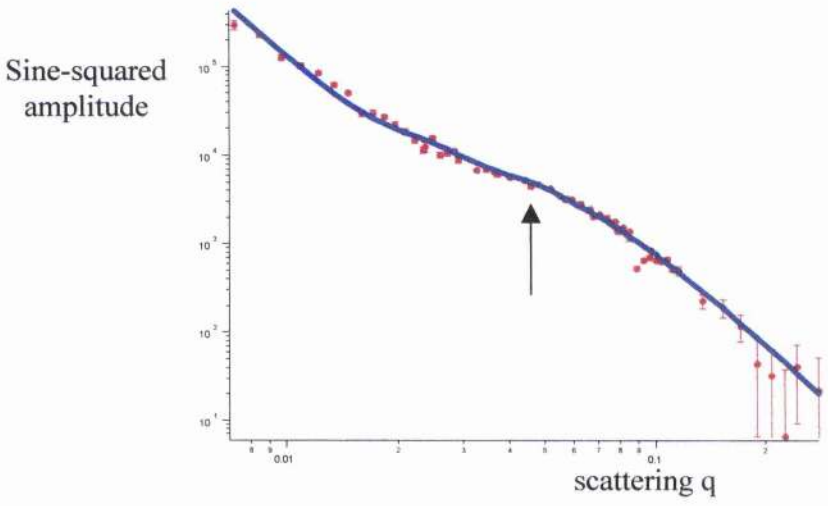

Figure 5.24. A fit to the sine-squared amplitude data for x341. The arrow indicates the presence of a non-magnetic shell in the saturated state.

5.6. Conclusions

Section 5.5.1. has shown that magnetic scattering is possible by removing a large fraction of the aluminium substrates; repeating runs at very high flux instruments on D11 and D22 at the ILL; subtraction of the isotropic nuclear scattering by magnetically saturating the film and then subtract the randomised state from the magnetised state, and the use of a large number of multilayers.

There are limitations to the model: there is the assumption of concentric ellipses as an approximation, which will introduce aberrations in fits. The results concerning the cores seem nonetheless robust over a range of fields, as shown in table 5.4. For future work, it is necessary to saturate the isotropic media, x1646 completely, preferably above 30kOe, in order to uniquely determine one element of

the function $FT\{x,m_y(x)\}$-$FT\{y,m_x(y)\}$ and also determine the direction of the moments in the hard core and soft shell. Further work is required in analysing the remanent state of the isotropic and anisotropic media.

5.7. References

[1] G.L. Squires, *Introduction to the Theory of Thermal Neutron Scattering*, Dover Publications, Inc, New York, 1996

[2] J.A. Dann, Ph.D thesis, St. Andrews, 2000

[3] J.R. Stewart, Ph.D thesis, St. Andrews, 1999

[4] R.J. Newport, B.D. Rainford, R. Cywinski, *Neutron Scattering at a Pulsed Source*, Adam Hilger, 1988

[5] D.J. Cebula, S.W. Charles, J. Popplewell, Colloid & Polymer Sci., 259 (1981) 395

[6] G. Kostorz, Treatise on Materials Science and Technology, vol 15, Academic Press, New York, 1979

[7] www.ill.fr

[8] N.W. Ashcroft, J. Lekner., Phys. Rev., 145 (1966) 83

[9] R. Heenan, *private communications*, 2001

[10] S.L.Lee, *private communications*, 2002

[11] T.Thomson, *private communications*, 2001

[12] J. Suzuki, K. Takei, Y. Maeda, Y. Morii, J. Magn. Magn. Mater., 184 (1998) 116

Chapter 6

Cobalt nanoclusters

6.1 Introduction

Magnetic nanoparticles are a subject of intensive research due to their unique magnetic properties, which make them of great interest both from theoretical and technical point of view, as discussed in chapter one [1,2].

This chapter presents FMR and VSM measurements of the magnetic properties of Co_xAg_{1-x} granular thin films with a concentration range $9 < x < 71$ at.%. The aim here is to compare and contrast previous measurements carried out by Pogorelov et al [3] on the granular systems which involved films with a concentration range $18 < x < 81$ at.%. There are three more samples in this chapter that were not previously measured on low field FMR and VSM whose concentration was below 18 at.%. There are also discussions on high field FMR, which aims to provide explanations to any changes in the sample's signal with that at lower frequencies.

6.2 Preparation

The films were prepared at the Institute of Magnetism, in Kiev, in the Ukraine. The Co_xAg_{1-x} films were deposited by electron beam co-evaporation of cobalt and silver atoms onto a glass substrate, from two independent sources, providing an initial film with gradually varying compositions along a total length of 450mm, figure 6.1 [3]. A whole set of separate film samples with cobalt volumetric factor f, ranging from 0.06 to 0.62 (equivalent to x ranging from 9 to 71 at.%), was subsequently obtained. The deposition rates of each component were controlled using calibrated quartz monitors.

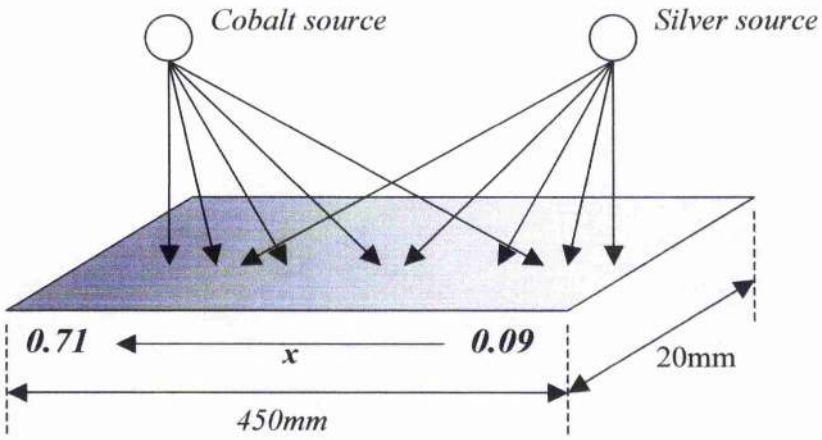

Figure 6.1. Deposition of cobalt and silver onto a glass substrate with x denoting the ferromagnetic concentration in at.%.

The volumetric packing fraction, f, is determined from the relation [3] $f = \frac{xV_{cobalt}}{xV_{cobalt} + (1-x)V_{silver}}$, where V_{cobalt} = 6.67 moles/cc, V_{silver} = 10.27 moles/cc [4] and x is the concentration in at.%, as shown in table 6.1.

As the volumetric filling factor grows, more granules aggregate into worm-like clusters. If the distance between such clusters gets smaller than their size (even without direct contact between them), they behave as a ferromagnetic continuum with respect to the dipolar forces; this is the **magnetic percolation point**. This is denoted as f_p and x_p for the volume fraction and in atomic percent, respectively. The samples in this chapter have a percolation point around 28 at.% cobalt; that is, $f_p = 0.20$ and $x_p = 0.28$ [5]. Films with $x > x_p$ have an in-plane uniaxial anisotropy, which is induced due to oblique deposition. The easy axis was formed perpendicular to an imaginary line connecting the two evaporation sources [5].

Sample	Cobalt concentration (at.%)	Volumetric packing fraction	Film thickness (nm)	
1.7	71	0.62	270	
2.7	64	0.54	350	$f > f_p$, $x > x_p$
3.9	54	0.43	370	
4.7	45	0.35	390	
5.8	34	0.25	420	
6.7	25	0.18	460	$f < f_p$, $x < x_p$
7.7	17	0.12	500	
8.7	11	0.07	510	
9.3	9	0.06	520	

Table 6.1. Cobalt clusters with increasing film thickness with respect to cobalt concentration [5]. Samples with cobalt concentrations above 28 at.% have an induced uniaxial anisotropy. The dotted line separates the volume fractions of the samples which are either greater or less than the percolation point, f_p.

6.3 Vibrating sample magnetometry

Magnetometry measurements were carried out at 10K, 100K and room temperature on a 12 Tesla Oxford Instruments vibrating sample magnetometer in St. Andrews, as shown below.

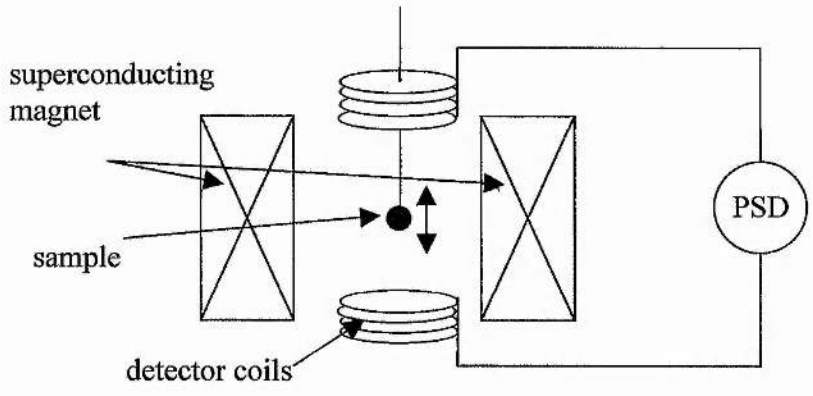

Figure 6.2 Schematic layout of the 12T vibrating sample magnetometer.

The sample is vibrated at a frequency of 66Hz along the vertical axis of the uniform field with amplitude of 1.5mm. This frequency avoids interference from the mains supply noise and larger frequencies could result in unwanted eddy currents. The motion of the sample induces an emf in two detector coils which is proportional to the rate of change of magnetic flux through them.

Typical M-H loops at different temperatures of the nanocluster samples are shown in figures 6.3a to 6.3c. Three examples are shown, one with the cobalt volume fraction, above, below and around the percolation point.

A

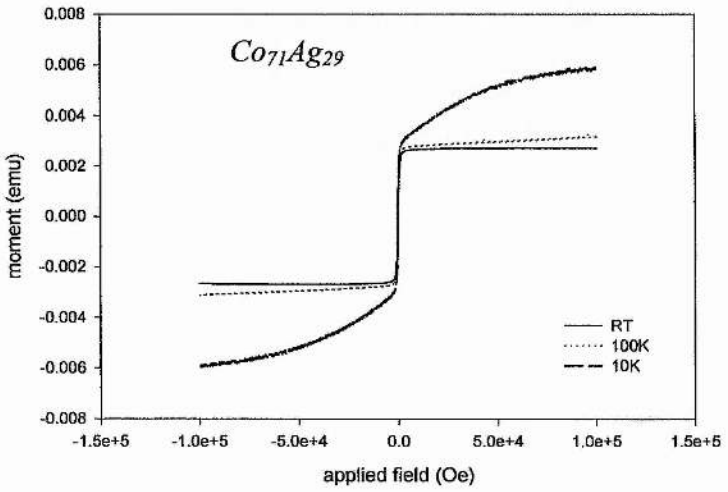

B

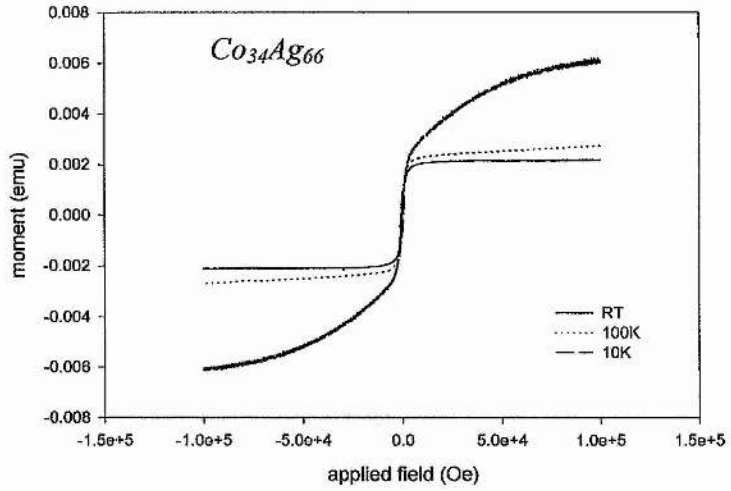

C

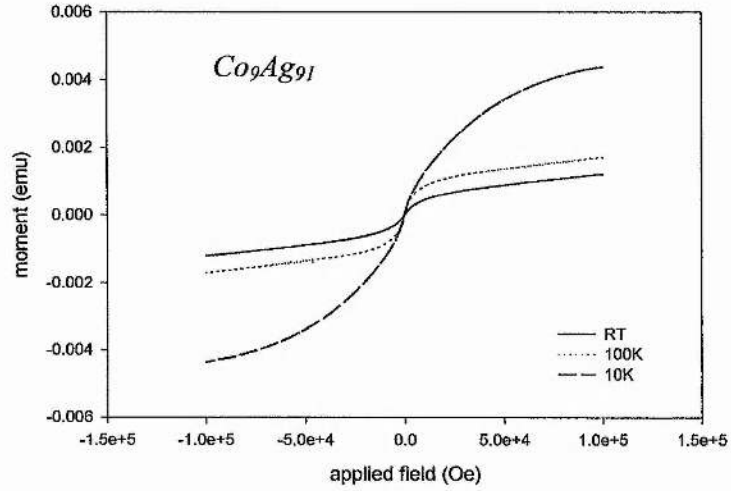

Figure 6.3. M-H loops of cobalt nanoclusters at three different temperatures. The films shown above are (A) $Co_{71}Ag_{29}$, (B) $Co_{34}Ag_{66}$ and (C) Co_9Ag_{91}.

These experimental magnetisation curves cannot be fitted using the classical Langevin law [2,6]:

$$M(H) = M_S\left[\coth\left(\frac{M_S vH}{kT}\right) - \frac{kT}{M_S vH}\right] \qquad (6.1)$$

The simulation of the Langevin function at 10, 100 and 300K is shown in figure 6.4. The volume of the grain is 10^{-22} cm^3, thus for spherical grains, the diameter of the grain is 0.6nm. From the simulation, at 10K (green line), the magnetisation saturates faster than at room temperature (red line); however, from the experiment, the magnetisation at room temperature saturates quicker than at 10K.

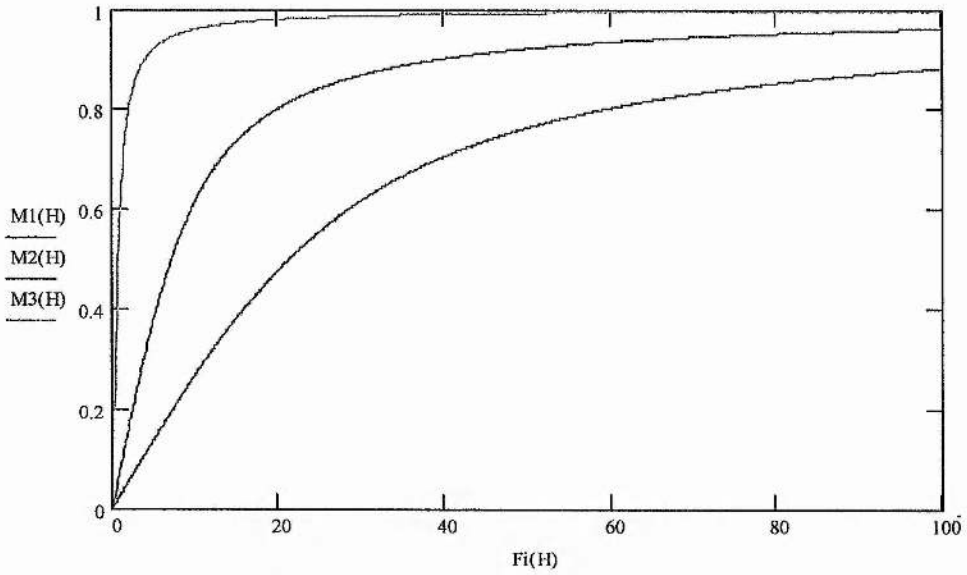

Figure 6.4. A mathcad simulation of the Langevin function (normalised), equation 6.1, for T=10K (green line), T=100K (blue line) and T=300K (red line).

With reference to figure 6.3, when the measurement temperature is increased, the magnetisation at a defined field falls down due to the thermal fluctuations phenomena. This is typical of superparamagnetic behaviour, with slow saturation and strong temperature dependence.

Films with higher cobalt concentrations show a ferromagnetic component, figure 6.3a, which saturates at a much lower field and is almost temperature independent (compare the curves at 100K and 300K in figures 6.3a and 6.3b). Previous work on the VSM/SQUID of cobalt nanoclusters [3] suggest that this feature agrees with the formation of a magnetically coupled network of large ferromagnetic domains at x larger than the magnetic percolation concentration (x_p). Pogorelov et al [3] fitted the M(H,T) data for $f = 0.25$ using the relation:

$$M = M_S \int L\left(\frac{M_s v H_i}{kT}\right) P(v) dv \qquad (6.2)$$

where $P(v)$ is the volume distribution, expressed in the form

$$P(v) = q\delta(v - v_1) + (1-q)\delta(v - v_2) \qquad (6.3)$$

with v_1 and v_2 representing the volume of the two grains. H_i is the internal field: for a spherical granule with the field applied within the film plane, H_i takes the form $H_i = H - \frac{4\pi}{3}(1-f)M$.

From their analysis on $f = 0.18$, they deduced that the sample is dominated by clusters with diameters of 3.6nm.

6.4 Ferromagnetic resonance

This section looks at two frequencies: 9.5GHz and 92GHz FMR.

6.4.1. 9.5GHz measurements

9.5 GHz FMR on cobalt nanoclusters was carried out on a 16kOe Bruker Instruments ESR spectrometer, at room temperature, in the School of Chemistry, in St. Andrews. Angle rotation measurements from 0 to 360 degrees were possible; however, the precision was as low as 3 to 5 degrees. A quartz sample holder was used for this type of measurement. Ref [7] provides further information on the 9.5GHz spectrometer.

Films with compositions above the percolation point:

It was observed that films that have less than 17 at.% cobalt ($f = 0.12$) have the same resonant field at different angles of orientation. As the concentration of cobalt increases from 17 at.% cobalt, there is a change in the resonant field between the in-plane and out-of-plane configuration, as shown in figure 6.5.

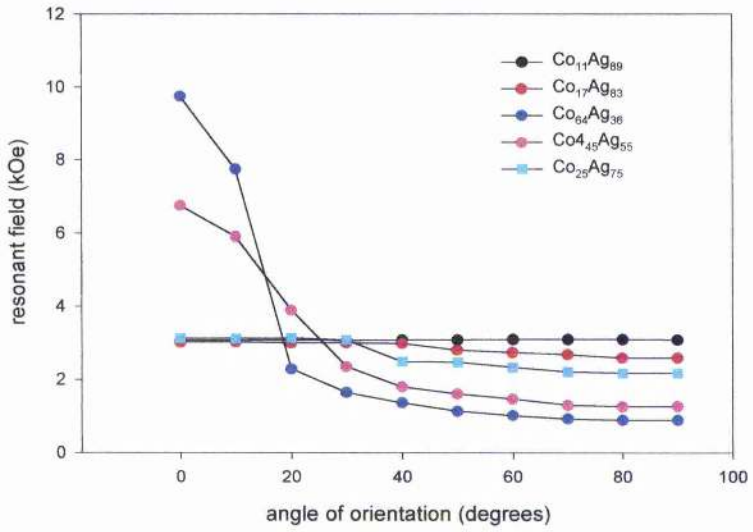

Figure 6.5. Angle rotation FMR at 9.5GHz of some granular thin films. The plots are those of the uniform mode only. Zero degrees represents the field normal to the film surface and ninety degrees is in-plane FMR. For in-plane measurements, the external field was applied along the easy-axis.

Figure 6.6 is an FMR spectrum of 9 at.% cobalt.

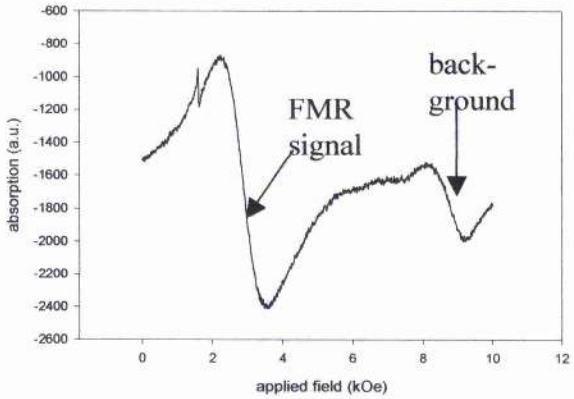

Figure 6.6. 9 at.% cobalt measured at 9.5GHz in the perpendicular configuration. The extra higher field signal is background from the cavity and quartz tube.

The angular dependence resonant field, $H_r(\theta_H)$, for a magnetically undersaturated thin film [3] for volume fractions less than the percolation point is given by:

$$H_r(\theta_H) = \frac{\omega}{\gamma}\left[1 + \frac{2\pi M_S^2 f\bar{v}\left(3\cos^2\theta - 1\right)}{kT}\right] \qquad (6.4)$$

where θ_H is the field angle relative to the film normal, $\bar{v}$ is the mean grain volume, θ is the magnetisation's equilibrium angle and f is the volumetric filling factor. The granules are assumed to be spherical and so the equation $d = \left(\frac{6v}{\pi}\right)^{1/3}$ is used to determine the granule diameter.

From Mathcad analysis, table 6.2 presents values to the sample's g-factor and mean grain diameter:

Cobalt content (at.%)	g-factor	Grain diameter (Angstroms)
9	2.28	4.6
11	2.23	5.6
17	2.28	11.0

Table 6.2. Values of the sample's g-factor and grain diameter from angle rotation measurements at 9.5GHz with the use of equation (6.4)

The g-factor is in good agreement to that of bulk cobalt: 2.20 [8]. It is also observed that the grain diameter deduced from FMR increases with composition. The analysis was not straightforward for 25 at.%. This may be due to the inaccuracy of the sample's position relative to the field direction: as mentioned previously, there may a three or five degree error, consequently, the resonant field may be out by a few tens of oersteds; therefore, it was difficult to compare the FMR result with that previously measured by SQUID.

Films with compositions above the percolation point:

At angles closer to and at the film normal, granular thin films with cobalt composition greater than 34 at.% ($f = 0.25$) have resonant fields that split into two or more peaks.

Figure 6.7, shows a typical X-band FMR spectrum of 71 at.% cobalt ($f = 0.62$).

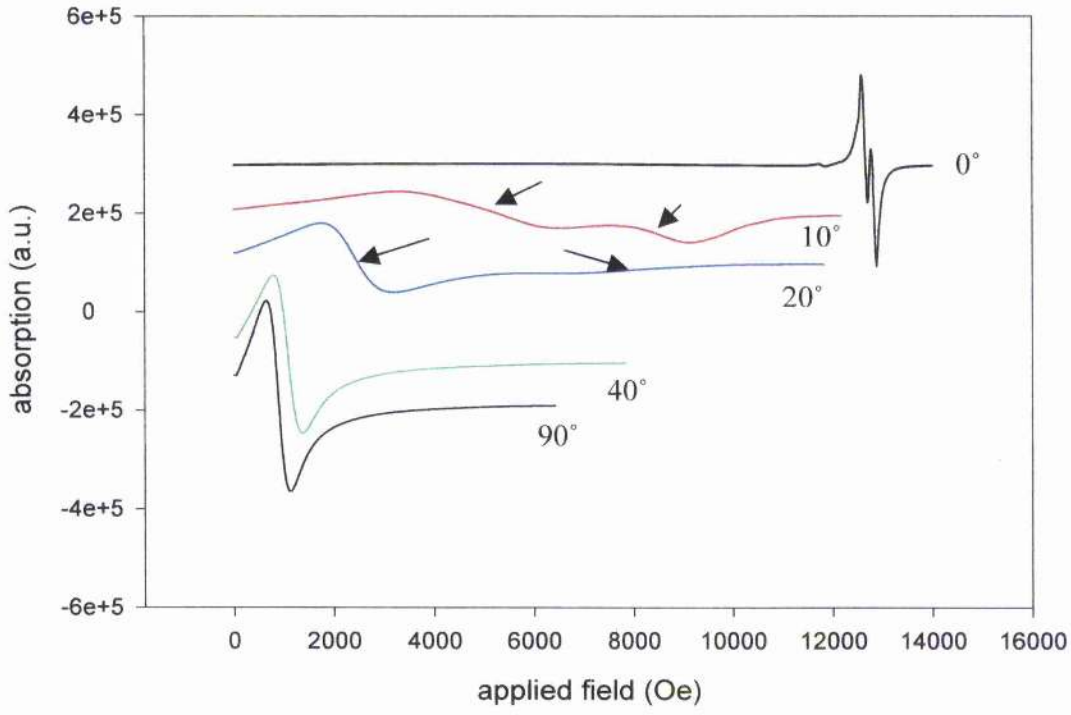

Figure 6.7. FMR spectra at 9.5GHz on 71at.% cobalt. The angles at the side of the spectra represent the direction of the field relative to the film normal. FMR spectra measured at ten degrees has a higher field signal at 8kOe, which is not attributed to background.

With reference to figure 6.7, for 71 at.% cobalt, there exists only one FMR signal when the field is applied at angles between thirty and ninety degrees to the film normal. However, at ten and twenty degrees, there exist only two signals: this may be attributed to coupling between the precessing magnetic moments of isolated granules and of infinite

ferromagnetic cluster in the mixed phase [3]. Previous angle rotation measurements at 9.4GHz, shows similar results, for *81* at.% cobalt [3]. However, it was not possible for the group in the Ukraine to carry out 9.5GHz FMR with the field normal to the film plane (for films whose concentrations are above 54at.%) as this requires fields higher than 10kOe.

The FMR signal measured in the perpendicular configuration has five peaks, as shown in figure 6.8. Such a structure was previously observed in Fe-SiO_2 granular films [9] where it was attributed to spin-wave resonance and surface modes near the uniform FMR line. (Here, they showed that the exchange constant, $8.3x10^{-30}$ $ergscm^2$ was smaller than that of bulk iron (at room temperature), $5x10^{-29}$ $ergscm^2$. The difference in the exchange constant was attributed to the abundance of magnetic surfaces or a cut off of the spin waves with wavelengths larger than the physical dimensions of the particles.)

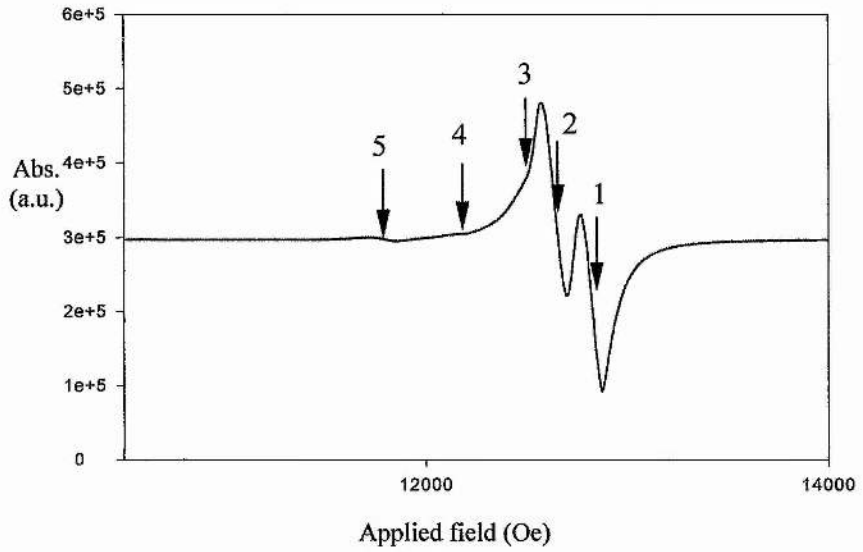

Figure 6.8. 9.5GHz FMR signal of 71at.% cobalt in perpendicular configuration.

From figure 6.8, the distance between peaks three and four and peaks four and five is 340 ± 40 Oe. This may suggest that these modes are

attributed to standing spin waves. The second peak may be a uniform mode while peak one is possibly a surface mode.

For bulk cobalt, the exchange constant is $1.3x10^{-6}$ ergs/cm [10]. From equation 2.42, the separation between consecutive lines is

$$\Delta H_n = \frac{8(n+1)A}{M_s}\left(\frac{\pi}{L}\right)^2, \text{ where } n \text{ is odd} \quad (6.5)$$

The exchange constant for this particular sample is $(2.2\pm0.3)x10^{-6}$ ergs/cm, which is higher than the bulk value and L is taken as the film thickness, 270nm. The value of n for peaks 3, 4 and 5 is 1, 3 and 5, respectively. For the above calculation, the saturation magnetisation was assumed to be the same as the bulk value, 1.43kOe. If the magnetisation term were to be replaced by fM_s, where f is the volume fraction, then the exchange constant is $(1.4\pm0.2)x10^{-6}$ ergs/cm. If the value L was the same as the grain size and not the film thickness, then the exchange constant will be reduced to 10^{-10} ergs/cm. More work is required in order to understand standing spin waves in the CoAg granular films.

The perpendicular FMR spectra of samples whose concentrations are above the percolation point ($f = 0.20$) are shown below. These lineshapes will be compared with higher frequency measurements in the next section.

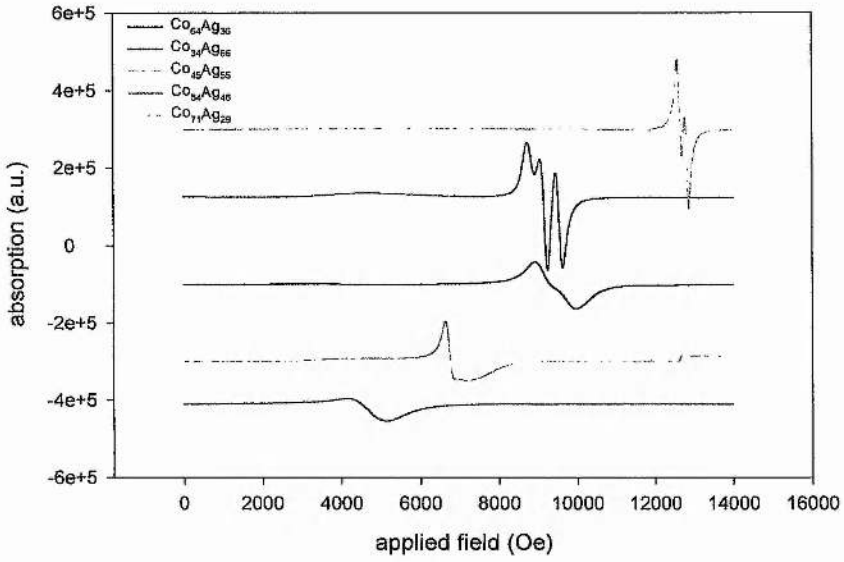

Figure 6.9. 9.5GHz spectra of granular films with concentrations above the percolation point. The external field was applied normal to the film surface.

The linewidth of the uniform mode for all samples measured in parallel and perpendicular configuration, are plotted in figure 6.10.

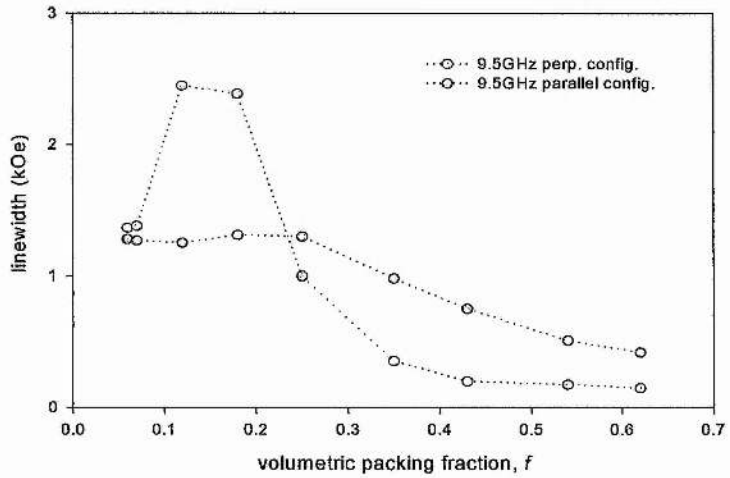

Figure 6.10. The measured linewidth in parallel and perpendicular configuration.

Further discussions on the low and high frequency measurements on the linewidth will be discussed in the next section.

6.4.2. 92GHz measurements

High field ferromagnetic resonance was carried out at 92 GHz. Figures 6.11 shows the lineshapes, which have a poor signal to noise ratio as the cobalt composition decrease. It was not possible to carry out in-plane measurements with the use of an in-plane sample holder, as discussed in section 2.2.4, due to the poor signal to noise.

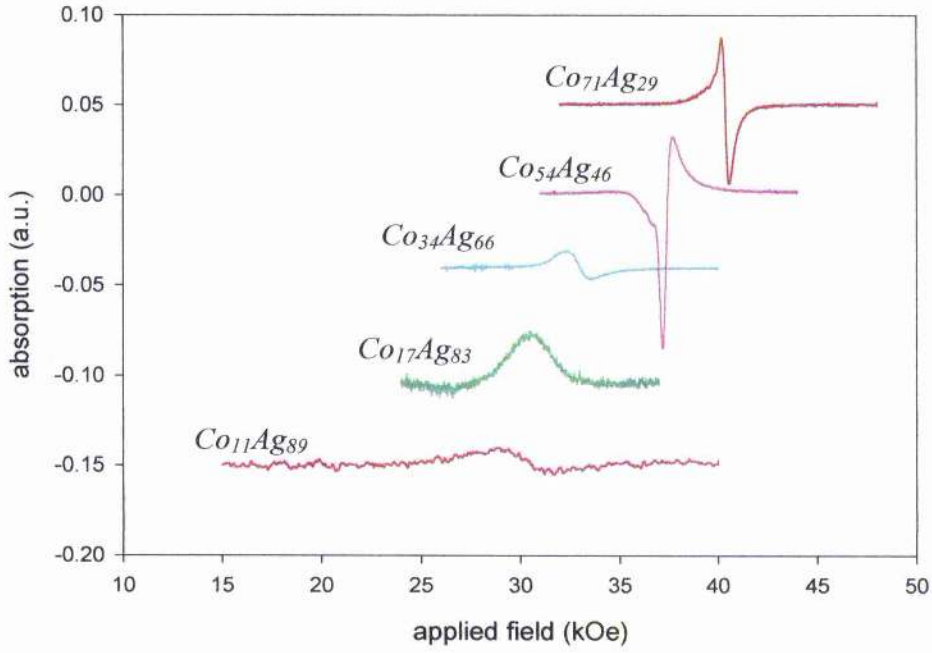

Figure 6.11. FMR lineshapes of granular thin films at 92GHz. The compositions of cobalt varies between 11 and 71 at.%.

It was observed that samples with composition greater than 34 at.% have at least two FMR signals: the usual Kittel mode and the lower field mode. The resolution at 92GHz for the case of 45 to 71 at.% is not as good as that at 9.5GHz. Consequently, it is difficult to observe

lower field modes. It is uncertain what mechanism is responsible for the lower field mode in the 45, 54 and 64 at.% sample.

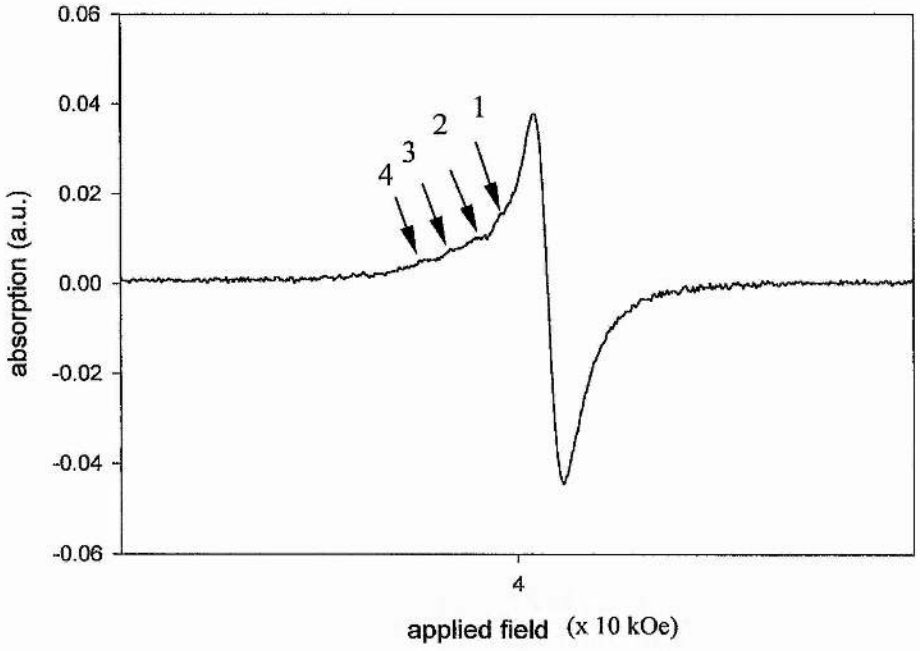

Figure 6.12. FMR spectra of 71at.% cobalt with faint lower field lines.

Figure 6.12 is an FMR signal of 71 at.% cobalt. The arrows point to lower field modes. There are five signals in the spectra: the main resonance line and four equally spaced lines, which were 320Oe apart. The spacing between the lower field modes is the same as in 9.5GHz. As previously mentioned in the low frequency section, this may be due to standing spin waves. Peak one in figure 6.8 may be a surface mode. However, there is no higher field signal above the uniform mode in figure 6.12.

Examples of smaller field modes that were observed in 54 and 64at.% are shown in figure 6.13. Here, there is the high intensity uniform mode and two lower field modes.

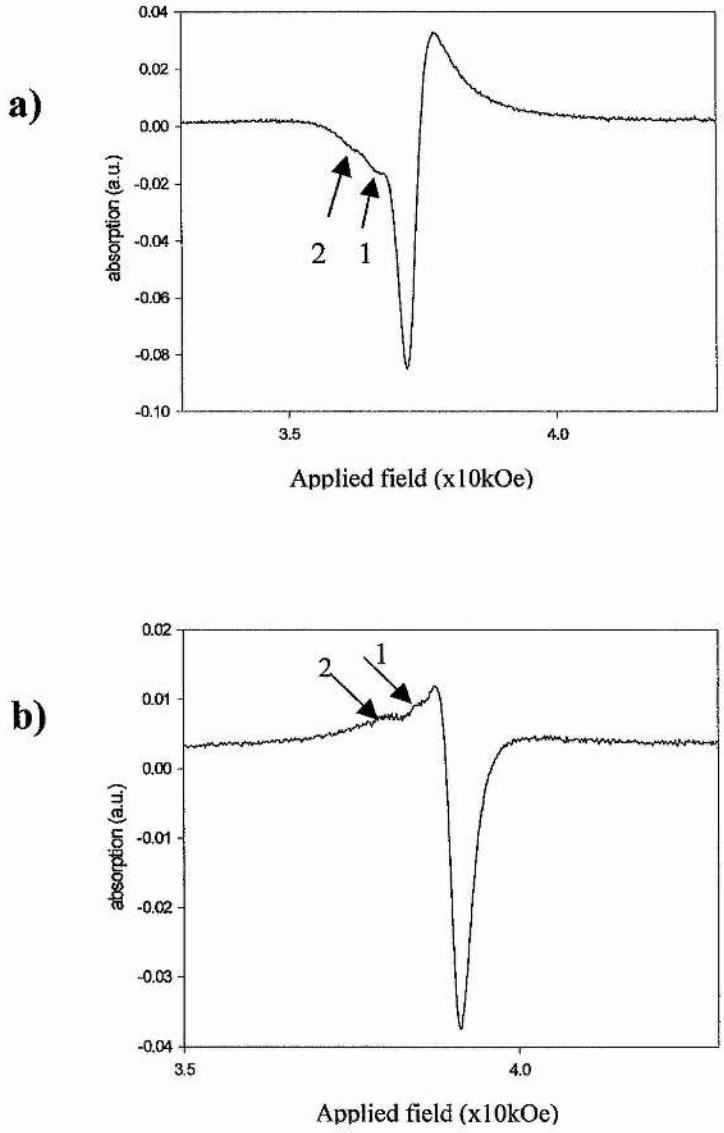

Figure 6.13. FMR spectra of 54at.% (a) and 64at.% (b).

Table 6.3 is a set of field values of the uniform and lower field mode. The data in the top and bottom table was collected from the FMR spectra at 92 and 9.5GHz, respectively.

Sample	Uniform mode	1st mode	2nd mode	3rd mode	4th mode
71 at.%	40.37 kOe	39.83 kOe	39.54 kOe	39.25 kOe	38.91 kOe
64 at.%	39.10 kOe	38.36 kOe	-	-	-
54 at.%	37.38 kOe	36.74kOe	36.25 kOe	-	-
45 at.%	35.42 kOe	34.70 kOe	-	-	-

Table 6.3A

Sample	Uniform mode	1st mode	2nd mode	3rd mode	Surface mode
71at%	12.63 kOe	12.49 kOe	12.17 kOe	11.89 kOe	12.82 kOe
64at%	9.74 kOe	9.13 kOe	4.19 kOe	-	-
54at%	9.58 kOe	9.18 kOe	8.92 kOe	4.50 kOe	-
45at%	6.75 kOe	3.10 kOe	-	-	7.05 kOe

Table 6.3B

Table 6.3. Values of the resonant fields for samples with compositions above 34 at.%. The values in tables A and B were taken at 92GHz and 9.5GHz, respectively.

From both tables, it is clear that the spectra measured at 9.5GHz has one more signal than that at 92GHz. Referring back to figure 6.12, which is the 71at.% cobalt signal, the spectra looks as though there is only the uniform mode of precession. Smoothing the data still shows faint lower field signals.

Figure 6.14 is a plot of the uniform resonant field (in perpendicular configuration) with respect to the volumetric filling factor at 9.5GHz and 92GHz.

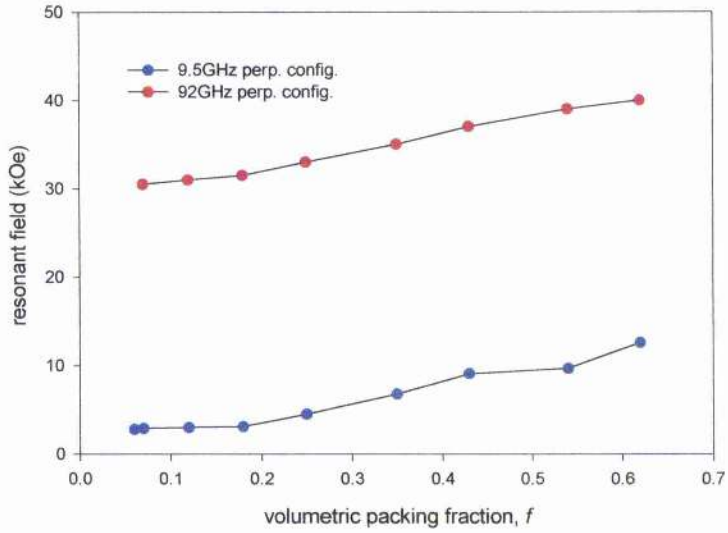

Figure 6.14. Plots of the uniform resonant field at 9.5GHz and 92GHz, in perpendicular configuration.

References [3] and [9] provide a detailed theoretical background on the FMR in granular thin films. For a thin film, for which the principal values of N are (0, 0, 4π) composed of spherical granules, the resonant conditions at $T \neq 0K$ are:

1. where the volume fraction is below the percolation point, $f < f_p$:

The perpendicular and parallel resonant field are $H_{r\perp} = \frac{\omega}{\gamma} + H_{eff}$ and

$$H_{r\|} = \sqrt{\left(\frac{\omega}{\gamma}\right)^2 + \frac{H_{eff}^2}{4}} - \frac{H_{eff}}{2}, \text{ respectively [3,11].} \qquad (6.6)$$

Here, $H_{eff} = 4\pi f M_\alpha$ with $M_\alpha = M_S L\left(vM_S H_i / kT\right)$ and $\alpha = \perp$, $\|$.

2. where the volume fraction is above the percolation point, $f > f_p$:

Here the magnetic material is distributed between the granular fraction, f_g, and ferromagnetic fraction, f_{FM}, so that $f = f_g + f_{FM}$ [11] and $H_{eff} = 4\pi(f_g M_g + f_{FM} M_{FM})$ [11]. The resonant field is given by

$$H_r^2 = \left(\frac{\omega}{\gamma} + H_{eff}\cos^2\theta\right)^2 + H_{eff}^2 \sin^2\theta\cos^2\theta \qquad (6.7)$$

where θ is the magnetisation's equilibrium angle, deduced from $H\sin(\theta_H - \theta) = H_{eff}\sin\theta\cos\theta$ [3].

M_{FM} is approximately the same as M_s, which is about 1.43 kOe and $M_g << M_{FM}$ [3]. Equations 6.6 and 6.7 apply to the uniform mode.

In the analysis, the g-factor was assumed to be 2.20 and M_s = 1.43kOe [3]. A plot of $H_{eff}/4\pi M_s$, deduced from equations (6.6) and (6.7), with respect to the packing fraction, f, for the field perpendicular to the film plane ($\theta=0$) is shown in figure 6.15. If one were to draw a dotted-line as shown in the $H_{eff}/4\pi M_s$ plot, then there exists a 'bump', which is lower than the percolation point ($f = 0.20$).

Previous work on 9.4GHz [11] have shown that this 'bump' exists at $f = 0.30$ near the percolation point, which is higher than that measured at 92GHz. This was the main point of this experiment: to locate the percolation point via FMR. One should note that the percolation point in [11] is different from that discussed in [3]. After private discussions [5], the percolation point is 0.20, as mentioned in the beginning of this chapter.

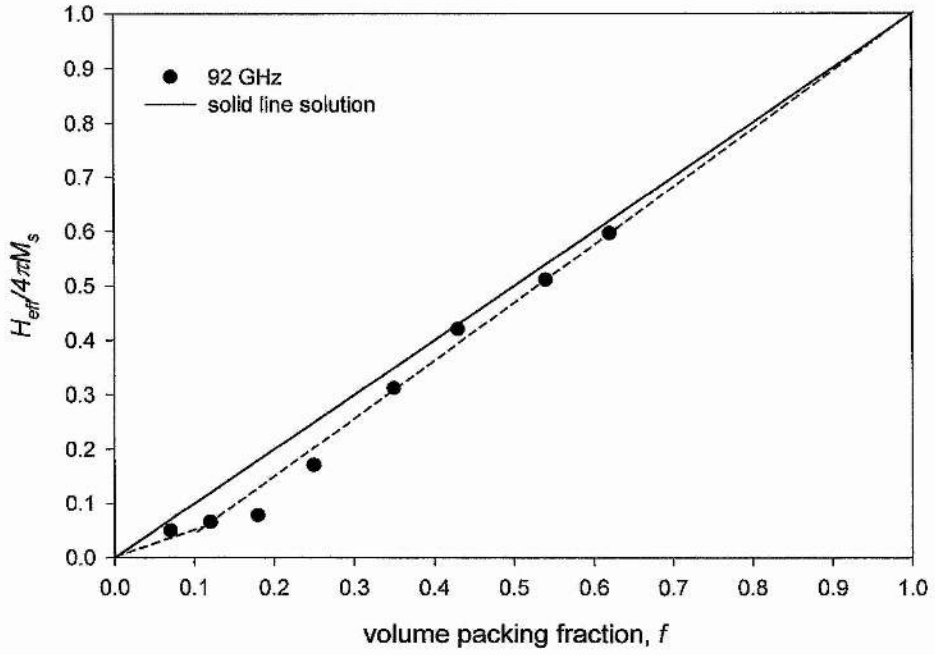

Figure 6.15. A plot of the ratio of the effective field, H_{eff}, and saturation magnetisation (at 0K) versus the cobalt packing fraction, f, deduced from perpendicular FMR. There exists a bump at $f = 0.12$ rather than 0.20, where the percolation point lies. The solid line is the ratio $4\pi fM_S/4\pi M_S$ (with $4\pi M_s = 17.6kG$) and $4\pi fM_s$ represents the demagnetising term of the effective field for spherical particles [9,11].

Linewidth measurements at 92GHz (figure 6.16), shows that the linewidth increases significantly as the volumetric filling factor decreases. It is uncertain what mechanisms take part in these granular films. However in-plane linewidth measurements on CoFe granular films in Al_2O_3 matrix was studied [12]. Here, they suggest that the standard treatment of the linewidth through the damping term in the Landau-Liftschitz equation is insufficient to describe its high values in granular systems and should be supplemented by the process of non-uniform broadening of the resonance line. Mechanisms such as the

random shape anisotropy of granules [13] or fluctuations of the local internal field H_i on them (from random configurations of neighbouring granules) were introduced to the linewidth problem.

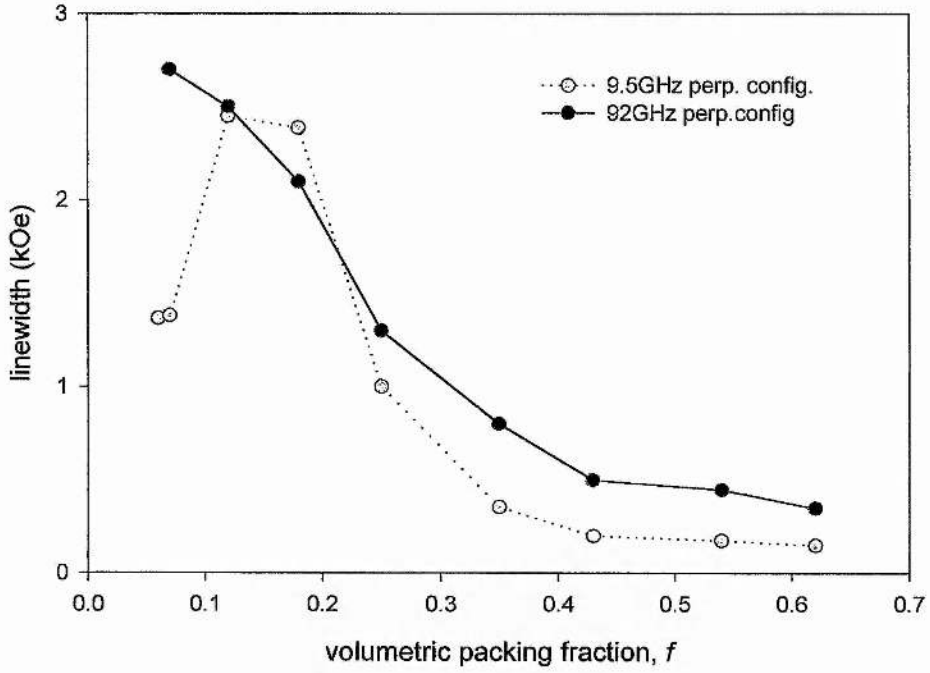

Figure 6.16. Linewidth plot versus the cobalt packing fraction.

It is clear that the difference in linewidth between the two frequencies is large at $f = 0.07$. For higher compositions, the difference is as much as 480 Oersted at 45at.% cobalt ($f = 0.35$). It is observed that films with compositions between 17 to 34 at.% ($f = 0.12$ *to* 0.25) have linewidths that are close to each other at 92 and 9.5GHz. This may suggest that there is no frequency dependence and that the only contribution to the linewidth is that of the inhomogeneity of the internal field and the random shape anisotropy. Determining the linewidth of 54at.% and 64at.% cobalt at 92GHz was not trivial. This is due to phase problems and the presence of a lower field signal. At both frequencies, the linewidth decreases with increasing volume fraction

(for samples whose compositions are above 17at.%). If an error was known, then the two curves may coincide and so one may suggest that their linewidths does not change dramatically with frequency, and so the mechanisms associated with these samples does not include damping . The change in linewidth at 11 at.% ($f = 0.07$) is considerable and so damping contributions may take place.

It is clear that more work is required in order to understand the mechanisms in the CoAg granular films.

6.5. Summary

Most of the work in this chapter is based on low and high frequency FMR. In contrast to previous works on low frequency FMR, this chapter has deduced the mean grain size for samples with concentrations below 25at.%. The mean grain size of 25at.% cobalt determined from SQUID [3] was 36 Angstroms; the mean grain size determined from FMR for 17at.% was 11 Angstroms, which seems to be in the right order of magnitude.

Samples such as 71 at.% cobalt have field lines that are equally separated, which may suggest that they may be standing spin waves. The exchange constant is higher than that of bulk cobalt. It is uncertain as to why that is. The effective field, H_{eff}, versus the packing fraction shows a bump, which should locate the percolation point. In contrast to Pogorelov et al, high frequency measurements located a 'bump' at $f = 0.12$ rather than $f = 0.20$. Perpendicular FMR linewidth measurements on samples with compositions greater than the percolation point have shown that the biggest difference in linewidth between the two frequencies is 500Oe at $f = 0.35$. It is clear that more work is required in order to fully understand the mechanisms of the linewidth and the lower field signals.

6.6. References

[1] M.L.Plummer, J. van Ek and D.Weller, *The Physics of Ultra-High Density Magnetic Recording*, Springer-Verlag, New York 2001

[2] M. Respaud, J. Appl. Phys., (1999)

[3] Yu. G. Pogorelov, G.N. Kakazei, J.B. Sousa, A.F. Kravets, N.A. Lesnik, M.M. Pereira de Azevedo, M. Malinowska, P. Panissod, Phys. Rev. B., 60 (1999) 12200

[4] www.webelements.com

[5] N.A. Lesnik, *private communications*, 2002

[6] A.H. Morrish, *The Physical Principles of Magnetism*, Wiley, New York, 1965

[7] Bruker Handbook on EPR Spectrometer, J.C.Walton, private communications, 2001

[8] S. Chikazumi, Physics of Magnetism Wiley, Inc (1964)

[9] A.Butera, J.N.Zhou, J.A.Barnard, Phys.Rev.B, 60 (1999) 12270

[10] M.Prutton, *Thin Ferromagnetic Films*, Butterworths, London, 1964

[11] G.N. Kakazei, A.F. Kravets, N.A. Lesnik, M.M. Pereira de Azevedo, Yu. G. Pogorelov, J.B. Sousa, J. Appl. Phys., 85 (1999) 5654

[12] V.O. Golub, G.N. Kakazei, A.F. Kravets, N.A. Lesnik, Yu.G. Pogorelov, J.B. Sousa, A.Ya.Vork, IEEE Trans. Magn., 2002 (In press)

[13] M. Rubinstein, B.N. Das, N.C. Koon, B.D. Chrisey, J. Horwitz, Phys. Rev. B. 50 (1994) 184

Chapter 7

Summary and Future Work

This chapter presents a synopsis on magnetic studies of cobalt-based granular thin films with discussions on some projects that are worth continuing. The layout of the summary and future work is based on experimental chapters, two to six.

Chapter two is split into two parts: the theory of FMR and the experimental layout of the 12 Tesla spectrometer. The latter includes discussions on an in-plane sample holder that was used on thin films as well as methods of analysing an asymmetric signal from a cobalt thin film, in order to determine the signal's resonant field and linewidth.
Since the in-plane sample holder was not used for cobalt based granular samples, it was not possible to carry out in-plane and out-of-plane FMR at the same frequency. Instead, multi-frequency FMR was used. 75 to 95GHz FMR on the cobalt film, allows one to determine its g-factor and perpendicular anisotropy field, which was found to be slightly higher than that deduced from torque magnetometry.
If there was more time, it would be worth finding another method of determining the resonant field and linewidth from an asymmetric non-Lorentzian lineshape. If the signal to noise ratio at 180 and 270GHz had improved, then it would be interesting to compare FMR results obtained from a narrow range, 20GHz, with that of a broader range, 90 to 270GHz.

Chapter three involves the FMR and torque magnetometry of two types of recording media. Each sample has its own grain size and size distribution, which affects the sample's recording properties. High field FMR was used to solve the g-factor, crystalline anisotropy field and the damping factor. It was observed that from non-linear

regression, the sum $\left(4\pi M_s + \frac{H_K}{2}\right)$ is well defined for these samples. For both types of media, the value of the g-factor and anisotropy were almost the same, but the damping factor was slightly different. Further work is required in order to back-up conclusions provided in section 3.2.5. A micromagnetic simulation on the FMR spectra as discussed in section 3.2.2. would be useful to compare the properties deduced from simulation with experiment. Previous work on the high and low noise media were carried out on torque magnetometry in Seagate and they showed that there is a difference in the crystalline anisotropy field. It was observed that high field FMR provided a higher value of H_k than low field torque magnetometry. Another section in chapter three involves determining the value of H_k and the intergranular interactions, which are likely to be present in the recording media, at fields lower than 10kOe. A broader frequency range would also have been useful in determining accurately the damping factor and inhomogeneous term.
The torque magnetometry section was split into two parts: the closing point and ΔT method. Both techniques are novel and involved a micromagnetic simulation of the torque signal, in order to solve for the recording medium's magnetocrystalline anisotropy and intergranular interactions. The ΔT method was carried out on the low noise media only, since there were problems with the measurement on the high noise sample. If there were more time, a ΔT measurement on the high noise sample would be useful. It would be interesting to compare the intergranular constant of both types of media and relate them to their recording properties.

Chapter four deals with the investigation of the trend in the crystalline anisotropy, g-factor and possibly the damping factor for CoCrPtB recording media with varying Pt and B content. The saturation magnetisation on both the platinum and boron varying media measured in Seagate and IBM were not the same. It was observed that for both sets of samples, there was in fact a trend: the anisotropy and g-factor

increases with Pt and B content, even though the sample's saturation magnetisation deduced from independent techniques were different.
It would be interesting to carry out an out-of-plane SQUID measurement (in St. Andrews) on the two series so that the crystalline anisotropy was determined and compared with 75–95 GHz FMR.
The Gilbert damping term for recording media measured in chapters three and four were in the range 0.01 to 0.04, which is in the region of that previously measured by Inaba and Igarashi et al, as discussed in section 3.2.1. It would be interesting to carry out damping measurements using the optical pump probe FMR system in Exeter and compare these results with the 75 – 95 GHz system.

Chapter five is concerned with small angle neutron scattering of 2D-isotropic and anisotropic longitudinal recording media. SANS analysis of the 2D isotropic media shows that the fitting to the sine-squared amplitude versus the scattering q is modelled by an ellipsoidal hard core and soft shell. It was observed that the dimensions of the core and shell at 14.5kOe is similar to that at 4.5kOe, as discussed in section 5.5.3. The orientation of the moments in the cobalt core and soft shell relative to the field direction was also determined.
2D isotropic and anisotropic media were also measured in the remanent state, but they were not discussed in this thesis, and it would be interesting, as future work, to compare the magnetic grain size at remanence with non-zero fields.

Chapter six presents 9.5GHz and 92GHz FMR of cobalt nanoclusters. Although M-H loops on the Co_xAg_{1-x} thin films were measured at different temperatures and were shown to exhibit superparamagnetism, an analysis with the equations derived by Pogorelov should be carried out in order to relate the mean grain size with respect to the film's cobalt content. A comparison of the mean grain size from M-H loops to 9.5GHz measurements for samples whose concentration are below 17at.% would be useful.

Angle rotation work at 92GHz was not possible, although it would have been useful to compare the grain sizes, for sample compositions less than 17at.%, with the 9.5GHz measurements. This sort of work requires designing an angle rotation sample holder, in addition, an FMR model for high frequency measurements. A model to solve the frequency dependent and independent linewidth, is also required to back my conclusions.

Appendix A

Gaussian beams and the in-plane sample holder

Gaussian Beams

At mm-wave, terahertz and higher frequencies, free space beams are a more convenient method to describe the way fields to travel from place to place. The Gaussian beam mode (GBM) approach is used for manipulating millimetre signals with free space beams. In the GBM theory:

1. the radiation is assumed to be a paraxial beam (travelling along the z-direction), whose width is not very large compared with the radiation wavelength;
2. the EM field satisfies a linked set of scalar wave equations of the form $\nabla^2\varphi + k^2\varphi = 0$ (A.1)

   where $k = \frac{2\pi f}{c}$, c is the speed of light, f is the signal frequency and φ is the field $\varphi = u(x,y,z)\exp(-jkz)\exp(j2\pi ft)$ (A.2)

The solution to (A.1) defines a series of free space Gaussian beam modes

$$\varphi_{mn} = \frac{1}{\omega}E_{mn}H_m\left\{\frac{x\sqrt{2}}{\omega}\right\}H_n\left\{\frac{y\sqrt{2}}{\omega}\right\}\exp\left(-j\left(kz - \Phi_{mn} - 2\pi ft\right) - r^2\left(\frac{1}{\omega^2} + \frac{jk}{2R}\right)\right)$$

(A.3)

where

$$\omega = \omega_0\sqrt{1+\left(\frac{\lambda z}{\pi\omega_0^2}\right)^2}, \qquad r^2 = x^2 + y^2, \qquad R = z\left[1+\left(\frac{\pi\omega_0^2}{\lambda z}\right)^2\right],$$

$$\Phi_{mn} = (m+n+1)\arctan\left\{\frac{\lambda z}{\pi\omega_0^2}\right\} \qquad \text{(A.4, A.5, A.6 \& A.7)}$$

and H_m is the Hermite polynomial of order m. E_{mn} is a complex number whose value is a measure of the field's overall amplitude and phase. r

is the distance from the beam axis ($x = y = 0$). The fundamental mode is where $m = n = 0$, thus

$$\varphi_{00} = \frac{1}{\omega} E_{00} \exp\left(-j\left(kz - \arctan\left(\frac{\lambda z}{\pi \omega_0^2} \right) - 2\pi f t \right) - r^2 \left(\frac{1}{\omega^2} + \frac{jk}{2R} \right) \right), \qquad (A.8)$$

which can in principle propagate power at any frequency.

ω is the beam's cross-sectional size at any z-plane and R is its phasefront radius of curvature at any z-plane. From (A.4) the beam radius varies hyperbolically along the beam with its minimum value ω_0, which is called the beam waist radius. For simplicity, the origin of the x, y and z Cartesian coordinate system used above has its origin at the beam centre in the beam waist plane. Therefore, z is the 'down-beam' distance measured from the waist plane. Figure A1 illustrates the behaviour of the fundamental Gaussian beam mode.

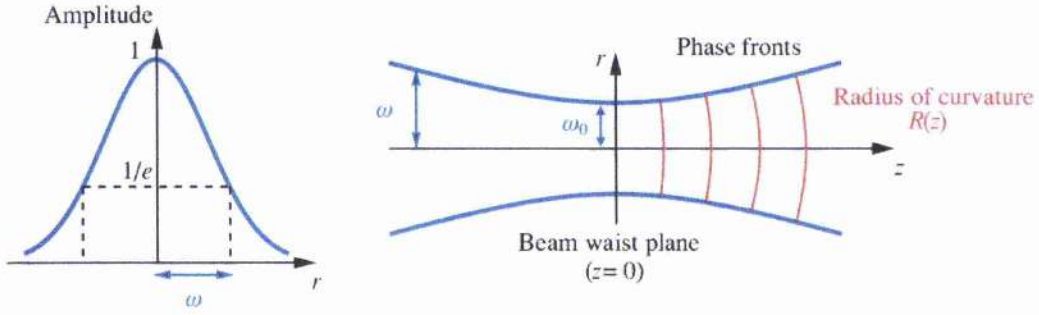

Figure A1. Gaussian beam plots: (A) side view of the beam with the intensity of the field decreasing with distance, r, from the beam centre.
(B) is a bird's eye view of the free space beam with features as discussed in the text.

Mathcad sheet: In-plane sample holder.

The mirrors were made of copper and the focussing lens, HDPE, was attached
to the bottom of the waveguide as illustrated in figure 2.12 in chapter two.
1. We need to know the dimensions of the sample mirror and
2. the distance between the mirror and sample holder which can be used for FMR/EPR/ESR measurements in the 12T magnet (with an inner bore of 49mm).

The frequency here is 94GHz

$d := 0.634 \cdot 13.4$

$d = 8.496$ Beam waist at the waveguide and 13.4mm is the radius of the 90GHz waveguide.

$\lambda := 3 \cdot 10^8 \cdot \frac{10^3}{94 \cdot 10^9}$ wavelength of the beam

$\lambda = 3.191$

$z1 := 20$ distance between HDPE lens and 45 deg. mirror

$w0 := \frac{d^2}{2} + \frac{\sqrt{d^4 - 4 \cdot \lambda^2 \cdot \frac{(z1)^2}{\pi^2}}}{2}$ equation A4

$waist := \sqrt{w0}$

$waist = 8.119$ beam waist at 45 degree mirror

$z2 := 15$ distance between 45 degree mirror and left side mirror

$$w2 := (waist)\cdot\left[1 + \left[\lambda^2 \cdot \frac{(z2)^2}{\pi^2 \cdot (waist)^4}\right]\right]^{\frac{1}{2}}$$

equation A4 re-written in terms of the waist size at a certain distance along the beam

$w2 = 8.333$ beam waist at sample mirror

$D1 := 27$ $\frac{D1}{w2} = 3.24$ ratio of side mirror

Appendix B

Lineshape analysis

Lineshape analysis: this appendix looks at lineshapes that were observed from FMR measurements. In some cases, one would observe a perfect absorption lineshape; however, there were traces of dispersion in the signal. In order to determine the resonant field and linewidth, a fit to the lineshape using an admixture of absorption and dispersion is required.
This sheet looks at
1. pure absorption and dispersion signals
2. the addition of background noise to the signal

If we assume the area under the lineshape defines the number of moments participating in the resonance experiment, then it is clear that the integral of the absorption and dispersion shapes are not the same, as shown below.

For a Lorentzian absorption lineshape, the integral is

$$\int \frac{1}{1+\left[\frac{(x-r)}{L}\right]^2}\,dx$$

where L is the half peak to peak linewidth, r is the resonant field and x is the scanning field.

which gives us:

$$L\cdot\operatorname{atan}\left[\frac{1}{2}\cdot\frac{(2\cdot x-2\cdot r)}{L}\right]$$

For a Lorentzian dispersion lineshape, the integral is

$$\int \frac{\left[\frac{(x-r)}{L}\right]}{1+\left[\frac{(x-r)}{L}\right]^2}\,dx$$

which gives us:

$$\frac{1}{2}\cdot L\cdot\ln\left(L^2+x^2-2\cdot x\cdot r+r^2\right)$$

Therefore, we introduce a factor A to the dispersion curve which will match the number of moments from the absorption line shape, where A>0.

From FMR measurements, we are measuring in first order derivative, therefore, the double derivative of the moments in absorption mode is:

$$\frac{d^2}{dx^2}L\cdot\operatorname{atan}\left[\frac{1}{2}\cdot\frac{(2\cdot x-2\cdot r)}{L}\right]$$

which is equal to

$$\frac{-1}{\left[1+\frac{1}{4}\cdot\frac{(2\cdot x-2\cdot r)^2}{L^2}\right]^2}\cdot\frac{(2\cdot x-2\cdot r)}{L^2}$$

Similarly for a dispersion mode:

$$\frac{d^2}{dx^2}\left[A\cdot\left(\frac{1}{2}\cdot L\cdot\ln\left(L^2+x^2-2\cdot x\cdot r+r^2\right)\right)\right]$$

this gives us $$A\cdot\frac{L}{\left(L^2+x^2-2\cdot x\cdot r+r^2\right)}-\frac{1}{2}\cdot A\cdot L\cdot\frac{(2\cdot x-2\cdot r)^2}{\left(L^2+x^2-2\cdot x\cdot r+r^2\right)^2}$$

AN EXAMPLE:

90GHz FMR on cobalt thin film where we have the resonant field 'r' at 40 kOe and the linewidth 'L' is 8kOe

$r := 4.0 \qquad L := 0.4 \qquad x := 0, 0.01 .. 8$

Absorption and dispersion lineshapes (from above) are:

$$absn(x) := \frac{-1}{\left[1+\frac{1}{4}\cdot\frac{(2\cdot x-2\cdot r)^2}{L^2}\right]^2}\cdot\frac{(2\cdot x-2\cdot r)}{L^2}$$

We introduce a value to the term A, say 0.5

$A := 0.5$

$$dispn(x) := A\cdot\frac{L}{\left(L^2+x^2-2\cdot x\cdot r+r^2\right)}-\frac{1}{2}\cdot A\cdot L\cdot\frac{(2\cdot x-2\cdot r)^2}{\left(L^2+x^2-2\cdot x\cdot r+r^2\right)^2}$$

The plots of dispersion and absorption curves using the above equations are shown below:

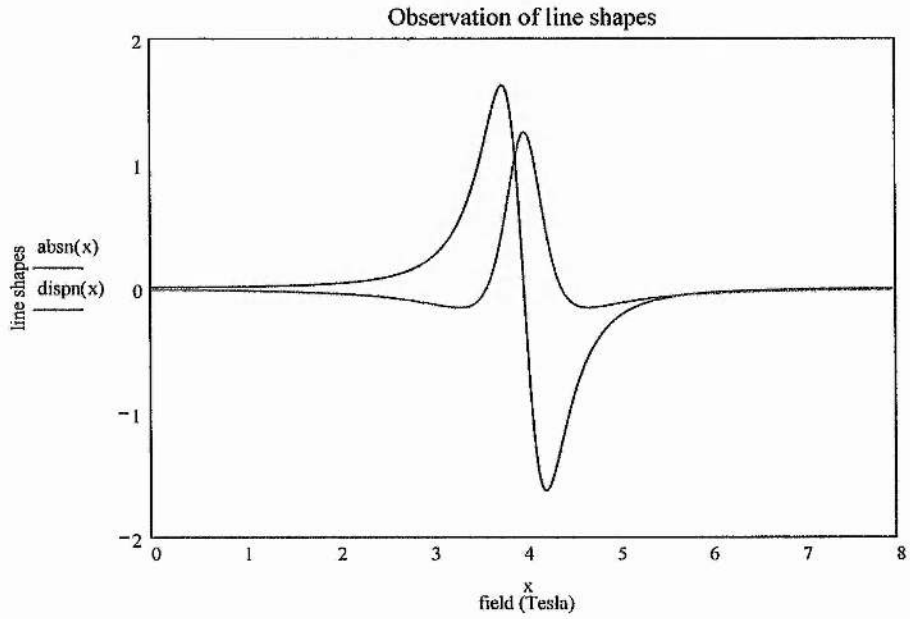

If we introduce background noise to the signal, then we have following lineshape:

absorption plus random noise

$ab(x) := absn(x) + (rnd(0.5) + rnd(-0.5))$

introduce noise

dispersion plus random noise

$dp(x) := dispn(x) + (rnd(0.5) + rnd(-0.5))$

introduce noise

$$sum(x) := ab(x) + dp(x) + 0.3x$$

Plot of line shape with random noise:

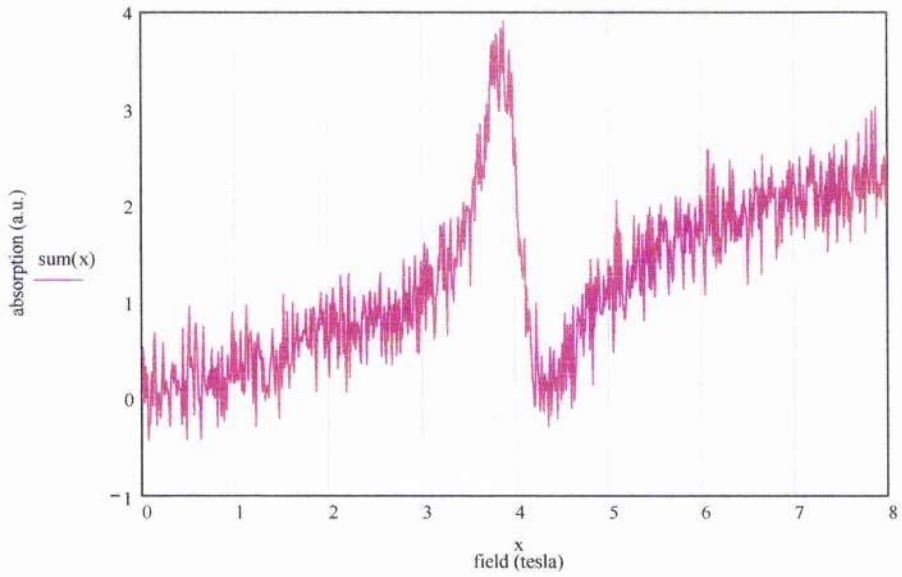

If say, seven grains contributed to the uniform mode, denoted absn#(x), then the resultant lineshape is:

First lineshape: resonant field 'r1' and linewidth 'La' $La := 0.1$ $r1 := 3.9$

$$absn1(x) := \frac{-1}{\left[1 + \frac{1}{4}\cdot\frac{(2\cdot x - 2\cdot r1)^2}{La^2}\right]^2}\cdot\frac{(2\cdot x - 2\cdot r1)}{La^2}$$

Second lineshape: resonant field 'r2' and linewidth 'Lb' $Lb := 0.1$ $r2 := 3.93$

$$absn2(x) := \frac{-1}{\left[1 + \frac{1}{4}\cdot\frac{(2\cdot x - 2\cdot r2)^2}{Lb^2}\right]^2}\cdot\frac{(2\cdot x - 2\cdot r2)}{Lb^2}$$

$Lc := 0.1 \quad r3 := 3.96$

$$absn3(x) := \frac{-1}{\left[1 + \frac{1}{4}\cdot\frac{(2\cdot x - 2\cdot r3)^2}{Lc^2}\right]^2}\cdot\frac{(2\cdot x - 2\cdot r3)}{Lc^2}$$

$Ld := 0.1 \quad r4 := 3.99$

$$absn4(x) := \frac{-1}{\left[1 + \frac{1}{4}\cdot\frac{(2\cdot x - 2\cdot r4)^2}{Ld^2}\right]^2}\cdot\frac{(2\cdot x - 2\cdot r4)}{Ld^2}$$

$Lf := 0.1 \quad r5 := 4.02$

$$absn5(x) := \frac{-1}{\left[1 + \frac{1}{4}\cdot\frac{(2\cdot x - 2\cdot r5)^2}{Lf^2}\right]^2}\cdot\frac{(2\cdot x - 2\cdot r5)}{Lf^2}$$

$Lh := 0.1 \quad r6 := 4.05$

$$absn6(x) := \frac{-1}{\left[1 + \frac{1}{4}\cdot\frac{(2\cdot x - 2\cdot r6)^2}{Lh^2}\right]^2}\cdot\frac{(2\cdot x - 2\cdot r6)}{Lh^2}$$

$Li := 0.1 \quad r7 := 4.08$

$$absn7(x) := \frac{-1}{\left[1 + \frac{1}{4}\cdot\frac{(2\cdot x - 2\cdot r7)^2}{Li^2}\right]^2}\cdot\frac{(2\cdot x - 2\cdot r7)}{Li^2}$$

The sum of all seven lineshapes (from each grain) is:

$ab(x) := absn1(x) + absn2(x) + absn3(x) + absn4(x) + absn5(x) + absn6(x) + absn7(x)$

Plots of all individual resonances from each grain and the main signal

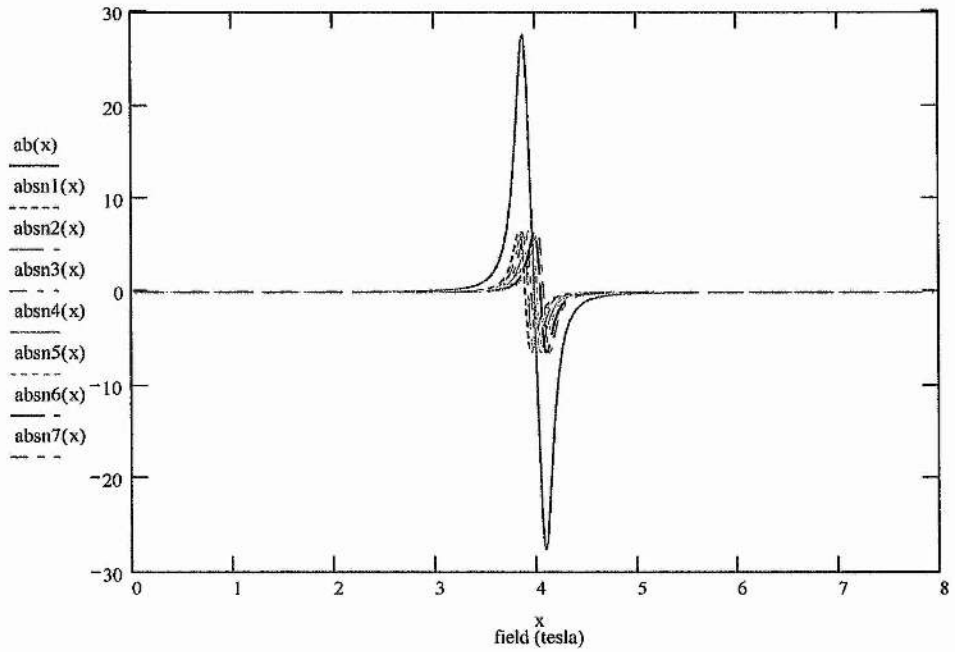

Appendix C

The FMR condition for longitudinal recording media

Verify that for any value of rho, the angle between the c-axis and the x-axis will generate the same resonant condition. We will look at the rhs of equation (3.13).

$Hk := 1.08$ in plane uniaxial anisotropy

$thH := \frac{\pi}{2}$ $phH := \frac{\pi}{2}$ field angles wrt film surface

$M := \frac{0.4872}{4 \cdot \pi}$ magnetisation

$Ku := M \cdot \frac{Hk}{2}$ anisotropy constant

$H := 4.17$ resonant field

$Ku = 0.021$ $Kperp := 0$

$th := \frac{\pi}{2}$ $ph := \frac{\pi}{2}$ assuming that the moments are along the field direction, then both the polar and azimuth angle of the moment is the same as the field

angle rotation of the c-axis, rho, relative to the x-axis as shown in chapter three, in radians.

$rho := 0, 0.01 .. 2\pi$

The equations below are parts of the resonant condition (3.13)

$$rh1(rho) := M \cdot H \cdot (\sin(th) \cdot \cos(phH - ph) \cdot \sin(thH) + \cos(th) \cdot \cos(thH)) + \left[\left(4 \cdot \pi \cdot M^2 - 2 \cdot Kperp\right) \cdot \cos(2 \cdot th) \right.$$

$$rh2(rho) := -2 \cdot Ku \cdot \left[\cos(2 \cdot th) \cdot (\cos(ph))^2 \cdot (\cos(rho))^2 - \cos(2 \cdot th) \cdot (\sin(rho))^2 - \sin(2 \cdot th) \cdot \cos(ph) \cdot \sin(2 \cdot rhc \right.$$

$$rh3(rho) := M \cdot H \cdot (\sin(th) \cdot \cos(phH - ph) \cdot \sin(thH)) + \left[\left(4 \cdot \pi \cdot M^2 - 2 \cdot Kperp\right) \cdot (\sin(th))^2 \cdot \cos(2 \cdot ph) \right]$$

$$rh4(rho) := Ku \cdot \left[2 \cdot (\sin(th))^2 \cdot \cos(2 \cdot ph) \cdot (\cos(rho))^2 + \frac{1 \cdot (\sin(2 \cdot th) \cdot \cos(ph) \cdot \sin(2 \cdot rho))}{2} \right]$$

$$rh5(rho) := M \cdot H \cdot (\cos(th) \cdot \sin(thH) \cdot \sin(th - thH)) + \left[\left(2 \cdot \pi \cdot M^2 - Kperp\right) \cdot \sin(2 \cdot th) \cdot \sin(2 \cdot ph) \right]$$

$$rh6(rho) := Ku \cdot \left[\sin(2 \cdot th) \cdot \sin(2 \cdot ph) \cdot (\cos(rho))^2 + \cos(2 \cdot th) \cdot \sin(ph) \cdot \sin(2 \cdot rho) \right]$$

$$rh7(rho) := \frac{\left[(rh1(rho) + rh2(rho)) \cdot (rh3(rho) + rh4(rho)) - (rh5(rho) + rh6(rho))^2 \right]}{M^2 \cdot (\sin(th))^2}$$

$$rh8(rho) := \sqrt{rh7(rho)}$$

The frequency of the mm-wave is $w := 93.38 \cdot 10^{9}$

Here we look at the g-factor, derived and observe how the g-factor varies with the angle rho.

$$g(rho) := w \cdot 6.63 \cdot \frac{10^{-34}}{\left(9.27 \cdot 10^{-24} \cdot rh8(rho)\right)}$$

The g-value is around 2.157 and it does not change with respect to the orientation of the moment relative to the x-axis

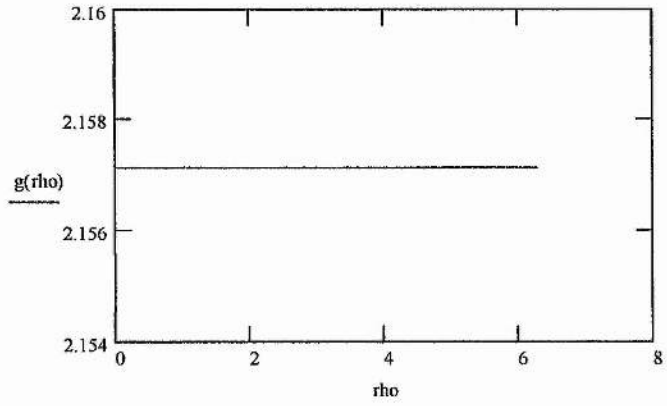

Appendix D

SQUID measurements on CoCrPtB (Pt series) thin films

Magnetisation measurements on the platinum varying media were carried out by a 5T SQUID (superconducting quantum interference device) in St. Andrews. The SQUID has a sensitivity of 10^{-8} emu and the physics of the SQUID magnetometer is found in the Institute of Physics postgraduate workshop handbook on Bulk Characterisation of Magnetic Materials (1999).

Here, the external field is applied within the film surface at room temperature.

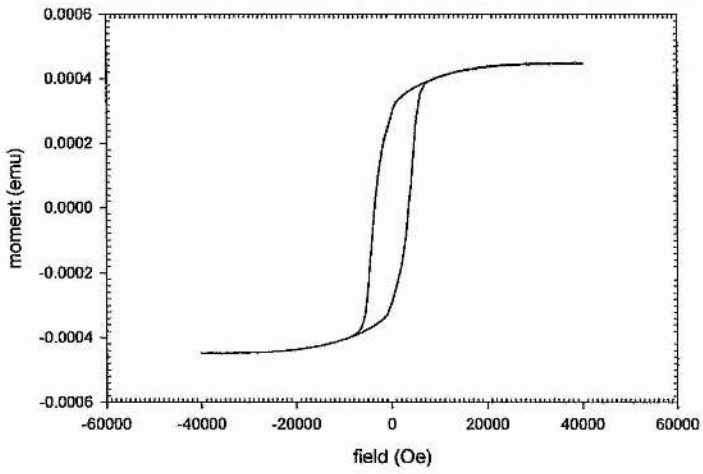

16 at.% platinum

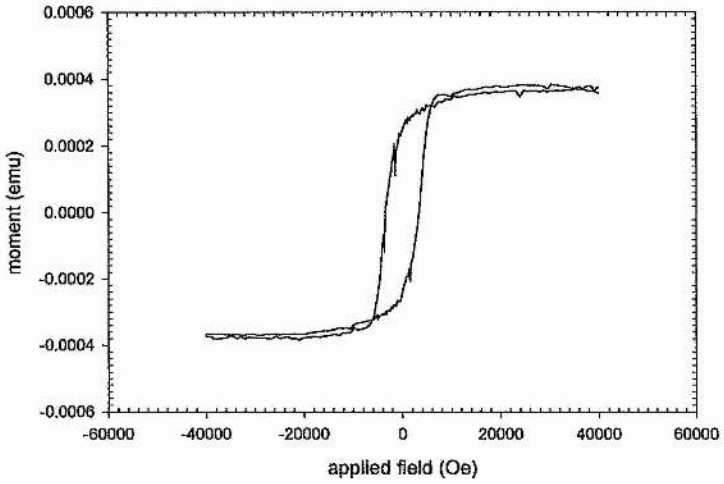

14 at.% platinum

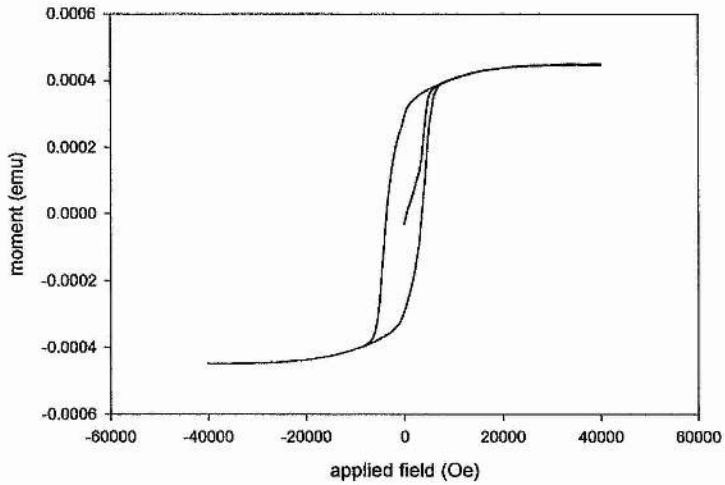

12 at.% platinum

Publications

High field ferromagnetic resonance measurements of the anisotropy field of longitudinal recording thin-film media

C. J. Oates, F. Y. Ogrin,[a] S. L. Lee, P. C. Riedi, and G. M. Smith
School of Physics and Astronomy, University of St. Andrews, KY16 9SS, United Kingdom

T. Thomson[b]
Seagate Technology, 47010 Kato Road, Fremont, California 94538

(Received 25 June 2001; accepted for publication 27 October 2001)

The average value of the magnetocrystalline anisotropy field, H_k, is an important parameter for the characterization of magnetic recording media but is difficult to measure accurately due in part to the effect of interactions between the grains. In order to evaluate H_k we have studied two model CoCrPtTa magnetic films using a number of complementary techniques: high field ferromagnetic resonance (FMR) (35.0–45.0 kOe), low field (<20 kOe) vector vibrating-sample magnetometry and torque magnetometry. The FMR measurements were performed at a number of discrete frequencies in the range 75–93 GHz using a new quasi-optical spectrometer developed at the University of St. Andrews. The values of H_k derived by FMR (10.8 kOe) are approximately 10% greater than those obtained from conventional magnetometry (9.6 kOe). This difference is believed to be due to the presence of intergranular exchange coupling which reduces the measured value of anisotropy when the applied field is not sufficiently large to completely align the magnetic moments. © *2002 American Institute of Physics.* [DOI: 10.1063/1.1428804]

I. INTRODUCTION

Anisotropy and saturation magnetization are the two fundamental properties that determine the static characteristics of ferromagnetic materials.[1] Magnetic anisotropy determines the difficulty of changing the state of the atomic magnetic moments for a given set of experimental conditions while the saturation magnetization measures the effect of alignment of the atomic magnetic moments. In addition the dynamic properties of ferromagnetic materials during reversal are characterized by the Gilbert damping constant, α.[2] Interest in α has recently increased particularly in materials used for data storage such as CoCr-based thin films as data rates, and hence the time available to switch the magnetization, decrease to below 1 ns.[3,4] Despite the fundamental nature of these quantities it remains an on-going experimental challenge to determine their values accurately, particularly when materials are in the form of thin films. In this study we report comprehensive work aimed at determining the anisotropy and the Gilbert damping constant by high field ferromagnetic resonance (FMR).

We have chosen two model CoCrPtTa thin films of interest as media for data storage with different magnetic recording properties. The two samples were sputtered on super-smooth glass-ceramic substrates using a standard commercial dc magnetron sputtering system. The magnetic layers of both media were sputtered from the same CoCrPtTa alloy target with the underlayers consisting of 50 nm thick CrMn for media A and 40 nm/10 nm thick NiAl/CrMn for media B. Previous work on these samples shows that they have substantially different recording properties; with media A having higher noise than media B which was attributed primarily to the differences in grain size and grain size distribution.[5,6]

This paper examines the relative merits of the techniques used to determine these fundamental magnetic properties of thin-film media and correlates the differences found in these model samples to differences in their recording performance.

II. EXPERIMENT

The FMR measurements were performed at a number of discrete frequencies in the range 75–93 GHz (35.0–45.0 kOe) using a new quasi-optical spectrometer developed at the University of St. Andrews.[7] As a preliminary experiment FMR and low field (<20 kOe) torque magnetometry methods were applied to a polycrystalline Co film. Good agreement was found between the two values derived for the effective anisotropy which is discussed later in section four. In the FMR experiments the field is applied normal to the film plane and is sufficiently large to decouple the interactions between the grains. In principle all the parameters required to characterize the material, Landé g-factor, saturation magnetization M_s, anisotropy field H_k and the Gilbert damping factor α, may be obtained from the field for resonance and the linewidth of the FMR signal as a function of frequency. In practice, it was found that a more accurate data set can be obtained when M_s was measured using a vibrating-sample magnetometer (VSM).

Magnetization measurements were taken using a ADE/Digital Measurement Systems model 10 vector VSM, with a maximum applied field of 20 kOe. The temperature was held constant at 20 °C during all measurements. The saturation magnetization was determined from hysteresis loops using

[a]Currently at the University of Exeter, School of Physics, University of Exeter, Stocker Road, Exeter EX4 4QL, UK.
[b]Currently at IBM, IBM—Almaden Research Center, 650 Harry Road, San Jose, CA 95120.

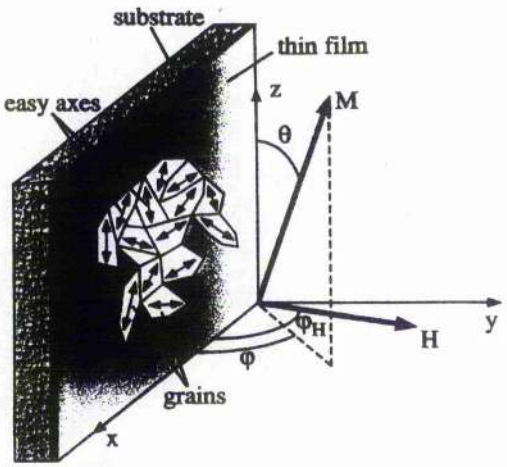

FIG. 1. Orientation of the magnetization M, applied field H and easy axes of the magnetic grains with respect to the film plane.

the instrument in conventional mode with the sample plane aligned parallel to the applied field. A Ni foil standard of the same diameter as the sample was used to calibrate the instrument. Corrections for the substrate and sample rod were attempted using two techniques. The first involved fitting a linear function to the high field region of the hysteresis loops and using the slope as a correction factor. The second technique consisted of removing the magnetic film from the substrate and remeasuring to give a point-by-point subtraction. The two techniques yielded extremely similar results and the linear function method was adopted as this minimized the error on individual data points.

Anisotropy was measured using our in-house torque magnetometer. In this technique, the film is rotated from 0 to 90 deg relative to the field direction. Details of this technique are further described in Ref. 8. [Table II (Sec. IV) provides values to the saturation magnetization and anisotropy that were derived from the above techniques.]

III. FMR MODEL OF LONGITUDINAL RECORDING MEDIA

A. Free energy density equation

In order to simulate the resonant conditions we applied a model in which the thin-film media consists of a large number of crystallites (grains), each containing an easy uniaxial anisotropy axis. The orientation of the uniaxial axes is isotropic and confined to the film plane (see Fig. 1). It is assumed that the interaction between the grains is negligible and that the properties of each crystallite in a high magnetic field is described by a single domain model. With these conditions the free energy per unit volume for each grain is written in the following form:

$$U=-\mathbf{M}_s\cdot\mathbf{H}+\tfrac{1}{2}NM_s^2+K\sin^2\phi, \tag{1}$$

where $\mathbf{M}_s$ is the saturation magnetization vector, $K=M_sH_k/2$ is the magnetocrystalline anisotropy constant, H_k is the anisotropy field and ϕ is the angle between the grain's magnetization and crystallographic axis. $N=N_x\alpha_x^2+N_y\alpha_y^2+N_z\alpha_z^2$ is the effective demagnetizing factor with directional cosines α_i which define the orientation of the magnetization vector with respect to the coordinate axes. In the thin film limit the demagnetizing factor N is simplified assuming that $N_x=N_z=0$ and $N_y=4\pi$. Minimizing Eq. (1) will determine the magnetization's static orientation which is used to simulate FMR and torque data.

B. Equation of magnetic motion

To calculate the FMR response the equation of motion of the magnetization vector is used:[9]

$$\omega=\frac{\gamma}{M_s\sin\theta_0}(E_{\theta\theta}E_{\varphi\varphi}-E_{\theta\varphi}^2)^{1/2}, \tag{2}$$

where ω is the resonance frequency, γ is the gyromagnetic ratio and $E_{\theta\theta}$, $E_{\varphi\varphi}$ and $E_{\theta\varphi}$ represent the second partial derivatives of the free energy taken at the magnetization vector's equilibrium position (θ_0,φ_0)

$$E_{\theta\varphi}=\left(\frac{\partial^2E}{\partial\theta\partial\varphi}\right)_{\theta=\theta_0,\varphi=\varphi_0},$$
$$E_{\theta\theta}=\left(\frac{\partial^2E}{\partial\theta\partial\theta}\right)_{\theta=\theta_0,\varphi=\varphi_0}, \tag{3}$$
$$E_{\varphi\varphi}=\left(\frac{\partial^2E}{\partial\varphi\partial\varphi}\right)_{\theta=\theta_0,\varphi=\varphi_0}.$$

From Eqs. (1), (2) and (3) the resonance frequency is easily related to the parameters g, H_k, $4\pi M_s$. In our configuration (Fig. 1) this relation is expressed as

$$\begin{aligned}\omega=[&((4\pi M_s^2\sin^2\varphi_0+M_sH_k)\cos 2\theta_0\\&+HM_s\sin\theta_0\cos(\varphi_H-\varphi_0))\\&\times(4\pi M_s^2\sin^2\theta_0\cos 2\varphi_0+HM_s\sin\theta_0\cos(\varphi_H\\&-\varphi_0))-(2\pi M_s^2\sin 2\theta_0\sin 2\varphi_0\\&-HM_s\cos\theta_0\sin(\varphi_H-\varphi_0))^2]^{1/2}\frac{\gamma}{M_s\sin\theta_0}.\end{aligned} \tag{4}$$

If the applied field H is sufficiently high and directed normal to the film surface (i.e., $\varphi_H=90°$), the equilibrium position of the magnetization vector will therefore align with the applied field: $\theta_0=90°$, $\varphi_0=90°$. Thus for the perpendicular configuration in the high field limit, the resonant condition, [Eq. (4)] is simplified to

$$\left(\frac{\omega}{\gamma}\right)^2=(H_r-4\pi M_s-H_k)(H_r-4\pi M_s), \tag{5}$$

where H_r is the resonant field.

C. Solution to the FMR condition

In principle it is possible to determine the three parameters g, H_k and $4\pi M_s$ using a minimum of three frequencies. However, in practice, due to the error in determining the resonant field it is difficult to determine $4\pi M_s$ and H_k separately but only the sum of the two variables, $(4\pi M_s+H_k)$.

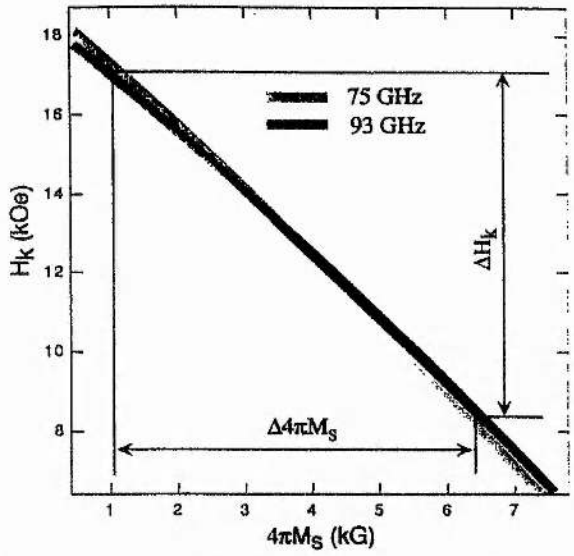

FIG. 2. Graphical representation of solution to Eq. (5) for two frequencies: 75 GHz and 93 GHz. The resonance fields were determined from the experimental measurements on sample 15A and equal to 35.85 kOe and 41.75 kOe, respectively. The resonance field error δH_r was estimated from fitting the resonance line shape into Eq. (7). With g fixed to 2.15, it was found that for both samples $\delta H_r \approx 100$ Oe (which corresponds to the thickness of the lines at 75 and 93 GHz).

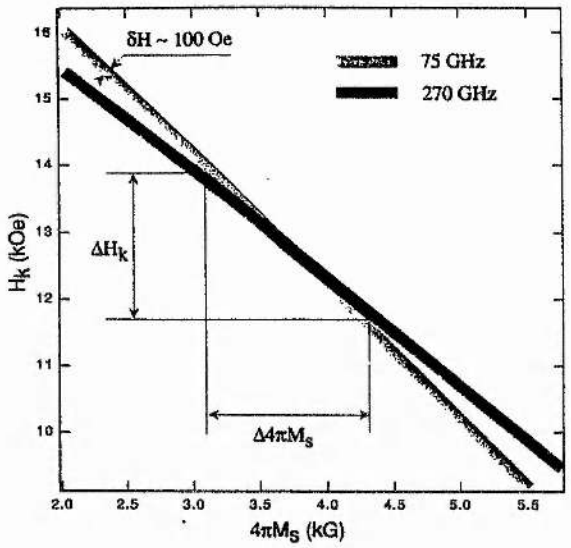

FIG. 3. Intersection of two solutions for 75 GHz and 270 GHz as simulated using Eq. (5). For both samples g is fixed to 2.15 and δH_r is taken as 100 Oe.

At high frequencies, the function form of the equation is such that a small variation in H_r lead to a significant change in the individual values of H_k and $4\pi M_s$ as shown by the size of the intersection area in Fig. 2. Even for a fixed value of g and a small error in H_r ($\approx$0.5%) an error as high as 50% in H_k is observed. This error can be reduced by applying frequencies with the maximum possible separation. The angle between the solution lines that correspond to the two frequencies increases resulting in a reduction to the area of intersection (see Fig. 3). Consequently, the spread in possible solutions of H_k and $4\pi M_s$ decreases. As an example, Table I provides results of the numerical simulation for two different frequencies with g and δH_r fixed to 2.15 and 100 Oe, respectively.

Applying frequencies over a broader range will reduce the error in the sample's saturation magnetization and anisotropy significantly. However, even at a maximum possible separation (for our spectrometer $\Delta f \approx 200$ GHz) the best error in H_k still remains not less than ± 1.1 kOe ($\delta H_r \approx 100$ Oe) which is similar to the uncertainty commonly reported for other techniques used to measure anisotropy. In order to reduce errors further one should either try to improve the precision of the resonance field H_r and/or employ other techniques that will measure one of the above parameters separately. In this work we follow both directions. We carefully analyze the resonance line shape by fitting it to an analytically derived distribution from which the resonance field can be extracted as a parameter. We also use vibrating sample magnetometry to measure precisely the value of the media's saturation magnetization M_s which is used as a fixed parameter in Eq. (5).

IV. RESULTS AND DISCUSSION

It has been shown previously that FMR can provide useful information on anisotropy in thin films.[10] In many cases the analysis of anisotropy is built upon the angular dependence of the resonance field.[11] For high field spectrometers based on superconducting coils it is not always easy to arrange experiments with an angular variation of the applied field. This is due to space restrictions or mechanical complexities of the rotational mechanisms. An alternative is to set up an experiment where the applied field angle is fixed and the excitation frequency is varied. This is the approach we adopt in high field, multi-frequency FMR measurements where the field was always normal to the plane of the film. As a preliminary example, multi-frequency measurements on a 30 nm polycrystalline Co film were performed to find the effective anisotropy H_{eff}. The cobalt film was grown using molecular beam epitaxy on a silicon substrate. The deposited cobalt layer consisted mainly of a polycrystalline hcp phase, with some fcc phase and stacking faults as determined by nuclear magnetic resonance.[12] Given that the direction of the easy axes is mainly out-of-plane for the Co film, the resonance equation in this case is different to that for the media samples and given by the following relation:

$$\frac{\omega}{\gamma} = H_r - H_{\text{eff}}, \tag{6}$$

TABLE I. Intersection of possible solutions for two different frequency ranges (see Figs. 2, 3) as simulated using Eq. (5). Parameters of g and δH_r are fixed to 2.15 and 100 Oe, respectively.

f_1	f_2	g	δH_r	ΔH_k	$\Delta 4\pi M_s$
75 GHz	93 GHz	2.15	100 Oe	8.4 kOe	5.0 kG
75 GHz	270 GHz	2.15	100 Oe	2.2 kOe	1.3 kG

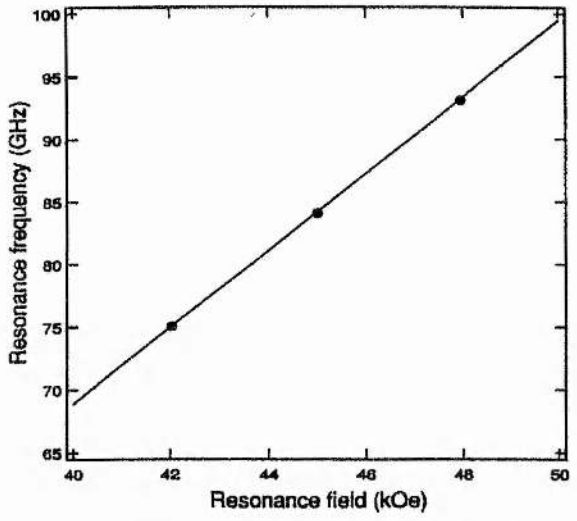

FIG. 4. Resonance frequency as a function of the resonance field for an hcp Co film. Solid line—fit using Eq. (6).

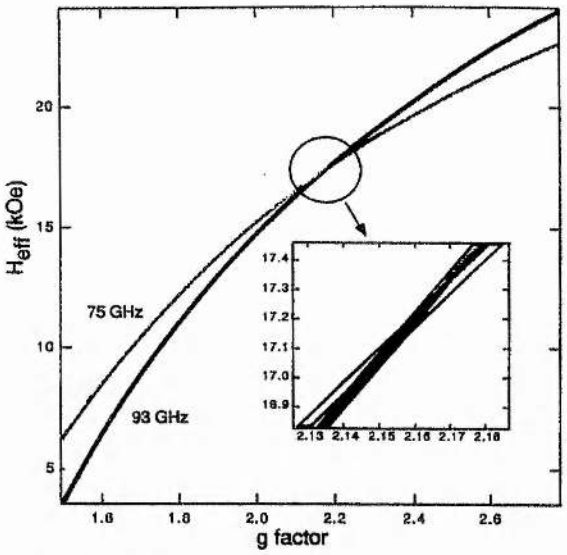

FIG. 5. Graphical solution to Eq. (6) for a polycrystalline Co film. H_{eff} =17.15(20) kOe, g=2.156(5). The resonance frequencies, 75 GHz and 93 GHz correspond to the resonance fields of 42.04 kOe and 47.95 kOe, respectively. The error in the estimate of the resonance field: δH_r=80 Oe.

where $H_{eff}=4\pi M_s-H_k$. Equation (6) was derived from Eqs. (1), (2) and (3) assuming that the orientation of the easy c axes and the applied field are *perpendicular* to the film plane. Figure 4 illustrates the resonance field dependence of the frequency measured for the Co film. The experimental points were fitted with Eq. (6). The extracted values of g and H_{eff} were 2.156(5) and 17.15(20) kOe, respectively. This was in reasonable agreement with previous measurement of H_{eff} on the same film by torque magnetometry which was 16.2(7) kOe.[13] If it is assumed that the saturation magnetization for this film is the same as for bulk Co, the crystalline anisotropy field H_k extracted in this way is of the order of 0.5 kOe. Consequently, the magnetocrystalline anisotropy constant K_u is deduced to be $(3.15\pm1.45)\times10^5$ ergs/cc. This value is much less than that of bulk cobalt, which is typically $(3-4)\times10^6$ ergs/cc.[14,1] and, most likely, is a result of the mixture in the crystalline phases and the polycrysalline nature of the sample.[13,15,16] However, the emphasis here is on the analysis of the perpendicular effective field H_{eff}, which is measured independently of the saturation magnetization and, therefore, is very useful for comparison with the equivalent measurements with other magnetization techniques, including torque magnetometry.

It should be noted that in the configuration of the Co film the magnetocrystalline anisotropy has the same symmetry as the demagnetizing field. This makes it impossible to measure H_k separately without contribution from the demagnetizing fields. Nevertheless, the effective field is measured with good precision from a relatively narrow range of frequencies without involving magnetometry. A simulation of Eq. (6) with the cobalt's effective field measured as a function of the g-factor for two different frequencies: 75 and 93 GHz is shown in Fig. 5. For thin film longitudinal media with easy axes *in-plane* of the film, unlike the cobalt film, it is theoretically possible to separate the magnetocrystalline anisotropy from the demagnetizing field [compare Eqs. (5) and (6)]. However, in practice, due to the high sensitivity to the resonance field error δH_r the spread in possible solutions to H_k and $4\pi M_s$ is very high and hence additional magnetization measurements are required.

The FMR measurements on the media samples were carried out in the range of frequencies between 75 GHz and 93 GHz. In contrast to previously published results by Igarashi *et al.*[17] we were able to obtain very well resolved resonance lines which allowed us to determine the resonance fields with a precision of better than ±0.25%. Figure 6 illustrates an example of a first order derivative absorption line shape of

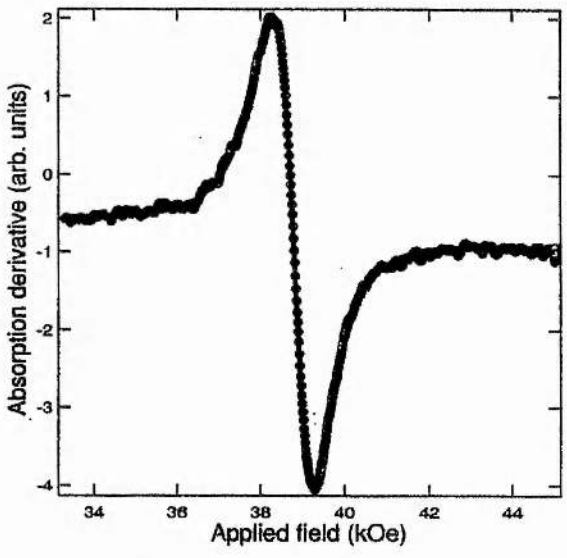

FIG. 6. FMR spectrum measured on high noise media at 84 GHz. Circles—experimental data. Solid line—fit using Eq. (7) H_r=38 750 Oe±50 Oe.

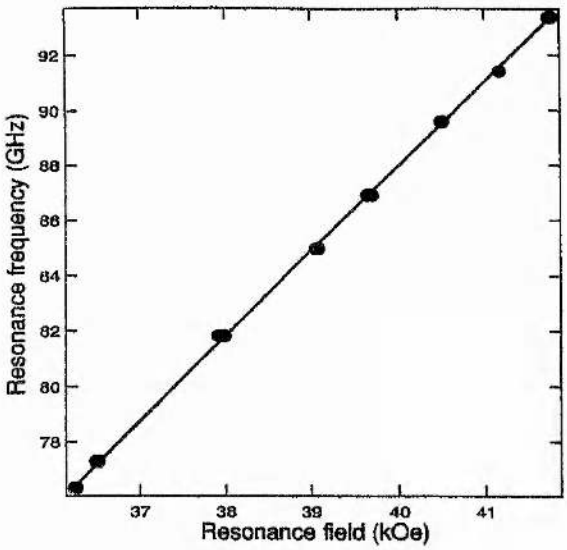

FIG. 7. Resonance frequency as a function of resonance field for high noise media (sample 15A).

high noise (sample 15A) media at 84 GHz. The resonance field is extracted from a fit to a first derivative Lorentzian line shape[18] which is in the form

$$y=\frac{a\left(\frac{H_r-H}{\Delta H_r}\right)+9b-3b\left(\left(\frac{H_r-H}{\Delta H_r}\right)\right)^2}{\left[3+\left(\frac{H_r-H}{\Delta H_r}\right)^2\right]^2}, \tag{7}$$

where y is the FMR response, H and H_r are the applied and resonance fields, ΔH_r is the resonance half peak-to-peak linewidth and a and b are the amplitudes of absorption and dispersion signals, respectively. The last two parameters are, in fact, very important for the determination of H_r. It is a common feature of FMR spectrometers that the output signal often contains a mixture of the absorption and dispersion phases. This is in contrast to the ideal situation when only the absorption signal should be detected. Thus, by adding the presence of a dispersion signal we can always fit the output signal correctly and determine the resonance field with high precision.

Figure 7 shows the variation of the excitation frequency ($\omega/2\pi$) as a function of resonance field H_r measured for the high noise (15A) sample. The solid line is the result of a fit using Eq. (5) with the value of the saturation magnetization given by the VSM measurement. The value of the anisotropy field H_k produced by the fit is given in Table II. It should be noted that the precision of the calculated value of H_k is directly dependent on the precision of M_s. In the present case the uncertainty in M_s arises as a combination of errors: the measured total magnetic moment μ, magnetic layer thickness d and the sample area S (e.g., for sample 15A: $\mu=209\pm1\times10^{-6}$ emu, $d=27.5\pm0.5$ nm, $S=19.6\pm0.2$ mm^2.)

TABLE II. Parameters of the anisotropy field and g-factor as a result of the fit using equation 5. $4\pi M_s$ is measured separately by vector VSM. The H_k value by torque magnetometer is taken from Ref. 8.

Sample name	H_k (kOe) Torque	H_k (kOe) FMR	$4\pi M_s$ (kG) VSM	g
15A (high noise media)	9.6(4)	10.8(2)	4.9(1)	2.150(5)
15B (low noise media)	9.6(4)	10.7(2)	4.5(1)	2.160(5)

It is interesting to note that similarly to the Co film, the values of the anisotropy field H_k measured by torque magnetometry were close, but slightly lower than those measured by FMR. This discrepancy in H_k is believed to be not just a lack of experimental precision but a consequence of the intrinsic characteristics of polycrystalline materials. In FMR the external field is of the order of 40 kOe which is several times larger than that required to saturate the media. As a result only uniform precession of the magnetic moments is produced. Any possible effects of coupling between the grains of the material will not affect the resonant conditions. In contrast to FMR, torque measurements are typically carried out at lower fields (up to 20 kOe). Within this field range both the magnetostatic and exchange interaction can play a significant role in the collective behavior of the magnetic grains which form the sample. This behavior is more complicated than that described by the simple model given here (1) and requires a more detailed micromagnetic approach. Although the interaction[5] in these samples is quite weak it is sufficient to give a lower value of the anisotropy field measured by low field (<20 kOe) torque magnetometry.[8]

V. DYNAMIC PROPERTIES

FMR linewidth measurements provide details on the sample's inhomogeneous broadening and relaxation constant. The relaxation constant is related to the switching mechanism of the magnetization vector M_s. In the present measurements the linewidth of the FMR signal was determined in the same way as the resonant field: a fit to the line shape using Eq. (7). The linewidth ΔH_r in Eq. (7) is defined as half of the field difference between the maximum and minimum of the first derivative absorption line shape. The frequency dependence of the peak-to-peak linewidth was derived from the following equation:[19]

$$\Delta\omega=\frac{\alpha\gamma}{M_s}\left(E_{\theta\theta}+\frac{1}{\sin^2\theta_0}E_{\phi\phi}\right), \tag{8}$$

where α is the Gilbert damping factor. An additional frequency independent term is included which contributes to the inhomogeneous broadening.[20] Thus the linewidth is expressed as:

$$\Delta H(\omega)=\Delta H(0)+\frac{2\alpha\omega}{\sqrt{3}\gamma}, \tag{9}$$

where $\Delta H(\omega)$ and $\Delta H(0)$ is the frequency dependent and independent peak-to-peak linewidth. Figure 8 shows a fit to the linewidth using Eq. (9) and Table III shows the results for both media samples.

The inhomogeneous broadening term in the low noise medium is twice that of the high noise medium. This may result from the following: The low noise media is comprised

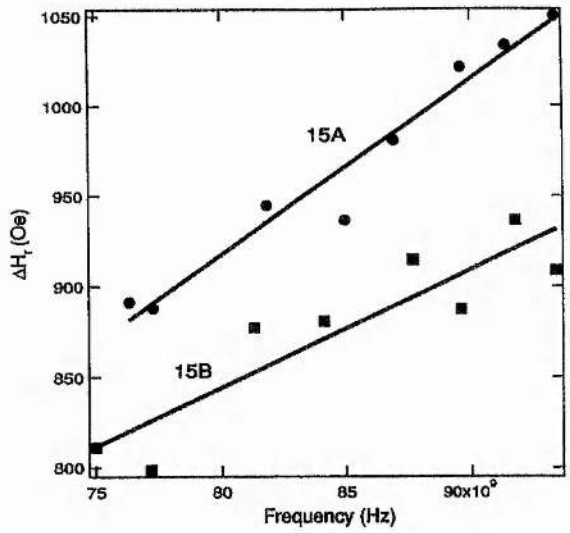

FIG. 8. Resonance linewidth for samples 15A (circles) and 15B (squares) as a function of frequency. Solid lines—result of fits using Eq. 9.

of smaller grains (11 nm) with better grain segregation than that of the high noise media where the mean grain size (42 nm) is approximately four times greater. The segregation leads to better isolation of the magnetic moments and, therefore, reduces exchange coupling between the grains. Consequently, the inhomogeneity of the medium is greater as a result of a larger number of spins in different local magnetic environments, nonetheless, the noise, associated with the exchange coupling, is lower. This interpretation is also supported by the values of the Gilbert damping factors. For the sample with larger grains (high noise medium) the damping factor is greater. This indicates a faster relaxation time which may again be a result of stronger intergrain coupling in this sample.

VI. CONCLUSIONS

In this paper we have for the first time shown convincingly that high field, multi-frequency (75–93 GHz) FMR may be used to determine the static (H_k) and dynamic properties (damping constant α) of realistic ($\approx$3 Gbits/in^2) longitudinal thin film recording media. While, in principle, H_k, M_s and the Landé g-factor may all be extracted from the FMR data, in practice we find that fixing the value of M_s, which is easily obtained from magnetometry measurements, reduces the uncertainty in the values obtained for the other parameters. The advantage of high applied fields is that neighboring grains are more decoupled, minimizing the effect of interactions. Interactions often lead to a lower value of magnetocrystalline anisotropy being reported when measuring materials such as CoCr based thin films ($H_k \approx 6-9$ kOe) using moderate applied fields from iron-cored electromagnets <20 kOe.

TABLE III. Parameters of the inhomogeneous broadening ΔH_r and the Gilbert damping factor α as a result of fitting to Eq. (9).

Sample	$\Delta H_r(0)$ (Oe)	α
15A (high noise)	150±84	0.0249±0.0025
15B (low noise)	358±69	0.0159±0.0021

Two thin-film recording media chosen for this investigation have already been extensively studied.[5,6] The media consisted of the same composition of CoCrPtTa alloy sputtered onto different underlayer structures leading to very different recording properties. The anisotropy field measured by FMR was 10.8 kOe for both media investigated which is 1.2 kOe greater than values of 9.6 kOe obtained from torque magnetometry. The Landé g-factor derived was 2.15. Differences in the damping constant α were measured for the two media, with the high noise medium having $\alpha=0.025$ and the medium with a superior recording performance having $\alpha=0.016$. Given the very different microstructures of these media it is possible to speculate that the anisotropy is more strongly dependent on the alloy composition whereas the damping factor and therefore the high frequency reversal properties are more strongly governed by the microstructure. However, significant extra work will need to be completed in order to validate such a speculation.

ACKNOWLEDGMENT

CJO gratefully acknowledges the EPSRC for providing funding to do this experiment.

[1] S. Chikazumi, *Physics of Magnetism* (Wiley, New York, 1964).
[2] T. L. Gilbert, Phys. Rev. **100**, 1243 (1955).
[3] A. F. Torabi, H. Zhou, and H. N. Bertram, J. Appl. Phys. **87**, 5669 (2000).
[4] M. E. Schabes, H. Zhou, and H. N. Bertram, J. Appl. Phys. **87**, 5666 (2000).
[5] E. T. Yen, S. Z. Wu, T. Thomson, R. Ristau, R. Ranjan, G. C. Rauch, C. Habermeier, and R. Sinclair, IEEE Trans. Magn. **35**, 2730 (1999).
[6] L. Halloway and H. Laidler, IEEE Trans. Magn. **37**, 1459 (2001).
[7] G. Smith, J. C. G. Lesurf, R. H. Mitchell, and P. C. Riedi, Rev. Sci. Instrum. **69**, 3924 (1998).
[8] F. Y. Ogrin, J. Magn. Magn. Mater. (to be published).
[9] J. Smit and H. G. Beljers, Philips Res. Rep. **10**, 113 (1955).
[10] J. F. Cochran, J. M. Rudd, M. From, B. Heinrich, W. Bennett, W. Schwarzacher, and W. F. Egelhoff, Phys. Rev. B **45**, 4676 (1992).
[11] F. Y. Ogrin, "Ferromagnetic resonance studies of cobalt films and cobalt based multilayers produced by MOCVD," Ph.D. thesis, University of Keele, U.K. (1996).
[12] P. C. Riedi, T. Thomson, and G. J. Tomka, *NMR of Thin Magnetic Films and Superlattices*, Handbook of Magnetic Materials 12 (1999), edited by K. H. J. Buskow, (Elsevier Science, B.V., 1999), Chap. 2.
[13] F. Y. Ogrin, S. L. Lee, and Y. F. Ogrin, J. Magn. Magn. Mater. **219**, 331 (2000).
[14] M. Prutton, *Thin Ferromagnetic Films* (Butterworth, London, 1964).
[15] L. Albini, G. Carlotti, G. Gubbiotti, L. Pareti, G. Socino, and G. Turilli, J. Magn. Magn. Mater. **199**, 363 (1999).
[16] T. Hill, S. Stempel, T. Risse, M. Baumer, and H. J. Freund, J. Magn. Magn. Mater. **199**, 354 (1999).
[17] M. Igarashi, T. Kambe, K. Yoshida, Y. Hosoe, and Y. Sugita, J. Appl. Phys. **85**, 4720 (1999).
[18] C. P. Poole, *Electron Spin Resonance—A Comprehensive Treatise on Experimental Techniques* (Wiley, New York, 1967).
[19] S. V. Vonsovskii, *Ferromagnetic Resonance* (Pergamon, New York, 1966).
[20] C. Chappert, K. Le Dang, P. Beauvillain, H. Hardequint, and D. Renard, Phys. Rev. B **34**, 3192 (1986).

ELSEVIER

Journal of Magnetism and Magnetic Materials 242–245 (2002) 402–404

Journal of magnetism and magnetic materials

www.elsevier.com/locate/jmmm

High field ferromagnetic resonance and torque magnetometry of longitudinal recording media

C.J. Oates[a,*], F.Y. Ogrin[a], P.C. Riedi[a], S.L. Lee[a], G.M. Smith[a], T. Thomson[b,1]

[a] *School of Physics and Astronomy, University of St. Andrews, St. Andrews, Fife, Scotland KY16 9SS, UK*
[b] *Seagate Technology, 47010 Kato Road, Fremont, CA 94538, USA*

Abstract

High field (>20 kOe) multi-frequency, 75–95 GHz, ferromagnetic resonance was used to determine the magnetocrystalline anisotropy and Gilbert damping parameter of two types of CoCrPtTa longitudinal recording media. The magnetocrystalline anisotropy as measured by FMR of both samples was 10.8 kOe which is larger than that measured from torque magnetometry which was 9.6 kOe. We suggest that this difference is due to the presence of exchange coupling between the grains. © 2002 Elsevier Science B.V. All rights reserved.

Keywords: Ferromagnetic resonance; Anisotropy–magnetocrystalline; Information storage—longitudinal

1. Introduction

FMR is a useful tool for determining the magnetocrystalline anisotropy and Gilbert damping factor of recording media [1,2]. The two samples concerned here have different grain size and grain size distributions which lead to their different recording properties; that is, one media sample has a higher noise than the other. The low noise media is comprised of smaller grains (11 nm) than that of the high noise media where the mean grain size (42 nm) is approximately four times greater [3]. The samples also have a different crystallographic texture as detailed in Ref. [3].

As a preliminary experiment, we examined a cobalt (30 nm) thin film. The NMR spectra, Fig. 1 shows the presence of different cobalt phases: HCP and FCC cobalt.

Analysis of 75–95 GHz FMR (with the external field, 40–50 kOe, applied normal to the plane of the thin film) showed that the Landé g-factor was 2.16 ± 0.01. This is in excellent agreement with previously measured g-factor of cobalt which is 2.15 ± 0.02 [4]. The effective anisotropy (which is the sum of the demagnetising field and crystalline anisotropy) was found to be 17.15 ± 0.20 kOe. From torque magnetometry the effective anisotropy is 16.20 ± 0.70 kOe [5] which is lower than that measured from FMR.

The high field FMR data from the recording media is modeled as non-interacting HCP CoCrPtTa grains with the c-axis distributed randomly within the film plane [2] and is derived from the Smit–Beljers equation [6]. The FMR resonant condition for the field normal to the plane is

$$\left(\frac{\omega}{\gamma}\right)^2 = (H_r - 4\pi M_s)\left(H_r - 4\pi M_s - \frac{2K_u}{M_s}\right), \quad (1)$$

where H_r is the resonant field, γ is the spectroscopic splitting factor, ω is the angular resonant frequency of the mm-wave, $4\pi M_s$ is the saturation magnetisation and K_u is the uniaxial anisotropy constant. The anisotropy field H_k is defined as $2K_u/M_s$.

A typical FMR signal of longitudinal recording media is shown in Fig. 2. (Note that the signal-to-noise is far better than that shown for earlier measurements [2].)

Since the significant error in our measurements comes from the value of the field for resonance, Eq. (1) is

*Corresponding author. Tel.: +44-1334-463079; fax: +44-1334-463104.

E-mail address: cjo@st-andrews.ac.uk (C.J. Oates).

[1] Present address. IBM, Almaden Research Center, San Jose, CA 95120, USA.

0304-8853/02/$ - see front matter
PII: S0304-8853(01)01226-4

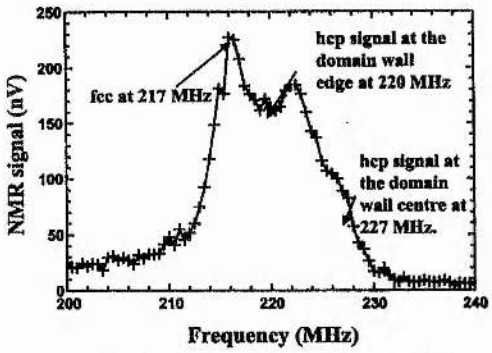

Fig. 1. Zero field ^{59}Co NMR spectra of the cobalt (30 nm) thin film at 4.2 K showing the presence of FCC and HCP phases.

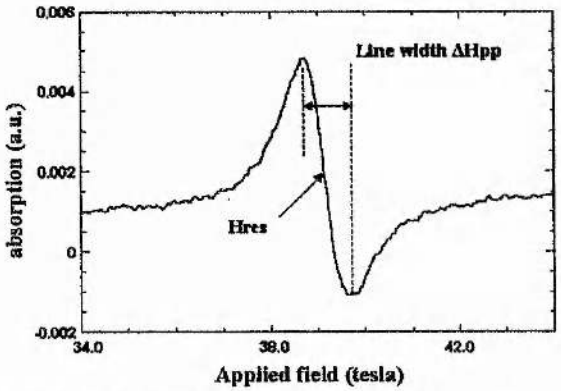

Fig. 2. FMR signal of low noise media at 84.96 GHz with the field normal to the film plane.

re-written as

$$H_r = 4\pi M_s + \frac{H_k}{2} + \frac{\sqrt{\gamma^2 H_k^2 + 4\omega^2}}{2\gamma}. \quad (2)$$

From the resonant condition over the range 75–95 GHz, it is not possible to determine the individual values of the Landé g-factor, saturation magnetisation and magnetocrystalline anisotropy uniquely. The application of a non-linear regression method to Eq. (2) showed that, while the sum $(M_s + H_k/2)$ is well defined, a range of values of M_s and H_k lead to an equally good fit to the data.

One way to overcome this problem is to introduce another technique, for example, vibrating sample magnetometry, which gives an independent determination of one of the parameters. VSM measurements gave the saturation magnetisation for the high and low noise media of 4.9 and 4.4 kOe, respectively.

The static properties (magnetocrystalline anisotropy and g-factor), determined by FMR, of both types of media were found to be similar: The higher noise sample has a g-factor of 2.15 ± 0.01 and magnetocrystalline anisotropy of 10.80 ± 0.20 kOe, while the low noise sample has a g-factor of 2.16 ± 0.01 and magnetocrystalline anisotropy of 10.70 ± 0.20 kOe.

The anisotropy was also measured using a DMS model 800 combined VSM/torque magnetometer. The angular dependence of the torque was measured in an applied field of 13 kOe and the resulting data fitted to a uniaxial anisotropy model containing a constant term K_0, a term in $K_1 \sin^2$ and a term in $K_2 \sin^4$. K_2 was found to be negligible allowing the anisotropy to be determined solely from K_1. The anisotropy field was subsequently calculated using $H_k = 2K_1/M_s$. Torque magnetometry measurements of both the high and low noise media gave a value of 9.6 kOe for the magnetocrystalline anisotropy. As in the case of the pure cobalt film, this value is lower than that derived from FMR. This may be attributed to a presence of exchange coupling between the grains of the medium. At lower fields, the exchange and magnetostatic interaction can play a significant role in the collective behaviour of the magnetic grains. In the magnetisation or torque measurements this may be seen as an effect of the reduced anisotropy. At high-field FMR, however, the effects of coupling are not significant as the sample is completely saturated and the resonance is only due to the uniform precession. As a result, the high-field FMR measurements demonstrate higher value of H_k. Consequently, the presence of a difference between the anisotropy field values for the two techniques is a good indicator of the presence of exchange coupling.

Frequency dependent line width measurements provide information on the Gilbert damping factor, which is related to the switching time of the magnetisation vector and is important in characterising the dynamic response of the media. The frequency-dependent peak to peak line width [8], Fig. 2, is expressed as

$$\Delta H_{pp}(\omega) = \Delta H_{pp}(0) + \frac{2\alpha\omega}{\sqrt{3}\gamma}, \quad (3)$$

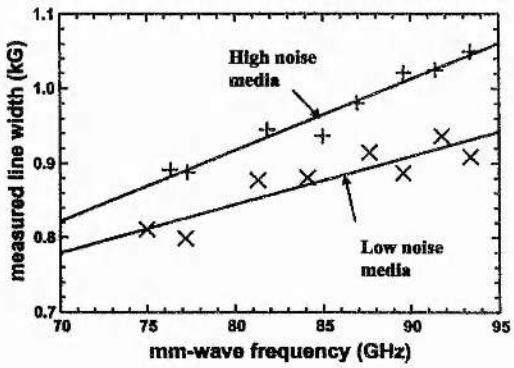

Fig. 3. Frequency-dependent line width plot of low and high noise media.

where α is the Gilbert damping factor and $\Delta H_{pp}(0)$ is related to the sample's inhomogeneous broadening.

In previous FMR work on cobalt-based recording media, the Gilbert damping factor varied between 0.013 and 0.040 [2,7]. The present line width measurements, Fig. 3, as a function of frequency showed that the Gilbert damping factor was 0.025 ± 0.003 and 0.016 ± 0.002 for high and low noise media, respectively.

The inhomogenous broadening term was found to be 0.36 ± 0.07 kOe in the low noise material and 0.15 ± 0.08 kOe in the high noise medium.

2. Conclusions

From our results it appears that there is little difference in the static and magnetic properties of the high and low noise media samples. However, it is clear that the Gilbert damping and inhomogenous broadening terms which characterises the dynamic response are significantly different.

The low noise media is comprised of smaller grains with better segregation than that of the high noise media [3]. This segregation leads to better isolation of the magnetic moments and hence reduces the exchange coupling between the grains. Consequently, the inhomogeneity of the medium is greater as a result of a larger number of spins in different local magnetic environments which is reflected in the value of $\Delta H_{pp}(0)$. Lower exchange coupling contributes to reduced noise in the case of the medium with smaller grains. This interpretation is supported by the values of the Gilbert damping factors. For the sample with larger grains (high noise medium) the damping factor is greater. The fastest relaxation time would occur for critical damping where the Gilbert damping factor is unity, thus the sample with larger grains has a faster relaxation time. This faster relaxation time may again be a result of stronger intergrain coupling in the high noise medium.

Acknowledgements

CJO gratefully acknowledges the EPSRC for providing funding to carry out these measurements.

References

[1] U. Netzelmann, J. Appl. Phys. vol. 68 (1990) 1800.
[2] M. Igarashi, T. Kambe, K. Yoshida, Y. Hosoe, Y. Sugita, J. Appl. Phys. 85 (1999) 4720.
[3] E.T. Yen, S.Z. Wu, T. Thomson, R. Ristau, R. Ranjan, G.C. Rauch, IEEE Trans. Magn. 35 (1999) 2730.
[4] F. Schreiber, J. Pflaum, Z. Frait, Th. Muhge, J. Pelzl, Sol. State Commun. 93 (1995) 965.
[5] F.Y. Ogrin, S.L. Lee, Y.F. Ogrin, J. Magn. Magn. Mater. 219 (2000) 331.
[6] J. Smit, H.C. Beljers, Philips Res. Rep. 10 (2) (1995) 113.
[7] N. Inaba, Y. Uesaka, A. Nakamura, M. Futamoto, Y. Sugita, IEEE Trans. Magn. 33 (1997) 2989.
[8] S.V. Vonsovskii, Ferromagnetic Resonance, Pergamon Press, New York, 1966.

ELSEVIER

Journal of Magnetism and Magnetic Materials 242–245 (2002) 321–324

Journal of magnetism and magnetic materials

www.elsevier.com/locate/jmmm

Torque magnetometry: investigation of the intergranular exchange interaction in longitudinal magnetic recording media

F.Y. Ogrin[a,*], C.J. Oates[b], S.L. Lee[b]

[a] *School of Physics, University of Exeter, Stocker Road, Exeter EX4 4QL, UK*
[b] *School of Physics and Astronomy, University of St. Andrews, KY16 9SS, UK*

Abstract

We demonstrate a new method for investigation of intergranular exchange coupling in longitudinal magnetic recording media by means of torque magnetometry. The technique we use is based on an analogy with the ΔM method where the analysis involves comparison of reversal processes in the sample with different initial magnetic states. We show that the ΔM curve has an equivalent torque representation $\Delta\tau$ which can be similarly exploited for studies on the longitudinal media. To validate the method we involve micromagnetic modeling, results of which are compared with the experimental measurements on a model CoCrPtTa media sample.

Keywords: Longitudinal magnetic recording media; Intergranular coupling; Magnetocrystalline anisotropy

Magnetocrystalline anisotropy and intergranular exchange coupling are the fundamental properties which determine recording characteristics of the storage media. Despite considerable efforts it still remains an experimental challenge to quantify correctly parameters of the anisotropy field H_k and the exchange stiffness constant for the longitudinal media. The main difficulty is that in a collective motion of the magnetic moments the exchange interaction acts in a similar manner to the anisotropy. As a result it is difficult to distinguish between the two effects. A number of methods have been utilised in order to deal with the effects separately. For instance, for the case of the magnetocrystalline anisotropy effect an application of high external field can help to reduce the influence of the intergranular exchange energy [1]. For the case of the exchange coupling not many techniques are available because of the inhomogeneous nature of the media samples. One method which has been utilised so far is the "ΔM" technique [2]. Using this technique the progress of the magnetisation reversal is compared for the system having the initial magnetisation in the maximum remanent state (magnetised) and in the zero remanent state (demagnetised). Using the fact that for the noninteractive media both processes are equivalent, a deviation from zero is then taken as a result of interaction between the moments. This explicit method has been shown to be useful for studying both dipole–dipole and exchange interactions in particulate and polycrystalline media. Here we extend this approach to torque magnetometry and describe a method which uses an analogy of the ΔM technique to measure the intergranular coupling in longitudinal media by means of torque magnetometry. Using this analogy we show that torque measurements can be equally useful as magnetisation measurements. As an example we demonstrate micromagnetic simulations and experimental data performed on a CoCrPtTa media sample.

The sample was prepared by sputtering on super-smooth glass–ceramic substrates using a standard commercial DC magnetron sputtering system [3]. The micromagnetic model is based on a simple two-dimensional thin film interpretation where the magnetic layer is represented by a square array of magnetic moments. Each moment corresponds to a crystalline magnetic grain with a uniaxial anisotropy. Easy directions of grains are random, but confined to the film plane. The interactions between the grains are governed by the dipolar and exchange forces. While the exchange field is calculated only for the local neighbouring moments the

*Corresponding author: Tel.: +44-1392-264116; fax: +44-1392-264111.
E-mail address: f.y.ogrin@exeter.ac.uk (F.Y. Ogrin).

0304-8853/02/$ - see front matter
PII: S0304-8853(01)01225-2

dipolar (or demagnetising) field is calculated as a contribution from all moments comprising the film. The latter is achieved by using a two-dimensional fast-Fourier transform (FFT). The total free energy for each grain is described by

$$E_i = -\vec{m}_i \cdot \vec{H} + \sum_j \frac{\vec{m}_i(\vec{m}_j \cdot \vec{n}_j)}{\vec{r}_{ij}} + K\sin^2\phi + C \sum_{j:r_{ij}<R_{loc}} \vec{m}_i \cdot \vec{m}_j, \quad (1)$$

where $\vec{m}_i = M/M_s$ is the unit magnetisation vector, $K = H_k/2M_s$ is the magnetocrystalline anisotropy constant, $\vec{n}_j$ normal to surface unit vector, C is the intergranular exchange constant and R_{loc} defines radius of the exchange interaction. The four terms in Eq. (1) represent consequently Zeeman, magnetostatic, anisotropy and exchange energies.

The main idea behind the ΔM technique is to measure only that part of the magnetisation which undergoes an irreversible transition. The experiment is performed by a successive increase of the applied field at each point followed by a return of the field to zero where the magnetisation is measured. To perform analogous measurements with the torque one can use the fact that when the applied field is perpendicular to the film plane, the resultant torque from the system is changed from the previous field value by only those moments which irreversibly "flipped" to a lower-energy minimum. To make an account of this and build a $\Delta\tau$ curve one can use the following procedure.

IRM curve: $T_r(H)$. The sample is primarily demagnetised. The external field is applied gradually starting with zero. At each point the field is first directed in the plane of the film and increased up to the next successive value. Then the field is rotated into the perpendicular orientation to the sample where the torque signal is measured. Any detected torque at this point is a contribution from the reversed moments and those which have the same easy axis orientation. Other moments do not produce torque as they cancel each other due to random distribution of the easy axes and randomisation during the demagnetisation process. If no reversal occurred the total torque is zero (see Fig. 1(a)).

DCD and $M_{r(\infty)}(H)$ curves: $T_d(H)$ and $T_{r(\infty)}(H)$. The sample is fully magnetised in an arbitrary direction within the film plane. At each point the external field is applied in the direction of the initial magnetising and then moved in to the perpendicular orientation where the value of $T_{r(\infty)}(H)$ is measured (see Fig. 1(b)). The torque here contains contributions from the all moments: due to the field-dependent nature of torque $T_{r(\infty)}(H)$ cannot be simply normalised to unity, as it is the case for $M_{r(\infty)}$ in the ΔM method, and therefore must be measured for all the field values. Next, the external field is moved back to the film plane, but in the opposite direction to the initial magnetising. By this point the moments which could overcome the energy barriers will have completed the reversal, whereas the others will still be residing at the local energy minima. Then, the field is moved back to the perpendicular direction where the value of $T_d(H)$ is measured. The resultant torque at this point contains contribution both from the moments which have reversed and from those which have not, however the difference between the values of $T_{r(\infty)}(H)$ and $T_d(H)$ give information only on the moments which performed the reversal (see Fig. 1(c)).

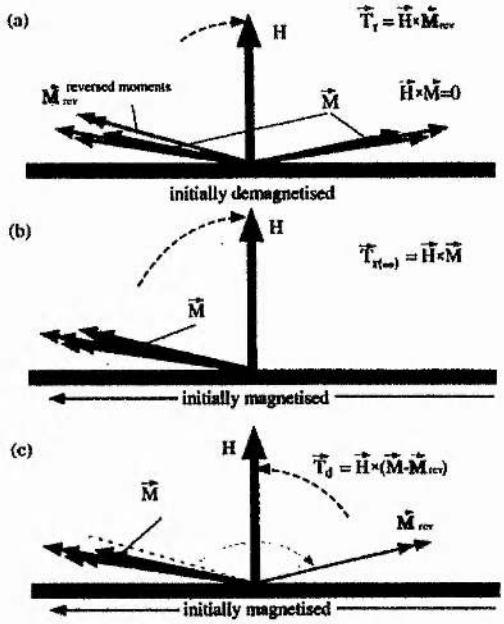

Fig. 1. Diagram of magnetic moment orientations in the torque measurements of (a) T_r, (b) $T_{r(\infty)}$ and (c) T_d.

It is easy to verify that for a noninteractive media the Wohlfarth relation [4] is also valid for the torque:

$$T_d(H) = T_{r(\infty)}(H) - 2T_r(H) \quad (2)$$

Fig. 2 shows an example of simulation on noninteractive media produced for an arbitrary field value. One can see from the inset diagram that relation (2) is perfectly satisfied in this case. For an interactive media (i.e. intergranular coupling is present) the situation can be considered explicitly, as in the case of ΔM curves, by introducing a parameter $\Delta\tau$ which can be defined in the following way:

$$\Delta\tau(H) = 2T_r(H) - (T_{r(\infty)}(H) - T_d(H)) \quad (3)$$

The meaning of $\Delta\tau(H)$ is to measure the deviation from the Wohlfarth relation (2). In a simplified interpretation a positive value of $\Delta\tau(H)$ is associated

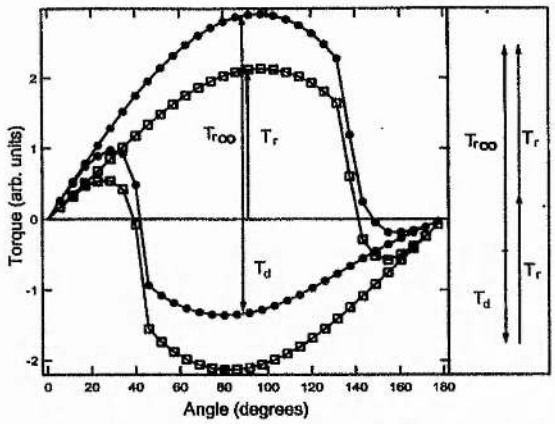

Fig. 2. Simulation of the angular dependence of torque for initially demagnetised (squares) and magnetised (filled circles) sample. Vectors T_r, $T_{r(\infty)}$ and T_d are determined by measuring the torque amplitude at 90°. The intergranular coupling (both dipolar and exchange) is not present in this case; the inset demonstrates that the Wohlfarth Relation (2) is satisfied.

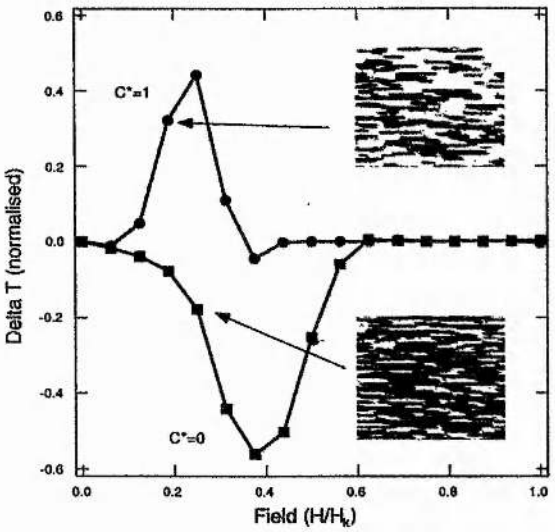

Fig. 3. $\Delta\tau$ curves produced by micromagnetic simulation for a media sample with no exchange coupling ($C = 0$) and strong exchange coupling ($C = 1$). The insets show domain patterns corresponding to these cases ($H/H_k \approx 0.2$).

with an increase of the intergranular exchange interaction; a negative value is associated with mostly dipolar coupling; and $\Delta\tau(H) = 0$ implies no interaction between the grains.

To check the validity of this interpretation we simulated $\Delta\tau(H)$ using our micromagnetic model. Fig. 3 demonstrates two examples of the $\Delta\tau(H)$ curves

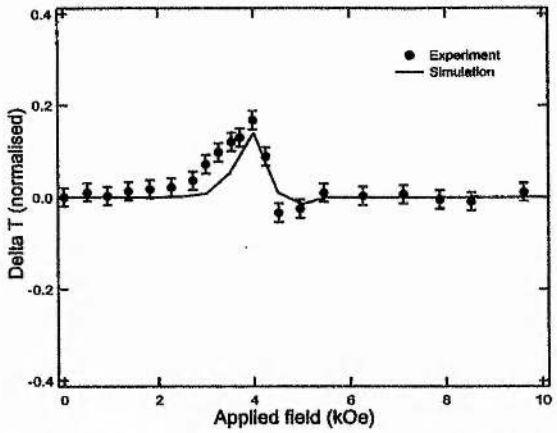

Fig. 4. Experimental and simulated $\Delta\tau$ curves produced for a sample of CoCrPtTa.

simulated for a sample with only dipole–dipole coupling and a sample with both dipolar and exchange coupling. For the sample with no exchange a negative peak is observed, whereas for the sample with a strong exchange coupling ($C = 1$) a positive peak takes place. For the intermediate values of C the $\Delta\tau(H)$ curve takes intermediate positions in a similar way as described by Walmsley and Chantrell [5] for ΔM curves. It should be noted that given the regular structure of the model (i.e. moments are arranged in a perfect lattice), and a simplified description of the exchange energy, the values of the exchange constant should only be treated as indicators of a different extent of interaction. In an irregular (or more realistic) system the exchange coupling is most likely to produce a different type of curve, however the general trend with the increase of C is expected to be the same.

Fig. 4 shows $\Delta\tau(H)$ curves measured and simulated for sample 15A, which has been previously investigated by other techniques, including ΔM measurements [3,6]. In the simulation we used the following parameters of the exchange coupling and the anisotropy: $C = 0.5, H_k = 9.0(4)$ kG. The anisotropy field value is consistent with that measured on vector/torque VSM (9.6 kG) [6] and H_k values previously determined on similar compounds [7]. However, it is found to be lower than the value measured on the same sample by FMR ($H_k = 10.7(2)$ kG) [6]. This might be explained by the restricted range of the applied field (up to 9.6 kG), which was not enough to completely magnetise/demagnetise the sample. The presence of intergranular exchange coupling in the sample comes in agreement with the suggested idea [6] that the low field measurements exhibit lower values of anisotropy ($H_k \approx 9.6$ kG) due to the influence of the exchange forces.

In conclusion, we have described a new method which can be applied for studies of coupling effects in longitudinal magnetic recording media using torque magnetometry.

References

[1] J.J.K. Chang, Q. Peng, H.N. Bertram, R. Sinclair, IEEE Trans. Magn. 32 (1996) 4902.
[2] P.E. Kelly, K. O'Grady, P.I. Mayo, R.W. Chantrell, IEEE Trans. Magn. 25 (1989) 3881.
[3] E.T. Yen, S.Z. Wu, T. Thomson, R. Ristau, R. Ranjan, G.C. Rauch, IEEE Trans. Magn. 35 (1999) 2730.
[4] E.P. Wohlfarth, J. Appl. Phys. 29 (1958) 595.
[5] N.S. Walmsley, R.W. Chantrell, J. Appl. Phys. 85 (1999) 6154.
[6] C.J. Oates, F.Y. Ogrin, S.L. Lee, P.C. Riedi, G. Smith, T. Thomson, J. Appl. Phys. 91 (2002), in press.
[7] N. Inaba, Y. Uesaka, A. Nakamura, M. Futamoto, Y. Sugita, IEEE Trans. Magn. 33 (1997) 2989.